

October 2022

How Do Galaxies Form Their Stars Over Cosmic Time?

Jed H. McKinney
University of Massachusetts Amherst

Follow this and additional works at: https://scholarworks.umass.edu/dissertations_2



Part of the [External Galaxies Commons](#), and the [Stars, Interstellar Medium and the Galaxy Commons](#)

Recommended Citation

McKinney, Jed H., "How Do Galaxies Form Their Stars Over Cosmic Time?" (2022). *Doctoral Dissertations*. 2676.

<https://doi.org/10.7275/31036263> https://scholarworks.umass.edu/dissertations_2/2676

This Open Access Dissertation is brought to you for free and open access by the Dissertations and Theses at ScholarWorks@UMass Amherst. It has been accepted for inclusion in Doctoral Dissertations by an authorized administrator of ScholarWorks@UMass Amherst. For more information, please contact scholarworks@library.umass.edu.

**HOW DO GALAXIES FORM THEIR STARS
OVER COSMIC TIME?**

A Dissertation Presented

by

JED H. MCKINNEY

Submitted to the Graduate School of the
University of Massachusetts Amherst in partial fulfillment
of the requirements for the degree of

DOCTOR OF PHILOSOPHY

September 2022

Astronomy

© Copyright by Jed H. McKinney 2022

All Rights Reserved

HOW DO GALAXIES FORM THEIR STARS OVER COSMIC TIME?

A Dissertation Presented

by

JED H. MCKINNEY

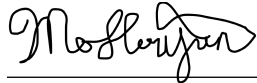
Approved as to style and content by:



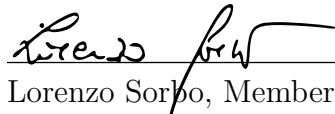
Alexandra Pope, Chair



Daniela Calzetti, Member



Houjun Mo, Member



Lorenzo Sorbo, Member



Daniela Calzetti, Chair of the Faculty
Astronomy

DEDICATION

*To Zoe;
for bringing me
closer to the stars
with each day*

ACKNOWLEDGMENTS

The contents of this thesis would not have been possible without the dedicated support I received from mentors, peers, family and friends. Looking back on these memories and experiences I realize how much of our science depends on the people who find us along the way.

For inspiring me to pursue study into the dusty Universe, I would like to begin by thanking my thesis advisor Dr. Alexandra Pope. Thank you for all of the guidance and mentoring over the past four years, the many comments and reviews on proposals and papers, and for the countless weekly discussions we have had. Your work on sub-millimeter galaxies with SCUBA and *Spitzer* sparked my imagination as a young scientist, and the prospect of working together was the reason I chose UMass for my graduate studies.

As my thesis research began to materialize, a number of colleagues were instrumental in helping me expand my work. Thank you to Dr. Lee Armus for hosting me at IPAC, and for passing along your careful attention to detail in writing and analysis. Dr. Tanio Diaz-Santos was instrumental in helping me with my early understanding of gas and dust physics in dusty galaxies, and has been an important mentor and friend ever since. In addition, I would like to thank Drs. Aaron Evans, George Privon, Vivan U and all of the GOALS collaboration members for welcoming me into their fold and showing me the beauty of resolved objects. For introducing me to the world of numerical simulations, I would like to thank Dr. Christopher Hayward for passing down guidance and style to a simple observer.

One of the most energizing elements of research is the incredible group of peers we come up with through undergraduate and graduate study. I would like to thank Julia

Fowler, Dr. Eric Roebuck, Dr. Erin Kado-Fong and Jesse Jedrusiak for welcoming me into my first cohort of astronomers. I owe a massive thank you to Nat DeNigris and Sarah Betti for being with me from the start of graduate school, and for being my very best of friends ever since. I know for certain that I am only here because of those long nights we shared reviewing notes over waffles. I would also like to thank Patrick Kamienesky, Zhiuyan Ji, Alyssa Sokol, and the many graduate students in the UMass department of astronomy for being a wonderful group to learn about the Universe alongside. Finally, I would like to thank my cohort of IPAC visiting graduate fellows for their friendship since we met in Pasadena: Dr. Gangadeep Anand, Brittney Vanderhoof, and Rachel Fernandes.

There are a handful of mentors who played a pivotal role in helping me find my way to the world of astronomy research. Thank you Mr. T for knowing I would succeed in math more advanced than my interest in school. Thank you Andrew Bramante for believing in my potential as a young scientist, and for giving me the time and resources to fully understand the granular realities of research. I would not be studying astronomy and astrophysics if it were not for my undergraduate advisor at Tufts University, Dr. Anna Sajina. One particular homework assignment where you tasked me with building a luminosity function crystallized my interest, and pushed me to pursue both a major in astronomy and research as an undergraduate. Thank you for taking me to UMass during junior year for a meeting with Dr. Pope, as I have enjoyed my time in Amherst, Massachusetts ever since.

I would like to thank all of the members of my thesis committee for taking the time to follow my research since defending my prospectus. Thank you in particular to Dr. Daniela Calzetti for modeling success in astronomy and on the climbing wall.

I owe the world to my family who supported me though graduate school. Thank you to my parents Joanne and Tim McKinney for giving me the freedom to find my

passion and the opportunity to realize it. Thank you to my brother Cal McKinney for being the one person I have always needed to impress.

For literally holding my hand every step of the way, I owe perhaps the largest thank you to my partner Zoe Baghdoyan. Thank you for listening, always, and for understanding. Your support through times both good and bad has become a Universal constant I depend upon. Thank you for finding our orange cat Wanda, to whom I would also like to thank for tolerating the many belly rubs I impart upon her daily.

Financial support for this work was provided by the NSF through award SOSPA5-008 from the NRAO, and through the Massachusetts Space Grant Consortium (MASGS). My time at Caltech/IPAC was supported by the IPAC Visiting Graduate Fellowship, and the last year of my dissertation has been supported by an ALMA archival SOS grant (SOSPADA-011).

ABSTRACT

HOW DO GALAXIES FORM THEIR STARS OVER COSMIC TIME?

SEPTEMBER 2022

JED H. MCKINNEY

B.S., TUFTS UNIVERSITY

Ph.D., UNIVERSITY OF MASSACHUSETTS AMHERST

Directed by: Professor Alexandra Pope

Galaxies in the past were forming more stars than those today, but the driving force behind this increase in activity remains uncertain. In this thesis I explore the origin of high star-formation rates today and in the past by studying the properties of gas and dust in the cold interstellar medium (ISM) of dusty galaxies over cosmic time. Critically, we do not yet understand how these galaxies could form so many stars. This work began with my discovery of unusual infrared (IR) emission line ratios in the class of dusty galaxies where most of the Universe's stars were formed. To fully understand the source of these unusual emission line ratios, I turn to local analogs of the distant galaxies I study at high-redshift to investigate in detail the ratio of far-IR fine-structure line emission to mid-IR Polycyclic Aromatic Hydrocarbons (PAHs). I find that gas within young star-forming regions heats and cools differently when it is compressed to high star-formation rate surface densities. I use radio spectroscopy of CO(1-0) and sub-millimeter dust continuum measurements to test how changes in heating and cooling impact the total gas reservoir, and find more efficient star-formation in compact galaxies at all redshifts. The high star-formation rates of distant

galaxies may be sustained by this more efficient mode. With spatially resolved studies, I find the IR properties of star-forming, dusty galaxies to be comparable for fixed IR surface density at low- and high-redshift. Finally, to match the formation of stars with the synchronous growth of supermassive black holes I analyze numerical simulations of galaxy formation to study the radiative feedback of active galactic nuclei on dust. Rapidly accreting supermassive black holes can heat the dust in their host galaxies, powering a significant fraction of the cold dust luminosity and biasing IR-derived star-formation rates if left unaccounted for. With the recent launch of the *James Webb Space Telescope*, the future of extragalactic infrared observations is wide open and this research provides motivation for the continued study of the cold gas and dust conditions from which new stars form.

TABLE OF CONTENTS

	Page
ACKNOWLEDGMENTS	v
ABSTRACT	viii
LIST OF TABLES	xiv
LIST OF FIGURES	xv
CHAPTER	
1. INTRODUCTION	1
1.1 Luminous infrared galaxies	4
1.2 Background on the gas and dust physics behind star-formation	7
1.3 Guide to this thesis	9
2. MEASURING THE HEATING AND COOLING OF THE INTERSTELLAR MEDIUM AT HIGH REDSHIFT: PAH AND [C II] OBSERVATIONS OF THE SAME STAR FORMING GALAXIES AT Z=2	11
2.1 Introduction	12
2.2 Sample and Observations	18
2.2.1 Sample Selection	18
2.2.2 Multiwavelength Observations	19
2.2.3 ALMA Observations and Data Processing	21
2.3 Analysis	22
2.3.1 [CII] Detection in GS IRS20	22
2.3.2 [C II] Line Searches and Upper Limits	23
2.3.3 Morphology	24
2.3.4 Comparison Samples	25
2.3.5 SED Fits to near-IR through sub-mm Photometry	30

2.4	Results	32
2.4.1	[CII] Line Luminosities	32
2.4.2	PAH Properties	33
2.4.3	The Ratio of [CII] to PAH Luminosity	35
2.5	Discussion	37
2.5.1	PAH Heating vs. Far-IR Cooling	37
2.5.2	Differences between GS IRS20 and GS IRS61	40
2.5.3	Future Outlook	41
2.6	Summary and Conclusions	41
3.	REGULATING STAR FORMATION IN NEARBY DUSTY GALAXIES: LOW PHOTOELECTRIC EFFICIENCIES IN THE MOST COMPACT SYSTEMS	44
3.1	Introduction	45
3.2	Sample Selection and Data	48
3.3	Analysis	49
3.3.1	PAH Properties	49
3.3.2	Aperture Matching	52
3.4	Results	53
3.4.1	Line-to-PAH Ratios	56
3.4.2	The Photoelectric Efficiency	58
3.5	Discussion	63
3.5.1	Alternate Explanations for decreasing ϵ_{PE} with Σ_{IR}	63
3.5.2	Dust Grain Properties and the Photoelectric Efficiency	65
3.5.3	Physical Interpretation	68
3.5.4	Prospects for Star-Formation at High-Redshift	70
3.6	Summary and Conclusion	71
4.	THE IR SIZES OF DUSTY GALAXIES SET STAR-FORMATION AND DUST PROPERTIES AT Z=0-2	74
4.1	Introduction	75
4.2	Data and Analysis	77
4.2.1	ALMA Archival Sample Selection	78

4.2.2	Source Detection	79
4.2.3	Measured Quantities	81
4.2.4	Final Sample Properties	83
4.2.5	Ancillary Data	84
4.2.6	Comparison Samples	86
4.3	Results	87
4.3.1	Dust masses	87
4.3.2	IR Sizes	91
4.3.2.1	Far-IR size as a function of mid-IR AGN fraction	97
4.4	Discussion	99
4.4.1	ISM conditions and dust composition scale with IR surface densities	99
4.4.2	Dust-obscured galaxies form stars more efficiently at high IR surface densities	103
4.5	Conclusion	105
5.	PHYSICAL GAS CONDITIONS FROM COMBINED FAR-INFRARED AND RADIO LINES AT Z=2	110
5.1	VLA Data	111
5.1.1	Description of Observations	111
5.1.2	Decoherence	111
5.1.3	Reduction, Imaging and Spectral Extraction	112
5.1.4	Spectral Line Detections	114
5.2	Results	116
5.2.1	Scaling between CO, PAH, and IR luminosity	116
5.2.2	Photo-dissociation Region Modeling	118
5.3	Unusual ISM conditions in GS IRS20	120
5.3.1	Empirical challenges to PDR modeling	122
5.3.2	Alternate heating sources in GS IRS20: X-ray dominated regions	123
5.3.3	Extreme densities in GS IRS20	124
5.4	Conclusions	125

6. DUST-ENSHROUDED AGN CAN DOMINATE HOST-GALAXY-SCALE COLD-DUST EMISSION	126
6.1 Introduction	127
6.2 Simulation and Radiative Transfer Details	130
6.3 Results	132
6.4 Discussion	141
6.4.1 Implications	141
6.4.2 Limitations of this work	145
6.5 Summary and Conclusions	145
7. SUMMARY AND FUTURE OUTLOOK	147
7.1 Summary of Dissertation	147
7.2 Future Work	148
7.3 Outlook for the next decade and beyond	150
7.4 Concluding Remarks	153
 APPENDICES	
A. PAH-DERIVED REDSHIFTS AND LUMINOSITIES	154
B. CALCULATING THE PROBABILITY OF OBSERVING LINES FROM TOTAL BANDPASS COVERAGE	159
 BIBLIOGRAPHY	 161

LIST OF TABLES

Table	Page
2.1 Sample Summary	13
2.2 ALMA Cycle 5 Band 9 Observations: Continuum Imaging and Spectral Line Data.....	22
2.3 Derived Parameters from IR-SED Fits.....	34
2.4 Existing <i>Spitzer</i> and <i>Herschel</i> Photometry	43
2.5 Existing <i>Spitzer</i> and <i>Herschel</i> Photometry (<i>continued</i>)	43
3.1 Best-fit Parameters to Line/PAH ratios vs. Σ_{IR}	56
3.2 Correlation Coefficients between the Photoelectric Efficiency, as defined by the ratio of IR cooling lines to mid-IR PAH emission between 6 – 12 μm , and other Quantities in GOALS star-forming Galaxies	59
4.1 Source characteristics for <i>Spitzer</i> /IRS targets matched to ALMA	85
4.2 Archival ALMA observed quantities and derived properties	88
4.3 Best-fit Parameters and their Uncertainties for Linear Fits to Data	99
5.1 IRS Sample and derived quantities from <i>Spitzer</i> spectra	114
5.2 Observations and CO measurements	115
6.1 Maximal boosting of host-galaxy FIR dust emission by a dust-enshrouded AGN at selected wavelengths, and for integrated IR luminosities.	141

LIST OF FIGURES

Figure	Page	
1.1	Images of the same extragalactic deep field observed at near-IR (<i>Left</i>) and sub-mm (<i>Right</i>) wavelengths.	5
1.2	Major paradigms in galaxy evolution.	6
1.3	Observing the ISM at IR and radio wavelengths.	10
2.1	The $z \sim 2$ star-forming main-sequence of Speagle et al. (2014) (dashed black line) assuming the same (Salpeter) IMF used in our calculations.	16
2.2	<i>Spitzer IRS</i> spectra for 6 targets observed with ALMA.	17
2.3	Postage stamp images for each of the targeted galaxies.	20
2.4	GS IRS20's ALMA Band 9 continuum-subtracted spectrum showing the robust detection of [C II]	26
2.5	Multiwavelength photometry and spectra for each ALMA target.	27
2.6	The ratio of cold dust emission, L_{cold} , to L_{IR} as a function of $f_{\text{AGN,MIR}}$, the AGN contribution to emission at mid-IR wavelengths.	29
2.7	The ratio of [C II] luminosity to L_{IR} in low- and $z \sim 2 - 3$ star-forming galaxies and AGN.	30
2.8	(<i>Left</i>) The ratio of $L_{6.2\mu\text{m}}$ to L_{IR} in low- and high-redshift IR-luminous galaxies as a function of L_{IR} . (<i>Right</i>) The ratio of $L_{6.2\mu\text{m}}$ to L_{IR} vs. IR surface density.	32
2.9	The ratio of [C II] luminosity to $6.2\mu\text{m}$ PAH luminosity in low-redshift and $z \sim 2$ IR-luminous star-forming galaxies as a function of IR surface density.	36
2.10	The ratio of $L_{6.2\mu\text{m}}$ to $L_{11.3\mu\text{m}}$ vs. effective IR surface density calculated at rest-frame $160 \mu\text{m}$	37

3.1	The ratio of [C II] emission to the sum of 6.2, 7.7, 8.6, 11.3 and 17 μm PAH emission in the nuclear regions of GOALS star-forming galaxies as a function of total IR luminosity.	50
3.2	(<i>Left</i>) The [C II] deficit in GOALS as presented by Díaz-Santos et al. (2017), calculated with galaxy-integrated measurements of $L_{[\text{C II}]}$ and L_{IR} . (<i>Right</i>) The ratio of $L_{[\text{C II}]}$ to L_{PAH} (summing over all features between 6 – 18 μm) for star-forming (U)LIRGs with <i>Herschel</i> /PACS [C II] measurements and <i>Spitzer</i> /IRS observations of the PAHs.	53
3.3	IR cooling lines over PAH emission in GOALS star-forming (U)LIRGs vs. IR surface densities.	54
3.4	The ratio of prominent IR cooling lines to total PAH luminosity, an estimate of the photoelectric efficiency in PDRs, vs. IR surface density.	55
3.5	The photoelectric efficiency calculated as the sum of [C II], [O I], and [Si II] emission over the flux of PAH emission including lines between 6 – 18 μm vs. G/n_{H} , the ratio of the average radiation field strength impinging upon PDRs to the mean neutral Hydrogen density.	62
3.6	(<i>Left</i>) The photoelectric efficiency vs. the ratio of 11.3 to 7.7 μm PAH emission in our sample of star-forming GOALS (U)LIRGs. (<i>Right</i>) Same as the <i>Left</i> panel, now as a function of the ratio of 7.7 to 6.2 μm PAH emission, a tracer of the average Cationic grain size as both features arise from ionized PAHs.	63
3.7	The photoelectric efficiency vs. the ratio of 11.3 μm to 3.3 μm PAH emission, a size tracer for PAH grains.	67
3.8	The $L_{11.3 \mu\text{m}}/L_{7.7 \mu\text{m}}$ vs. $L_{11.3 \mu\text{m}}/L_{3.3 \mu\text{m}}$ PAH ratio in GOALS (U)LIRGs with AKARI observations of the 3.3 μm PAH feature.	69
4.1	(<i>Top</i>) Distribution in L_{IR} amongst galaxies matched to ALMA archival detections (blue) compared against non-detections within the footprint of an archival observation (brown) and the parent GOODS-S sample (grey). (<i>Bottom</i>) Peak flux vs. L_{IR} for detections and non-detections.	80

4.2	Distribution in specific star-formation rates relative to the main-sequence (Δ sSFMS) for fixed M_* and redshift using the MS parameterization of Speagle et al. (2014).	84
4.3	The ratio of the $6.2 \mu\text{m}$ PAH luminosity relative to the total dust mass in our $z \sim 1 - 2$ ALMA-detected <i>Spitzer</i> /IRS sample, GOALS, and KINGFISH as a function of Σ_{IR}	89
4.4	The effective IR size as a function of total infrared luminosity.	92
4.5	A comparison between the effective IR size and the total dust mass for this work (blue symbols, following $f_{\text{AGN,MIR}}$ classifications in Fig. 4.4), GOALS (purple circles), and KINGFISH (grey diamonds).	93
4.6	The ratio of total infrared luminosity to total dust mass as a function of IR size in $z \sim 0 - 2$ (U)LIRGs (GOALS, this work) and KINGFISH galaxies at lower star-formation rate surface densities.	94
4.7	IR size vs. the fractional contribution of AGN to the integrated mid-IR emission ($f_{\text{AGN,MIR}}$).	95
4.8	PAH/ L_{IR} vs. IR surface density.	100
4.9	(<i>Left</i>) The ratio of AGN-corrected IR luminosity to total dust mass, a tracer of the star-formation efficiency, as a function of IR surface density. (<i>Right</i>) Distance from the specific star-forming main-sequence as a function of Σ_{IR} for each galaxy's redshift and stellar mass.	101
4.10	ALMA contours (red levels) on <i>HST</i> /F160W and <i>Spitzer</i> /IRAC4 images for each of the targets in our ALMA-detected catalog.	108
4.11	Continuation of Fig. 4.10.	109
5.1	Collapsed CO(1-0) channel maps in GN IRS18 (<i>left</i>), GN IRS25 (<i>center</i>), and GS IRS20 (<i>right</i>) represented as black contours overlaid over <i>HST</i> /WFC3 H_{160} images from 3D-HST (Skelton et al., 2014; Grogin et al., 2011; Koekemoer et al., 2011).	113
5.2	VLA/Q-band detections of CO(1-0) in GN IRS18 (<i>Left</i>) and GN IRS25 (<i>Right</i>).	115
5.3	CO(1-0) in GS IRS20 (black), with a gaussian fit shown in red.	116

5.4	CO(1-0) upper limits for GS IRS45 (<i>Left</i>), GS IRS 54 (<i>Middle</i>), and GS IRS 61 (<i>Right</i>).	116
5.5	Scaling relations between tracers of dust-obscured star-formation and molecular gas.	117
5.6	Radiation field strength (G_0) and hydrogen density (n_H) determined from PDR modeling using PDR ToolKit for GS IRS20.	119
5.7	A collection of radiation field strengths (G/G_0) and densities in PDRs ($n/[\text{cm}^{-3}]$) for galaxies in the literature compared against GS IRS20 (red square).	121
6.1	Rest-frame SED for the AGN-10x model (dashed line) at the time of peak $L_{\text{AGN}}/L_{\text{SF}}$, where the AGN dominates the bolometric luminosity and the time at which the AGN contributes maximally to the FIR luminosity during this simulation.	133
6.2	Emission maps of the simulated merger at a representative time following the peak SFR and peak bolometric AGN luminosity (marked by the dashed line in the top panel).	134
6.3	The ratio of flux within a simulated <i>JWST</i> /MIRI beam placed on the center of the galaxy relative to the total flux across the PSF-convolved map, for various MIRI filters.	137
6.4	The ratio of the IR luminosity integrated in different bands for RT calculations with AGN+host galaxy-powered dust emission ('fiducial' or 'AGN 10x') relative to those with only host galaxy dust emission ('AGN off') vs. the ratio of bolometric AGN to star formation luminosity.	138
6.5	(<i>Left</i>) <i>Herschel</i> PACS $100\mu\text{m}/70\mu\text{m}$ vs. $160\mu\text{m}/100\mu\text{m}$ colors (assuming $z = 2$). (<i>Right</i>) <i>Herschel</i> SPIRE $350\mu\text{m}/250\mu\text{m}$ vs. $500\mu\text{m}/350\mu\text{m}$ colors (assuming $z = 2$) following the same color scheme as the left panel.	139
6.6	The total (<i>dotted black line</i>) and effective AGN (<i>solid black line</i>) SEDs already shown in Figure 6.1, but now compared against the dusty AGN torus models from Fritz et al. (2006).	143
7.1	<i>JWST</i> observations of NGC7469, a star-forming galaxy in the GOALS sample that hosts a bright AGN.	151

7.2	Snapshots from state-of-the art simulations that resolve the ISM over six orders of magnitude in spatial scale and gas mass surface density.	151
7.3	(<i>Left</i>) Predicted far-IR fine-structure line fluxes as a function of redshift for a galaxy with $\log L_{\text{IR}}/L_{\odot} = 11$. (<i>Right</i>) Histogram of the number of galaxies in $L_{\text{IR}}-z$ space detected in a blind spectral line survey given the design specifications of a potential probe-class IR space telescope.	153
A.1	The importance of model selection in estimating redshifts from PAH spectra.	156

CHAPTER 1

INTRODUCTION

The science of extragalactic astronomy seeks to explain the objects we see in the dark sky that exist outside of our home galaxy, the Milky Way. In 1912 Henrietta Swan Leavitt published a relationship between the luminosity and period of Cepheid variable stars which would go on to provide conclusive evidence that the spiral nebulae of the Great Debate were indeed galaxies exterior to the Milky Way (Leavitt & Pickering, 1912; Hubble, 1926). The Universe was much larger, and more interesting, than previously thought, and Astronomers have worked to find more distant galaxies ever since.

The images in Figure 1.1 capture one such pivotal effort where, by pointing space telescopes (*The Hubble Space Telescope*, Fig. 1.1 *Left*) and ground observatories (James Clerk Maxwell Telescope, Fig. 1.1 *Right*) at a small and dark patch of sky for over 50 hours revealed thousands of galaxies, some dating back to the dawn of our Universe. Efforts to understand how these galaxies came to be have progressed rapidly in recent years, and while major paradigms within extragalactic astrophysics and its subfield “galaxy evolution” are coalescing, the answers to many fundamental questions remain obscure. Over the course of my thesis research, I have worked to study the origins of stars in galaxies both today and in the distant past to shed light on a fundamental story about the past history of our Universe:

Ten billion years ago, well before Earth had coalesced from the rubble around our sun, galaxies were forming more stars than ever before. In fact, the average galaxy was about thirty times more active back then compared to today (e.g., Lilly et al.,

1996; Madau et al., 1996; Chary & Elbaz, 2001; Madau & Dickinson, 2014; Speagle et al., 2014). For its first two to three billion years, when the Universe was young, galaxies were becoming progressively more active (e.g., Finkelstein et al., 2015; Zavala et al., 2021). After a moment in time about eight to ten billion years ago this growth spurt faded and galaxies have formed fewer and fewer stars ever since. The volume-averaged history of star-formation in galaxies over time is commonly referred to as the “star-formation rate density” and is sketched in Figure 1.2 as a function of redshift (z). Within the context of studying distant galaxies, a galaxy’s redshift refers to the doppler shifting of its light from shorter to longer wavelengths. The Universe is expanding, causing more distant galaxies to have higher redshift. Therefore, redshift is also a measure of distance to a galaxy. Portions of my research focus on galaxies in the local Universe ($z \sim 0$) with distances below ~ 250 Mpc, equivalent to ~ 800 million light years. I also study the properties of galaxies at $z \sim 1 - 3$ which are approximately 15,000 Mpc or ~ 50 billion light years away. The light from these distant “high-redshift” galaxies has travelled ~ 10 billion years before reaching Earth, which allows astronomers to effectively look back in time to study the history of the Universe.

The rise and fall of the star-formation rate density is a fundamental paradigm in galaxy evolution: it contextualizes galaxies at all epochs, and is an essential record of the Universe’s growth from infancy into its present state. Nevertheless, a number of fundamental aspects remain the subject of debate and many open questions remain. What physical mechanisms govern changes in the star-formation rates of galaxies? In other words, why do we see the historical record of star-formation as-is? What is the link between the growth of stars and galaxies and the assembly of their central supermassive black holes, both today and in the past? Do we have a complete census of the star-formation rate density, or are we critically limited by the wavelengths at which the history of the Universe can be measured at? For instance, the two

images taken at short and long wavelengths shown in Figure 1.1 reveal vastly different galaxy populations. The path forwards towards answering these questions is long and often splits. In this thesis I present my journey along one such winding way, using telescope observations and computer simulations to better understand the history of star-formation over cosmic time.

This dissertation focuses on the question: *Why are the star-formation rates of galaxies in the past greater than those today?* We know from cosmological computer simulations that around the peak of the star-formation rate density gas accretion rates from the intergalactic medium onto galaxies are at their highest (Kereš et al., 2005). Galaxies were able to feed off the gas in their surrounding environments. This provides the fuel for galaxies to form new stars, and subsequent decline in star-formation up to the present day may reflect the consumption of gas as re-supply from the intergalactic medium diminishes (e.g., Walter et al., 2020); however, when measuring the gas budget of galaxies up to high-redshift, many empirical studies cannot account for the amount of star-formation with accretion alone (Scoville et al., 2017b; Liu et al., 2019; Tacconi et al., 2018). These works must invoke evolution in the efficiency of star-formation to reconcile the gas budget with the star-formation rate density. The star-formation efficiency ($\text{SFE} \equiv \text{SFR}/M_{\text{gas}}$) is the observed ratio of a galaxy’s star-formation rate to its gas mass, and is sensitive to physics on different spatial scales ranging from interactions between gas and photons within individual clouds ($\sim 10 - 100$ pc) to gas accretion from the environment (~ 1 Mpc). These processes also play out on different timescales over the lifetime of giant molecular clouds (~ 10 Myr) and accretion from the intergalactic medium (~ 100 Myr – 1 Gyr), which further complicates the assignment of efficient star-formation averaged over the star-forming burst of a galaxy to any single mechanism. Nevertheless, a higher efficiency yields more stars for fixed input gas mass. As is shown in 1.2 (*Right*), different works come to disparate conclusions as to how much evolution in the efficiency of star-formation

is needed to reconcile the gas budget in galaxies with the amount of star-formation. This reflects a massive gap in our knowledge about how most of the stars in the Universe were formed. Evolution over time in the efficiency of star-formation could be a critical factor driving the high star-formation rates of galaxies (Scoville et al., 2017b; Liu et al., 2019), or not (Walter et al., 2020). In either case, galaxies with unusually high star-formation rates do exhibit high efficiencies up to $z \sim 2.5$ (Genzel et al., 2015). My dissertation research focuses on the conditions of gas from which new stars form to better understand the mechanisms regulating star-formation on scales of individual star-forming regions and molecular clouds.

1.1 Luminous infrared galaxies

The first steps towards measuring the star-formation rate density were made at optical/near-IR wavelengths (Lilly et al., 1996; Madau et al., 1996), and were shortly followed by observations in the sub-millimeter (Hughes et al., 1998). Figure 1.1 shows deep fields in both wavelength regimes that were state-of-the-art as of 1998. Near-IR observations trace the rest-frame optical emission dominated by hot, young stars, while far-IR/sub-mm observations are sensitive to cold dust emission heated by young stars embedded within clouds of gas and dust that have yet to shed their natal envelopes. The study of galaxies was historically focused on shorter wavelengths owing to superior spatial resolution of cutting edge facilities like the *Hubble Space Telescope* in operation; however, the sky-averaged energy (“background”) in the IR is equal to that of the optical/near-IR (e.g., Franceschini et al., 2008) meaning that both perspectives are equally important for studying the energetics of galaxies. Moreover, the inferred IR star-formation rate density is a factor of ~ 6 times greater than its counterpart in the optical/near-IR between $z \sim 0 - 3$ as shown in Fig. 1.2 *Left* (Madau & Dickinson, 2014). When corrected for dust attenuation, the UV/optical and IR star-formation rate density agree (Madau & Dickinson, 2014).

We know from observations that most of the dust-obscured star-formation happens preferentially within galaxies with IR luminosities integrated between $8 - 1000 \mu\text{m}$ (L_{IR}) exceeding 100 billion times the energy output of the sun (Murphy et al., 2011; Zavala et al., 2021) (Fig. 1.2 *Left* bottom panel). Because the dust-obscured star-formation rate density is dominant between $z \sim 0 - 3$, approximately $\sim 85\%$ of the lifetime of the Universe, these massive and IR-luminous star-factories must be well-characterized if the history of star-formation for most of cosmic time is to be understood. This concept is foundational for the scope of my dissertation research, which focuses on such dusty galaxies.

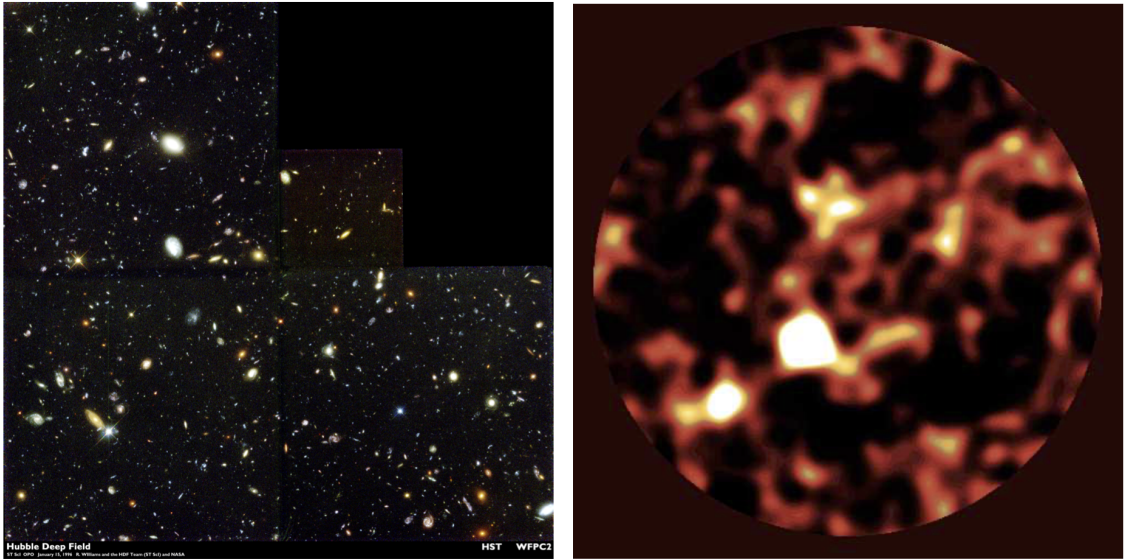


Figure 1.1 Images of the same extragalactic deep field observed at near-IR (*Left*) and sub-mm (*Right*) wavelengths. The different wavelength perspectives paint distinct pictures of the galaxies in each field. Data from the *Hubble Space Telescope*/WFPC2 (courtesy of STScI and NASA) and the James Clerk Maxwell Telescope/SCUBA respectively (Hughes et al., 1998).

Luminous IR galaxies (LIRGs) are by definition bright at IR wavelengths, tend to be massive galaxies with high star-formation rates, and commonly host active supermassive black-holes (Casey et al., 2014). At low-redshift, LIRGs represent a rare population of galaxies with excessively high star-formation rates relative to more typical galaxies of equal stellar mass and contribute little to the total star-formation

budget (Armus et al., 2009; Murphy et al., 2011). The number of LIRGs grows with increasing redshift (e.g., Chapin et al., 2009; Yun et al., 2012; Smolčić et al., 2012), and LIRGs eventually dominate the star-formation rate density by $z \sim 0.5$ (Murphy et al., 2011; Zavala et al., 2021). Therefore, high-redshift LIRGs represent an excellent galaxy population in which to study star-formation. Moreover, it remains an open question whether or not the LIRGs we find nearby are the same as LIRGs observed at earlier times, or if they form stars in fundamentally different ways as might be the case if the star-formation efficiency evolves strongly with redshift. I address this question in my work through the multi-wavelength analysis of LIRGs at low- and high-redshift.

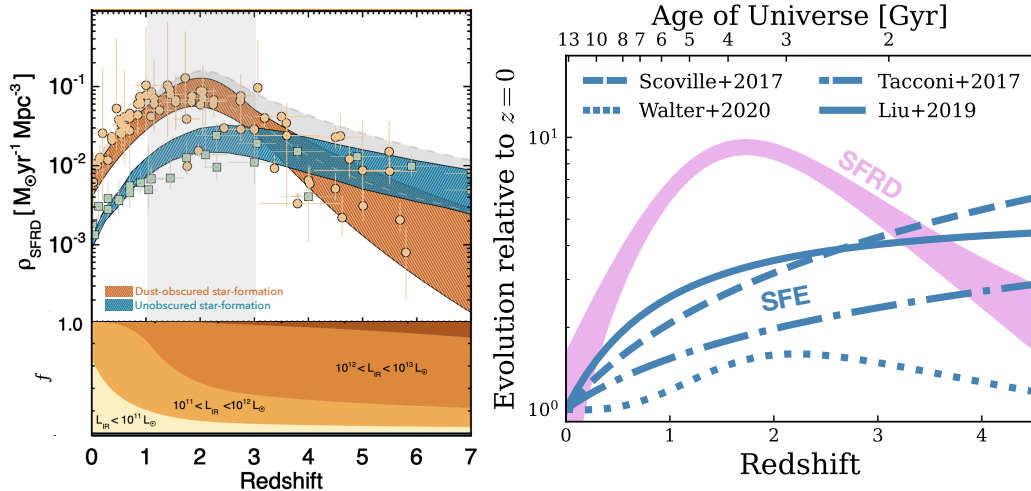


Figure 1.2 Major paradigms in galaxy evolution. (*Left*) Redshift evolution in the volume-averaged star-formation rate density (SFRD) as measured at IR (orange) and UV/optical/near-IR (blue) wavelengths tracing respectively dust-obscured and unobscured stars. The shaded grey region highlights the peak epoch for star-formation, “cosmic noon”, between $z \sim 1 - 3$. The bottom panel corresponds to the fraction of dust-obscured star-formation attributed to galaxies within bins of increasing IR luminosity (L_{IR}). At cosmic noon, most of stars form within galaxies exceeding $\log L_{\text{IR}}/L_{\odot} > 11$. Figure adapted from Zavala et al. (2021). (*Right*) Evolution relative to today ($z = 0$) in the SFRD out to ~ 12.4 Gyr in the past ($z \sim 4.5$). The SFRD parametrization shown in purple is from Walter et al. (2020). Blue lines correspond to different estimates in the star-formation efficiency (SFE) required to reconcile the SFRD with the gas budget within galaxies (Scoville et al., 2017b; Tacconi et al., 2018; Liu et al., 2019; Walter et al., 2020). Whether or not galaxies formed their stars systematically more efficiently in the past remains the subject of debate.

1.2 Background on the gas and dust physics behind star-formation

The study of gas and star-formation in distant galaxies is anchored by observations of objects within the Milky Way and in very nearby galaxies. From the rich literature on local star-formation, the dynamic structure of the gas in galaxies - the interstellar medium - is well understood. Cold molecular gas clouds collapse, while stellar ultraviolet (UV) photons create hot, ionized bubbles. Photo-dissociation regions (PDRs) bridge these extremes by shielding protostellar environments from ionizing photons as sketched schematically in the top panel of Figure 1.3. PDRs represent a transitional phase in the life-cycle of gas and appear around sights of recent star-formation (Tielens & Hollenbach, 1985b; Wolfire et al., 1990). Therefore, the interplay between gas heating and cooling within PDRs has strong implications for future generations of new stars that will form once the gas has sufficiently cooled.

The gas around star-forming regions emits strongly in low energy atomic and molecular transitions that are bright at IR and radio wavelengths. Studies with the Infrared Space Observatory (*ISO*) were key in unveiling the 5 – 200 μm regime of the electro-magnetic spectrum of galaxies, and identified atomic fine-structure emission lines containing as much as 1% of the total IR emission, namely [C II] 157.7 μm and [O I] 63 μm emission from singly ionized carbon and neutral oxygen respectively which collectively account for most of the gas cooling budget in PDRs (Malhotra et al., 1997, 2001). The Herschel Space Telescope was used to significantly increase the number of galaxies detected in these lines (Kennicutt et al., 2011; Díaz-Santos et al., 2013), and radio observations of CO rotational lines help constrain the molecular gas content of galaxies. The total dust content can be measured using sub-mm observations (Scoville et al., 2017b), and studies with The *Spitzer Space Telescope* have folded in complimentary mid-IR measurements of the smallest dust grains: Polycyclic Aromatic Hydrocarbons (PAHs).

Containing ~ 100 carbon atoms or less, PAHs play a critical role in heating interstellar gas (Wolfire et al., 1990). PAHs are toxic and produced on Earth by cigarettes and auto exhaust (Rosen & Novakov, 1978; Wingen et al., 1998). They are also well-studied in laboratories where they have been tested under various radiation and density conditions (e.g., Oomens et al., 2003; Tielens, 2008). These studies on Earth have helped contextualize the role played by PAHs in space. Photoelectrons from PAHs are one of the dominant mechanisms by which the dense gas phase of the ISM is heated, albeit inefficiently, around sites of active and recent star-formation (Gerola & Schwartz, 1976; de Jong, 1977). Following the absorption of UV photons emitted by hot, young stars, PAH grains release a photoelectron with energy equal to the difference between the absorbed photon energy and the grain’s work function. Afterwards, the PAH relaxes and emits broad vibrational features at mid-IR wavelengths. The photo-electron goes on to share its energy with atomic and molecular Hydrogen, which collisionally excite atomic fine-structure lines like [C II], [O I], and [Si II], thereby removing energy from the gas. In summary, the cycle of gas cooling and heating in PDRs can be traced by observations of PAH and IR emission lines, which collectively make for a powerful diagnostic of the ISM in extragalactic sources. Examples of such observations from my work are shown in the middle panel of Figure 1.3.

From a simple Jeans Mass perspective, star-formation can be made more efficient (or equivalently, the timescale for gravitational collapse shortens) if the external pressure impinging upon a molecular cloud increases. Theoretical models explore this alongside turbulent support, magnetic fields, and other dynamic phenomenon, but often gloss over the radiative properties of the gas itself. This may be appropriate for normal star-forming regions like those in the Milky Way, but cannot accurately describe the extreme conditions of starburst galaxies and PDRs (e.g., Sarmiento & Scannapieco, 2022). As high- z star-formation is preferentially obscured, character-

izing the cold gas conditions of LIRGs at all epochs is critical for understanding the physics driving efficient star-formation. Using multi-wavelength spectroscopy, my dissertation research tests the radiative coupling efficiency of gas in star-forming galaxies. I perform similar analyses for nearby and distant luminous IR galaxies to study how such changes fit within the overarching evolution in the star-formation rate density with cosmic time.

1.3 Guide to this thesis

Chapters 2 through 4 of this thesis are structured chronologically to capture the natural flow of my empirical research using telescope observations of IR galaxies. Chapter 2 presents my published work from McKinney et al. (2020) on far-infrared observations of [C II] and dust emission in a sample of galaxies at $z \sim 2$. During this project I developed methodology for analyzing mid- and far-IR spectroscopy which I have included in this thesis as Appendices. The results of my first paper motivated a careful study of [C II] and PAH emission in nearby luminous IR galaxies, presented in Chapter 3 as written in McKinney et al. (2021a) during my time at Caltech/IPAC as a visiting research fellow. Chapter 4 details work soon to be submitted for publication that brings together these low- and high-redshift studies by controlling for the spatial extent of dust-obscured star-formation out to $z \sim 3$. In Chapter 5, I present recent work combining multiple spectral line diagnostics to unpack the physical ISM conditions in a unique $z = 2$ galaxy, including new CO(1-0) observations using the Very Large Array. Chapter 6 documents my foray into numerical simulations where I use synthetic observations of a simulated galaxy to test the heating of dust by active supermassive black holes, a key step towards expanding the empirical analysis presented in earlier chapters to such galaxies. This simulation-based project is published in McKinney et al. (2021b). I summarize the work presented in this thesis in

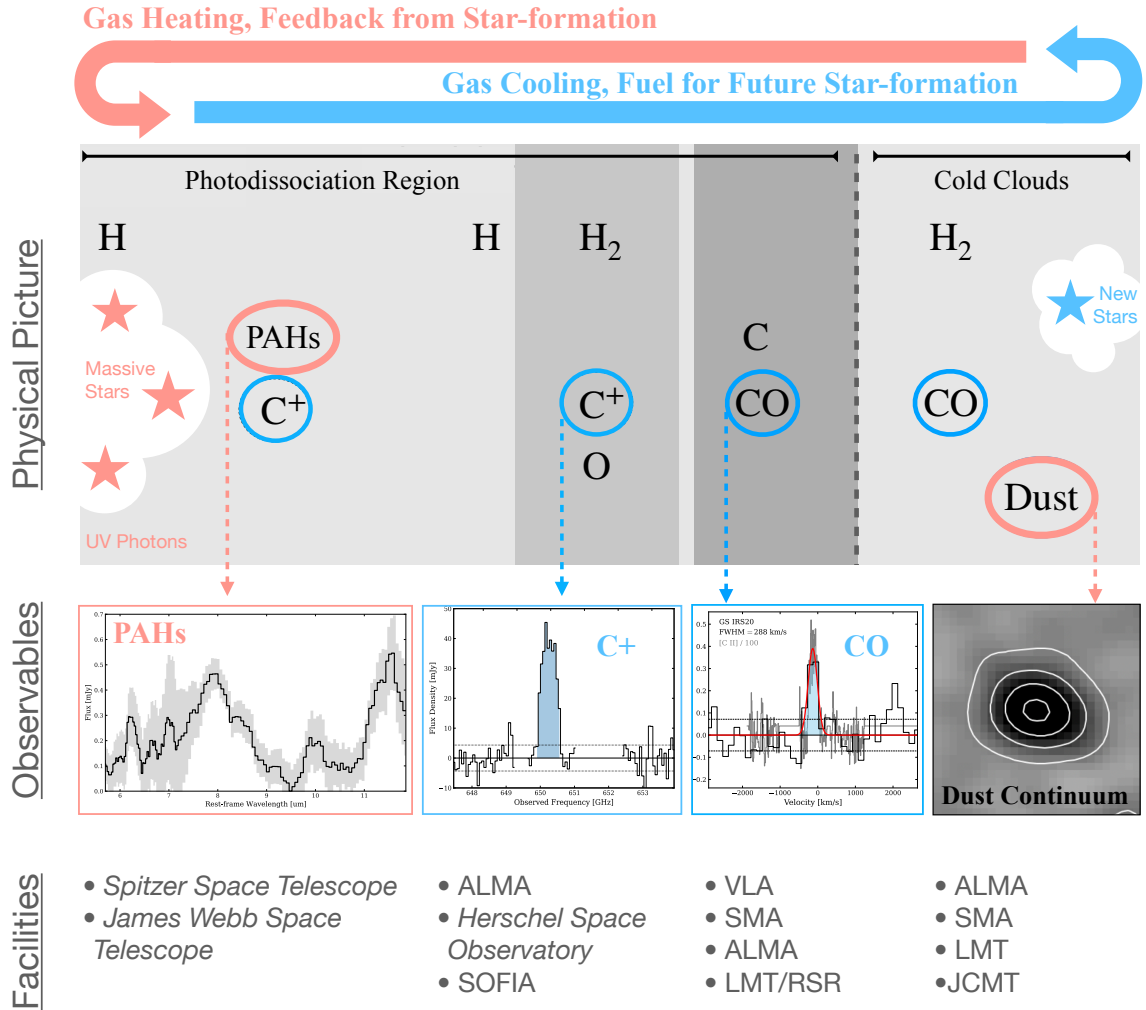


Figure 1.3 Observing the ISM at IR and radio wavelengths. (*Top*) Schematic of a star-forming region hosting young, massive stars and a cold molecular cloud, with a PDR between shielding the proto-stellar nursery from harsh radiative feedback. Emission from atomic and molecular emission lines as well as dust continuum play a key role in allowing gas to cool to the cold cloud stage. PAH grains absorb UV photons, releasing photo-electrons that heat the gas. IR and radio spectroscopy from ground- and space-based facilities provide observational handles on this cycle of heating and cooling. This figure is adapted from Hollenbach & Tielens (1999) and is not to-scale. (*Middle*) Spectral lines and continuum emission measured in distant galaxies, demonstrating the empirical tracers of gas in star-forming regions. (*Bottom*) Summary list of ground- and space-based facilities capable of measuring the corresponding diagnostic.

Chapter 7, and discuss next steps in the short term as well as the future prospect of IR extragalactic astronomy.

CHAPTER 2

MEASURING THE HEATING AND COOLING OF THE INTERSTELLAR MEDIUM AT HIGH REDSHIFT: PAH AND [C II] OBSERVATIONS OF THE SAME STAR FORMING GALAXIES AT $Z=2$

This chapter is adapted from McKinney et al. (2020) originally published in the Astrophysical Journal.

Star formation depends critically on cooling mechanisms in the interstellar medium (ISM); however, thermal properties of gas in galaxies at the peak epoch of star formation ($z \sim 2$) remain poorly understood. A limiting factor in understanding the multiphase ISM is the lack of multiple tracers detected in the same galaxies, such as Polycyclic Aromatic Hydrocarbon (PAH) emission, a tracer of a critical photoelectric heating mechanism in interstellar gas, and [C II] $158\mu\text{m}$ fine-structure emission, a principal coolant. In this chapter, I present ALMA Band 9 observations targeting the [C II] far-IR fine-structure line in six $z \sim 2$ star-forming galaxies with strong *Spitzer* IRS detections of PAH emission. All six galaxies are detected in dust continuum and marginally resolved. I compare the properties of PAH and [C II] emission, and constrain their relationship as a function of total infrared luminosity (L_{IR}) and IR surface density. [C II] emission is detected in one galaxy at high signal-to-noise (34σ), and I place a secure upper limit on a second source. The rest of our sample are not detected in [C II] likely due to redshift uncertainties and narrow ALMA band-pass windows. Our results are consistent with the deficit in [C II]/ L_{IR} and PAH/ L_{IR} observed in the literature. However, the ratio of [C II] to PAH emission at $z \sim 2$

is possibly much lower than what is observed in nearby dusty star-forming galaxies. This could be the result of enhanced cooling via [O I] at high- z , hotter gas and dust temperatures, and/or a reduction in the photoelectric efficiency, in which the coupling between interstellar radiation and gas heating is diminished.

2.1 Introduction

Ten billion years ago ($z \sim 2$), the star-formation rate density of the Universe peaked and individual galaxies were forming more stars than at any other time in cosmic history (e.g., Lilly et al., 1996; Madau et al., 1996; Chary & Elbaz, 2001; Madau & Dickinson, 2014). Enhanced star-formation was promoted by gas resupply through cold mode accretion onto galaxies (e.g., Kereš et al., 2005, 2009; Genzel et al., 2008; Tacconi et al., 2010), accompanied by a change in the efficiency of star-formation (e.g., Tacconi et al., 2010, 2013, 2018; Genzel et al., 2015; Scoville et al., 2017b; Liu et al., 2019)), which suggests evolution in the heating and cooling mechanisms of interstellar gas.

The internal transfer of thermal energy is critical for any physical system. Photoelectrons ejected from polycyclic aromatic hydrocarbons (PAHs) are thought to be the most important, albeit inefficient, mechanism for converting stellar radiation to thermal energy in and around sites of active star-formation (Watson & Salpeter, 1972; Bakes & Tielens, 1994; Helou et al., 2001). PAH molecules are complex grains comprised mostly of C and H, and are common in photodissociation regions (PDRs) where gas densities of $n \sim 10^3 - 10^6 \text{ cm}^{-3}$ are illuminated by far-UV stellar radiation fields (Tielens & Hollenbach, 1985a). Once excited by stellar photons, PAHs emit vibrational lines between $5 - 15 \mu\text{m}$ that can contain as much as $\sim 20\%$ of total IR emission (L_{IR} , $8 - 1000 \mu\text{m}$) (Smith et al., 2007; Sajina et al., 2007; Pope et al., 2008; Dale et al., 2009). Therefore, mid-IR PAH features are direct probes of photoelectric heating in dense PDRs and a key diagnostic of the interstellar medium (ISM).

Table 2.1. Sample Summary

Target	R.A. [J2000]	Dec. [J2000]	z_{IRS}	L_{IR} [L_{\odot}]	$L_{6.2\mu\text{m}}$ [L_{\odot}]	$L_{11.3\mu\text{m}}$ [L_{\odot}]	M_{*}^{a} [M_{\odot}]	SFR_{IR} [$M_{\odot} \text{ yr}^{-1}$]	$f_{\text{AGN}}^{\text{b}}$
GS IRS20	03:32:47.58	-27:44:52.0	$1.923^{+0.030}_{-0.030}$	13.06 ± 0.12	$9.99^{+0.12}_{-0.12}$	$10.11^{+0.10}_{-0.10}$	10.98	717	0.2
GS IRS46	03:32:42.71	-27:39:27.0	$1.850^{+0.014}_{-0.011}$	12.63 ± 0.29	$9.90^{+0.15}_{-0.15}$	- ^c	- ^d	376	0.0
GS IRS50	03:32:31.52	-27:48:53.0	$1.900^{+0.081}_{-0.041}$	12.46 ± 0.15	$10.17^{+0.09}_{-0.09}$	$9.66^{+0.33}_{-0.33}$	11.03	184	0.0
GS IRS52	03:32:12.52	-27:43:06.0	$1.824^{+0.018}_{-0.020}$	12.53 ± 0.29	$9.91^{+0.12}_{-0.12}$	$10.10^{+0.13}_{-0.13}$	10.64	232	0.0
GS IRS58	03:32:40.24	-27:49:49.0	$1.890^{+0.017}_{-0.042}$	12.52 ± 0.17	$9.91^{+0.10}_{-0.10}$	$9.96^{+0.25}_{-0.25}$	11.07	207	0.0
GS IRS61	03:32:43.45	-27:49:01.0	$1.759^{+0.016}_{-0.008}$	12.46 ± 0.13	$10.18^{+0.04}_{-0.04}$	$9.75^{+0.10}_{-0.10}$	10.90	243	0.0

Note. — When calculating M_{*} and SFR_{IR} , I assume a Salpeter IMF and $\text{SFR}_{\text{IR}} \approx 1.8 \times 10^{-10} L_{\text{IR}}$ (Kennicutt, 1998a). We assume a systematic error of 10% for L_{IR} and include this in the quoted 1σ uncertainty, all calculations, and on all figures. Appendix Section A describes our procedure for calculating PAH line luminosities and z_{IRS} .

^aSee Kirkpatrick et al. (2012) for details on stellar mass calculations.

^bThe integrated AGN power-law emission divided by the total mid-IR IRS flux, and is calculated using the mid-IR decomposition technique of Pope et al. (2008) and Kirkpatrick et al. (2015). We re-fit this template-based model using MCMC and calculate $f_{\text{AGN,MIR}}$ at each step in the Markov chain. Tabulated values for $f_{\text{AGN,MIR}}$ correspond to the mean of this distribution. Given the data in hand, $f_{\text{AGN,MIR}}$ can be measured with an accuracy of ± 0.1 (e.g., Pope et al. 2008; Kirkpatrick et al. 2015).

^cThe 11.3 μm PAH feature is redshifted out of GS IRS46’s *IRS* spectrum.

^dGS IRS46 is outside of GOODS-S and CANDELS, preventing the calculation of a stellar mass with comparable methods to the rest of the sample for which deeper data is available.

The energy injected into the ISM by photoelectrons is radiated away in the infrared (IR). Far-IR fine-structure emission lines such as [C II] at 158 μm and [O I] at 63 μm can contain 0.1 – 1% of L_{IR} (Tielens & Hollenbach, 1985a; Stacey et al., 2010; Díaz-Santos et al., 2013; Brisbin et al., 2015; Ibar et al., 2015). [C II] in particular is emerging as a powerful, but complicated diagnostic of the ISM because it comes from different regions in a galaxy. With a critical density of $n_{\text{crit}} \sim 3 \times 10^3 - 6 \times 10^3 \text{ cm}^{-3}$ at $\sim 100 \text{ K}$, [C II] is collisionally excited by H and H_2 in PDRs, as well as by warm electrons at 8,000 K (Goldsmith et al., 2012). Ancillary observations of [N II] 205 μm emission constrain the fraction of [C II] emission originating from PDRs (e.g., Croxall et al., 2012), which is greater for lower metallicities (Croxall et al., 2017; Cormier et al., 2019), and approaches unity in warm and compact, dusty, star forming regions (Sutter et al., 2019). Thus, [C II] can be used to trace PDR cooling in warm, compact environments, a critical physical process in atomic gas for star-formation to occur.

PDR densities are much greater than the critical density of [C II] with its primary collisional partners H and H_2 ($n_{\text{crit,H}} = 3000 \text{ cm}^{-3}$, $n_{\text{crit,H}_2} = 6100 \text{ cm}^{-3}$), both of which are heated by photoelectrons from PAH grains (Tielens & Hollenbach, 1985a;

Wolfire et al., 1990; Kaufman et al., 1999; Malhotra et al., 2001; Goldsmith et al., 2012). Thus, a correlation between [C II] and PAH emission is likely if both lines originate from the same PDR regions. Indeed, Helou et al. (2001) found the ratio of [C II] emission over integrated $5 - 10 \mu\text{m}$ flux in star-forming galaxies to be independent of far-IR color, which strongly favors a co-spatial origin.

Pope et al. (2013) report a deficit of $6.2 \mu\text{m}$ PAH emission at higher L_{IR} in (ultra) luminous IR galaxies (LIRGs: $\log L_{\text{IR}}/L_{\odot} = 11 - 12$, ULIRGs: $\log L_{\text{IR}}/L_{\odot} > 12$) and sub-millimeter (mm) galaxies, a feature also observed for [C II] emission in similar galaxy populations. Indeed, the luminosity ratio of [C II] to L_{IR} decreases at higher L_{IR} in local and high- z galaxies.¹ In low- z (U)LIRGs, Díaz-Santos et al. (2013, 2017) find $L_{[\text{C II}]} / L_{\text{IR}}$ empirically anti-correlates with average dust temperatures and IR luminosity surface densities, suggesting that either harder and more intense radiation fields lower the $L_{[\text{C II}]} / L_{\text{IR}}$ ratio, or larger dust grains out-compete PAHs for ionizing photons, starving the gas. Smith et al. (2017) find the star-formation rate surface density to be a primary factor driving the [C II]-deficit, reconciling nearby resolved measurements and high- z galaxies with a relation that spans over six orders of magnitude. At $z \sim 3$, Rybak et al. (2019) find evidence for thermal saturation of C^+ as the primary driver of the deficit (see also Muñoz & Oh 2016). Other potential contributors to the [C II]-deficit include positive PAH grain charging where fewer photoelectrons are available to collisionally excite [C II] (e.g., Helou et al. 2001), density effects (e.g., Smith et al. 2017), and/or [C II] self-absorption, although the latter scenario requires unusually large gas column densities in PDRs and is unlikely (Luhman et al., 1998; Malhotra et al., 2001).

¹E.g., Malhotra et al. 1997, 2001; Luhman et al. 1998, 2003; Helou et al. 2001; Díaz-Santos et al. 2013, 2014, 2017; Stacey et al. 2010; Magdis et al. 2014; Rigopoulou et al. 2014; Brisbin et al. 2015; Ibar et al. 2015; Zanella et al. 2018; Rybak et al. 2019.

Regardless of its origin, the [C II]-deficit implies that one of the most important cooling lines for star-formation falls off in luminosity at higher L_{IR} , or equivalently, higher star-formation rate (SFR, Kennicutt 1998a). This implies a change in one or all of the following: the photoelectric heating efficiency of the ISM, far-UV radiation field strength and hardness, gas density and PDR geometry (Smith et al., 2017). Furthermore, galaxies have higher SFR per unit stellar mass at earlier times than they do locally (e.g., Madau & Dickinson 2014), suggesting that ISM conditions evolve as a function of redshift and SFR (Scoville et al., 2017b; Tacconi et al., 2018; Liu et al., 2019). Indeed, Stacey et al. (2010) found that the [C II]-deficit is pushed to higher L_{IR} at higher redshifts; however, Zanella et al. (2018) did not observe this offset in a sample of main-sequence galaxies at $z \sim 2$. In either case, all galaxies may follow the same $L_{[\text{C II}]} / L_{\text{IR}}$ trend as a function of L_{IR} normalized by molecular gas mass (Stacey et al., 2010; Graciá-Carpio et al., 2011). Thus, the gas cooling properties and stellar radiation field strengths in local and $z > 1$ star-forming galaxies could be comparable for a given star-formation efficiency ($\text{SFE} \equiv \text{SFR} / M_{\text{H}_2}$). If this is the case, high- z star-formation could be a scaled up version of star-formation today with comparable ISM conditions, and therefore, similar mid- and far-IR PDR line ratios.

In this paper, we combine new observations using the Atacama Large Millimeter/submillimeter Array (ALMA) to investigate the properties of ISM heating and cooling in $z \sim 2$ star-forming galaxies through combined observations of [C II] and PAH emission. With archival *Spitzer Infrared Spectrograph (IRS)* spectra, we can identify pure star-forming galaxies to study the properties of $z \sim 2$ PDRs and star-formation without concern for feedback from an active galactic nucleus (AGN). Using ratios of [C II] to PAH emission, we investigate the photoelectric efficiency in PDRs near the peak in the Universe’s star-formation rate density, a critical epoch for galaxy evolution during which most of the stellar mass in the present day Universe was assembled (e.g., Madau & Dickinson 2014). We investigate the evolution in [C II]/PAH

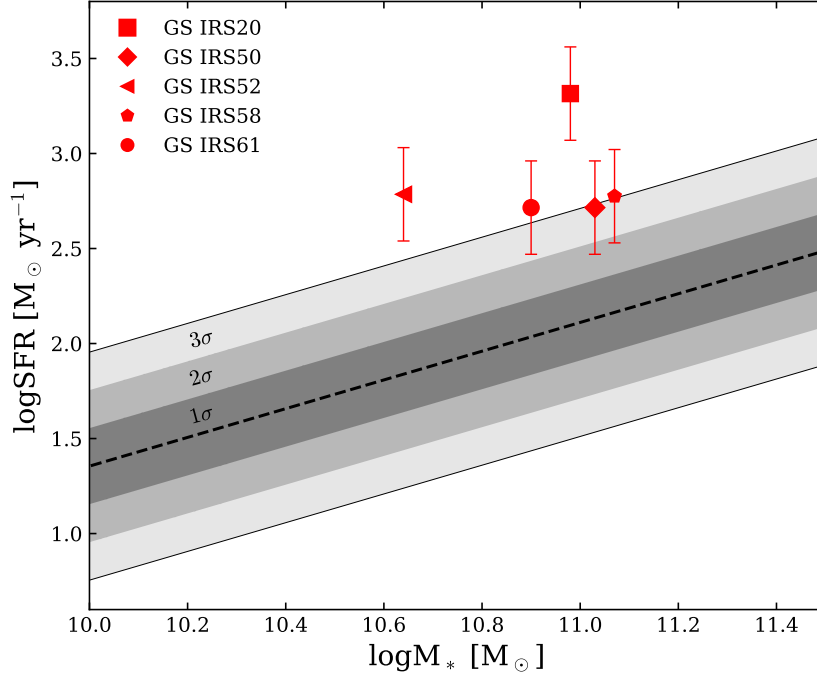


Figure 2.1 The $z \sim 2$ star-forming main-sequence of Speagle et al. (2014) (dashed black line) assuming the same (Salpeter) IMF used in our calculations. We shade 1, 2, and 3σ intrinsic scatter about the main-sequence in gray. Galaxies from our sample are shown in red, excluding GS IRS46 which does not have a robust stellar mass estimate and is not detected in [C II] with ALMA. We only detect [C II] emission in GS IRS20 (red square), the starburst galaxy located $> 5\sigma$ above the main sequence.

emission with redshift, and comment on the technical aspects of synergistic surveys combining ALMA and mid-IR spectrographs, with applications to the *James Webb Space Telescope* Mid-Infrared Instrument (*JWST*/MIRI).

The chapter is organized as follows: In Section 2.2 we present the galaxy sample, selection criterion, and observations including novel and archival data. Our analysis techniques and emission line measurements are described in Section 2.3. We present our results in Section 2.4 and discuss their implications in Section 2.5. Section 2.6 summarizes our conclusions. Throughout this work we assume a Salpeter IMF and adopt a Λ CDM cosmology with $\Omega_m = 0.3$, $\Omega_\Lambda = 0.7$, and $H_0 = 70 \text{ km s}^{-1} \text{ Mpc}^{-1}$.

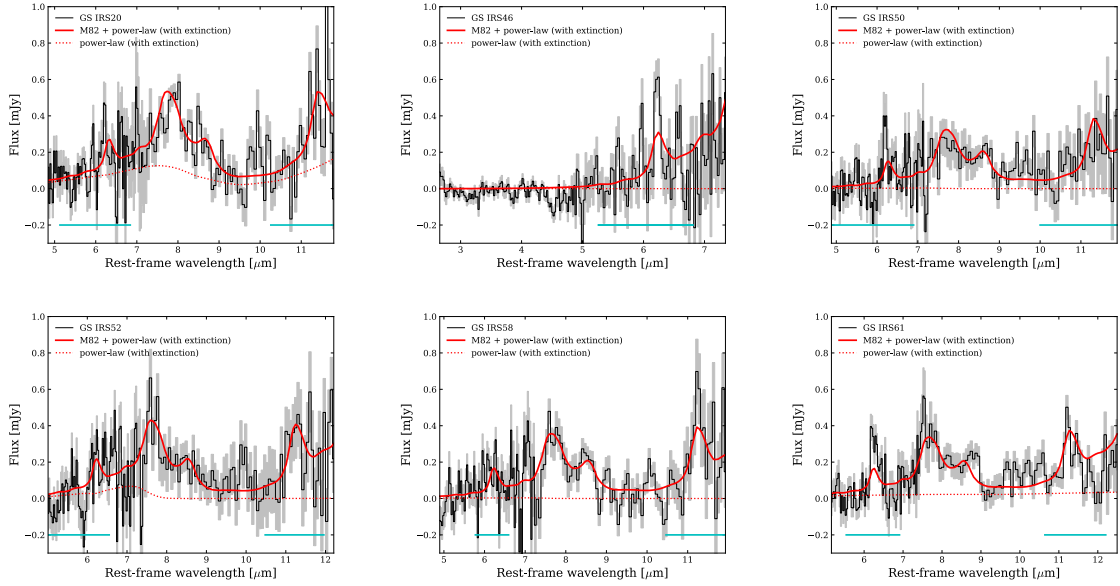


Figure 2.2 *Spitzer* *IRS* spectra for 6 targets observed with ALMA. The *IRS* spectra are shown in black, with uncertainties shaded in gray. The red solid line corresponds to best-fit empirical M82 templates on top of a power-law continuum component (red dotted line). The simple fit is used too quantify the AGN fraction in the mid-IR and we employ a more sophisticated model to measure individual line luminosities and redshifts (see Appendix A). Horizontal cyan lines show the regions where we fit Lorentzian profiles to the $6.2 \mu\text{m}$ and $11.3 \mu\text{m}$ PAH features.

2.2 Sample and Observations

2.2.1 Sample Selection

We have assembled a sample of six IR-luminous galaxies ($\log L_{\text{IR}}/L_{\odot} > 12$) at $z = 1.7 - 2$ with extensive coverage from restframe ultraviolet to sub-mm wavelengths, selected primarily by the presence of luminous PAH features in the mid-IR and little to no underlying power-law continuum. These systems are dominated by star-formation: an AGN would heat dust to high temperatures and emits warm black-body emission at mid-IR wavelengths which we do not detect (e.g., Laurent et al. 2000; Sturm et al. 2000; Tran et al. 2001; Sajina et al. 2007). Our sample comes from a larger multiwavelength parent catalog described in Kirkpatrick et al. (2015). To summarize, multiwavelength data was collected for 343 (U)LIRGs between $z = 0.3 - 2.8$ in the Great Observatories Origins Deep Survey North/South (GOODS-N/S), Extended *Chandra* Deep Field Survey (ECDFS), and the *Spitzer* Extragalactic First Look Survey fields. The primary target selection criterion was the presence of mid-IR spectroscopy from *Spitzer IRS*. For more details on the parent sample selection method, we refer readers to Section 2.1 of Kirkpatrick et al. (2015).

With our ALMA cycle 5 program targeting [C II] emission at $z \sim 2$, we observed six star-forming galaxies between $z = 1.7 - 1.9$ from the Kirkpatrick et al. (2015) sample with $L_{\text{PAH},6.2}/L_{\text{IR}} > 0.004$ and $\log L_{\text{IR}}/L_{\odot} > 12$. These galaxies all have little to no evidence of AGN contamination to the mid-IR spectrum ($f_{\text{AGN,MIR}}$), based on *IRS* spectral decomposition, and as evidenced by their $6.2\mu\text{m}$ PAH equivalent widths $\text{EW}_{6.2} > 0.5\mu\text{m}$, which is the threshold established in nearby (U)LIRGs for star-formation dominated systems (Stierwalt et al., 2014). The selection of sources based on strong PAH features in high IR-luminosity galaxies has been shown in the literature to be a robust way for selecting galaxies with minimal AGN contamination (e.g., Houck et al. 2005; Yan et al. 2005; Brandl et al. 2006; Sajina et al. 2007; Smith

et al. 2007; Armus et al. 2007; Pope et al. 2008; Veilleux et al. 2009; Kirkpatrick et al. 2012).

Configuring the ALMA Band 9 Local Oscillator to efficiently target [C II] over the redshift range spanned by our sample was a challenging factor in the design of our experiment. Efficient programs capable of observing multiple targets with minimal baseband tunings are optimal for taking advantage of limited high-frequency ALMA observing time. To maximize sample size while minimizing overhead, we manually configured each spectral window within the Band 9 constraints to cover [C II] in multiple galaxies in a given ALMA Science Goal.

Most of the galaxies in our sample have robust stellar masses constrained by deep *HST* and *Spitzer* photometry. Galaxies in our sample are high mass, $\text{Log}M_*/M_\odot = 10.6 - 11$, and dusty, as evidenced by *Spitzer* and *Herschel* photometry. Figure 2.1 shows the star-forming main-sequence (MS) of galaxies at $z \sim 2$ taken from Speagle et al. (2014). Our sample lies above the $z \sim 2$ SFMS, with $\log \Delta\text{SFMS}$ (the observed SFR over the MS SFR for the same stellar mass) between $0.6 - 1$ dex for most galaxies in our sample and as high as ~ 1.2 dex in GS IRS20, well within the starburst domain. Table 2.1 summarizes global properties for galaxies in our sample.

2.2.2 Multiwavelength Observations

Our sources are in ECDFS and were selected to have mid-IR spectroscopy from the *Spitzer IRS* (Fadda et al., 2010; Kirkpatrick et al., 2012, 2015). A full description of *IRS* observations, data reduction, and sample-selection can be found in Pope et al. (2008) and Kirkpatrick et al. (2012). The extracted spectra are shown in Figure 2.2 with simple fits to the mid-IR emission that we use to calculate $f_{\text{AGN,MIR}}$; more sophisticated model fits are employed to measure PAH line luminosities (see Appendix A). In addition to *Spitzer IRS* spectra, photometry from *Herschel* (PACS and SPIRE),

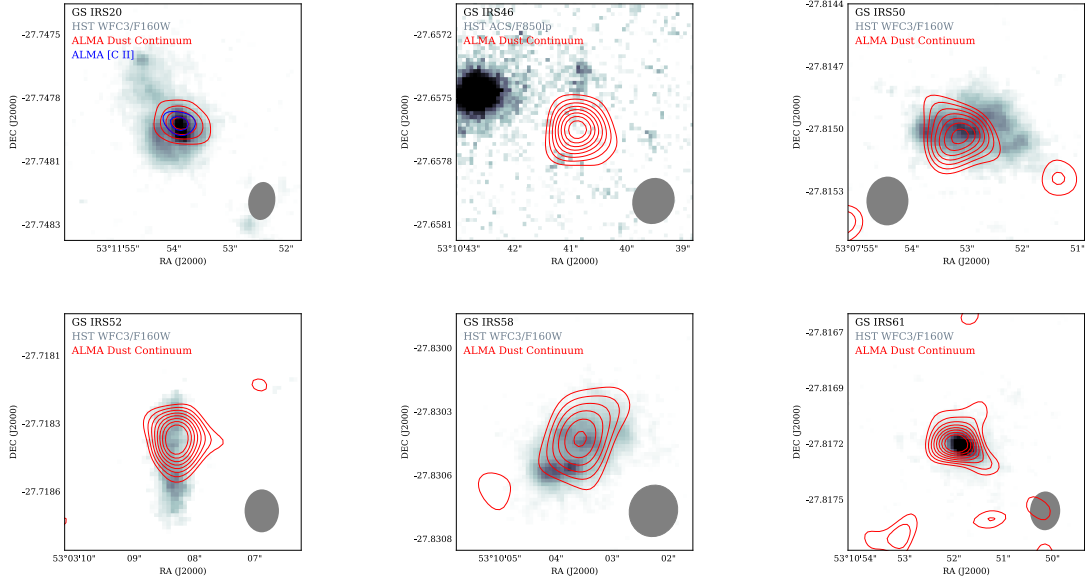


Figure 2.3 Postage stamp images for each of the targeted galaxies. *HST*/WFC3 H_{160} imaging is shown in the background when available, and ALMA dust continuum contours are overplotted in red. For GS IRS46, we show *HST*/ACS F850lp (z-band) maps in the background (Giavalisco et al., 2004). In the case of GS IRS20, we also show integrated [C II] emission contours in blue. The ALMA beam is represented by a gray ellipse in all images.

and *Spitzer* (IRAC and MIPS) is available for all targets (see Kirkpatrick et al. 2015 for details).

ECDFS includes the GOODS-S field, which was covered by the Cosmic Assembly Near-IR Deep Extragalactic Legacy Survey (CANDELS; Grogin et al. 2011; Koekoer et al. 2011), providing deep WFC3/IR imaging for five out of six galaxies in our sample. We downloaded the H_{160} and Z_{850lp} field maps, and correct for the known systematic astrometric offset of $0.08''$ in RA and $0.26''$ in DEC relative to ALMA’s astrometry in GOODS-S (Elbaz et al., 2018). Thumbnail images for our sample are shown in Figure 2.3. We also matched our galaxies to visual morphological classifications presented in Kartaltepe et al. (2015) to assess the incidence of mergers in the sample.

2.2.3 ALMA Observations and Data Processing

We carried out ALMA Band 9 observations of our targets during Cycle 5 (PI A. Pope, Project ID: 2017.1.01347.S) targeting [C II] emission at restframe $157.74 \mu\text{m}$. For the range of redshifts in our sample, [C II] is redshifted to an observed frequency of $653.36 - 686.38 \text{ GHz}$. We estimated integration times necessary to detect the [C II] line at 10σ for galaxies in our sample by assuming a conservative $L_{[\text{C II}]} / L_{\text{IR}}$ ratio of 0.002 and [C II] line width of 300 km s^{-1} , characteristic of existing [C II] detections $z \sim 2$ galaxies prior to our observations (Stacey et al., 2010). The minimum predicted [C II] flux for all galaxies in the sample was 15 Jy km s^{-1} , which we used to set the integration time for each observation by requiring a $> 10\sigma$ line detection, or equivalently, a sensitivity of 5 mJy over 300 km s^{-1} bandwidth.

To avoid resolving out [C II] emission at $z \sim 2$, we requested an angular resolution of $\sim 0.5''$. The observations took place in July 2018 in ALMA configuration C43-1 which has an angular resolution of $0.52''$ at 650 GHz and maximum recoverable scale of $4.4''$, corresponding to 36.5 kpc at $z = 2$. The expected radii of sub-mm and *HST* H_{160} emission in $z \sim 2$ star-forming galaxies is $< 8 \text{ kpc}$ (e.g., Fig. 2.3, Zanella et al. 2018; Calistro Rivera et al. 2018; Lang et al. 2019), so it is unlikely that our observations are missing flux on large scales due to interferometric spatial filtering. Six galaxies in our proposal were observed for ~ 18 minutes on-source, achieving the target sensitivity of 5 mJy over 300 km s^{-1} bandwidth at a native resolution of 31.250 MHz (13.6 km s^{-1}) which was later re-binned to lower spectral resolutions.

The data were reduced using the standard ALMA pipeline in CASA v5.1.1-5 (McMullin et al., 2007). We first imaged the data using `tclean` with Briggs weighting in continuum-mode, iteratively adjusting the robust parameter R to maximize the ratio of peak continuum emission to map RMS. We extracted peak and integrated continuum flux densities through elliptical apertures which were set by fitting a 2D Gaussian function to the bright continuum emission in each observation. We detect

Table 2.2. ALMA Cycle 5 Band 9 Observations: Continuum Imaging and Spectral Line Data

Target	Beam FWHM [arcsec]	Continuum Maps						
		$\lambda_{\text{obs}}^{\text{a}}$ [μm]	rms [mJy/beam]	S_{peak} [mJy/beam]	S_{int} [mJy/beam]	R_{eff} [kpc]	$p(l z)^{\text{b}}$	$F_{[\text{CII}]}^{\text{c}}$ [mJy]
GS IRS20	0.51×0.37	466.60	0.87	14.38 ± 0.87	17.3 ± 1.1	1.81	0.68	331.59 ± 9.66
GS IRS46	0.74×0.66	456.95	0.54	6.55 ± 0.60	9.3 ± 1.0	2.63	0.56	(< 10.5)
GS IRS50	0.78×0.67	465.07	0.41	4.82 ± 0.67	7.1 ± 1.2	2.72	0.29	(< 14.0)
GS IRS52	0.63×0.51	444.77	0.10	5.21 ± 0.51	8.64 ± 0.92	2.15	0.01	(< 4.3)
GS IRS58	0.93×0.86	456.95	0.13	5.49 ± 0.70	10.5 ± 2.4	3.36	0.22	(< 5.3)
GS IRS61	0.70×0.54	441.62	0.95	3.70 ± 0.35	4.22 ± 0.64	2.34	0.93	< 4.6

^a Effective wavelength of collapsed ALMA Band 9 cube.

^b The probability of observing the target’s redshifted [CII] line given all redshift uncertainty and the ALMA Band 9 spectral window configuration. See Equation B.1 in Section 3.3.

^c [CII] line flux. Upper limits are 3σ and given for each galaxy, although values in parenthesis are considered unreliable given the low probability of having observed the line.

continuum emission at representative frequencies of 652 – 699 GHz in all of our targets at signal-to-noise (SNR) between 7.5 – 17.8. After verifying the presence of underlying continuum, we created a linear continuum model in the uv -plane, taking care to mask out high-amplitude visibilities that could correspond to potential line emission. Next, we continuum-subtracted the ALMA cubes in the uv -plane and imaged the spectral windows with `tclean` and Briggs weighting using $R = 0.5$. Final continuum measurements, ALMA beam characteristics, and spectral line statistics are given in Table 2.2.

2.3 Analysis

2.3.1 [C II] Detection in GS IRS20

Whereas the dust continuum is clearly detected with ALMA for all 6 galaxies (red contours in Fig. 2.3), [C II] $158\mu\text{m}$ emission is clearly detected in one of six galaxies in the sample, GS IRS20, at an observed frequency of 650.2505 GHz. This corresponds to a redshift of $z_{[\text{C}2]} = 1.9239 \pm 0.0002$, in excellent agreement with the PAH-derived redshift: $z_{[\text{C}2]} - z_{\text{PAH}} = 0.001$.

We imaged the cube in 30 km s^{-1} bins, and extracted a spectrum through an elliptical aperture with FWHM and centroid taken from a 2D Gaussian fit to con-

tinuum emission. Figure 2.4 shows the detection of [C II] in GS IRS20’s ALMA Band 9 spectrum. Gaps in spectral coverage are the result of limitations when configuring ALMA’s spectral windows. We integrated the line over the frequency range where emission rose above the continuum level and measured a flux density of $S_{[\text{C II}]} \Delta v = 9.95 \pm 0.07 \text{ Jy km s}^{-1}$ at a SNR of 34.3 and line velocity width of $\sim 330 \text{ km s}^{-1}$. Next, we calculated the [C II] line luminosity $L_{[\text{C II}]}$ in solar units following Carilli & Walter (2013):

$$L_{\text{line}} = 1.04 \times 10^{-3} \times (S_{\nu} \Delta v) D_L^2 \nu_{\text{obs}} [L_{\odot}] \quad (2.1)$$

where D_L is the luminosity distance in Mpc, and ν_{obs} is the observed frequency of the line in GHz. From the Band 9 spectrum, we calculate $\log L_{[\text{C II}]} / L_{\odot} = 9.169 \pm 0.003$ in GS IRS20, the highest SNR detection of [C II] emission in a $z \sim 2$ galaxy to date. From a collapsed ALMA data cube containing only line emission, we find that [C II] in GS IRS20 is marginally resolved with a spatial FWHM of $0.56''$, corresponding to $\approx 4.7 \text{ kpc}$ at $z = 1.9239$.

2.3.2 [C II] Line Searches and Upper Limits

No [C II] emission lines were obvious in the ALMA cubes of GS IRS46, GS IRS50, GS IRS52, GS IRS58, and GS IRS61. To search for marginally detected emission lines, we used a circular aperture with radius $0.5''$ to extract a 50 km s^{-1} spectrum centered on the source’s dust continuum position. Next, we extracted additional spectra through the same circular apertures offset by $0.5''$ from the source’s center at various angles, as optical light, dust continuum and [C II] emission can be spatially offset from one another in high redshift ULIRGs (e.g., Zanella et al. 2018; Calistro Rivera et al. 2018). From the set of extracted spectra, we searched each spectral window for the presence of three channels greater than $2\times$ the local rms. No marginally-significant line emission was discovered in this manner, or in stacks of the extracted spectra.

Given that 83% of our observations yielded non-detections, and no data was discarded because of poor atmospheric transmission, two explanations are possible. Either the observations were not deep enough to detect [C II] and an upper limit may be placed on $L_{[\text{C II}]}$; or, the line was missed by our ALMA bandpass tunings. To determine which observations can yield a secure upper limit on $L_{[\text{C II}]}$, we calculate $p(l|\text{ALMA}, \Delta z)$: the probability our ALMA tunings covered the [C II] line given all redshift uncertainties and the comparatively narrow bandpass widths. The technique adopted for calculating $p(l|\text{ALMA}, \Delta z)$ is described in detail in Appendix Section B. In summary, we integrate redshift probability distribution functions in spectral domains with ALMA coverage. We found this detailed analysis to be crucial for interpreting the data. Table 2.2 includes values of $p(l|\text{ALMA}, \Delta z)$ for all targets.

Amongst the non-detections, only GS IRS61 has $p(l|\text{ALMA}, \Delta z) > 90\%$. For this galaxy, we first calculate the rms over a spectrum at 50 km s^{-1} resolution (rms_{50}), extracted from an aperture centered on the dust continuum. Then, we calculate the 3σ upper limit on the line luminosity using Equation 2.1 with $S_{[\text{C II}]} \Delta v = 3\Delta v(\sqrt{6} \text{rms}_{50})$, assuming $\Delta v = 300 \text{ km s}^{-1}$ as is observed in GS IRS20. Our upper limits for GS IRS61 on $L_{[\text{C II}]}$ are summarized in Table 2.2, and could be a factor 1.8 (0.25 dex) larger than what is reported if we assume a more extreme $\Delta v = 600 \text{ km s}^{-1}$, greater than the noise-weighted average of $\sim 430 \text{ km s}^{-1}$ as observed in [C II]-emitters at $z \sim 2 - 3$ (e.g., the sample of Gullberg et al. 2015).

2.3.3 Morphology

In all of our observations, dust continuum emission is marginally resolved: the major and minor axes of 2D Gaussian fits to dust emission are equal to $0.5 - 2''$, slightly greater than the ALMA beam in all cases. We use these size measurements to calculate $R_{\text{eff},160}$, the radius containing 50% of the total continuum flux at the effective rest-frame wavelengths (approximately $160\mu\text{m}$) of our observations. Table

2.2 includes values of $R_{\text{eff},160}$, which we use to calculate IR surface densities. Given that the extent of dust continuum is marginally greater than the ALMA beam in all cases, our measurements of $R_{\text{eff},160}$ may be thought of as upper limits.

Our ability to distinguish substructure in the ALMA maps is limited; however, extended H_{160} emission in the *HST* thumbnails of GS IRS20, GS IRS50 and GS IRS58 suggests disturbed, perhaps merger-driven, morphologies in some cases. We matched our sources to the morphological classification catalog of Kartaltepe et al. (2015) to determine the incidence of mergers in our sample. Each of our targets had the maximum 68 classifications per galaxy. GS IRS20 is considered to be a merger by 80% of classifiers, and irregular by 100%, consistent with its position $> 5\sigma$ above the $z = 2$ galaxy main sequence (Fig. 2.1), and the presence of faint extended H_{160} emission to the North-East, reminiscent of a tidally disrupted stellar population. Dust continuum and [C II] emission in GS IRS20 are co-spatial and coincide with the H_{160} maximum.

The rest of the sample was not classified as mergers, and GS IRS61 is classified as a spheroid by the full set of classifiers. The spatial extent of H_{160} -band and dust continuum in GS IRS61 is ~ 5 kpc (FWHM), making this galaxy extremely compact. GS IRS46 is offset from the *HST*/ACS z-band map by $0.70''$ after correcting for the astrometry offset between *HST* and ALMA (see Section 2.2.2). This corresponds to ~ 6 kpc physical offset between the detected stellar light and dust continuum emission in this galaxy. Given the uncertainty introduced by this offset, we do not report a stellar mass or show optical data points for this dusty galaxy.

2.3.4 Comparison Samples

Since we have selected our $z \sim 2$ sample to include only star-formation dominated systems, we emphasize literature comparison samples with comparable selections ($\text{EW}_{6.2\mu\text{m}} > 0.5 \mu\text{m}$, Stierwalt et al. 2014). For comparison with local (U)LIRGs,

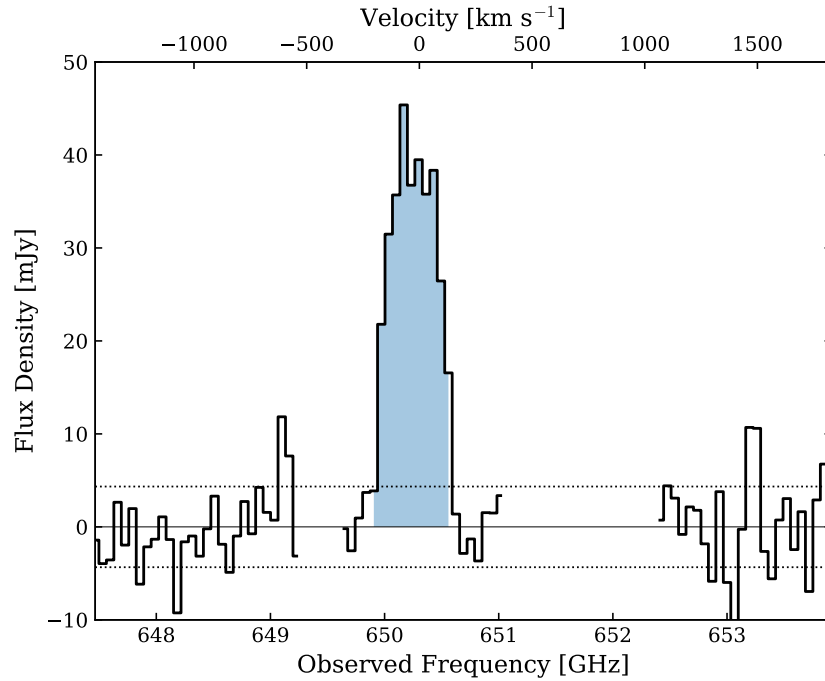


Figure 2.4 a

t $z = 1.924$, binned to 30 km s^{-1} resolution.]GS IRS20's ALMA Band 9 continuum-subtracted spectrum showing the robust detection of [C II] at $z = 1.924$, binned to 30 km s^{-1} resolution. The top axis shows relative velocities in km s^{-1} from the line's centroid. The horizontal dotted lines correspond to $\pm 1\sigma$ noise, and the shaded blue region indicates where line emission was integrated: the peak is detected at an SNR of 19.1σ and the integrated emission at an SNR of 34.3σ . Gaps in the spectra are due to the observation's spectral window configuration.

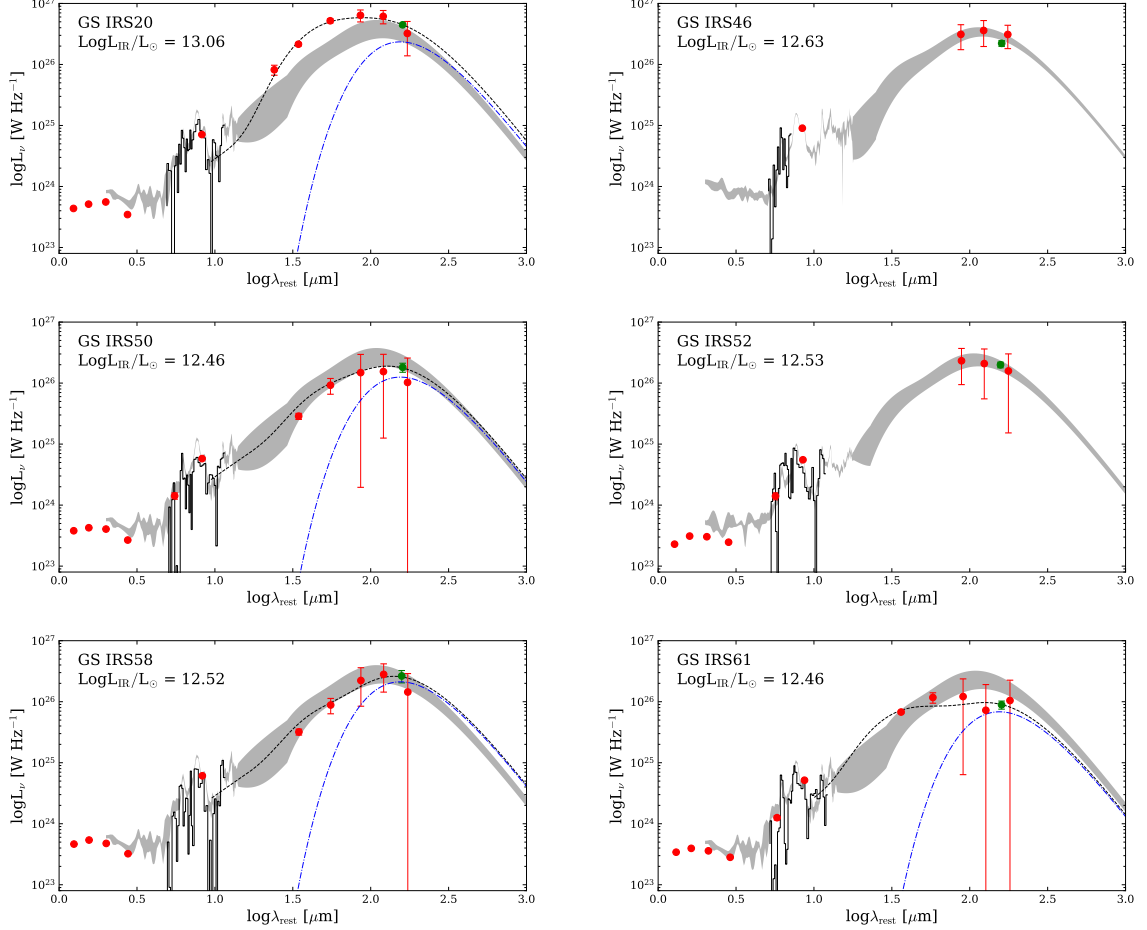


Figure 2.5 Multiwavelength photometry and spectra for each ALMA target. Shaded gray SEDs correspond to the best-fit $z \sim 2$ template SED from the empirical library presented in Kirkpatrick et al. (2015). The solid black line corresponds to a two-temperature modified blackbody + near-IR power-law fit, which we integrate to estimate L_{IR} for each target. The dot-dashed blue line is the cold dust component from this fit which we integrate to calculate L_{cold} . Photometry in red correspond to *Spitzer* and *Herschel* observations. ALMA dust continuum is shown in green, and *Spitzer* IRS spectra are over-plotted in black. We do not fit the blackbody + power-law models to GS IRS46 and GS IRS52 because these galaxies lack observations between rest-frame 30 – 70 μm .

we use mid- and far-IR spectral line measurements from Díaz-Santos et al. (2013, 2014, 2017) and Stierwalt et al. (2014) for galaxies in the Great Observatories All Sky LIRG Survey (GOALS; Armus et al. 2009). To contextualize PAH and [C II] line luminosities at lower L_{IR} , we also compare our data to the intermediate- z 5 mJy Unbiased Spitzer Extragalactic Survey (5MUSES; Wu et al. 2010), nearby galaxies from Sargsyan et al. (2014), Magdis et al. (2014), and Ibar et al. (2015). To characterize the landscape of [C II] observations at $z \sim 2$, we also compare our [C II] measurements to $z \sim 2 - 3$ galaxies with data from ALMA, APEX, or *Herschel* FTS (Ivison et al., 2010; Valtchanov et al., 2011; Schaerer et al., 2015; Gullberg et al., 2015; Zanella et al., 2018; Hashimoto et al., 2018; Rybak et al., 2019). Prior observations of both PAH and [C II] in the same galaxy at $z \sim 2$ are limited to a handful of systems observed with *Spitzer* and the Redshift (z) and Early Universe Spectrometer (ZEUS) on the Caltech Submillimeter Observatory (CSO) (Stacey et al., 2010; Brisbin et al., 2015).

For GOALS, 5MUSES and the ZEUS/CSO [C II] sample, $6.2\mu\text{m}$ luminosities were derived using PAHFIT (Smith et al., 2007) or CAFE (Marshall et al., 2007). It has been shown that PAHFIT-derived PAH line luminosities are greater than the those produced via continuum fitting methods by a factor of $\sim 1.6 - 1.9$ for $L_{6.2\mu\text{m}}$ and $L_{11.3\mu\text{m}}$ (e.g., Sajina et al. 2007; Smith et al. 2007; Pope et al. 2008). This is because PAHFIT is able to measure line emission in extended Lorentzian wings whereas continuum fitting methods do not. The $z \sim 2$ *Spitzer* IRS spectra do not have sufficient SNRs to use PAHFIT reliably, so we instead measure PAH lines using a continuum fitting technique described in Appendix Section A. In summary, we fit a continuum + line model to isolated $6.2\mu\text{m}$ and $11.3\mu\text{m}$ regimes allowing the line strength, and galaxy redshift to vary. We also re-measure PAH luminosities in GOALS star-forming galaxies using our method, and divide PAHFIT values by a

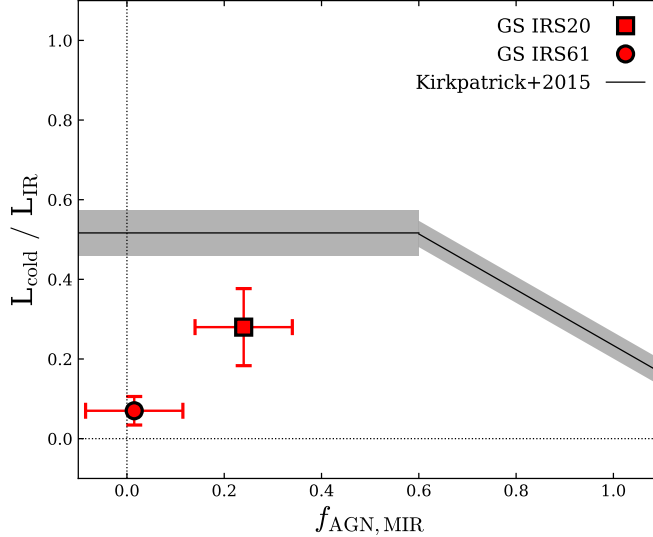


Figure 2.6 The ratio of cold dust emission, L_{cold} , to L_{IR} as a function of $f_{\text{AGN,MIR}}$, the AGN contribution to emission at mid-IR wavelengths. L_{cold} comes from integrating the cold dust component in our two-temperature SED fits shown in Figure 2.5. Our data is shown in red. The solid black line indicates the best-fit trend for 343 (U)LIRGs between $z = 0.3 - 2.8$ from Kirkpatrick et al. (2015), with the 1σ uncertainty shaded in gray.

statistical conversion factor of 1.6 and 2.3 for $L_{6.2\mu\text{m}}$ and $L_{11.3\mu\text{m}}$ respectively to match our quantities derived at higher redshift.

The GOALS sample is nearby and resolved by the *Spitzer* IRS slit, which is centered on the nuclear region of each galaxy and will not capture the total mid-IR continuum and PAH flux (Armus et al., 2009; Stierwalt et al., 2013). For fair comparison with high- z galaxies that are completely covered by the IRS slit, we correct the PAH line fluxes of GOALS using slit-corrections in Stierwalt et al. (2014) determined from the ratio of total *Spitzer* IRAC $8\mu\text{m}$ flux to total IRS $8\mu\text{m}$ flux. These corrections have a median value of 1.14 and a negligible impact on the average value of GOALS galaxies in the diagnostic plots.

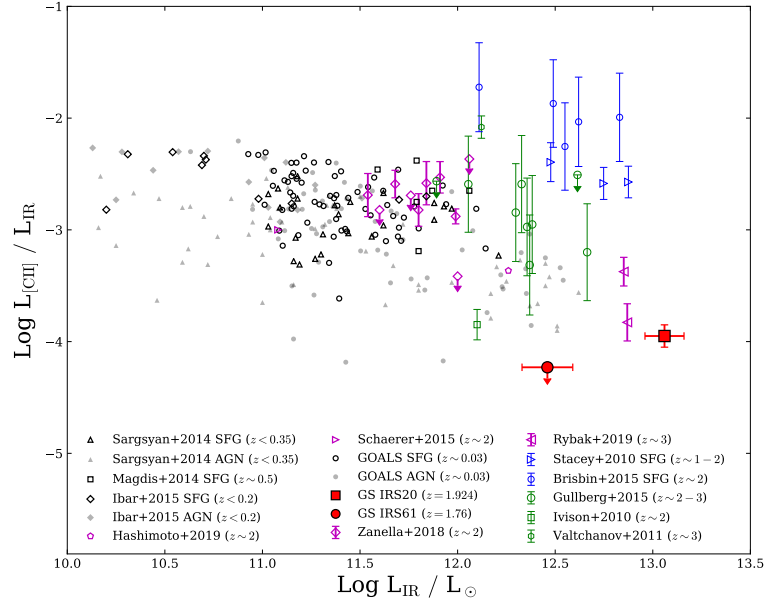


Figure 2.7 The ratio of [CII] luminosity to L_{IR} in low- and $z \sim 2 - 3$ star-forming galaxies and AGN. We show local star-forming galaxies as black open symbols and low- z AGN as gray symbols. At $z = 2 - 3$, we show both star-forming and AGN systems with colored symbols: ALMA-derived [CII] luminosities are shown in red (this work) and magenta. Blue symbols indicate [CII] observations from ZEUS/CSO, which we re-calculate as described in Section 2.4.1. Green symbols correspond to galaxies targeted using APEX and *Herschel*, including the lensed SPT DSFG sample of Gullberg et al. (2015), which we de-magnify using their average magnification factor of 14.1. We include AGN in this figure to demonstrate the spread in $L_{\text{[CII]}}/L_{\text{IR}}$ observed in all galaxies; however, we emphasize that this work focuses on the range of star-formation properties in galaxies without AGN.

2.3.5 SED Fits to near-IR through sub-mm Photometry

Near-IR through sub-mm photometry are shown in Figure 2.5. For comparison, we overplot the average SED of $z \sim 2$ $\log L_{\text{IR}}/L_{\odot} = 12.5$ star-forming galaxies from Kirkpatrick et al. (2015), scaled to best match the observations. The excellent agreement at $5 - 15 \mu\text{m}$ is due to the fact that our galaxies are part of the sample used in generating the Kirkpatrick et al. (2015) templates, which were normalized in the mid-IR.

To calculate total $8 - 1000 \mu\text{m}$ IR luminosities, we fit a two-temperature modified blackbody + power-law model between the *IRS* spectra at rest wavelengths above

9 μm out to the far-IR photometry, motivated by Kirkpatrick et al. (2015) who find that a two-temperature model yields good fits to the far-IR SEDs of $z = 0.3 - 2.8$ (U)LIRGs. For all fits we keep the dust emissivity β fixed to a value of 1.5, and the temperature of the cold dust component fixed at $T_{\text{cold}} = 26.1$ K corresponding to the average value of galaxies in the Kirkpatrick et al. (2015) sample with $f_{\text{AGN,MIR}} \leq 0.3$. From the fits, we measure L_{IR} and the fraction of IR emission originating from the cold dust component ($L_{\text{cold}}/L_{\text{IR}}$). Table 2.3 reports best-fit values for T_{warm} , the modified-Blackbody temperature of the warm dust component, and L_{cold} with their associated 1σ uncertainties for GS IRS20 and GS IRS61. GS IRS46 and GS IRS52 do not have rest-frame photometry between 30 – 70 μm , so we determine a best-fit template from the Kirkpatrick et al. (2015) library by matching to the available observations above rest-frame 9 μm . The scale-factors for each template are 11.7 and 2.6 in GS IRS46 and GS IRS52 respectively. We then integrate the scaled Kirkpatrick et al. (2015) template to calculate L_{IR} in these two galaxies.

Models fits are shown in Figure 2.5 as dashed black lines. Kirkpatrick et al. (2015) find that $L_{\text{cold}}/L_{\text{IR}} \approx 0.5$ on average for $z = 0.3 - 2.8$ (U)LIRGs with $0 < f_{\text{AGN,MIR}} < 0.6$. In GS IRS20, the one galaxy where [C II] was detected at high significance, and GS IRS61, the target with a secure [C II] upper limit, we measure $L_{\text{cold}}/L_{\text{IR}} = 0.28$ and 0.07 respectively, at the extreme lower end of the distribution for galaxies of similar $f_{\text{AGN,MIR}}$ and L_{IR} (Figure XX). GS IRS20 and GS IRS61 deviate from the mean of the Kirkpatrick et al. (2015) sample by $\approx 2.5\sigma$ and $\approx 12\sigma$ respectively. Both systems have T_{warm} comparable to stacked templates of similar $f_{\text{AGN,MIR}}$ (Table 2.3), indicating that low $L_{\text{cold}}/L_{\text{IR}}$ is driven by an increase in the warm dust content of these two galaxies, and not a rise in the warm dust temperature.

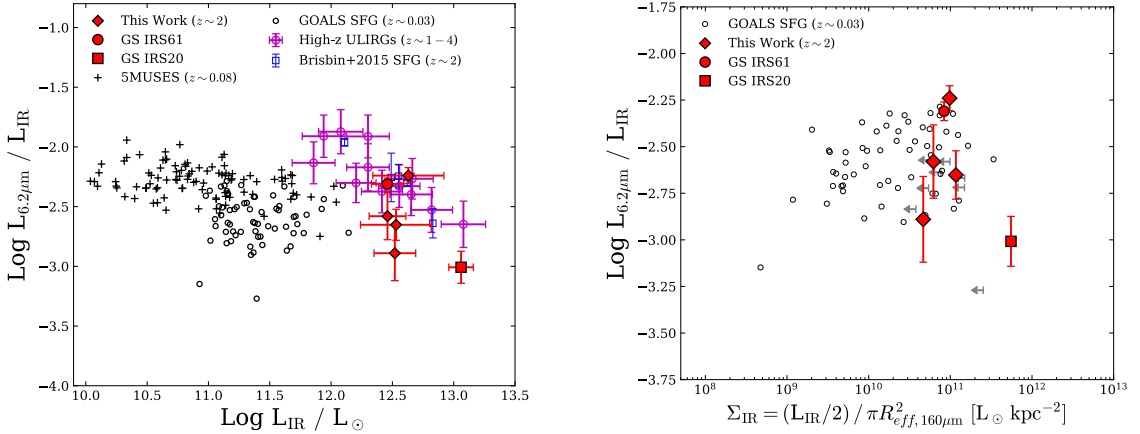


Figure 2.8 (*Left*) The ratio of $L_{6.2\mu\text{m}}$ to L_{IR} in low- and high-redshift IR-luminous galaxies as a function of L_{IR} . Local galaxies are taken from 5MUSES (Wu et al., 2010) and the GOALS sample (Díaz-Santos et al., 2013, 2014, 2017; Stierwalt et al., 2014) and follow the color scheme of previous figures. High redshift galaxies are represented with colored symbols: red corresponds to our sample, and blue indicates galaxies from Brisbin et al. (2015). (U)LIRGs shown in purple are tabulated in Pope et al. (2013). (*Right*) The ratio of $L_{6.2\mu\text{m}}$ to L_{IR} vs. IR surface density. Upper limits on Σ_{IR} for GOALS galaxies smaller than the Herschel beam are shown in gray. The offset between low- and high-redshift galaxies observed in the *Left* panel is removed when normalizing L_{IR} by the cold dust surface density traced by rest-frame $160\mu\text{m}$ emission with ALMA and Herschel.

2.4 Results

2.4.1 [C II] Line Luminosities

Of six galaxies targeted with ALMA, we only detect the $158\mu\text{m}$ [C 2] fine-structure line in one galaxy, GS IRS20, the most IR-luminous source in our sample. For one other galaxy in our sample, GS IRS61, the [C II] line was reliably covered by our ALMA observations ($p(l|\text{ALMA}, \Delta z) = 93\%$). For the other targets, our ALMA observations have a probability $> 40\%$ that we missed the redshifted [C II] line given prior redshift uncertainties and the sparse frequency coverage of ALMA spectral windows in Band 9. For the remainder of the paper we only include GS IRS20 and GS IRS61 in any analysis that involves [C II].

Figure 2.7 shows the [C II] deficit for low-redshift (U)LIRGs and star-forming galaxies at $z \sim 2 - 3$ from this sample and the literature. We note that the number

of IR-luminous galaxies at $z \gtrsim 4$ with [C II] detections is growing²; however, we restrict our current analysis of the high- z landscape to $z \sim 2 - 3$ to focus on galaxy properties near the cosmic star-formation rate density peak. The ratio of $L_{[\text{C II}]}$ to L_{IR} in GS IRS20 is comparable to other $z \sim 3$ ALMA [C II] detections from Rybak et al. (2019) and possibly consistent with the extrapolation of the low- z [C II]-deficit to $\log L_{\text{IR}}/L_{\odot} \geq 12.5$. GS IRS61 is ~ 2 dex below GOALS star-forming galaxies of $\log L_{\text{IR}}/L_{\odot} \approx 12$.

There is a significant offset on the order of $0.5 - 1.5$ dex between $L_{[\text{C II}]} / L_{\text{IR}}$ at $z = 2 - 3$ found with ALMA and those reported by Stacey et al. (2010) and Brisbin et al. (2015) using ZEUS/CSO (blue in Fig. 2.7). The spectral resolution of ZEUS is $150 - 300 \text{ km s}^{-1}$, comparable to the expected line-width of [C II] emission in some cases, making the flux measurements sensitive to the number of spectral pixels included when integrating a low SNR line. We re-calculate all ZEUS/CSO [C II] luminosities using only the peak pixel flux assuming a line-width of $150 - 300 \text{ km s}^{-1}$. After these corrections, the $0.5 - 1.5$ dex offset between ALMA and ZEUS observations in $z \sim 2$ SFGs persists. There are multiple factors that could contribute to this offset, including physical variations in $[\text{C II}] / L_{\text{IR}}$ with star-formation rate surface density (e.g., Smith et al. 2017; Díaz-Santos et al. 2017), or observational limitations such as large beam sizes, lower spectral resolution, and flux calibration uncertainties on the order of 30% (Brisbin et al., 2015).

2.4.2 PAH Properties

The relationship between PAH emission and dust emission evolves with redshift and is likely related to a number of factors, including $f_{\text{AGN,MIR}}$, SFR, and the number

²E.g., Gallerani, S. et al. 2012; Walter et al. 2012; Riechers et al. 2013; Bussmann et al. 2013; Rawle et al. 2014; De Breuck et al. 2014; Maiolino et al. 2015; Capak et al. 2015; Oteo et al. 2016; Pentericci et al. 2016; Carniani et al. 2017; Jones et al. 2017; Matthee et al. 2017; Smit et al. 2018; Carniani et al. 2018; Gullberg et al. 2018; Decarli et al. 2018; Hashimoto et al. 2018; Le Fèvre et al. 2019; Tadaki et al. 2019; Hashimoto et al. 2019

Table 2.3. Derived Parameters from IR-SED Fits

Target	T_{cold} [K]	T_{warm} [K]	L_{cold}/L_{IR}
GS IRS20	26.1 (fixed) ^a	57 ± 1	0.28 ± 0.10
GS IRS61	26.1 (fixed) ^a	59 ± 2	0.07 ± 0.04
MIR0.0 ^b	25.7 ± 0.6	66 ± 2	0.51 ± 0.04
MIR0.2 ^b	24.6 ± 1.3	62 ± 1	0.44 ± 0.06

^a T_{cold} was fixed in the SED fits of both GS IRS20 and GS IRS61 to the average of galaxies in the Kirkpatrick et al. (2015) sample with $f_{AGN,MIR} \leq 0.3$

^bEmpirical templates from Kirkpatrick et al. (2015) of comparable $f_{AGN,MIR}$ to GS IRS20 and GS IRS61. MIR0.0 and MIR0.2 correspond to $f_{AGN,MIR} = 0.0$ and $f_{AGN,MIR} = 0.2$ respectively.

of PDRs per unit molecular gas mass (Smith et al., 2007; Pope et al., 2013). Star-forming galaxies in our sample at $z \sim 2$ have $6.2 \mu\text{m}$ PAH luminosities 0.3 dex brighter than local (U)LIRGs of comparable L_{IR} after accounting for the differences in $L_{6.2\mu\text{m}}$ measurement techniques (see Section 2.3.4), but follow a deficit in PAH emission towards higher L_{IR} whose magnitude of decline is equal to or greater than the deficit between other far-IR fine-structure lines and L_{IR} (Pope et al., 2008, 2013; Sajina et al., 2008; Graciá-Carpio et al., 2011; Stierwalt et al., 2014; Shipley et al., 2016; Cortzen et al., 2019). In addition to being a function of L_{IR} , $L_{6.2\mu\text{m}}/L_{IR}$ also changes with z (e.g. Pope et al. 2013), as demonstrated in Figure 2.8 (*Left*) which shows the ratio of $L_{6.2\mu\text{m}}$ to L_{IR} for low- and high- z star-forming galaxies. Galaxies at $z \sim 2$ in our sample are brighter in L_{IR} by a factor of $\gtrsim 0.5$ dex compared to low- z (U)LIRGs of comparable $L_{6.2\mu\text{m}}/L_{IR}$; changes in either/both of $L_{6.2\mu\text{m}}$ and L_{IR} could drive the difference between low-redshift and $z \sim 2$ galaxies in Fig. 2.8. In any case, this trend persists if we instead use the ratio of $11.3 \mu\text{m}$ PAH luminosity to L_{IR} as

well as values for $L_{6.2\mu\text{m}}$ in GOALS measured using our method described in Section A.

Díaz-Santos et al. (2017) show that the IR surface density is a good predictor of physical PDR conditions such as gas density and incident radiation field strength. Furthermore, spatially resolved studies of nearby and $z \sim 3$ star-forming galaxies have shown the star-formation rate surface density (Σ_{SFR}) to be a major driver of the [C II]-deficit (Díaz-Santos et al., 2014; Smith et al., 2017; Rybak et al., 2019). In light of these results, and without spatial information at shorter wavelengths more aptly suited for tracing Σ_{SFR} , we calculate $\Sigma_{\text{IR}} = (L_{\text{IR}}/2)/\pi R_{\text{eff},160}^2$, the effective IR surface density using $R_{\text{eff},160}$ as measured with ALMA for our sample and *Herschel* PACS in GOALS. Figure 2.8 (*Right*) demonstrates that the offset between high- and low- z galaxies in $L_{6.2\mu\text{m}}/L_{\text{IR}}$ disappears when plotted against Σ_{IR} .

2.4.3 The Ratio of [C II] to PAH Luminosity

Figure 2.9 shows $L_{[\text{C II}]} / L_{6.2\mu\text{m}}$ as a function of Σ_{IR} for our sample, and local (U)LIRGs. GOALS star-forming galaxies ($\text{EW}_{6.2\mu\text{m}} \geq 0.5 \mu\text{m}$) have a tight ratio of $L_{[\text{C II}]} / L_{6.2\mu\text{m}}$ with a dispersion of 0.18 dex, less than the ~ 0.3 dex dispersion observed in both $L_{[\text{C II}]} / L_{\text{IR}}$ and $L_{6.2\mu\text{m}} / L_{\text{IR}}$. We fit a linear relation to star-forming GOALS galaxies on Figure 2.9, and find that $L_{[\text{C II}]} / L_{6.2\mu\text{m}}$ and Σ_{IR} anti-correlate with a slope of -0.23 ± 0.08 and zero-point 2.2 ± 0.9 . Although high-redshift observations remain limited by small sample statistics, the spread in $L_{[\text{C II}]} / L_{6.2\mu\text{m}}$ between GS IRS20 and GS IRS61 at $z \sim 2$ is 0.98 dex, five times greater than the dispersion of local star-forming (U)LIRGs, an observation that holds regardless of how the PAH luminosities are measured in GOALS (see Section 2.3.4).

GS IRS20 and GS IRS61 are ~ 0.67 and ≥ 1.65 dex respectively below the mean of $L_{[\text{C II}]} / L_{6.2\mu\text{m}}$ observed in GOALS star-forming galaxies, after accounting for the differences in how the PAHs were measured. GS IRS20 is possibly consistent with

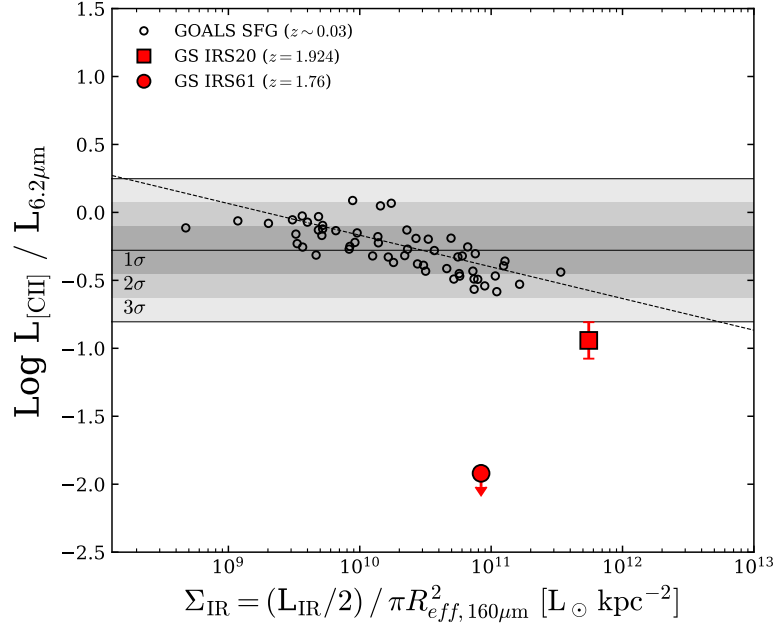


Figure 2.9 The ratio of [C II] luminosity to $6.2\mu\text{m}$ PAH luminosity in low-redshift and $z \sim 2$ IR-luminous star-forming galaxies as a function of IR surface density. The effective radius for all sources shown is calculated at rest-frame $160\mu\text{m}$ continuum. The gray shaded regions contain the 1σ , 2σ , and 3σ dispersions around the mean of $L_{[\text{C II}]} / L_{6.2\mu\text{m}}$ in star-forming GOALS galaxies. The dotted black line corresponds to the best-fit trend in GOALS, and has a slope of -0.23 ± 0.08 and zero-point equal to 2.2 ± 0.9 . The dearth of high- z points on this Figure demonstrates the need for more observations of [C II], PAH, and IR size measurements in the same galaxies.

the extrapolation of the low- z negative trend between $L_{[\text{C II}]} / L_{6.2\mu\text{m}}$ and Σ_{IR} beyond the most compact GOALS star-forming galaxy; however, this cannot explain the extremely low ratio observed in GS IRS61. GS IRS61 shows no indication of a deeply buried AGN (Figure 2.2), and there is a low probability that we missed the redshifted [C II] line (see Section 2.3.2). The dust continuum is marginally more extended than the ALMA beam and would have to be extraordinarily compact (Σ_{IR} would have to increase by > 2 orders of magnitude) to be consistent with the extrapolated low- z trend. For these reasons, GS IRS61 is likely a highly unusual source when compared to low- z star-forming galaxies of comparable Σ_{IR} .

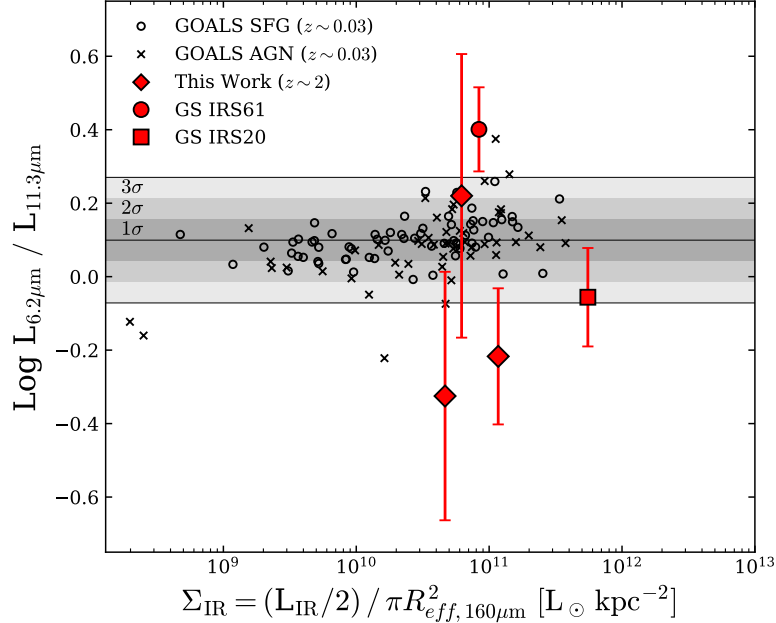


Figure 2.10 The ratio of $L_{6.2\mu\text{m}}$ to $L_{11.3\mu\text{m}}$ vs. effective IR surface density calculated at rest-frame $160\ \mu\text{m}$. The color scheme follows previous figures. $L_{6.2\mu\text{m}}/L_{11.3\mu\text{m}}$ does not change drastically with Σ_{IR} in star-forming GOALS galaxies, with minimal 1σ scatter ~ 0.06 dex shaded in gray about an average value of 0.08.

If we assume that the relevant physical parameters of the $z \sim 2$ galaxies are drawn from the same distribution that is observed in GOALS, then GS IRS20 and GS IRS61 would be $\sim 3\sigma$ and $\gtrsim 6\sigma$ below the low- z mean. The likelihood of observing two galaxies at 3σ and 6σ from the norm is $\approx 10^{-11}$. Therefore, the offset in $L_{[\text{C II}]} / L_{6.2\mu\text{m}}$ between low- z (U)LIRGs and what we measure in our sample may relate to changes in the physical ISM conditions.

2.5 Discussion

2.5.1 PAH Heating vs. Far-IR Cooling

We find a difference in the ratio of $[\text{C II}]$ to PAH emission between local ULIRGs and observations of two $z \sim 2$ dusty star-forming galaxies including one upper limit (Fig. 2.9), which could be due to changes in heating and cooling mechanisms. As opposed to being scaled up versions of nearby star-forming galaxies, starbursts at

earlier times may exhibit evolution in their ISM conditions. While the behavior of both PAH and [C II] changes at a low metallicity (Shivaei et al., 2017; Croxall et al., 2017), we do not expect this to affect our massive ($\log M_*/M_\odot \sim 11$) $z \sim 2$ galaxies given the $z \sim 2$ mass-metallicity relation (Sanders et al., 2015).

PAHs and other small grains are important sources of photoelectrons in PDRs (e.g., Bakes & Tielens 1994), and the ratio of far-IR line to PAH emission is sensitive to the photoelectric heating efficiency (ϵ_{PE}) of the PDR gas. As noted by Helou et al. (2001), L_{PAH} (or $L_{6.2\mu\text{m}}$) may be more appropriate normalization factors for $L_{[\text{C II}]}$ than L_{IR} given the direct relationship with ϵ_{PE} :

$$\frac{L_{[\text{C II}]} + L_{[\text{O I}]}}{L_{\text{PAH}}} = (\eta_{[\text{C II}]} + \eta_{[\text{O I}]})\epsilon_{\text{PE}} \approx \frac{\Gamma_{\text{gas}}^{e^-}}{\Gamma_{\text{dust}}^{\text{PAHs}}} \quad (2.2)$$

where following Croxall et al. (2012), $\eta_{[\text{C II}]}$ and $\eta_{[\text{O I}]}$ represent the relative contribution of the two principal cooling channels to the total gas cooling. $\Gamma_{\text{gas}}^{e^-}$ is the total gas heating via photoelectrons, and $\Gamma_{\text{dust}}^{\text{PAHs}}$ the total dust heating accounted for by PAHs. Cooling from other far-IR such as [C I] and [Si 2] are assumed to be negligible (i.e., $\eta_{[\text{C II}]} + \eta_{[\text{O I}]} \sim 1$).

Assuming that the $6.2\mu\text{m}$ PAH feature linearly scales with total PAH luminosity (e.g., Smith et al. 2007), and the fraction of [C II] emission originating from PDRs is roughly constant, then the ratio $L_{[\text{C II}]} / L_{6.2\mu\text{m}}$ probes the difference of photoelectric efficiency and normalized cooling via [O I]. Knowing that the ratio of [O I] emission to [C II] emission of PDR origin varies by an order of magnitude in nearby (U)LIRGs (Díaz-Santos et al., 2017), the location of GS IRS20 and GS IRS61 on Fig. 2.9 could be interpreted as evidence for enhanced [O I] cooling in these galaxies if the total ϵ_{PE} is constant. Díaz-Santos et al. (2017) demonstrate that [O I]/[C II] correlates with gas and dust temperature within PDRs, and [O I]/[C II] > 1 where dust temperatures exceed ~ 35 K. Indeed, warm-dust blackbodies ($T_{\text{warm}} \sim 60$ K) dominate the IR SEDs of both GS IRS20 and GS IRS61 ($L_{\text{cold}}/L_{\text{IR}} \lesssim 0.3$, Table 2.3), consistent with

enhanced PDR cooling through [O I] emission. Moreover, our $z \sim 2$ sample has high Σ_{IR} compared to the average of GOALS (Fig. 2.8 *Right*), implying more star-formation in smaller volumes. In such physical conditions, PDR densities are expected to be higher and exposed to more intense radiation fields where [O I] naturally arises as the dominant cooling channel (Díaz-Santos et al., 2017). If the positions of GS IRS20 and GS IRS61 on Fig. 2.9 are solely due to enhanced [O I] cooling ($\epsilon_{\text{PE}} = \text{constant}$), then we calculate $L_{[\text{O I}]} = 7 \times 10^9 L_{\odot}$ and $L_{[\text{O I}]} \gtrsim 10^{10} L_{\odot}$ for these two galaxies respectively in order to bring both in line with the GOALS sample. In this scenario, $L_{[\text{O I}]} / L_{[\text{C II}]} \sim 5$ in GS IRS20 and [O I] dominates far-IR line cooling in both galaxies.

Alternatively, low $L_{[\text{C II}]} / L_{6.2\mu\text{m}}$ could indicate a low ϵ_{PE} by Equation 2.2 if [O I] emission is not significantly enhanced in GS IRS20 and/or GS IRS61. We speculate that a decrease in the photoelectric efficiency in high- z dusty star-forming galaxies could play a role in enhancing star-formation rates compared to the galaxy main-sequence by reducing the coupling efficiency between interstellar radiation fields and gas heating. In other words, the colder ISM phases become less susceptible to temperature increases via stellar feedback as the reservoir of electrons in PAHs is diminished. Consequently, galaxies above the main-sequence would not exhibit strong far-IR line cooling at higher star-formation rates, as has been observed locally and tentatively at high- z (Díaz-Santos et al., 2017; Zanella et al., 2018). A comprehensive study of far-IR fine-structure emission lines combined with mid-IR PAH spectra is needed to test this hypothesis, and the nature of gas heating and cooling at $z \sim 2$ will be a function of ϵ_{PE} , $\eta_{[\text{C II}]}$, and $\eta_{[\text{O I}]}$. Systematically low ϵ_{PE} in dusty star-forming galaxies at $z \sim 2$ would be associated with $[\text{O I}]/[\text{C II}] \sim 1$ in a statistical sample controlled for $f_{\text{AGN,MIR}}$, whereas $[\text{O I}]/[\text{C II}] > 1$ would favor higher density PDRs with more [O I] cooling. These far-IR cooling line ratios will be key for accessing the physical conditions in which most of the Universe’s stellar mass was formed.

2.5.2 Differences between GS IRS20 and GS IRS61

The data in hand portrays an interesting dichotomy of ISM conditions between GS IRS20 and GS IRS61. A 1 dex difference in $L_{[\text{C II}]} / L_{6.2\mu\text{m}}$ exists between the two galaxies, and is likely a function of PAH ionization state and therefore ϵ_{PE} . Whereas the 6.2 μm feature traces ionized PAHs, the 11.3 μm complex arises from neutral PAHs yet to lose their surface electrons (Tielens, 2008). As a result, the ratio of $L_{6.2\mu\text{m}} / L_{11.3\mu\text{m}}$ is sensitive to the PAH ionization fraction in a galaxy, and also changes in the grain size distribution as observed near the nuclei of AGN (Smith et al., 2007; Tielens, 2008). Figure 2.10 shows this ratio as a function of Σ_{IR} for GOALS and our sample at $z \sim 2$. GS IRS20 has a PAH line ratio near the local average, as may be expected if star-formation in this merging galaxy is proceeding in a comparable manner to what is found in GOALS, which are mostly mergers themselves. On the other hand, GS IRS61 has the highest ratio of $L_{6.2\mu\text{m}} / L_{11.3\mu\text{m}}$ amongst galaxies at low- and high-redshift. This is consistent with the location of GS IRS61 in Fig. 2.9: an increase in PAH ionization would lower ϵ_{PE} , decoupling PAH and [C II] emission to produce the extreme deficit in $L_{[\text{C II}]} / L_{6.2\mu\text{m}}$ observed.

The only low- z galaxies within 1σ of GS IRS61 on Fig. 2.10 are a handful of GOALS AGN, and the ratio of $L_{6.2\mu\text{m}} / L_{11.3\mu\text{m}}$ appears larger than most star-forming GOALS galaxies, even after correcting for PAH extinction (see Fig. 2 of Stierwalt et al. 2014). Whether or not this is common at high-redshift remains to be explored; however, the scatter in $L_{6.2\mu\text{m}} / L_{11.3\mu\text{m}}$ we measure at $z \sim 2$ is nearly three times larger than what is seen in the GOALS star-forming sample, although we note that error bars at higher z are large. While both GS IRS20 and GS IRS61 have comparable far-IR colors, GS IRS61 has a lower $L_{\text{cold}} / L_{\text{IR}}$ (Fig. XX), indicating warmer dust conditions dominating the galaxy, consistent with low ϵ_{PE} as larger dust grains absorb more of the incident radiation field in PDRs. The parameter space of PAH line ratios at cosmic noon has yet to be statistically explored, and may prove key for our understanding of

dust properties and the link between stellar radiation fields and the ISM at the peak epoch of galaxy evolution.

2.5.3 Future Outlook

Testing the nature of gas heating and cooling in the ISM of high-redshift galaxies will be possible with future ALMA observations targeting [C II] in IRS sources. Mid-IR spectra are crucial for constraining $f_{\text{AGN,MIR}}$, from which the properties of star-formation at high- z can be reliably characterized in the absence of or presence of an AGN. *Spitzer's* cryogenic lifetime has ended, so the number of galaxies with available mid-IR spectra is currently limited. Future surveys with *JWST*/MIRI will re-open the mid-IR Universe at high spectral sensitivity.

Pending the launch of *JWST*, ALMA can continue targeting IRS galaxies to explore the relationship between [C II] and PAH emission as a function of L_{IR} and $f_{\text{AGN,MIR}}$. Understanding the intrinsic scatter in these relations will be crucial when designing efficient surveys that maximize the science potential of *JWST*, and key for understanding the physics of gas heating and cooling in the early Universe, which observations with future facilities like *Origins Space Telescope*³ or *SPICA*⁴ will revolutionize.

2.6 Summary and Conclusions

We have observed [C II] emission in a sample of $z \sim 2$ star-forming galaxies with existing detections of PAH dust emission in order to explain the balance of heating and cooling in the ISM and how it may be different from $z \sim 0$. Our main conclusions are as follows :

³<https://origins.ipac.caltech.edu/>

⁴<https://spica-mission.org/>

1. We detect the dust continuum near the peak of the IR SED ($\lambda_{\text{rest}} \sim 160 \mu\text{m}$) in all six targets. After correcting for known astrometry offsets between ALMA and *HST*, the position of the dust continuum emission coincides with the rest-frame optical light in all but GS IRS46. Our most luminous target GS IRS20 is classified as a merger and is a clear starburst on the main-sequence diagnostic diagram.
2. We detect [C II] in one target, GS IRS 20 at high SNR of 34. The bright [C II] emission and interesting optical morphology makes this an excellent target for follow-up ALMA observations to study its gas dynamics at higher spatial resolution. We place a deep upper limit on $L_{[\text{C II}]}$ in one other galaxy, GS IRS61, after calculating the probability the redshifted [C II] line fell into our ALMA bandpass tuning. For other targets in our sample, our observations likely missed the galaxy's [C II] line. Our $z \sim 2$ galaxies follow the [C II]-deficit relation observed for nearby (U)LIRGs, as found by several other $z \sim 2 - 3$ studies.
3. As found in previous studies, our $z \sim 2$ galaxies and other high- z samples show decreasing $L_{6.2\mu\text{m}}/L_{\text{IR}}$ with L_{IR} . Star-forming galaxies at $z \sim 2$ have more PAH emission per unit L_{IR} compared to low- z star-forming galaxies of comparable L_{IR} ; however, this offset disappears when comparing $L_{6.2\mu\text{m}}/L_{\text{IR}}$ in all galaxies as a function of IR surface density.
4. We explore the balance of heating and cooling in the ISM by looking at the ratio of [C II] to PAH luminosity. For nearby (U)LIRGs, this ratio is relatively tight as a function of L_{IR} . Our $z \sim 2$ galaxies are low relative to this relation. This may be because of warmer environments, suppressed photoelectric efficiencies in PDR gas, and/or the importance of cooling from other far-IR lines such as [O I]

Table 2.4. Existing *Spitzer* and *Herschel* Photometry

Target	3.6 μ m	4.5 μ m	5.8 μ m	8 μ m	16 μ m	24 μ m	70 μ m
	[μ Jy]	[μ Jy]	[μ Jy]	[μ Jy]	[μ Jy]	[μ Jy]	[μ Jy]
GS IRS20	16.91 \pm 0.05	19.89 \pm 0.07	21.59 \pm 0.32	13.42 \pm 0.35	–	275.0 \pm 6.0	3170.0 \pm 590.5
GS IRS46	68.87 \pm 0.06	51.16 \pm 0.08	42.72 \pm 0.47	25.45 \pm 0.45	–	378.0 \pm 6.6	–
GS IRS50	14.9 \pm 0.03	16.7 \pm 0.04	15.88 \pm 0.22	10.49 \pm 0.23	55.6 \pm 6.6	227.0 \pm 8.1	–
GS IRS52	9.93 \pm 0.05	13.47 \pm 0.06	13.15 \pm 0.33	10.7 \pm 0.33	60.9 \pm 8.1	240.0 \pm 8.6	–
GS IRS58	18.45 \pm 0.04	21.48 \pm 0.06	18.92 \pm 0.27	12.82 \pm 0.31	–	243.0 \pm 8.7	–
GS IRS61	16.21 \pm 0.04	18.73 \pm 0.05	17.05 \pm 0.25	13.37 \pm 0.27	59.6 \pm 5.0	245.0 \pm 8.7	–

Table 2.5. Existing *Spitzer* and *Herschel* Photometry (*continued*)

Target	100 μ m	160 μ m	250 μ m ^a	350 μ m ^a	500 μ m ^a
	[mJy]	[mJy]	[mJy]	[mJy]	[mJy]
GS IRS20	8.32 \pm 0.56	20.15 \pm 1.6	24.78 \pm 2.3	23.82 \pm 3.08	12.49 \pm 5.08
GS IRS46	–	–	13.05 \pm 2.8	15.11 \pm 4.7	13.0 \pm 2.0
GS IRS50	1.12 \pm 0.13	3.62 \pm 1.05	5.83 \pm 2.84	6.06 \pm 2.44	4.03 \pm 3.44
GS IRS52	–	–	10.06 \pm 3.26	9.05 \pm 4.4	6.86 \pm 3.66
GS IRS58	1.27 \pm 0.14	3.51 \pm 0.99	8.85 \pm 2.28	11.15 \pm 2.14	5.73 \pm 2.88
GS IRS61	3.21 \pm 0.16	5.56 \pm 1.08	5.76 \pm 2.2	3.44 \pm 2.58	4.96 \pm 2.8

^aConfusion noise for 250 μ ., 350 μ m and 500 μ m is \sim 5 mJy (see Nguyen et al. 2010 for exact values) and has been included in all SED fits.

at $z \sim 2$. GS IRS61, the galaxy with the lowest [CII]/PAH, shows evidence for high PAH ionization, consistent with inefficient gas heating in PDR regions.

We caution that our study shows that [CII] and PAH emission may not have a simple relation to L_{IR} , and therefore SFR, in $z \sim 2$ dusty star-forming galaxies. Further observations are needed to validate our results and test the ideas of warmer dust environments and additional cooling channels. These can be obtained by getting more [CII] detections of galaxies with existing PAH measurements from *Spitzer/IRS* or from future programs tracing the mid-IR and far-IR lines with *JWST* and ALMA.

CHAPTER 3

REGULATING STAR FORMATION IN NEARBY DUSTY GALAXIES: LOW PHOTOELECTRIC EFFICIENCIES IN THE MOST COMPACT SYSTEMS

This chapter is adapted from McKinney et al. (2021a) originally published in the Astrophysical Journal.

Star formation in galaxies is regulated by the heating and cooling in the interstellar medium. In particular, the processing of molecular gas into stars will depend strongly on the ratio of gas heating to gas cooling in the neutral gas around sites of recent star-formation. In this chapter, we combine mid-infrared (mid-IR) observations of Polycyclic Aromatic Hydrocarbons (PAHs), the dominant heating mechanism of gas in the interstellar medium (ISM), with [C II], [O I], and [Si II] fine-structure emission, the strongest cooling channels in dense, neutral gas. The ratio of IR cooling line emission to PAH emission measures the photoelectric efficiency, a property of the ISM which dictates how much energy carried by ultraviolet photons gets transferred into the gas. We find that star-forming, IR luminous galaxies in the Great Observatories All-Sky LIRG Survey (GOALS) with high IR surface densities have low photoelectric efficiencies. These systems also have, on average, higher ratios of radiation field strength to gas densities, and larger average dust grain size distributions. The data support a scenario in which the most compact galaxies have more young star-forming regions per unit area, which exhibit less efficient gas heating. These conditions may be more common at high- z , and may help explain the higher star-formation rates at cosmic noon. We make predictions on how this can be investigated with *JWST*.

3.1 Introduction

Star-formation in a galaxy is dependent on processes which remove energy allowing gas to cool. Only the coldest phases will collapse under self-gravity to form stars, and so characterizing the mechanisms by which gas heats and cools is critical to our understanding of star-formation, and galaxy evolution. The cold gas associated with star-formation emits strongly in low energy atomic and molecular transitions, bright at infrared (IR) wavelengths.

Studies with the *Infrared Space Observatory (ISO)* were key in unveiling the 5 – 200 μm wavelength regime of the electro-magnetic spectrum of galaxies, which is rich in strong atomic and molecular emission lines that trace the ISM (Malhotra et al., 1997, 2001; Dale et al., 2000). Amongst the brightest of these features are [O I] 63 μm , and [C II] 157.7 μm which can contain 0.1–1% of total infrared luminosities (Malhotra et al., 2001; Stacey et al., 2010; Díaz-Santos et al., 2013; Brisbin et al., 2015; Ibar et al., 2015). The *Herschel Space Telescope* was used to significantly increase the number of galaxies detected in the far-IR lines (e.g., Sturm et al. 2000; van der Wel et al. 2014; Díaz-Santos et al. 2011), and studies with the *Spitzer Space Telescope* added other prominent cooling lines such as [Si II] 34.8 μm , as well as Polycyclic Aromatic Hydrocarbon (PAH) vibrational lines between 3 – 17 μm that trace photoelectric heating.

[C II], [O I], and [Si II] are well-established as strong coolants in Milky Way photodissociation regions (PDRs), the transition zones between H 2 regions and the cold-neutral-medium (e.g., Wolfire et al. 1990, 2003). As the boundary layer between warm and cold gas, PDRs are an excellent place to study the processes of heating and cooling, as the relative balance of energy gains and losses can impact future star-formation. Emission from small grains, PAHs, provide an excellent tracer of the photoelectric heating of gas in PDRs (Galliano et al., 2008; Tielens, 2008). Photoelectrons ejected from PAH grains share energy with H and H₂, which go on to

collisionally excite fine-structure transitions of C^+ , O , and Si^+ . Although [C II] and [O I] emission are the dominant cooling channels in more normal PDRs (e.g., Tielens & Hollenbach 1985b; Kaufman et al. 1999), [Si II] can also act as a significant coolant at high interstellar radiation field densities (Kaufman et al., 2006). Thus, the cycle of gas heating and cooling in PDRs is traced by [C II], [O I], [Si II], and PAH emission, which collectively make for a powerful diagnostic of the ISM in extragalactic sources (e.g., Malhotra et al. 2001; Helou et al. 2001; Croxall et al. 2012; Beirão et al. 2012; Sutter et al. 2019).

The deficit of [C II] emission per unit L_{IR} in warmer (higher dust temperatures; T_{dust}), and more compact Luminous IR Galaxies (LIRGs: $\log L_{IR}/L_{\odot} = 11 - 12$, ULIRGs: $\log L_{IR}/L_{\odot} > 12$) as compared to less extreme galaxies is a well-studied phenomenon (e.g., Malhotra et al. 1997, 2001; Luhman et al. 1998, 2003; Stacey et al. 2010; Herrera-Camus et al. 2015; Díaz-Santos et al. 2013, 2014, 2017; Ibar et al. 2015; Smith et al. 2017). Moreover, PAH emission and other far-IR fine-structure lines key to PDR heating and cooling show similar deficits (e.g., Brauher et al. 2008; Wu et al. 2010; Graciá-Carpio et al. 2011; Pope et al. 2013; Stierwalt et al. 2014; De Looze et al. 2014; Cormier et al. 2015; Díaz-Santos et al. 2017). The IR emission line deficits can be due to changes in ISM densities and the strength of the radiation field impinging upon PDR surfaces (e.g., Díaz-Santos et al. 2017), and/or opacity effects, thermal line saturation, and evolution in dust grain properties (Luhman et al., 1998; Malhotra et al., 2001; Helou et al., 2001; Muñoz & Oh, 2016; Smith et al., 2017); however, the deficits largely disappear in normal star-forming galaxies when the line emission is normalized by total PAH emission (Helou et al., 2001; Croxall et al., 2012; Sutter et al., 2019). This reinforces the link between the ejection of photoelectrons from PAH grains and the collisional excitation of [C II] and other fine-structure lines, and suggests that the heating and cooling processes within PDRs behave similarly for normal star-forming conditions over a range of T_{dust} and L_{IR} .

Interestingly, McKinney et al. (2020) found lower [C II]/PAH emission at $z \sim 2$ than $z \sim 0$, suggesting evolution in the heating and cooling balance with redshift. However, the cooling/heating ratio has yet to be fully characterized in $z \sim 0$ starbursts, which represents a key step for future studies of the early Universe.

In this work, we explore the range of the ratio between fine-structure line cooling to photoelectric heating in local dusty, star-forming galaxies by comparing [C II], [O I], and [Si II] emission to PAH emission in the *Great Observatories All Sky LIRG Survey* (GOALS; Armus et al. 2009). GOALS is comprised of 244 galaxy nuclei within 202 LIRGs and ULIRGs spanning a range in merger stage and morphology. The range in IR luminosities and stellar masses of galaxies in GOALS makes the sample a bridge between normal star-forming galaxies and the most extreme, compact starbursts that host atypical PDR conditions exposed to stronger radiation fields (Díaz-Santos et al., 2017). Whether or not the gas cooling/heating properties are fundamentally different in such extreme environments remains an open question which this work aims to address.

GOALS has been the subject of extensive study with observations spanning the electromagnetic spectrum¹, including mid- and far-IR measurements of PDR cooling lines and PAHs, the ratio of which is an empirical measure of the photoelectric efficiency, ϵ_{PE} : the fraction of energy, in UV photons, emitted by hot stars that is absorbed by small dust grains and transferred into the neutral PDR gas via the photoelectric effect (e.g., Gerola & Schwartz 1976; de Jong 1977). There is evidence that ϵ_{PE} is a constant amongst normal star-forming galaxies (Helou et al., 2001; Sutter et al., 2019); however, this has yet to be tested in the starburst regime typical in luminous and ultra-luminous infrared galaxies powered by star formation..

¹For a complete list, visit <http://goals.ipac.caltech.edu/publications.html>.

The chapter is organized as follows: We review the multi-wavelength observations in Section 3.2, and discuss the sample selection. Section 3.3 summarizes important derived quantities of GOALS galaxies presented in other works, as well as key analysis steps we take to appropriately combine the multi-wavelength data. Our results are presented in Section 3.4, which we discuss in Section 3.5 in the context of local star-formation and trends in galaxy evolution. Section 3.6 summarizes the chapter.

3.2 Sample Selection and Data

This work focuses on data from *Spitzer*/IRS (Díaz-Santos et al., 2010, 2011; Petric et al., 2011; Stierwalt et al., 2013, 2014; Inami et al., 2013), *Spitzer*/IRAC (Mazzarella et al. 2020, in prep.), *Herschel* PACS and SPIRE (Zhao et al., 2013; Díaz-Santos et al., 2013, 2014, 2017), and AKARI/IRC (Inami et al., 2018).

To measure the ratio of cooling and heating in star-forming gas, we select from the 244 galaxies in GOALS all sources with $[\text{Ne } 5]_{14.3\mu\text{m}} / [\text{Ne } 2]_{12.8\mu\text{m}} < 0.5$ and/or $[\text{O } 4]_{25.9\mu\text{m}} / [\text{Ne } 2]_{12.8\mu\text{m}} < 1$ in order to exclude from the sample those galaxies with significant heating from a central AGN (Inami et al., 2013; Petric et al., 2011). Sources with low PAH equivalent widths (EW) but no high-ionization emission lines are not removed from the sample to avoid biasing the results concerning grain properties such as size and ionization. As a result, 16 strong AGN systems are removed from consideration. Heavily dust obscured AGN could still be lurking in the sample, and we use mid-IR AGN fractions ($f_{\text{AGN,MIR}}$) derived in Díaz-Santos et al. (2017) to identify sources with excess warm dust in the remaining sample, which we show in Figures to concentrate on the star-forming properties of the sample galaxies.

To fully explore the properties of interstellar PAH grains, we use AKARI 2.5–5 μm spectra of 145 GOALS (U)LIRGs presented in Inami et al. (2018), in which the 3.3 μm PAH feature was detected for 133 targets. This sub-sample spans the full range of

L_{IR} and luminosity distance, and is representative of the range in star-formation properties of GOALS.

3.3 Analysis

In addition to measured line fluxes, this work makes use of a number of quantities from *Herschel*/PACS observations derived in Díaz-Santos et al. (2017): We subtract out the ionized component of [C II] emission using the neutral [C II] PDR fractions (f_{PDR}), estimated with $[\text{N } 2]_{122}$ and $[\text{N } 2]_{205}$ available for 54% of the sample, and far-IR colors $S_{\nu,63\mu\text{m}}/S_{\nu,158\mu\text{m}}$ otherwise, as described in Díaz-Santos et al. (2017). We use IR surface densities from Díaz-Santos et al. (2017) which are calculated from the effective area measured at $70 \mu\text{m}$, and total IR luminosities from Armus et al. (2009). We also use measurements of the average intensity of the UV interstellar radiation field impinging onto the surface of PDRs, G , measured in local units ($G_0 = 1.6 \times 10^{-3}$ erg s $^{-1}$ cm $^{-2}$, Habing 1968), and neutral gas volume densities, n_{H} , derived using the Kaufman et al. (1999, 2006) PDR models through PDR TOOLKIT (PDRT; Pound & Wolfire 2008) which depend principally on the galaxy-integrated [C II] and [OI] line fluxes, as well as L_{IR} .

3.3.1 PAH Properties

The PAH line fluxes used in our analysis are reported in Stierwalt et al. (2013, 2014), and Inami et al. (2018). We take the PAH luminosity, L_{PAH} , to be the sum of features measured between $\sim 5 - 18 \mu\text{m}$ by *Spitzer* IRS. Specifically, L_{PAH} includes the 6.2, 7.7, 8.6, 11.3, and $17 \mu\text{m}$ PAH lines and all sub-features therein, as measured by CAFE which fits the line fluxes, continuum and the extinction simultaneously (Marshall et al., 2007). On average, these five PAH lines account for $76\% \pm 9\%$ of the total PAH luminosity measured by both the Short-Low (SL, $5.5 - 14.5 \mu\text{m}$) and Long-Low (LL, $14 - 38 \mu\text{m}$) slits in GOALS galaxies (Stierwalt et al. 2014). Because the SL and LL

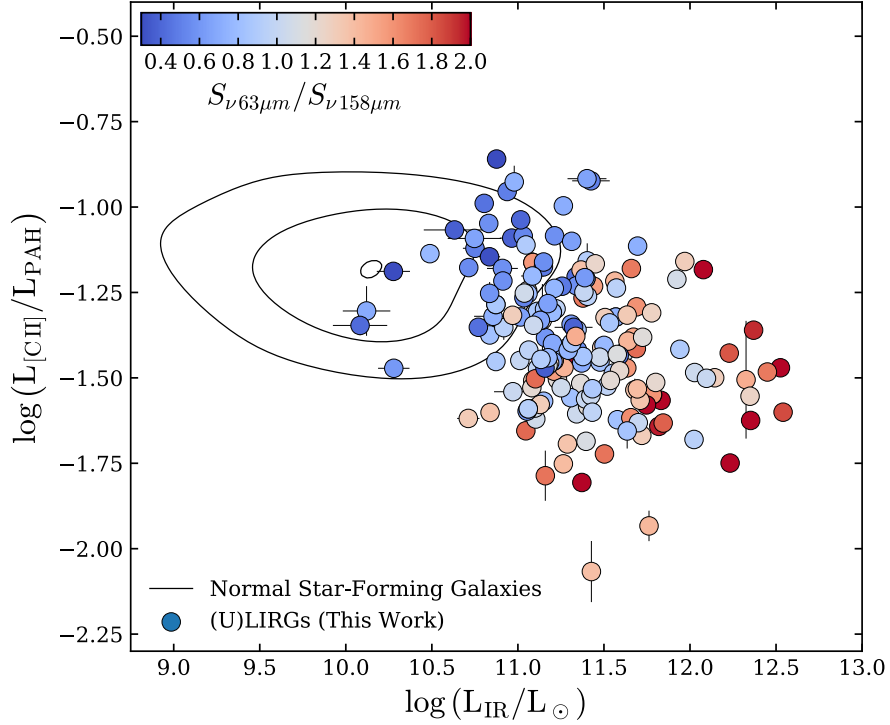


Figure 3.1 The ratio of [C II] emission to the sum of 6.2, 7.7, 8.6, 11.3 and 17 μm PAH emission in the nuclear regions of GOALS star-forming galaxies as a function of total IR luminosity. The ionized gas contribution to $L_{[\text{C II}]}$ has not been subtracted out. Each data point is colored by the far-IR color measured with the ratio of continuum at 63 μm and 158 μm . Black contours contain 33%, 66%, and 95% of normal star-forming galaxies measured by *ISO* (Helou et al., 2001; Malhotra et al., 2001; Dale et al., 2000). Note that we have scaled the ISOCAM PAH measurements by a factor of 42% to estimate L_{PAH} from the 6.75 μm broadband photometry, correcting for the underlying continuum and longer wavelength features. The correlation between [C II]/PAH and L_{IR} in local LIRGs and ULIRGs is weak, with a great deal of scatter, but warmer objects tend to have lower [C II]/PAH ratios compared to normal star-forming galaxies and cooler LIRGs.

slits have different widths, tied to the changing PSF with wavelength, some highly resolved galaxies show a small jump between their SL and LL IRS spectra. This is discussed fully in Stierwalt et al. (2013), and we combine the SL and LL data using their scale factors derived from the wavelength overlap between the two slits. L_{PAH} is normalized to the SL slit. The $3.3 \mu\text{m}$ PAH luminosities ($L_{3.3}$) are also matched to the aperture extraction of IRS/SL data (see Inami et al. 2018 Section 3); however, $L_{3.3}$ represents a small component of L_{PAH} ($5\% \pm 1.5\%$), and is therefore only used to investigate the properties of PAH line ratios. In general, the fraction of total PAH power measured through the SL slit compared to the LL slit does not correlate with galaxy distance, or other quantities we compare against in this work, namely Σ_{IR} . The sum of PAH features between 6 and $18 \mu\text{m}$ traces the bulk of the total power of PAH emission in GOALS.

From the sub-sample of GOALS galaxies with AKARI observations, 50 objects were selected as test-cases for CAFE-NG (Advanced CAFE; Bonfini et. al., in prep., Marshall et al. 2007), which simultaneously fits continuum and spectral features in the $0.6 - 35 \mu\text{m}$ range. These galaxies have full spectral model fits to the AKARI+Spitzer data, which explicitly includes silicate absorption and $3.05 \mu\text{m}$ ice feature absorption which are fit independently. Joint fits to IR continuum and line measurements are important to get accurate line fluxes e.g., Smith et al. 2007; Lai et al. 2020), and we use these new CAFE fits to estimate extinction-corrected $3.3 \mu\text{m}$ luminosities, $L_{3.3}$, for the full AKARI sample. In general, the measured PAH intensity depends on how the local continuum is estimated. Inami et al. (2018) adopt a spline technique ($L_{3.3,\text{spline}}$), which is known to under-estimate the extinction-corrected flux of PAH features between $6 - 17 \mu\text{m}$ by $30 - 60\%$ (Smith et al., 2007). From careful fits to the full PAH features (Bonfini et al., in prep.) we find that $L_{3.3,\text{spline}}/L_{3.3} = 0.29 \pm 0.07$. For the sample here we use this conversion and the results from Inami et al. (2018) to estimate $L_{3.3}$ for each source before comparing to the other PAH features.

3.3.2 Aperture Matching

Galaxies in GOALS vary from extended sources spatially resolved by *Spitzer* to unresolved point-like sources, which motivates a careful approach to aperture matching when comparing *Spitzer* and *Herschel* measurements. The effective area of the *Spitzer*/IRS SL slit is $3''.7 \times 9''.5$ (Stierwalt et al., 2013). To best match this area, we begin by using [C II] and [O I] line fluxes measured through the central spaxel of the PACS/IFU with dimensions of $\sim 9''.4 \times 9''.4$ (See Sect. 3.2 in Díaz-Santos et al. 2017). Next, we project the effective SL slit and PACS central-spaxel aperture onto the *Spitzer*/IRAC $8 \mu m$ images, assuming that it traces the co-spatial PAH and far-IR line emission from star-forming regions in LIRGs, which is reasonable for the 2 – 7 kpc-scale observations in this work (Peeters et al., 2004; Alonso-Herrero et al., 2010; Pereira-Santaella et al., 2010; Salgado et al., 2016; Hughes et al., 2016). Smith et al. (2007) show the fractional power of PAHs to the IRAC $8 \mu m$ band to have a median value of 70% in normal star-forming galaxies, which increases only marginally when a more careful subtraction of stellar continuum is done using the IRAC 3 – 5 μm channels (e.g., Helou et al. 2004). We use the ratio of the $8 \mu m$ flux through each aperture to derive a correction, which is then used to scale down the PACS measurements to match the IRS aperture. The median of aperture corrections derived in this manner is 0.62 with upper and lower quartiles of 0.69 and 0.55 respectively. We note that aperture matching does not introduce any bias in the slope of trends we explore in this chapter.

The [Si II] $34.8 \mu m$ emission was measured in the *Spitzer*/IRS LL slit, using an effective extraction aperture of $\sim 10''.6 \times 36''.6$ (Stierwalt et al., 2013). To match measurements made through the IRS/SL slit, we scale the [Si II] line flux down to the normalization of the SL spectrum using the same multiplicative factors applied to the $17 \mu m$ PAH fluxes (Stierwalt et al., 2013). As noted in Stierwalt et al. (2014), 15 LIRGs in GOALS have scale factors > 2 due to extended structure in the LL slit not

captured by the SL slit. To avoid complications, we do not include these sources in our analysis. In summary, we have matched the apertures between *Herschel*/PACS and *Spitzer*/IRS, and the measurements reported here are for the central regions ($\sim 2 - 7$ kpc) of GOALS systems unless explicitly stated otherwise.

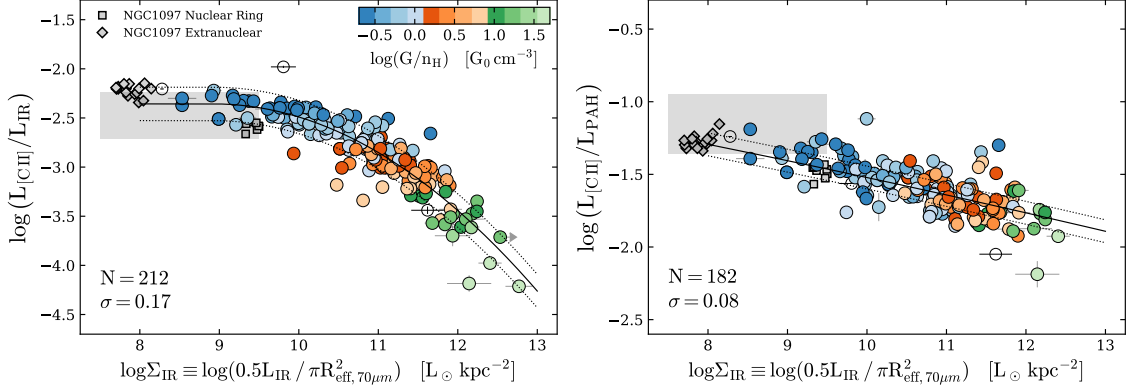


Figure 3.2 (*Left*) The [CII] deficit in GOALS as presented by Díaz-Santos et al. (2017), calculated with galaxy-integrated measurements of $L_{[\text{CII}]}$ and L_{IR} . The data are colored by their average ratio of UV radiation field strength to neutral hydrogen density in PDRs (G/n_{H}). The solid black line indicates the best-fit to the data from Díaz-Santos et al. (2017) using Equation 3.1. Dotted lines correspond to $\pm 1\sigma$ about the best-fit. (*Right*) The ratio of $L_{[\text{CII}]}$ to L_{PAH} (summing over all features between $6 - 18 \mu\text{m}$) for star-forming (U)LIRGs with *Herschel*/PACS [CII] measurements and *Spitzer*/IRS observations of the PAHs. To compare our results with more normal star-forming conditions, we show measurements of the spatially resolved nuclear ring and extranuclear bar in NGC 1097 as open symbols (squares and circles respectively) from Beirão et al. (2012) on both panels, as well as the range in [CII]/ L_{IR} and [CII]/PAH observed in the normal star-forming galaxy sample of Helou et al. (2001) and Malhotra et al. (2001) (shaded grey regions), scaled by a factor of 2.3 in the *Right* panel as described in Figure 3.1. Both [CII]/ L_{IR} and [CII]/PAH trend towards lower values in more compact systems, and the use of PAH emission as a normalization for [CII] yields a lower scatter about the overall trend.

3.4 Results

Following early [CII] surveys of low-redshift, mostly normal star-forming galaxies with *ISO*, Helou et al. (2001) measured a constant [CII]/PAH ratio over a range of far-IR colors that showed significantly less scatter than [CII]/ L_{IR} . This reinforced the link

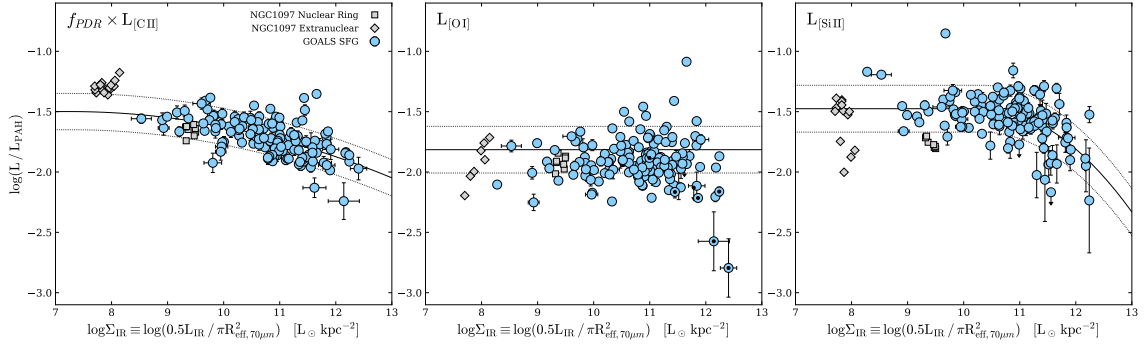


Figure 3.3 IR cooling lines over PAH emission in GOALS star-forming (U)LIRGs vs. IR surface densities. On all panels, we show the best-fit of Eq. 3.1 to the data (solid black line), where all parameters are left free. Dotted black lines indicated $\pm 1\sigma$ scatter about the trend. (*Left*) $[\text{C II}]/\text{PAH}$ with the ionized component of $[\text{C II}]$ subtracted out using the $[\text{C II}]/[\text{N 2}]_{205}$ and $[\text{N 2}]_{122}/[\text{N 2}]_{205}$ ratio as described in Díaz-Santos et al. (2017). (*Center*) $[\text{O I}]/\text{PAH}$. Galaxies with signs of $[\text{O I}]$ self-absorption are marked with black dots, which comprise 5% of the sample. (*Right*) $[\text{Si II}]$ $34.8 \mu\text{m}$ over PAH. In all panels, we compare GOALS star-forming galaxies to the star-forming, compact nuclear ring, and extranuclear emission from NGC 1097 presented in Beirão et al. (2012). The spatially resolved emission in a normal star-forming galaxy is consistent with extrapolation of the trends observed in LIRGs and ULIRGs to low Σ_{IR} . While the fraction of cooling-to-heating in $[\text{C II}]$ falls in the most compact systems, $[\text{O I}]/\text{PAH}$ remains relatively constant over Σ_{IR} in (U)LIRGs. The lack of a positive trend between $[\text{O I}]/\text{PAH}$ and Σ_{IR} suggests that $[\text{O I}]$ cooling does not compensate for the negative trends observed in the other features.

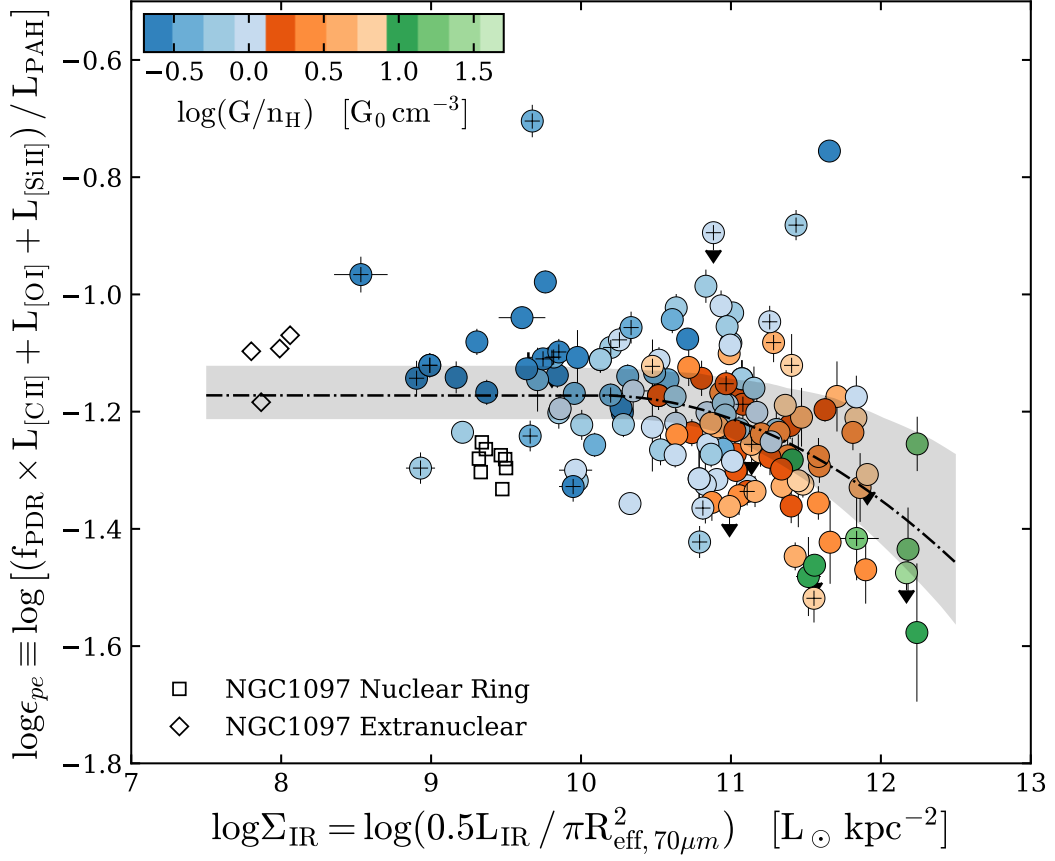


Figure 3.4 The ratio of prominent IR cooling lines to total PAH luminosity, an estimate of the photoelectric efficiency in PDRs, vs. IR surface density. All measurements along the y -axis have been aperture-matched as discussed in Section 3.3. The data are color-coded by $\log(G/n_H)$, following previous Figures. The dash-dotted line corresponds to the best-fit of Eq. 3.1 to the data, with all parameters set to free. The shaded grey region contains the top 95% of 1000 boot-strapped model fits. Data points marked with a + symbol have mid-IR AGN fractions $> 30\%$, and low $6.2 \mu m$ equivalent widths, either due to a deeply buried starburst or AGN. For comparison with more normal star-forming conditions, we show measurements of the spatially resolved nuclear ring and extranuclear bar in NGC 1097 as open symbols (squares and circles respectively) from Beirão et al. (2012). The Kendall’s τ and two-tailed $\log p$ -value for the (U)LIRGs are -0.3 and -7.1 respectively, indicating an anti-correlation between ϵ_{PE} and Σ_{IR} at a confidence level of $\approx 5\sigma$ (Tab. 3.2), driven largely by the turn-over in ϵ_{PE} at $\log \Sigma_{IR} > 10.5$ in galaxies with $\log(G/n_H) \gtrsim 0.5$. At these high surface densities, the average physical properties of PDRs depart from the more normal star-forming conditions observed at lower Σ_{IR} .

Table 3.1. Best-fit Parameters to Line/PAH ratios vs. Σ_{IR}

Line	a_0	a_1	a_2	1σ (dex)
[C II]	-0.278	-0.124	0.00	0.08
$f_{\text{PDR}} \times [\text{C II}]$	-2.378	0.242	-0.016	0.15
[O I]	-1.997	0.013	0.00	0.19
[Si II]	-14.325	2.487	-0.120	0.19
$\epsilon_{\text{PE}}^{\text{a}}$	-6.277	1.010	-0.050	0.12

Note. — All line luminosities have been calculated from aperture matched flux measurements as described in Section 3.3 unless otherwise noted. Fits are a function of $\log_{10}\Sigma_{\text{IR}} = \log_{10}(0.5L_{\text{IR}}/\pi R_{\text{eff},70\mu\text{m}}^2)$ in units of $L_{\odot} \text{ kpc}^{-2}$. The right-most column corresponds to the 1σ scatter about the trend.

^aSee Equation 3.2.

between PAHs and [C II] emission via photoelectric heating inside PDRs. We find that the galaxy-integrated [C II]/PAH ratio in luminous, infrared, star-forming galaxies does not correlate strongly with either far-IR color or L_{IR} as shown in Figure 3.1, although warmer LIRGs and ULIRGs tend to have lower [C II]/PAH ratios compared to galaxies at $\log L_{\text{IR}}/L_{\odot} \lesssim 11$. Trends in PDR gas cooling/heating within the GOALS sample are likely to be more clear when measured against quantities that better reflect the ionizing radiation or luminosity density surrounding the young stars.

3.4.1 Line-to-PAH Ratios

The IR surface density is a more direct tracer of far-IR fine-structure line properties than color or L_{IR} (Díaz-Santos et al., 2013, 2017; Smith et al., 2017), both of which exhibit little to no influence on the ratio of [C II]/PAH (Fig. 3.1). As Σ_{IR} should scale with the number density of massive star-forming regions in the beam,

we expect Σ_{IR} to be more sensitive to statistical trends across the sample. The [C II] deficit vs. Σ_{IR} among luminous infrared star-forming galaxies presented in Díaz-Santos et al. (2017) is re-created for comparison in Figure 3.2 (*Left*). To test for trends in gas cooling over photoelectric heating, we calculate the [C II]/PAH ratio as a function of Σ_{IR} , shown in Figure 3.2 (*Right*), color coded by $\log G/n_{\text{H}}$ which scales linearly with IR surface density above $\log \Sigma_{\text{IR}}/[L_{\odot} \text{ kpc}^{-2}] \sim 10.7$ (Díaz-Santos et al., 2017). Whereas the [C II]/ L_{IR} ratio exhibits a maximum deficit of ~ 2 dex between $\log \Sigma_{\text{IR}}/[L_{\odot} \text{ kpc}^{-2}] = 8 - 13$, the [C II]/PAH ratio falls by a factor of ~ 0.5 dex over the same range. LIRGs at low Σ_{IR} exhibit [C II]/ L_{IR} and [C II]/PAH ratios comparable to those found in the spatially-resolved regions of NGC 1097 (Beirão et al., 2012), and the normal star-forming galaxies in Helou et al. (2001).

Following Díaz-Santos et al. (2017), we fit a second-order polynomial function to the [C II]/PAH ratio of the form:

$$\log(L_{\text{line}}/L_{\text{IR}}) = a_0 + a_1 \log \Sigma_{\text{IR}} + a_2 (\log \Sigma_{\text{IR}})^2 \quad (3.1)$$

Note that the function is forced to a constant maximum at values of Σ_{IR} less than where the turn-over occurs. While we do not include normal star-forming galaxies in the fit, a constant line-to-PAH ratio below the turn-over yields the best agreement with observations of low Σ_{IR} galaxies (e.g., Helou et al. 2001; Beirão et al. 2012; Croxall et al. 2012). The best-fit is shown as a black solid line in Fig. 3.2 (*Right*), the parameters for which are given in Table 3.1. While the [C II]/PAH ratio is not constant, the magnitude of the drop with Σ_{IR} is significantly less.

In addition to [C II], [O I] and [Si II] are important PDR cooling lines in terms of their overall contribution to the cooling budget (e.g., Rosenberg et al. 2015), and their strengths relative to the PAH emission are a diagnostic of PDR structure. Large [O I]/PAH ratios where [C II]/PAH is low could indicate greater gas densities, which would preferentially cool through the higher critical density [O I] line. In Figure

3.3, we show the [C II]/PAH, [O I]/PAH, and [Si II]/PAH ratios in separate panels for LIRGs and ULIRGs as a function of Σ_{IR} . Because we are comparing different fine-structure cooling lines here and would like to focus on the PDR emission alone, we subtract out the non-PDR component of the [C II] emission using f_{PDR} (e.g., Díaz-Santos et al. 2017). At low IR surface densities, the line-to-PAH ratios are consistent with spatially-resolved measurements of NGC 1097 (Beirão et al., 2012), representative of more normal star-forming conditions.

[C II]/PAH falls in the most compact sources at $\log \Sigma_{\text{IR}}/[L_{\odot} \text{ kpc}^{-2}] \gtrsim 10$. [O I]/PAH does not exhibit a turn-over at high Σ_{IR} , but shows an increasingly larger scatter (higher than the other line ratios), mostly with a constant lower envelope. This could arise from varying degrees of line self-absorption, as [O I] originates from deeper regions within PDRs, and/or the presence of intervening (foreground) cold, neutral material. Indeed, IRASF1224-0624, and ICO860, the two galaxies $> 2\sigma$ below the [O I]/PAH trend both show signs of self-absorption in the PACS spectra and have some of the highest $\tau_{9.7}$ optical depths observed in the sample; however, [O I] self-absorption is only observed in $\sim 5\%$ of GOALS in total (12 objects, see Díaz-Santos et al. 2017) spanning $\log \Sigma_{\text{IR}}/[L_{\odot} \text{ kpc}^{-2}] = 10 - 12.5$, and is therefore unlikely to influence statistical trends in the sample over the full range in Σ_{IR} .

3.4.2 The Photoelectric Efficiency

The photoelectric efficiency (ϵ_{PE}) is the fraction of energy that photoelectrons from PAHs transfer from UV photons into the gas relative to the total heating of dust. Observationally, ϵ_{PE} can be traced by the ratio of far-IR line emission to total PAH emission because photoelectrons from PAHs are one of the dominant heating mechanisms in PDRs, which cool predominantly via far-IR fine-structure line emission (e.g., Bakes & Tielens 1994; Malhotra et al. 2001; Croxall et al. 2012; Beirão et al. 2012). In practice, the cooling budget is dominated by [C II], [O I], and [Si II], and

Table 3.2. Correlation Coefficients between the Photoelectric Efficiency, as defined by the ratio of IR cooling lines to mid-IR PAH emission between $6 - 12 \mu\text{m}$, and other Quantities in GOALS star-forming Galaxies

	τ_k	$\log p$	SNR [σ] [‡]
$L_{\text{IR}} [L_{\odot}]$	$-0.15_{-0.2}^{-0.1}$	$-2.21_{-3.7}^{-1.1}$	$2.7_{1.7}^{3.7}$
$S_{\nu, 63\mu\text{m}}/S_{\nu, 158\mu\text{m}}$	$0.00_{-0.09}^{0.08}$	$-0.35_{-0.91}^{-0.09}$	$0.8_{0.2}^{1.5}$
$\Sigma_{\text{IR}} [L_{\odot} \text{ kpc}^{-2}]^{\text{b}}$	$-0.30_{-0.4}^{-0.2}$	$-7.1_{-9.5}^{-4.9}$	$5.3_{4.4}^{6.3}$
$G/n_{\text{H}} [G_0 \text{ cm}^{-3}]^{\text{c}}$	$-0.31_{-0.35}^{-0.26}$	$-9.0_{-11.6}^{-6.6}$	$6.1_{5.2}^{7.0}$
$\text{EW}(6.2 \mu\text{m}) [\mu\text{m}]$	$0.08_{0.01}^{0.1}$	$-0.8_{-1.9}^{-0.2}$	$1.5_{0.4}^{2.5}$
$f_{\text{AGN,MIR}}$	$0.08_{0.03}^{0.1}$	$-0.9_{-2.1}^{-0.3}$	$1.6_{0.6}^{2.6}$
f_{PDR}	$0.06_{0.0}^{0.1}$	$-0.6_{-1.5}^{-0.1}$	$1.1_{0.3}^{2.2}$
$L_{11.3 \mu\text{m}}/L_{7.7 \mu\text{m}}$	$0.06_{0.0}^{0.12}$	$-0.6_{-1.7}^{-0.2}$	$1.2_{0.4}^{2.3}$
$L_{7.7 \mu\text{m}}/L_{6.2 \mu\text{m}}$	$-0.23_{-0.3}^{-0.2}$	$-4.9_{-7.1}^{-3.1}$	$4.3_{3.3}^{5.4}$
$L_{11.3 \mu\text{m}}/L_{3.3 \mu\text{m}}^{\text{d}}$	$-0.37_{-0.42}^{-0.32}$	$-7.5_{-9.5}^{-5.7}$	$5.5_{4.8}^{6.2}$

Note. — Kendall’s τ correlation coefficients (τ_k) and p -values were calculated using `pymccorrelation` (Privon et al., 2020), which implements bootstrap error estimation on τ_k and p with censored data (upper limits) as described in Curran (2014) and Isobe et al. (1986) respectively. We report 16%, 50%, and 84% percentiles for each quantity.

^a Assuming normally distributed posteriors.

^b See Figure 3.4.

^c See Figure 3.5.

^d For the subset of GOALS (U)LIRGs with AKARI $3.3 \mu\text{m}$ PAH detections. See Figure 3.7.

$L_{\text{PAH}} \gg (L_{[\text{C II}]} + L_{[\text{O I}]} + L_{[\text{Si II}]})$. Assuming that the PAHs and ions are co-spatial such that the energy input into the gas by photoelectric heating powers the [C II], [O I], and [Si II] lines, an empirical tracer of the photoelectric efficiency is

$$\epsilon_{\text{PE}} \approx \frac{L_{[\text{C II}]} + L_{[\text{O I}]} + L_{[\text{Si II}]}}{L_{\text{PAH}}} \quad (3.2)$$

where the relative contribution of far-IR lines to ϵ_{PE} can vary across the PDR (Kaufman et al., 2006). Nevertheless, combined observations of these features capture an average ϵ_{PE} of PDRs over a galaxy.

We measure the average ϵ_{PE} for 152 GOALS star-forming galaxies including five upper limits, and show the combined sum of neutral [C II], [O I], and [Si II] cooling over L_{PAH} in Figure 3.4. A Kendall’s τ test supports an anti-correlation between ϵ_{PE} and Σ_{IR} at $\sim 5\sigma$ (see Table 3.2). As shown in Fig. 3.4, LIRGs at low Σ_{IR} exhibit fairly constant photoelectric efficiencies comparable to observations of normal star-forming galaxies (Beirão et al., 2012; Croxall et al., 2012). At high Σ_{IR} , the sum of all cooling lines relative to the PAHs shows a decreasing photoelectric efficiency, which suggests that the net cooling to photoelectric heating ratio is falling across the density and temperature structure of PDRs in compact objects. The relative contributions of [C II], [O I], and [Si II] to the cooling budget within PDRs (i.e., the numerator of Eq. 3.2) are on average 32%, 20%, and 48% respectively, and these values do not change significantly when splitting the sample above and below $\log \Sigma_{\text{IR}} / [L_{\odot} \text{ kpc}^{-2}] = 10.7$. Therefore, low photoelectric efficiencies are the product of overall less cooling in PDRs in all channels relative to PAH heating.

The anti-correlation between ϵ_{PE} and Σ_{IR} is robust against outliers, as demonstrated by the bootstrap fits on Figure 3.4. Nevertheless, there exist galaxies deviating from the trend by more than $\pm 2\sigma$ that warrant closer inspection. At all IR surface densities, objects in this class collectively have higher mean and median $f_{\text{AGN,MIR}}$ compared to the rest of the sample. Thus, the scatter above and below the

best-fit trend may be partially due to sources with an excess of hot dust continuum emission in their mid-IR spectra. This may be due to a weak, deeply buried AGN, even in sources where L_{IR} is dominated by star formation, which in turn may change the ionization structure and the PAH properties (Voit, 1992; Langer & Pineda, 2015; Langer et al., 2017). Alternatively, these objects may harbor heavily obscured star-forming regions with high levels of line self-absorption and/or continuum opacities. This absorption should appear in the PACS line profiles, but only 12 GOALS sources show evidence for absorption in the [OI] line (Díaz-Santos et al., 2017). We note that the detection of these signatures, presumably due to compact (narrow velocity) foreground clouds, may be limited by the coarse spectral resolution ($\sim 85 \text{ km s}^{-1}$) of *Herschel*/PACS (Gerin et al., 2015).

The photoelectric efficiencies we measure represent averages over the local properties of PDRs in the central ($\sim 2 - 7 \text{ kpc}$) star-forming regions of luminous infrared galaxies, and the trend in Fig. 3.4 suggests a departure from the typical ISM and PDR conditions at high Σ_{IR} . Indeed, galaxies in this domain with low ϵ_{PE} also have the largest ratios of G/n_{H} , which is also sensitive to the local physics of PDRs. We fit Equation 3.1 to the data, the parameters of which are given in Table 3.1, and find that the photoelectric efficiency turns over at $\log \Sigma_{\text{IR}}/[L_{\odot} \text{ kpc}^{-2}] \sim 10.5$, close to where G/n_{H} scales linearly with $\log \Sigma_{\text{IR}}$ (Díaz-Santos et al., 2017). Models of heating and cooling in PDRs predict an anti-correlation between G/n_{H} and ϵ_{PE} as the size and charge of dust grains are modified by the stellar radiation field (e.g., Bakes & Tielens 1994; Tielens 2008), a trend which we recover in Figure 3.5 at high ($\sim 6\sigma$) significance (see Tab. 3.2). We find general agreement between modeled and measured ϵ_{PE} for $T_{\text{gas}} = 50 - 1000 \text{ K}$, reasonable values for temperatures across the phase structure of PDRs (e.g., Tielens & Hollenbach 1985b; Bakes & Tielens 1994; Draine & Bertoldi 1996), and the two sets of models are able to account for the range in ϵ_{PE} we measure in GOALS. The most extreme ULIRGs at high Σ_{IR} and low ϵ_{PE} also

show the highest values of $\log(G/n_H) \gtrsim 0.25$ supporting a link between the strength of the radiation field and the heating efficiency within the PDR, which is mediated by the properties of PAH grains.

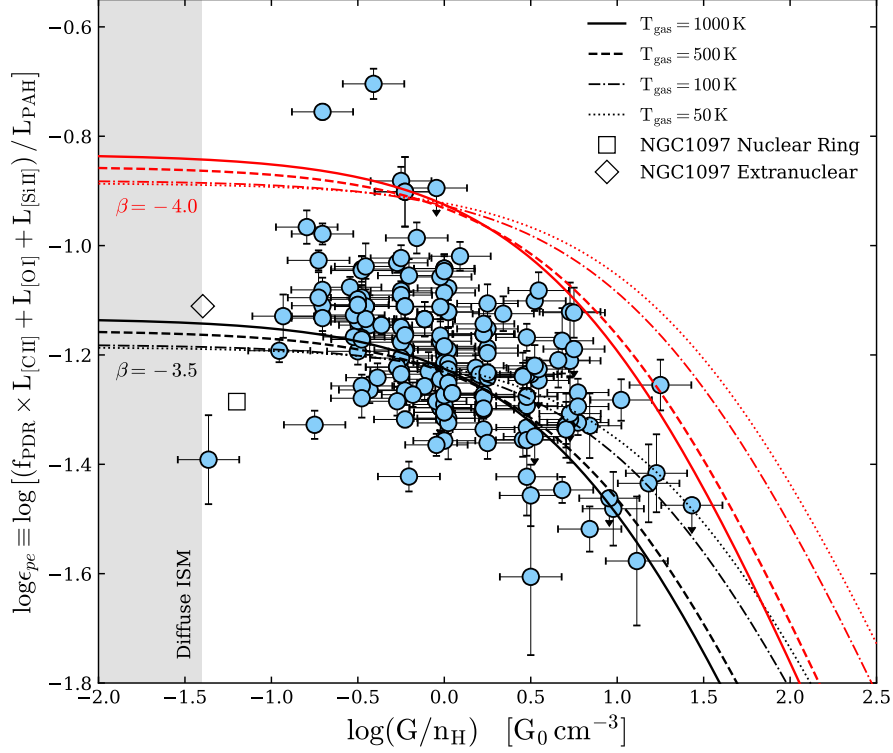


Figure 3.5 The photoelectric efficiency calculated as the sum of [CII], [OI], and [SiII] emission over the flux of PAH emission including lines between $6 - 18 \mu m$ vs. G/n_H , the ratio of the average radiation field strength impinging upon PDRs to the mean neutral Hydrogen density. The curves correspond to theoretical photoelectric efficiencies of PAH grains from Bakes & Tielens (1994) for gas temperatures between 50 – 1000 K, and for grain size distributions of the form $n(a) \sim a^\beta$. Black and red curves indicate $\beta = -3.5$ and $\beta = -4.0$ respectively, with the more negative exponent corresponding to a distribution weighted more towards smaller grains. Note that the L_{PAH} we use to measure ϵ_{PE} includes only $\sim 75\%$ of the total power in PAHs for GOALS (see Sect. 3.3.1), and we have scaled the models accordingly to account for this difference. The shaded grey region corresponds to G/n_H typical of the cold, diffuse ISM. Open symbols correspond to the average values of ϵ_{PE} and G/n_H for spatially resolved measurements of the nuclear ring and extranuclear bar (square and circle respectively) in NGC 1097, a more normal star-forming galaxy (Beirão et al., 2012). The models, which depend on the PAH grain ionization state and size distribution, can account for both the overall trend and scatter observed in (U)LIRGs, suggesting that the strong correlation between the photoelectric efficiency and G/n_H originates from the photoelectric properties of the PAH grains within PDRs.

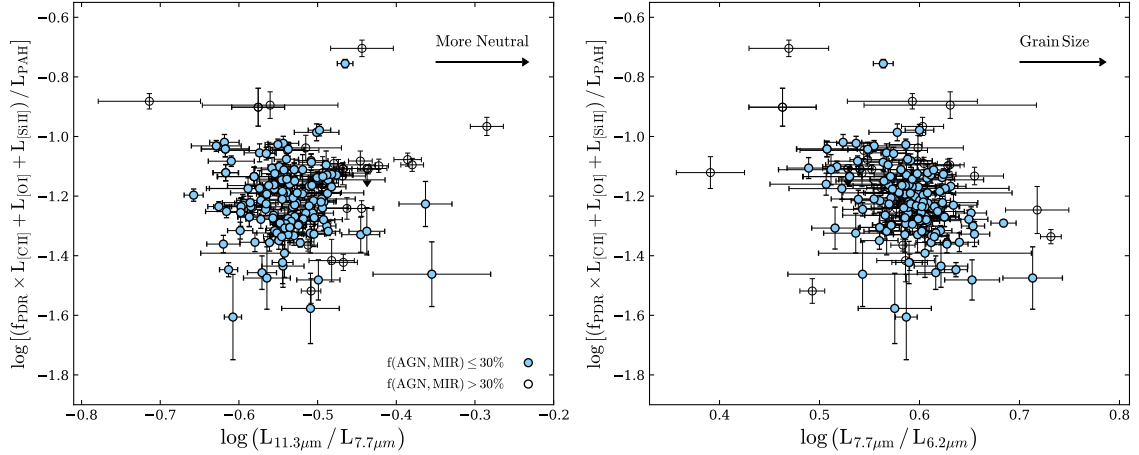


Figure 3.6 (*Left*) The photoelectric efficiency vs. the ratio of 11.3 to 7.7 μm PAH emission in our sample of star-forming GOALS (U)LIRGs. The $L_{11.3\mu\text{m}}/L_{7.7\mu\text{m}}$ PAH ratio is a tracer of the average grain ionization, with higher values associated with more neutral grains. (*Right*) Same as the *Left* panel, now as a function of the ratio of 7.7 to 6.2 μm PAH emission, a tracer of the average Cationic grain size as both features arise from ionized PAHs. The low values of ϵ_{PE} observed at high Σ_{IR} and high G/n_{H} do not exhibit notably different grain charge states and Cation grain sizes.

3.5 Discussion

In this work, we find that the cooling-to-heating ratios observed in the most compact luminous infrared galaxies are low, and are accompanied by an increase in the mean energy density per H atom (G/n_{H}) incident upon the surfaces of PDRs. The IR surface density is a global property of a galaxy, and both ϵ_{PE} and G/n_{H} measure the average physical conditions local to the PDRs. The trends between ϵ_{PE} , G/n_{H} , and Σ_{IR} suggest a link between the global properties of a starburst and the conditions of individual star-forming regions.

3.5.1 Alternate Explanations for decreasing ϵ_{PE} with Σ_{IR}

The low photoelectric efficiencies we measure in galaxies with high Σ_{IR} (Fig. 3.4) and high G/n_{H} (Fig. 3.5) suggests a change in the thermal regulation of star-forming

gas in compact LIRGs; however, a number of alternative physical conditions may conspire to produce the trends we observe with ϵ_{PE} .

The relative strengths of the far-IR cooling or PAH emission may be affected by any or all of the following: (1) Far-IR line fluxes may be suppressed by optically thick continuum absorption (e.g., Scoville et al. 2017a). In this case, the $[\text{O I}]/L_{\text{IR}}$ -deficit would have a steeper slope than $[\text{C II}]/L_{\text{IR}}$ (e.g., Malhotra et al. 2001), a trend that is not observed (Díaz-Santos et al., 2017). (2) Ionized gas from diffuse or H 2 regions, and/or AGN may contribute to the $[\text{C II}]$ and $[\text{Si II}]$ line fluxes owing to their ionization potentials being lower than that of neutral hydrogen. This is unlikely to drive trends in our sample, as the photoelectric efficiency does not correlate with the fraction of $[\text{C II}]$ emission from PDRs (f_{PDR} ; Tab. 3.2). Moreover, the neutral PDR fraction of $[\text{Si II}]$ would have to be larger at low Σ_{IR} or smaller at high Σ_{IR} to maintain constant ϵ_{PE} , both of which are inconsistent with the increase in PDR area filling factor with Σ_{IR} in LIRGs and ULIRGs (Díaz-Santos et al., 2017). (3) PAH molecules in galaxies with large G/n_{H} absorb and re-emit more energy per unit dust mass because of the large UV opacities of grains (Li & Draine, 2001). If the PAHs and ions (C^+ , O , and Si^+) were de-coupled spatially, L_{PAH} could increase with Σ_{IR} without a corresponding increase in $(L_{[\text{C II}]}+L_{[\text{O I}]}+L_{[\text{Si II}]})$, lowering the observed IR line-to-PAH ratio by Eq. 3.2. However, this spatial decoupling of PAHs and ions is inconsistent with observations of PDRs in the Milky Way (Okada et al., 2013; Salgado et al., 2016), the LMC (Lebouteiller et al., 2012; Chevance et al., 2016), and local galaxies (Croxall et al., 2012; Abdullah et al., 2017; Bigiel et al., 2020). (4) Metallicity may influence the strength of cooling lines and the PAHs (Cormier et al., 2015; Smith et al., 2017; Croxall et al., 2017; Cormier et al., 2019; Aniano et al., 2020). However, direct effects on the PAH grains appear most pronounced at metallicities well below those seen in GOALS galaxies, which typically have $Z/Z_{\odot} \sim 1 - 2$ (Inami et al., 2013; Díaz-Santos et al., 2017). Therefore, the trends observed in Fig. 3.4 and Fig. 3.5 likely

reflect variations in the heating and cooling mechanisms on the scale of individual PDRs.

3.5.2 Dust Grain Properties and the Photoelectric Efficiency

The photoelectric efficiency is not only a function of G/n_{H} , but also the size and ionization state of PAH grains (Bakes & Tielens, 1994; Galliano et al., 2008; Tielens, 2008). Observations of PDRs in the Milky Way indicate that ϵ_{PE} falls as the grain charging parameter ($\gamma \equiv G_0 T^{1/2}/n_e$) rises, and grains become more ionized (Tielens, 2008; Okada et al., 2013; Salgado et al., 2016). Indeed, the models of Bakes & Tielens (1994) shown in Figure 3.5 predict low ϵ_{PE} at high G/n_{H} , and the data falls closer to the model with a grain size distribution weighted more towards larger grains. Thus, a link between PAH properties and ϵ_{PE} is to be expected if the decrease in ϵ_{PE} at high Σ_{IR} arises from a change in the local physics of gas heating in PDRs as mediated by the charge and size of PAHs.

Ratios between the 6.2, 7.7, 8.6, and 11.3 μm PAH lines are well-established as tracers of grain size and ionization (e.g., Draine & Li 2001; Tielens 2008), and local LIRGs exhibit comparable ratios to nearby, normal star-forming galaxies and high- z ULIRGs (Stierwalt et al., 2014; Smith et al., 2007; Pope et al., 2008; Wu et al., 2010; Shipley et al., 2013). For example, star-forming LIRGs cluster tightly in $L_{6.2\mu\text{m}}/L_{7.7\mu\text{m}}$ vs. $L_{11.3\mu\text{m}}/L_{7.7\mu\text{m}}$, tracing grain size and ionization respectively, which show a larger scatter in sources with AGN (Stierwalt et al., 2014).

Figure 3.6 shows ϵ_{PE} as a function of the $L_{11.3\mu\text{m}}/L_{7.7\mu\text{m}}$ ratio, a tracer of grain charge, and the $L_{7.7\mu\text{m}}/L_{6.2\mu\text{m}}$ ratio, a tracer of the average cationic grain size (Draine & Li, 2001). We do not detect a correlation between ϵ_{PE} and the grain ionization state at a significant confidence level (Tab. 3.2); however, ϵ_{PE} and $L_{7.7\mu\text{m}}/L_{6.2\mu\text{m}}$ are anti-correlated at a $\sim 4\sigma$ confidence level, albeit with large scatter, suggesting that the average size of PAH grains may influence the observed photoelectric efficiencies in

local (U)LIRGs, consistent with the sensitivity of theoretical photoelectric efficiencies on the grain size distribution (Fig. 3.5).

Smaller PAH grains emit more strongly in the shorter wavelength bands, whereas larger grains are brighter at longer wavelengths (Allamandola et al., 1989; Schutte et al., 1993; Draine & Li, 2001). Thus, the diagnostic utility of a PAH line ratio as a grain-size indicator is a function of the separation in wavelength of the two features. The $7.7/6.2\ \mu\text{m}$ ratio has been a wide-spread tool in the literature as both features are bright in extragalactic sources, relatively unaffected by the $9.7\ \mu\text{m}$ silicate ice feature, and were observable simultaneously with IRS aboard *Spitzer* (Draine & Li, 2001; O’Dowd et al., 2009; Sandstrom et al., 2012; Stierwalt et al., 2014). With the advent of AKARI/IRC, the $3.3\ \mu\text{m}$ PAH feature became accessible for large numbers of extragalactic sources while unlocking a longer baseline diagnostic of grain size.

The ratio of $11.3\ \mu\text{m}$ to $3.3\ \mu\text{m}$ PAH intensity is one of the most robust tracers of PAH grain size because of the large baseline in wavelength (Allamandola et al., 1989; Jourdain de Muizon et al., 1990; Schutte et al., 1993; Mori et al., 2012; Ricca et al., 2012; Croiset et al., 2016; Maragkoudakis et al., 2020). Using the available AKARI spectra in GOALS, we plot ϵ_{PE} vs. $L_{11.3\ \mu\text{m}}/L_{3.3\ \mu\text{m}}$ in Figure 3.7 to further test if low ϵ_{PE} is associated with larger or smaller PAHs. We find that galaxies in the AKARI sub-sample of GOALS with low ϵ_{PE} show systematically higher values of $11.3/3.3\ \mu\text{m}$ PAH emission (Tab. 3.2). This trend is not driven by systematic variations in the $11.3\ \mu\text{m}$ feature strength, as the $L_{11.3\ \mu\text{m}}/L_{\text{PAH}}$ ratio is constant over the range in $L_{11.3\ \mu\text{m}}/L_{3.3\ \mu\text{m}}$, and exhibits minimal 1σ scatter of 0.05 dex about the average (Fig. 3.7, bottom panel). Instead, the strength of the $3.3\ \mu\text{m}$ features relative to L_{PAH} decreases dramatically by nearly an order of magnitude (Fig. 3.7, center panel). The anti-correlation between ϵ_{PE} and $L_{11.3\ \mu\text{m}}/L_{3.3\ \mu\text{m}}$ reinforces the importance of the mean grain size in dictating the observed photoelectric efficiency.

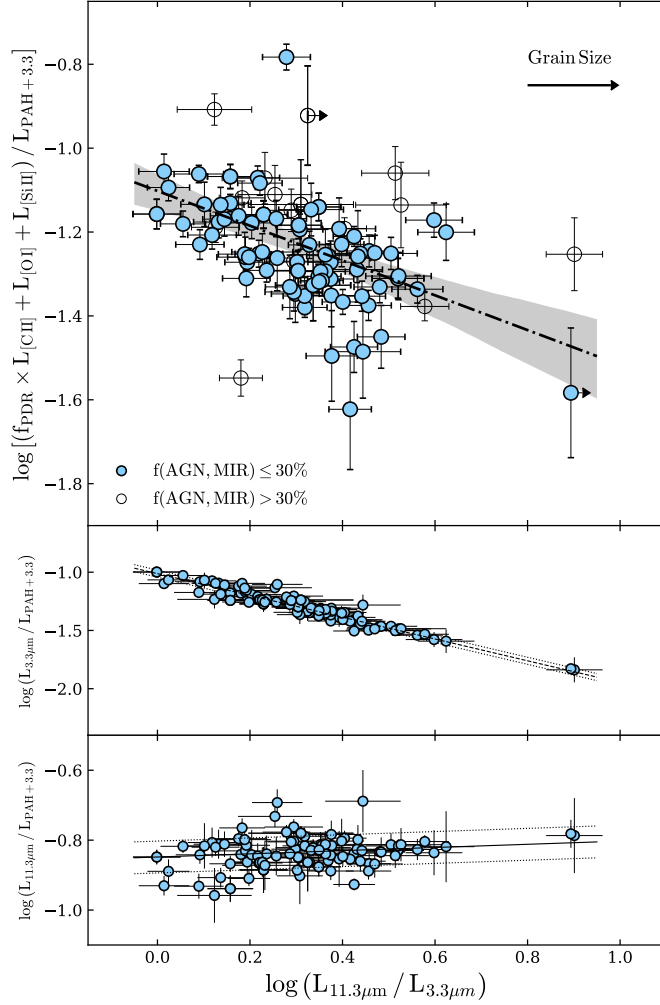


Figure 3.7 (*Top*) The photoelectric efficiency vs. the ratio of $11.3\ \mu\text{m}$ to $3.3\ \mu\text{m}$ PAH emission, a size tracer for PAH grains. Note that $L_{3.3}$ is not included in L_{PAH} . (U)LIRGs with higher ϵ_{PE} are low in $11.3/3.3\ \mu\text{m}$. We fit a linear relation to the data letting the slope and y -intercept vary freely, and find that $y = -0.41x - 1.10$. The shaded grey region spans the domain of 1000 bootstrapped model fits. A Kendall's τ test returns $(\tau_k, \log p) = (-0.37, -7.5)$, indicating an anti-correlation at $\sim 5.5\sigma$ confidence. Galaxies with $f_{\text{AGN,MIR}} > 30\%$ (open circles) exhibit a 1σ scatter about the best-fit of 0.11 dex, larger than the 0.07 dex scatter in low $f_{\text{AGN,MIR}}$ (U)LIRGs ($\leq 30\%$, filled circles). (*Center*) The $L_{3.3}/L_{\text{PAH}}$ ratio as a function of the $11.3/3.3\ \mu\text{m}$ ratio. (*Bottom*) The contribution of the $11.3\ \mu\text{m}$ PAH feature to the total PAH luminosity. (U)LIRGs with lower photoelectric efficiencies tend towards higher values of $11.3/3.3\ \mu\text{m}$ PAH ratios without exhibiting changes to the fractional strength of the $11.3\ \mu\text{m}$ feature with respect to L_{PAH} , supporting a link between ϵ_{PE} and the PAH grain-size distribution probed by the $3.3\ \mu\text{m}$ feature luminosity.

3.5.3 Physical Interpretation

The photoelectric heating efficiency of PAHs falls as the number of carbon atoms per particle increases (e.g., Bakes & Tielens 1994), and small grains are preferentially destroyed in the presence of harsh radiation fields (e.g., Jochims et al. 1994). This provides a simple physical interpretation of the data presented so far: PDRs in the most compact starbursts ($\log \Sigma_{\text{IR}}/[\text{L}_{\odot} \text{kpc}^{-2}] \gtrsim 10.7$) have, on average, more intense radiation fields per gas density (Díaz-Santos et al., 2017), which leads to a preferential destruction of the smallest PAH grains, raising the average grain size and leaving behind large PAHs capable of releasing both less and weaker photo-electrons. This decreases the energy of a typical photoelectron available to heat the gas, and results in a lower gas heating efficiency.

This scenario is consistent with principles of PDR evolution. The strength of the radiation field impinging upon PDRs (i.e., G) is inversely proportional to the distance between the ionization front and the ionizing photon source (Kaufman et al., 1999). Therefore, higher values of G/n_{H} are associated with younger PDR systems that have yet to evolve away from their host star, and are more likely to be found in galaxies with higher star-formation rate surface densities (e.g., Díaz-Santos et al. 2017). The low photoelectric efficiencies at high Σ_{IR} are plausibly linked to higher fractions of young, short-lived, and dust-cocooned star-forming regions, where the high ratios of G/n_{H} destroy small dust grains, hindering the coupling between the radiation field strength and PDR gas temperatures. Such PDRs may be continuously replenished by the compaction of gas and dust during a major merger (Sanders et al., 1988a; Hopkins et al., 2008). Indeed, the majority of late-stage mergers (80%) are above $\log \Sigma_{\text{IR}}/[\text{L}_{\odot} \text{kpc}^{-2}] \sim 10.7$ (Stierwalt et al., 2013; Díaz-Santos et al., 2017), where photoelectric efficiencies are low.

As shown in Figure 3.8, the $L_{11.3\mu\text{m}}/L_{7.7\mu\text{m}}$ and $L_{11.3\mu\text{m}}/L_{3.3\mu\text{m}}$ ratios in LIRGs and ULIRGs are consistent with predominantly ionized PAHs containing on average

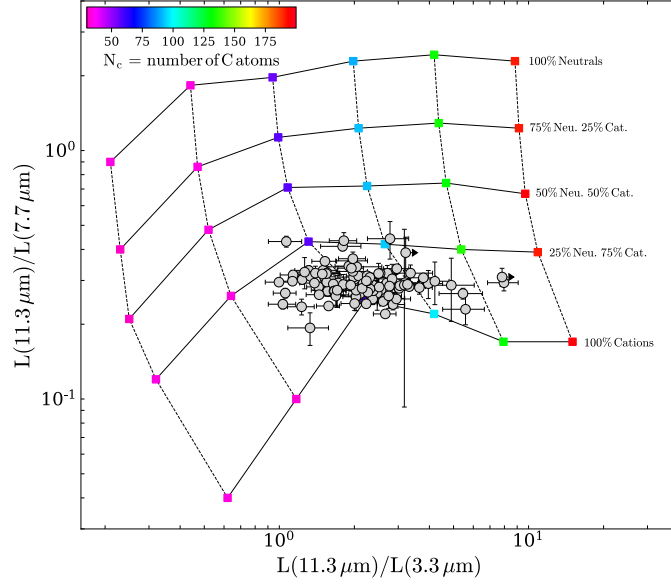


Figure 3.8 The $L_{11.3\ \mu\text{m}}/L_{7.7\ \mu\text{m}}$ vs. $L_{11.3\ \mu\text{m}}/L_{3.3\ \mu\text{m}}$ PAH ratio in GOALS (U)LIRGs with AKARI observations of the $3.3\ \mu\text{m}$ PAH feature. The model grid from Maragkoudakis et al. (2020) is a function of grain size (N_C , see colorbar), and the relative mix of neutral and cationic PAH grains as indicated on the Figure, all assuming an average photon energy of 10 eV. (U)LIRGs have, on average, mostly ionized PAHs with sizes between 60 and 150 C atoms per grain.

$\sim 60 - 150$ C atoms per particle when compared to the modeled PAH spectra of Maragkoudakis et al. (2020)². PAHs with $N_C \lesssim 40$ tend to be photo-destroyed in PDRs (Jochims et al., 1994), which is close to the lower bound on grain sizes we observe for LIRGs and ULIRGs in Fig. 3.8. Other mechanisms for grain destruction include shock-induced fragmentation and/or shattering; however, interstellar shocks tend to destroy larger grains which is the opposite effect we see in the data (Jones et al., 1996). Therefore, G/n_H may be a critical factor for determining the photoelectric efficiency in (U)LIRGs with the grain size distribution acting as an intermediary between the radiation field, and gas cooling and heating.

²We adopt the Maragkoudakis et al. (2020) models corresponding to a mean photon energy of 10 eV.

3.5.4 Prospects for Star-Formation at High-Redshift

The rise and fall of the cosmic star-formation rate density may be accompanied by an increase in the efficiency of star-formation at earlier times, although this remains a subject of debate (e.g., Lilly et al. 1996; Madau et al. 1996; Madau & Dickinson 2014; Tacconi et al. 2010, 2013, 2018; Genzel et al. 2015; Scoville et al. 2017b; Liu et al. 2019; Decarli et al. 2019). Nevertheless, starbursts above the main-sequence have higher star-formation efficiencies (star-formation rate per unit molecular gas mass) than normal galaxies, independent of redshift (Saintonge et al., 2013; Genzel et al., 2015; Scoville et al., 2017b). Can changes in the global star-formation efficiency of a galaxy, with redshift and/or distance from the main-sequence, be linked to variations in the ISM conditions on small scales?

Given that photoelectric heating is the dominant coupling mechanism between gas temperatures and stellar radiation fields, ϵ_{PE} could play a role in mediating the star-formation efficiency today and in the past by raising or lowering the energy transfer from stellar photons into the gas. When the photoelectric efficiency is low, photoelectrons convert a lower fraction of the incident radiation field into raising the gas temperature. In other words, gas may remain cold despite overall less cooling relative to photoelectric heating because the mechanism by which gas heats in the first place is weak at low ϵ_{PE} . This may be more common at earlier times, because normal star-forming galaxies at high-redshift are more compact than local galaxies at a given stellar mass (Buitrago et al., 2008; Conselice, 2014; van der Wel et al., 2014; Mowla et al., 2019), and Σ_{IR} anti-correlates with ϵ_{PE} . In addition, efficient star-formation in the thick disks of high- z dusty, star-forming galaxies could contain a number of star-forming regions that each resemble the central regions of local (U)LIRGs (e.g., Tacconi et al. 2008; Bothwell et al. 2010; Stacey et al. 2010; Brisbin et al. 2015), in which case high G/n_{H} and low ϵ_{PE} could be common in PDRs across a high- z starburst. These conditions may play a more important role at high-redshift as the

contribution of ULIRGs to the total star-formation rate density increases from $z = 0$ to $z = 2$ by a factor of ~ 21 (Murphy et al., 2011).

Recent efforts to combine mid- and far-IR measurements of gas heating and cooling at $z \sim 1 - 2$ are largely limited to handfuls of ULIRGs with archival *Spitzer*/IRS spectra (Brisbin et al., 2015; McKinney et al., 2020). Using ALMA, McKinney et al. (2020) compared the [C II] and $6.2\ \mu\text{m}$ PAH emission for GS IRS20, a luminous, compact starburst galaxy at $z = 1.9239$ and found a low [C II]/ $6.2\ \mu\text{m}$ ratio at high IR surface density that could indicate a low photoelectric efficiency. This galaxy has a $L_{[\text{C II}]} / L_{11.3}$ ratio of 0.11, which would correspond to a $11.3/3.3\ \mu\text{m}$ ratio of 21.5 if $z \sim 2$ galaxies follow similar scaling relations between the PAH features and [C II] as in local (U)LIRGs. If this is the case, then GS IRS20 would have a $3.3\ \mu\text{m}$ PAH flux of $7 \times 10^{-17}\ \text{W m}^{-2}$, which can be easily detected in under 15 minutes by *JWST*/MIRI. While MIRI will be excellent at measuring bright PAH lines at high- z , our ability to probe much of the rest-frame mid and far-IR regime at high- z remains limited. Future facilities, such as the *Origins Space Telescope*³, a proposed flagship mission covering the near-far infrared with powerful imaging and spectroscopic capabilities and a large, cold telescope, would be a powerful tool for measuring the full energy budget in distant star-forming galaxies, and testing the idea that the star-formation efficiency is linked to the balance of gas cooling and heating.

3.6 Summary and Conclusion

We combine observations of PAH emission with measurements of the far-infrared fine-structure [C II], [OI], and [Si II] lines to infer the properties of gas heating and cooling in local, star-forming, luminous infrared galaxies. The ratio of IR cooling lines to PAH emission traces the photoelectric efficiency, ϵ_{PE} , and measures the cou-

³<https://origins.ipac.caltech.edu/>

pling between stellar radiation field and gas temperatures in photodissociation regions (PDRs). Our main conclusions are:

1. In local LIRGs, the ratio of [C II] to PAH emission does not correlate with L_{IR} or far-IR color, both of which trace a mix of the diffuse and PDR dust.
2. We find an anti-correlation between [C II]/PAH and IR surface density (Σ_{IR}) where the most compact ULIRGs have low ratios of [C II] cooling to PAH emission compared to normal star-forming galaxies by ~ 0.5 dex. The [C II]/PAH ratio exhibits less overall scatter in GOALS than $L_{[\text{C II}]} / L_{\text{IR}}$, as well as a lower magnitude of decline between low- and high- Σ_{IR} galaxies.
3. [Si II]/PAH and [O I]/PAH exhibit constant ratios up to the most compact ULIRGs, where some objects fall below the average value by a factor of ~ 5 in both line ratios. Notably, [O I]/PAH does not increase when [C II]/PAH is low: enhanced cooling via the [O I] channel is not sufficient to compensate for the deficiencies observed in the [C II] line when considering the total cooling budget.
4. We measure the photoelectric efficiency as $(L_{[\text{C II}]} + L_{[\text{O I}]} + L_{[\text{Si II}]}) / L_{\text{PAH}}$, which is a factor of ~ 3 lower in galaxies with $\log \Sigma_{\text{IR}} / [L_{\odot} \text{ kpc}^{-2}] > 10.7$, which also have high ratios of UV radiation field strength to neutral hydrogen density (G/n_{H}). Compact ULIRGs have low photoelectric efficiencies and more extreme ISM conditions, indicating a link between the large-scale energy density of a starburst and the gas cooling and heating properties on PDR scales.
5. LIRGs with low photoelectric efficiencies have high ratios of 11.3 to $3.3 \mu\text{m}$ PAH emission, a tracer of the mean PAH grain size. We estimate typical grain sizes of $N_{\text{C}} \sim 60 - 150$ C atoms per grain in LIRGs, and find that the PAHs are predominantly ionized. Large, ionized grains produce both less and weaker

photo-electrons, which may contribute to the low photoelectric efficiencies in the most compact ULIRGs if small grains are preferentially destroyed. Spectral signatures of grain emission can be used to understand the role played by dust in regulating the star-formation of galaxies.

The photoelectric efficiency may be key for regulating the evolution of the ISM, and can influence the overall star-formation efficiency by mediating the coupling between stellar radiation fields and gas temperatures. The trends between ϵ_{PE} , Σ_{IR} , and G/n_{H} reflect vigorous, compact star-formation where dusty and young PDRs exhibit less efficient gas heating. Low photoelectric efficiencies may be common in the high-redshift Universe where compact star-formation is ubiquitous, and may also contribute to changes in the star-formation efficiency. The link between the efficiency of star-formation and the cooling/heating balance will be further tested with *JWST* and ALMA, but ultimately a large space-based IR telescope like *Origins* is needed to measure the mid and far-infrared emission and track the full energy budget in star-forming galaxies over a significant fraction of cosmic time.

CHAPTER 4

THE IR SIZES OF DUSTY GALAXIES SET STAR-FORMATION AND DUST PROPERTIES AT $Z=0-2$

Surface densities of gas and stellar light provide a window into the physics of star-formation that, until the advent of high-resolution far-infrared/sub-millimeter observations, has been historically difficult to assess amongst the population of dusty galaxies. To study the link between infrared (IR) surface densities and dust, we leverage the Atacama Large Millimetre/Submillimetre Array (ALMA) archive to measure the extent of cold dust continuum emission in 19 IR galaxies selected on the basis of existing mid-IR spectroscopy from *Spitzer*. We use the mid-IR spectra to constrain the relative balance between star-formation and dust heating by an active galactic nucleus (AGN) as well as to measure emission from Polycyclic Aromatic Hydrocarbons (PAHs), small dust grains that play a key role in the photoelectric heating of star-forming gas. In general, we find that dust-obscured star-formation at high IR surface densities exhibits similar properties at low- and high-redshift. Local luminous IR galaxies have comparable PAH dust mass fraction as high- z galaxies, and at all redshifts star-formation is more efficient at high IR surface densities despite the fact that high- z galaxies are closer to the main-sequence than local luminous IR galaxies. High star-formation efficiencies are coincident with a decline in the PAH/IR luminosity ratio reminiscent of the deficit observed in far-infrared fine-structure lines. Changes in the gas and dust conditions arising from high star-formation surface densities might help drive the efficiency up, which could help explain redshift evolution in the star-formation efficiency needed to reconcile star-formation and gas volume densities up to cosmic noon.

4.1 Introduction

The sizes of galaxies are a critical axis along which to study star-formation in galaxies. In general, galaxies get progressively smaller towards higher-redshifts at fixed star-formation rate and stellar mass (Buitrago et al., 2008; Conselice, 2014; van der Wel et al., 2014; Shibuya et al., 2015; Fujimoto et al., 2017; Mowla et al., 2019), and smaller star-forming galaxies tend to support larger star-formation rate surface densities (Lutz et al., 2016; Fujimoto et al., 2017). Changes in the sizes of galaxies also correlate with the conditions of the interstellar medium (Díaz-Santos et al., 2017; McKinney et al., 2020, 2021a; Puglisi et al., 2021), which may drive changes in the underlying mode of star-formation. Indeed, the scaling relationship between star-formation rate surface densities and molecular gas surface densities is sensitive to the physics of stellar mass assembly in galaxies (e.g., Schmidt, 1959; Kennicutt, 1998b), and departures from canonical scaling surface density scaling laws have been attributed to changes in the star-formation efficiency (Elbaz et al., 2018). Thus, controlling for galaxy sizes is an important factor when studying star-formation today and at high-redshift.

Star-formation from $z \sim 0.5 - 4$ around the peak of the star-formation rate density is predominantly obscured by dust (Madau & Dickinson, 2014), and happens within luminous, infrared galaxies with infrared luminosities (L_{IR}) exceeding $10^{11} L_{\odot}$ (Murphy et al., 2011; Zavala et al., 2021); however, the spatial extent of star-formation in such distant systems was historically difficult to measure. Until the Atacama Large Millimetre/Submillimetre Array (ALMA) introduced capability for high spatial resolution observations at sub-millimeter wavelengths, studying the extent of star-formation in such dust-obscured galaxies was principally limited by a lack of resolution at infrared wavelengths. Deep radio imaging with the VLA and IRAM PdBI were key in revealing the compact sizes of luminous sub-millimeter galaxies (SMGs) detected in single dish survey (e.g., Chapman et al., 2004; Biggs & Ivison, 2008;

Tacconi et al., 2008; Riechers et al., 2011). Recently, much progress has been made towards spatially resolving dust-obscured star-formation on \sim kpc scales in $z \sim 1 - 4$ luminous infrared galaxies using ALMA, finding characteristically small sizes $< 1 - 2$ kpc (Fujimoto et al., 2017; Gómez-Guijarro et al., 2022b; Chapman et al., 2004; Engel et al., 2010; Hodge et al., 2016; Ikarashi et al., 2015; Spilker et al., 2016; Kaasinen et al., 2020; Pantoni et al., 2021; McKinney et al., 2020) which are reproduced by numerical simulations coupled to far-IR radiative transfer codes (Cochrane et al., 2019; Popping et al., 2022). Similarly, low-redshift luminous IR galaxies also show small IR sizes $\lesssim 1 - 3$ kpc (Lutz et al., 2016; Bellocchi et al., 2022); however, these are commonly confined to merger nuclei whereas high- z targets often show kinematic evidence for disks with high star-formation rate surface densities (Hodge et al., 2016; Calistro Rivera et al., 2018; Pantoni et al., 2021). Nevertheless, the ISM conditions found within high- z dusty star-forming disks appear to resemble those within the cores of local LIRGs (Spilker et al., 2016; McKinney et al., 2020, 2021a; Rybak et al., 2022).

From high-resolution ALMA observations, a number of scaling relations between the IR size of galaxies and their star-formation and gas properties have emerged. Fujimoto et al. (2017) statistically demonstrated that the effective radius containing 50% of the total IR light correlates with L_{IR} , and that for fixed L_{IR} galaxies at high redshift are on-average smaller than those at low redshift. Elbaz et al. (2018) and Puglisi et al. (2021) target IR-luminous *Herschel* sources at $z \sim 1 - 2$, and find that luminous infrared galaxies with high surface densities tend to have higher star-formation efficiency and higher CO excitation relative to more extended infrared sources at the same redshift. At $z \sim 0$ and for galaxies that reach the IR luminosities found at $z \sim 1 - 3$, Díaz-Santos et al. (2017) showed how the IR surface density is a critical axis for understanding key far-IR cooling line emission like [C II] $157.7 \mu\text{m}$. Radiation field intensities and the far-IR line emission they power depart from typical

values above a threshold of $\sim 5 \times 10^{10} L_{\odot} \text{ kpc}^{-2}$, which may also change the underlying heating and cooling physics in $z \sim 0$ luminous IR galaxies (McKinney et al., 2021a). Similar far-IR line ratios and ISM conditions are seen in some high-redshift galaxies with ALMA detections of [CII] (Zanella et al., 2018; Rybak et al., 2019; McKinney et al., 2020). Fundamentally, the apparent IR size of dust-obscured star-forming galaxies reflects the surface density of dusty star-forming regions (Díaz-Santos et al., 2017), and is therefore sensitive to the physical mechanisms regulating gas conditions and star-formation rates.

In this work, we measure IR sizes using archival ALMA observations in a sample of $z \sim 1 - 2$ galaxies with mid-IR *Spitzer Space Telescope* spectra. Comparing to low-redshift dusty galaxies with comparable multi-wavelength observations, we study the link between infrared surface densities (Σ_{IR}) and the content and conditions of dust between $z \sim 0 - 3$. Building on Kirkpatrick et al. (2017) who look at purely star-forming galaxies, we expand our analysis to include galaxies hosting intermediate to strong buried active galactic nuclei (AGN). We decompose the infrared emission from galaxies into their star-forming and AGN components, and measure key dust emission features from polycyclic aromatic hydrocarbons (PAHs).

The Chapter is organized as follows: In Section 4.2 we describe our sample and detail the archival ALMA analysis used to measure IR sizes and dust masses. Section 4.3 outlines our major results, which we discuss in Section 4.4. Section 4.5 summarizes our main conclusions. Throughout this work we adopt a Λ CDM cosmology with $\Omega_m = 0.3$, $\Omega_{\Lambda} = 0.7$, and $H_0 = 70 \text{ km s}^{-1} \text{ Mpc}^{-1}$. We assume a Kroupa IMF.

4.2 Data and Analysis

The main goal of this study is to measure IR sizes from the ALMA archive for dusty, $z \sim 1 - 2$ galaxies with *Spitzer/IRS* spectra. We use the *Spitzer* spectra to calculate mid-IR diagnostics of dust and buried AGN. In this section we describe

the archival matching process and source detection methods, define key measured properties, and comment on the final sample statistics. We also describe similar measurements made for $z \sim 0$ comparison samples.

4.2.1 ALMA Archival Sample Selection

We select our galaxies from a parent sample of 151 (Ultra) luminous, IR galaxies (LIRGs: $\log L_{\text{IR}}/L_{\odot} > 11$, ULIRGs $\log L_{\text{IR}}/L_{\odot} > 12$) at $z \sim 1 - 2$ with *Spitzer*/IRS spectra (Kirkpatrick et al., 2012, 2015). The original “supersample” includes galaxies in the Great Observatories Origins Deep Survey North/South (GOODS-N/S) and is representative of $24 \mu\text{m} > 0.9 \text{ mJy}$ selected galaxies (Sajina et al., 2012; Kirkpatrick et al., 2012). Our initial selection criterion is on sources that can be observed by ALMA due to their location in the sky, which narrows the candidates from 151 (U)LIRGs across the GOODS fields to 81 (U)LIRGs in GOODS-S. We search for ALMA detections for these 81 GOODS-S galaxies.

Mid-IR spectroscopy of galaxies is key for decomposing the IR spectral energy distribution (SED) into the components powered by AGN vs. star-formation. Nuclear toroidal dust heated to high temperatures by buried AGN emits strongly in the mid-IR (e.g., Laurent et al., 2000; Sturm et al., 2000; Tran et al., 2001), whereas star-forming regions are bright in broad PAH emission features and exhibit relatively shallower mid-IR spectral indices (Allamandola et al., 1989; Pope et al., 2008; Sajina et al., 2007). We use the spectral decomposition between AGN and star-formation available for our sample from Kirkpatrick et al. (2012), which fit power-law and star-forming templates to the mid-IR spectra to calculate the mid-IR AGN fraction ($f_{\text{AGN,MIR}}$), defined as the fraction of emission within the *Spitzer*/IRS bandpass attributed to an obscured AGN (Pope et al., 2008). Following Kirkpatrick et al. (2015), we distinguish between three general $f_{\text{AGN,MIR}}$ categories: star-forming (SFG) dominated galaxies ($f_{\text{AGN,MIR}} < 20\%$), composite (COM) galaxies with intermediary balances between SF

and AGN ($20\% < f_{\text{AGN,MIR}} < 80\%$), and AGN dominated galaxies ($f_{\text{AGN,MIR}} > 80\%$). Galaxies from each class can be found spanning the redshift and L_{IR} range of the parent sample (Kirkpatrick et al., 2015). Mid-IR AGN with $f_{\text{AGN,MIR}} > 80\%$ exhibit a warmer SED, but the average dust temperature of the cold component powered by star-formation is remarkably constant at all $f_{\text{AGN,MIR}}$ around $T_d \sim 25$ K (Kirkpatrick et al., 2015).

4.2.2 Source Detection

We use the following methods to search for ALMA counterparts to the 81 *Spitzer* targets in GOODS-S. We search through the ALMA archive, which includes several large surveys, namely ASAGAO (Ueda et al., 2018) and GOODS-ALMA 2.0 (Gómez-Guijarro et al., 2022a). ASAGAO contains a smaller subset of the GOODS-S field than GOODS-ALMA 2.0 but has greater sensitivity and greater spatial resolution. We take as many detections out of ASAGAO, then move to GOODS-ALMA 2.0, and then search the archive for sources not detected in either of the large surveys.

For a given ALMA cutout centered on the *Spitzer* coordinates, we first derive a local RMS within 100 – 150 pixels from the center after masking potential source emission. Next, we find all peaks above 2.5σ which we use as priors to create a segmentation map using `photutils.detect_sources` with a Gaussian smoothing kernel while enforcing a minimum number of 5 connected pixels, typically less than the number of pixels across the beam FWHM and suitable for flagging spatially unresolved and resolved candidates. We then compare the IRAC coordinates against each source found in the segmentation map, and we take the closest match for further analysis. After this step we find 33 possible detections. As a final check, we next overlay the ALMA contours on top of *Spitzer*/IRAC Ch. 4 (IRAC4) and *HST*/WFC3 F_{160W} images to visually confirm the association. We identify all targets with $\geq 3\sigma$ contours coincident with the IRAC4 coordinates as confirmed ALMA detections. Fig. 4.10

shows these contour overlays for each galaxy in our final ALMA-detected catalog, which includes 19 sources.

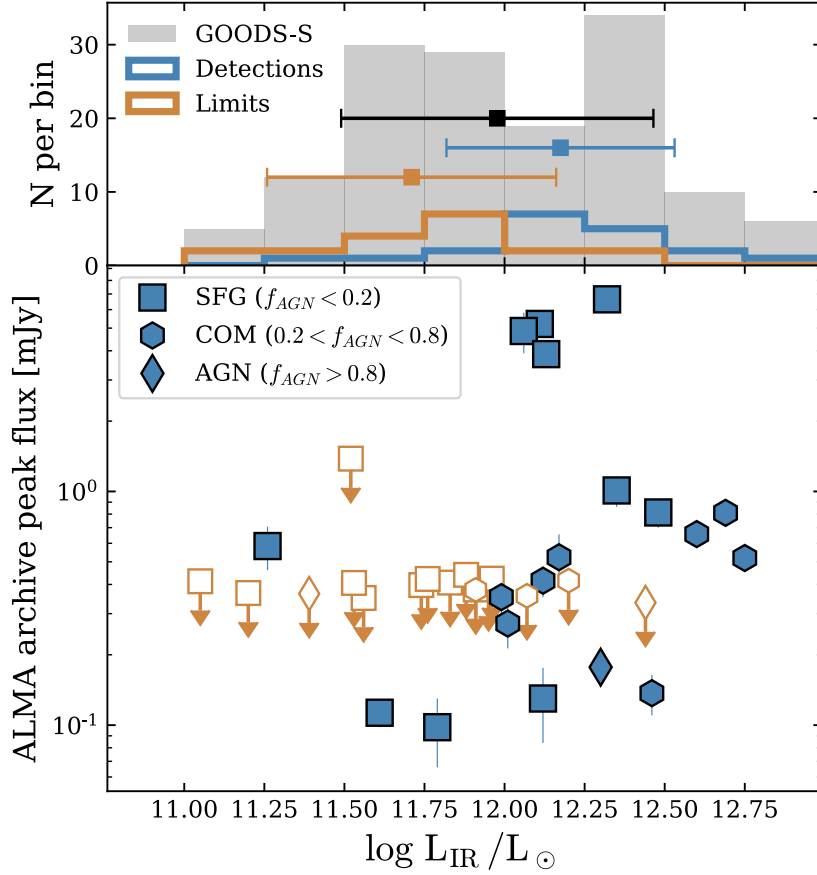


Figure 4.1 (*Top*) Distribution in L_{IR} amongst galaxies matched to ALMA archival detections (blue) compared against non-detections within the footprint of an archival observation (brown) and the parent GOODS-S sample (grey). Colored squares and their errors show the mean and standard-deviation of the corresponding distribution. Our catalog of ALMA-detected sources spans the range in L_{IR} of the parent sample, but is biased high on-average by ~ 0.2 dex. (*Bottom*) Peak flux vs. L_{IR} for detections and non-detections. Different symbols correspond to the mid-IR AGN classifications as labeled in the caption. Upper limits generally cluster around ~ 0.3 mJy as most fall within the ASAGAO footprint (Ueda et al., 2018; Fujimoto et al., 2018).

4.2.3 Measured Quantities

Fourteen of the archival ALMA observations span a range in wavelength between 1100-1250 μm , which probes the Rayleigh-Jeans tail of cold dust emission over the range in redshifts spanned by our sample. This regime is aptly suited to measuring the total dust mass because the emission is optically thin at sub-mm wavelengths, and the temperature-dependence is linear meaning uncertainties on dust temperature (T_d) have modest impact on the total dust mass (Scoville et al., 2017b). Following Kirkpatrick et al. (2017), we use the ALMA flux densities (S_ν) to measure the dust mass using:

$$M_{\text{dust}} = \frac{S_\nu D_L^2}{\kappa_\nu B_\nu(T_d)} \quad (4.1)$$

where D_L is the luminosity distance, B_ν is the Planck equation, and κ_ν is the dust opacity from Weingartner & Draine (2001) assuming MW-like dust and $R_V = 3.1^1$. As noted by Kirkpatrick et al. (2017), the variation in κ_ν at longer wavelengths is negligible across common models (e.g., MW, SMC, LMC) and for different R_V . We choose to fix the cold dust temperature to $T_d = 25$ K because most of the dust is cold with a temperature remarkably constant over (1) the full range of mid-IR AGN fractions when the SED is decomposed into its AGN- and SF-powered components using mid-IR spectroscopy (Kirkpatrick et al., 2015; Scoville et al., 2017b), and (2) redshift for fixed L_{IR} (Drew & Casey, 2022).

Four of the archival ALMA observations were taken at wavelengths below 500 μm . For two of these targets, we use the dust masses derived using 870 μm APEX/LABOCA photometry from Kirkpatrick et al. (2017) under the same assumptions and formula listed above. Two final sources do not have sub-mm observations along the RJ tail, in which case we place upper limits on the total dust mass using the 3σ RMS derived from the ASAGAO map. All dust masses are listed in Table 4.2.

¹At 850 μm the dust opacity is $\kappa_{850} = 0.15 \text{ m}^2 \text{ kg}^{-1}$ (Weingartner & Draine, 2001)

For each target detected in an archival ALMA map, we measure the integrated flux density ($S_{\nu,int}$) and deconvolved (intrinsic) source size by fitting a 2D elliptical Gaussian using `CASA.imfit`. For four spatially unresolved sources, we use the convolved size (typically negligibly larger than the clean beam) as an upper limit on the extent of the continuum emission, and the peak flux ($S_{\nu,peak}$). We then derive half-light radii ($R_{\text{eff},160}$) from the FWHM by first averaging over the major and minor axes, then using $R_{\text{eff},160} \approx \langle \text{FWHM} \rangle / 2.43$ which converts the FWHM to the radii containing 50% of the light assuming a $n \sim 1$ Sérsic index common amongst radio/sub-mm targets with sub-arcsecond ALMA/VLA imaging (Hodge et al., 2016; Murphy et al., 2017; Jiménez-Andrade et al., 2019; Gullberg et al., 2019).

The majority of the ALMA data we use to measure IR sizes were observed at $\lambda_{obs} \sim 1.1$ mm (Tab. 4.2), which at the median z of our sample traces rest-frame $\sim 380 \mu\text{m}$ emission. Two of the high- z galaxies in our sample have spatially resolved, high SNR continuum detections from both the ASAGAO map as well as higher frequency Band 9 observations (McKinney et al., 2020) which trace the rest-frame $\sim 160 \mu\text{m}$ emission that we use to measure sizes at $z \sim 0$. Following the same procedure outlined in Section 4.2.2, we measure intrinsic (PSF-corrected) $\lambda_{obs} \sim 450 \mu\text{m}$ $R_{\text{eff},160}$ for GS IRS20 and GS IRS50 to be 1.8 ± 0.5 kpc and 2.7 ± 0.9 kpc respectively (see Table 2 in McKinney et al. 2020), in agreement with their intrinsic sizes from the $\lambda_{obs} \sim 1.2\text{mm}$ ASAGAO maps within 1σ (Tab. 4.2). This is consistent with radiative transfer simulations of dusty and massive $z \sim 1 - 3$ galaxies that find a maximal difference of $\sim 15\%$ for sizes at $\lambda_{obs} \sim 450 \mu\text{m}$ vs. $\lambda_{obs} \sim 850 - 1100 \mu\text{m}$ (Cochrane et al., 2019; Popping et al., 2022). This is close the accuracy at which we can measure IR sizes, and we choose not to apply any size corrections accounting for variation in the observed wavelengths when comparing our high- z sizes against those derived from *Herschel*/PACS in low- z galaxies. This is physically motivated because the emission

is optically thin at $\lambda_{rest} > 200 \mu\text{m}$, and the coldest dust component dominating the far-IR emission also dominates the total dust mass (Scoville et al., 2017b).

4.2.4 Final Sample Properties

Of the 81 *Spitzer* targets in GOODS-S, we find 23 unique matches detected in both or either of ASAGAO and GOODS-ALMA 2.0. Of these, 14 are of sufficient SNR to measure an IR size. From searching the archive for observations within $5''$ of our *Spitzer* targets we find 10 more matches of which seven are not detected in the ASAGAO and/or GOODS-ALMA 2.0 maps. Of these seven matches, five are of sufficient SNR to measure the IR size and come from the following ALMA programs: 2017.1.01347.S (PI: A. Pope, see McKinney et al. 2020), and 2018.1.00992.S (PI: C. Harrison, see Lamperti et al. 2021). Our final sample with measurements of the sub-mm flux and IR size consists of 19 galaxies. We tabulate the general properties of each galaxy in Table 4.1, and the ALMA-derived quantities are listed in Table 4.2. Image cutouts from *HST*/WFC3 F160W and *Spitzer*/IRAC Ch. 4 with ALMA contour overlays are shown in Fig. 4.10.

Due to the nature of un-targeted archival observations at IR wavelengths, we expect our final matched catalog to be biased towards higher L_{IR} . To test for such bias, we compare the subset of galaxies with robust flux and size measurements from the ALMA archive against sources covered by archival observations but with no detectable signal (Figure 4.1). The mean L_{IR} of our final ALMA-detected catalog is ~ 0.2 dex greater than that of the whole GOODS-S sample, and ~ 0.5 dex greater than the non-detections. We detect 84% of all $\log L_{\text{IR}}/L_{\odot} \geq 12$ candidates with footprint overlap in an archival observation. While our final catalog is not, on-average, representative of L_{IR} and z in GOODS-S $24 \mu\text{m}$ -selected galaxies (Sajina et al., 2012; Kirkpatrick et al., 2015), it does span the range of both quantities. As shown in the bottom panel of Fig. 4.1, we do not preferentially detect any particular mid-IR AGN classification.

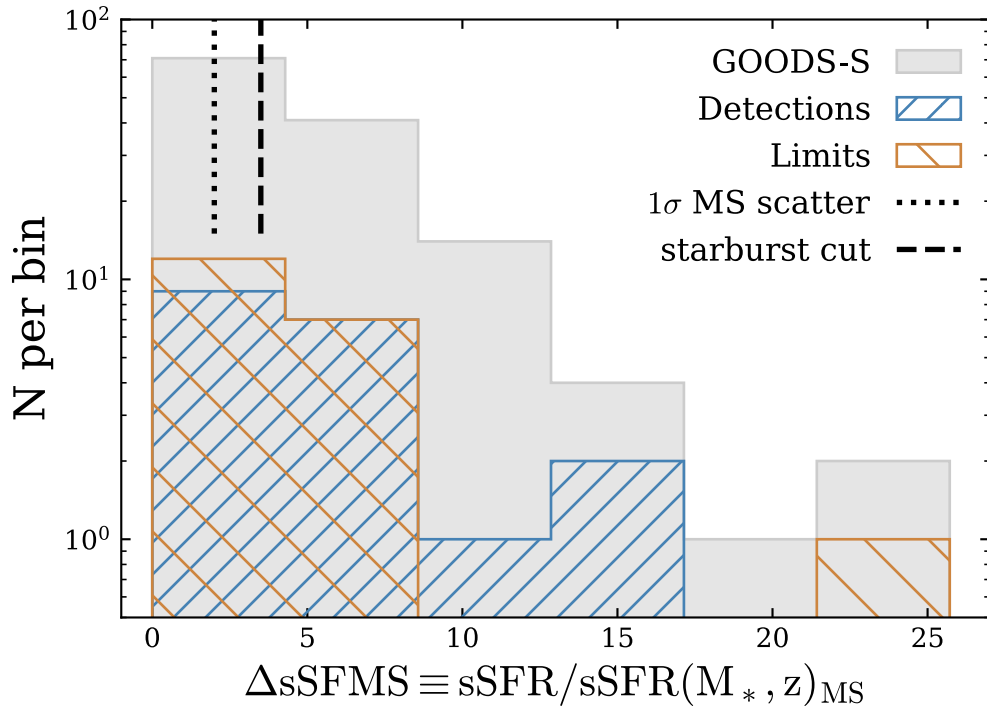


Figure 4.2 Distribution in specific star-formation rates relative to the main-sequence (ΔsSFMS) for fixed M_* and redshift using the MS parameterization of Speagle et al. (2014). The color scheme follows the top panel of Fig. 4.1. ALMA-detected sources have ΔsSFMS distributed similarly to undetected archival targets, and consist of 7 (36%) galaxies below common thresholds used to identify starbursts (dashed black line, Puglisi et al. 2021) and 12 (64%) galaxies above.

Most importantly, the ALMA archival detection criterion does not impose a bias on the distribution in specific star-formation rates relative to the main-sequence as shown in Figure 4.2. Roughly 66% of the galaxies in our final ALMA-detected sample are starbursts, comparable to the starburst fraction amongst the parent sample and ALMA non-detections.

4pt 4pt

4.2.5 Ancillary Data

The parent sample from which our targets are selected from have robust multi-wavelength photometry and mid-IR spectroscopy from *Spitzer*/IRS. A full description

Table 4.1. Source characteristics for *Spitzer*/IRS targets matched to ALMA

ID	RA [J2000]	DEC [J2000]	z^a	$\log L_{\text{IR}}$ [L_{\odot}]	$\log M_*$ [M_{\odot}]	$f_{\text{AGN,MIR}}$	$\log L_{6.2\mu\text{m}}$ [L_{\odot}]	$\log L_{11.3\mu\text{m}}$ [L_{\odot}]
GS IRS1	03:32:44.00	-27:46:35.0	2.69	12.69	10.95	39	9.62 ± 0.18	...
GS IRS2	03:32:34.85	-27:46:40.0	1.10	11.61	10.14	17	9.30 ± 0.08	...
GS IRS15	03:32:40.74	-27:49:26.0	2.11	12.17	10.78	39
GS IRS20	03:32:47.58	-27:44:52.0	1.91	12.60	10.77	25	9.90 ± 0.18	10.05 ± 0.07
GS IRS23	03:32:17.23	-27:50:37.0	1.96	12.35	10.99	0	9.11 ± 0.99	9.80 ± 0.15
GS IRS29	03:32:22.53	-27:45:38.0	2.08	12.12	10.62	31	9.89 ± 0.19	9.84 ± 0.16
GS IRS33	03:32:23.43	-27:42:55.0	2.14	12.30	10.75	95	9.10 ± 0.10	...
GS IRS35	03:32:43.00	-27:46:50.0	1.04	11.79	10.39	0	9.48 ± 0.02	...
GS IRS45	03:32:17.45	-27:50:03.0	1.62	12.48	10.39	6	10.19 ± 0.06	9.78 ± 0.09
GS IRS46	03:32:42.71	-27:39:27.0	1.85	12.32	...	0	10.30 ± 0.08	...
GS IRS50	03:32:31.52	-27:48:53.0	1.90	12.01	10.82	28	9.84 ± 0.19	9.93 ± 0.12
GS IRS52	03:32:12.52	-27:43:06.0	1.79	12.11	10.43	15	9.62 ± 0.26	9.83 ± 0.14
GS IRS58	03:32:40.24	-27:49:49.0	1.85	12.06	10.86	7	9.51 ± 0.31	9.99 ± 0.11
GS IRS60	03:32:40.05	-27:47:55.0	2.02	12.46	10.88	23	10.12 ± 0.16	...
GS IRS61	03:32:43.45	-27:49:01.0	1.77	12.13	10.69	15	10.07 ± 0.06	9.71 ± 0.06
GS IRS70	03:32:27.71	-27:50:40.6	1.10	11.99	10.78	23	...	9.14 ± 0.14
GS IRS73	03:32:43.24	-27:47:56.2	0.67	11.26	10.47	0	8.66 ± 0.09	...
GS IRS74	03:32:44.32	-27:49:11.9	2.00	12.12	10.49	0	9.34 ± 1.05	10.19 ± 0.26
GS IRS81	03:32:38.49	-27:46:31.9	2.55	12.75	10.34	38	9.90 ± 0.40	...

Note. — IR luminosities are derived from fitting *Spitzer* and *Herschel* photometry. M_* was originally calculated assuming a Salpeter initial mass function (IMF, see Kirkpatrick et al. 2012), which we have corrected here to a Chabrier IMF.

^a Spectroscopic redshifts are derived from fits to the broad PAH features detected in mid-IR *Spitzer*/IRS spectra (following Appendix A of McKinney et al. 2020), and have typical uncertainties of $\Delta z \sim 0.02$.

of the IRS observations can be found in Pope et al. (2008) and Kirkpatrick et al. (2012), and a comprehensive discussion of the ancillary *Herschel* (PACS and SPIRE) and *Spitzer* (IRAC and MIPS) photometry is presented in Kirkpatrick et al. (2015). We take stellar masses derived in Kirkpatrick et al. (2012) using a Salpeter IMF, which we convert to a Chabrier framework following Kirkpatrick et al. (2017). The appendix of McKinney et al. (2020) provides a detailed description of how PAH luminosities and spectroscopic redshifts are derived for our sample using a custom Markov Chain Monte Carlo fitting routine. The GOODS-S targets are within the coverage of 3D-HST which provides deep WFC3/IR imaging (Brammer et al., 2012; Momcheva et al., 2016). Key derived properties from the ancillary data are listed in Table 4.1. In summary, galaxies in our sample have L_{IR} in the range of $10^{11.6} - 10^{12.8} L_{\odot}$, stellar masses between $\sim 10^{10} - 10^{11} M_{\odot}$, and redshifts from $z \sim 0.7 - 2.7$.

4.2.6 Comparison Samples

We compare our data against local galaxies in the Great Observatories All Sky LIRG Survey (GOALS; Armus et al. 2009), a $60 \mu\text{m}$ flux-limited sample of LIRGs with multi-wavelength data comparable to the coverage of our targets including *Spitzer*/IRS mid-IR measurements of $f_{\text{AGN,MIR}}$ and PAH emission (Stierwalt et al., 2013, 2014), intrinsic IR sizes from *Herschel*/PACS (Lutz et al., 2016), and sub-mm photometry (Chu et al., 2017) from which we derive dust masses. U et al. (2012) also present dust masses derived from SED fitting; however, we choose to re-calculate the total dust mass under the same assumptions and with the same method as applied to the high-redshift galaxies to avoid introducing systematic offsets (Kirkpatrick et al., 2017). We use $850 \mu\text{m}$ photometry from the *James Clerk Maxwell Telescope* where possible to measure the dust mass, and $500 \mu\text{m}$ *Herschel*/SPIRE photometry otherwise (Chu et al., 2017). Dust masses derived from both agree within $\sim 20\%$ on average.

To contextualize the measurements of PAHs in the ISM for both GOALS and our high star-formation rate targets with the general galaxy population, we compare against galaxies from the KINGFISH survey (Kennicutt et al., 2011), a sample of nearby ($D < 30$ Mpc) galaxies spanning a range in star-formation rate between $0.001 - 7 M_{\odot} \text{ yr}^{-1}$. We download the *Herschel*/PACS160 maps of KINGFISH targets (Dale et al., 2012), and perform a simple aperture-based measurement to derive the effective radii containing 50% of the $160 \mu\text{m}$ flux analogous to the methodology used in measuring effective sizes in GOALS and our ALMA-detected high- z (U)LIRGs. KINGFISH was designed to overlap with existing *Spitzer*/IRS spectroscopy from the SINGS program (Kennicutt et al., 2003), which we use to extend our analysis of dust to low Σ_{IR} using PAH line fluxes presented in Smith et al. (2007). We scale the PAH luminosities measured through the IRS slit by the ratio of total L_{IR} to L_{IR} measured through the slit (Smith et al., 2007), an approximate aperture correction assuming the extent of PAHs follows the cold dust continuum (e.g., Bendo et al., 2008; Calapa et al., 2014; Gregg et al., 2022). We note that none of the quantities we derive for KINGFISH correlate with distance or the adopted aperture correction. Finally, we measure dust masses in KINGFISH using *Herschel*/SPIRE $500 \mu\text{m}$ photometry (Dale et al., 2012, 2017) under the same assumptions made for the other data sets.

4pt 5pt

4.3 Results

4.3.1 Dust masses

Kirkpatrick et al. (2017) present an analysis of the dust masses of galaxies selected from the Kirkpatrick et al. (2015) supersample on the availability of sub-mm/mm single-dish photometry. Seven of the galaxies we find ALMA archival matches to also have single-dish sub-mm detections in Kirkpatrick et al. (2017), which we use to test for systematic differences in the dust mass measurements from single-dish and the

Table 4.2. Archival ALMA observed quantities and derived properties

ID	λ_{obs} [mm]	$S_{\nu,int}$ [mJy]	$S_{\nu,peak}$ [mJy]	σ [mJy]	R_{eff} [kpc]	$\log M_{dust}$ [M_{\odot}]	Ref
1	1.223	1.03	0.81	0.035	0.91 ± 0.06	8.67 ± 0.03	1
2	1.223	0.20	0.11	0.031	< 1.12	7.67 ± 0.06	1
15	1.171	0.76	0.52	0.15	1.66 ± 0.4	8.45 ± 0.17	2
20	1.223	1.10	0.66	0.062	1.35 ± 0.13	8.71 ± 0.06	1
23	1.171	1.41	1.01	0.13	1.78 ± 0.23	8.72 ± 0.11	2
29	1.223	0.19	0.42	0.11	< 2.61	8.19 ± 0.06	1
33	0.873	0.50	0.18	0.03	0.70 ± 0.21	8.0 ± 0.08	3
35	1.223	0.26	0.10	0.032	2.29 ± 0.46	8.01 ± 0.19	1
45	1.171	1.05	0.81	0.14	< 3.1	8.47 ± 0.06	2
46	0.450 ^a	9.30	6.55	0.60	1.42 ± 0.15	8.70 ± 0.16	4
50	1.223	1.04	0.27	0.072	2.98 ± 0.31	8.68 ± 0.12	1
52	0.450 ^a	8.65	5.21	0.92	1.32 ± 0.11	8.50 ± 0.25	4
58	0.450 ^a	10.50	5.50	0.70	2.61 ± 0.30	< 8.35	4
60	1.223	0.65	0.14	0.030	3.64 ± 0.28	8.48 ± 0.1	1
61	0.450 ^a	4.22	3.70	0.35	1.64 ± 0.18	< 7.95	4
70	1.171	0.37	0.35	0.11	< 2.63	8.05 ± 0.1	2
73	1.171	0.68	0.58	0.15	1.30 ± 0.30	8.2 ± 0.15	2
74	1.223	0.51	0.13	0.068	3.25 ± 0.50	8.37 ± 0.19	1
81	1.223	0.80	0.52	0.030	1.32 ± 0.07	8.57 ± 0.03	1

Note. — Table columns are as follows; (ID) Identification following Table 4.1. (λ_{obs}) Observed continuum effective wavelength. ($S_{\nu,int}$) Source-integrated flux. ($S_{\nu,peak}$) Peak continuum flux. (σ) Map noise. (R_{eff}) Effective radius containing half of the total integrated flux. (M_{dust}) Dust mass derived using Eq. 4.1. (Ref) ALMA program from which properties are derived: 1 =ASAGAO (Ueda et al., 2018), 2 =GOODS-ALMA (Gómez-Guijarro et al., 2022a), 3 =2018.1.00992.S (Lamperti et al., 2021), 4 =2017.1.03147.S (McKinney et al., 2020)

^aFor these objects only detected only in ALMA Band 9 ($\lambda_{obs} \sim 450 \mu\text{m}$), we use single-dish dust mass estimates from Kirkpatrick et al. (2017) where possible. Otherwise, we place 3σ upper limits using local noise properties derived from the target’s position within the ASAGAO map.

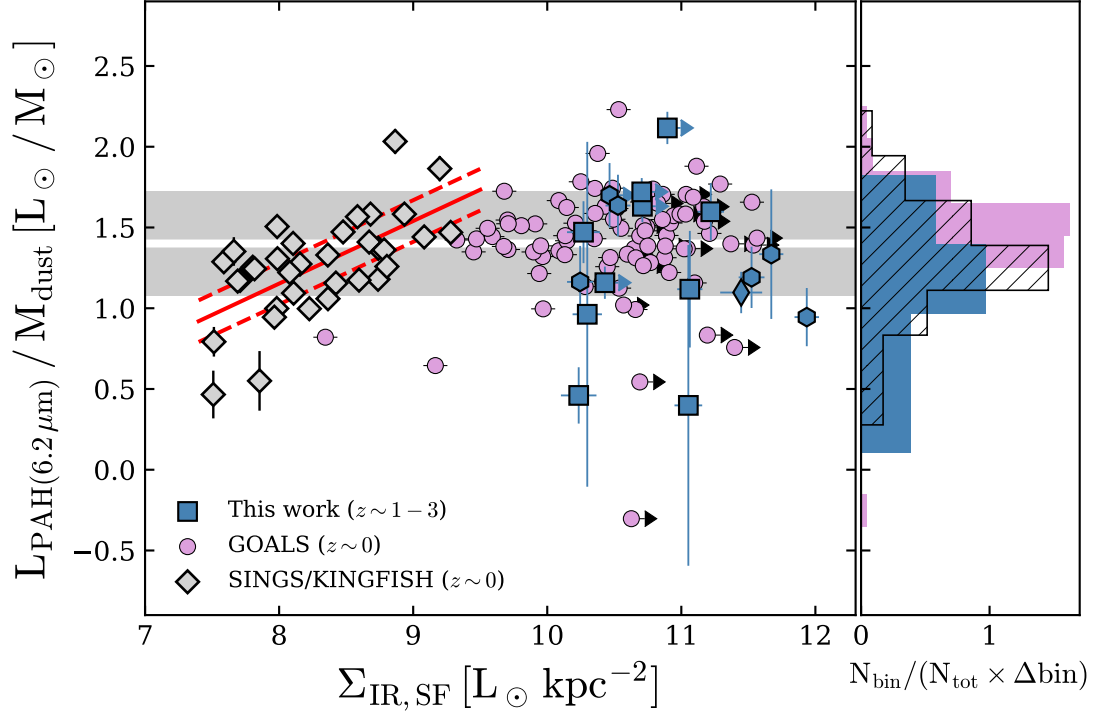


Figure 4.3 The ratio of the $6.2\ \mu\text{m}$ PAH luminosity relative to the total dust mass in our $z \sim 1 - 2$ ALMA-detected *Spitzer*/IRS sample, GOALS, and KINGFISH as a function of Σ_{IR} . A histogram showing the distribution in $L_{\text{PAH}(6.2\ \mu\text{m})}/M_{\text{dust}}$ for each sample is shown along the right. The scatter in $L_{\text{PAH}(6.2\ \mu\text{m})}/M_{\text{dust}}$ is marginally larger for $z > 0$ relative to GOALS owing to the lower SNR mid-IR spectra and larger errorbars. Nevertheless, both (U)LIRG samples cluster around an average $\log L_{\text{PAH}(6.2\ \mu\text{m})}/M_{\text{dust}} \sim 1.3 \pm 0.4 L_{\odot}/M_{\odot}$ as shown with the shaded region in the left panel with no clear correlation against Σ_{IR} . KINGFISH galaxies on the other hand do show a positive correlation between $L_{\text{PAH}(6.2\ \mu\text{m})}/M_{\text{dust}}$ and Σ_{IR} (solid red line) with small 1σ dispersion about the best-fit (dashed red line), but the overall distribution is consistent with ratios found amongst (U)LIRGs.

ALMA interferometer. Flux densities in confusion-limited sub-mm observations are often boosted by the unresolved background as steeply rising source number counts preferentially scatter flux densities upwards (e.g., Hogg & Turner, 1998; Scott et al., 2002; Simpson et al., 2015). Indeed, we find that single-dish derived dust masses tend to be greater than those derived using the ALMA observations by $\sim 25\% - 50\%$ but both agree within 1σ .

The dust mass is dominated by large grains which also dominate the far-IR emission, whereas PAHs populate the smaller end of the grain size distribution and emit strong mid-IR features (Draine & Li, 2001). Despite this size difference, mid- and far-IR emission tracing the PAHs and cold dust respectively are correlated with the spatial extent of star-formation in galaxies (e.g., Gregg et al., 2022) which is, amongst other reasons, why PAHs have been commonly used to trace dust-obscured star-formation rates (e.g., Genzel et al., 1998; Peeters et al., 2004; Wu et al., 2005; Lutz et al., 2007; Pope et al., 2008). In Figure 4.3 we show the ratio of L_{PAH} to the total dust mass, assuming this empirically traces the PAH mass fraction in the ISM (Draine & Li, 2001) which is otherwise commonly inferred in the literature by fitting dust model grids to spectral energy distributions (e.g., Draine & Li, 2007; Aniano et al., 2020). We use only the $6.2\ \mu\text{m}$ PAH feature because it is isolated from adjacent lines and distant from the strong silicate absorption making it the cleanest PAH line to measure in low SNR *Spitzer*/IRS spectra. We find no correlation between $L_{\text{PAH}}/M_{\text{dust}}$ and Σ_{IR} for (U)LIRGs, and that all galaxies included in this analysis cluster around a common L_{PAH} -to-total dust mass ratio of $\log L_{\text{PAH}(6.2\ \mu\text{m})}/M_{\text{dust}} \sim 1.3 \pm 0.4 L_{\odot}/M_{\odot}$ (Tab. 4.3). The significant 1σ scatter should discourage the use of PAHs to trace the dust content of star-forming galaxies. We do find a positive correlation between $L_{\text{PAH}}/M_{\text{dust}}$ in KINGFISH with Σ_{IR} , which could be driven by the higher metallicity and PAH mass fractions in warmer, high IR surface density galaxies in the sample (Aniano et al., 2020). The scatter about the best-fit trend in KINGFISH galaxies

is substantially lower than for (U)LIRGs at $z \sim 0 - 2$, which could justify the use of PAH emission to trace the total dust mass at $\log \Sigma_{\text{IR}} / [\text{L}_{\odot} \text{kpc}^{-2}] < 9.5$ if Σ_{IR} is known. Further studies of high-redshift, low Σ_{IR} galaxies are needed to test if this correlation holds at earlier cosmic epochs.

4.3.2 IR Sizes

Fujimoto et al. (2017) presents a systematic analysis of IR sizes using Cycles 0-3 ALMA programs made public through the ALMA archive. Their sample spans a range in star-formation rates between $\sim 100 - 1000 \text{ M}_{\odot} \text{ yr}^{-1}$, stellar masses between $\log M_{*} / \text{M}_{\odot} = 10 - 11.5$ and $z \sim 0 - 6$. We compare the sizes measured in our ALMA-detected sample to their results in Figure 4.4, as well as the distribution in sizes found for $z \sim 0$ GOALS and KINGFISH galaxies. Note that we have subtracted the AGN-powered component from L_{IR} using the IR AGN fraction in GOALS and $z \sim 1 - 2$ (U)LIRGs (see Eq. 5 in Kirkpatrick et al. 2015) such that $L_{\text{IR,SF}} = (1 - f_{\text{AGN,IR}}) \times L_{\text{IR}}$. This has minimal impact on the nature of the $L_{\text{IR}} - R_{\text{eff},160}$ relation because $f_{\text{AGN,IR}}$ reaches a maximum of ~ 0.5 for $f_{\text{AGN,MIR}} \sim 1$ (Kirkpatrick et al., 2015).

Our far-IR size measurements are consistent with the sizes measured for LIRGs and ULIRGs from $z \sim 0 - 6$ spanning a range of star-formation rate surface densities found at all redshifts between $\Sigma_{\text{SFR}} = 10^2 - 10^4 \text{ M}_{\odot} \text{ yr}^{-1} \text{ kpc}^{-2}$. (U)LIRGs and ALMA-selected galaxies from Fujimoto et al. (2017) have on-average smaller $R_{\text{eff},160}$ than KINGFISH galaxies by a factor of ~ 2.5 . No galaxy exceeds the theoretical Eddington limit of $\Sigma_{\text{SFR}} \sim 1000 \text{ M}_{\odot} \text{ yr}^{-1} \text{ kpc}^{-2}$ (Andrews & Thompson, 2011) even if we omit the AGN correction to L_{IR} . Cochrane et al. (2019) demonstrate using cosmological zoom-in simulations that temperature gradients in the dust across a star-forming galaxy can change the inferred far-IR size derived from long wavelength observation; however, this is unlikely to be producing systematic effects between different samples because GOALS and the *Spitzer* (U)LIRGs at $z \sim 1 - 2$ have similar IR colors (Kirkpatrick

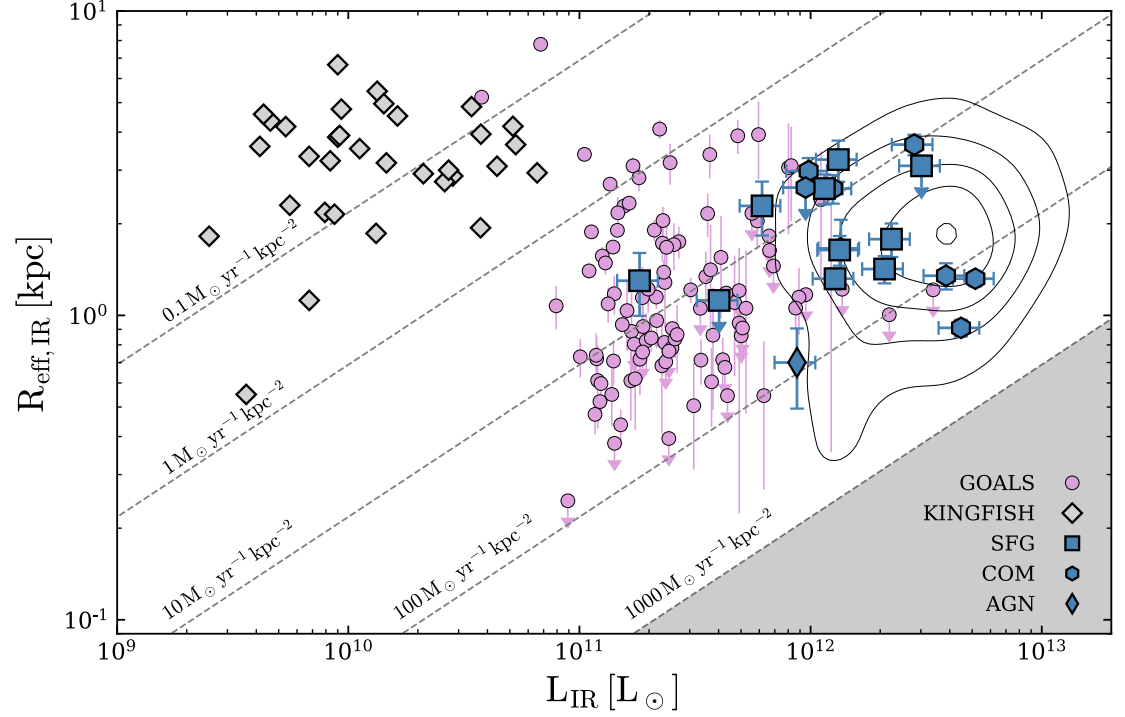


Figure 4.4 The effective IR size as a function of total infrared luminosity. Galaxies in our ALMA-detected sample are shown with symbols corresponding to their $f_{\text{AGN,MIR}}$ classification. We compare against the archival sample of Fujimoto et al. 2017 (black contours), GOALS (purple circles) and KINGFISH (grey diamonds). We have subtracted out the contribution to L_{IR} from AGN in our sample and GOALS using $f_{\text{AGN,MIR}}$ and Eq. 5 from Kirkpatrick et al. (2015). Dashed lines correspond to constant star-formation rate surface densities assuming $\text{SFR}_{\text{IR}}/[\text{M}_{\odot} \text{yr}^{-1}] = 1.49 \times 10^{-10} L_{\text{IR}}/L_{\odot}$ (Murphy et al., 2011). The shaded grey region indicates $\Sigma_{\text{SFR}} > 1000 \text{M}_{\odot} \text{yr}^{-1}$ where star-formation exceeds the Eddington limit (Andrews & Thompson, 2011). Our size results are consistent with the range observed in the literature amongst other high- z galaxies.

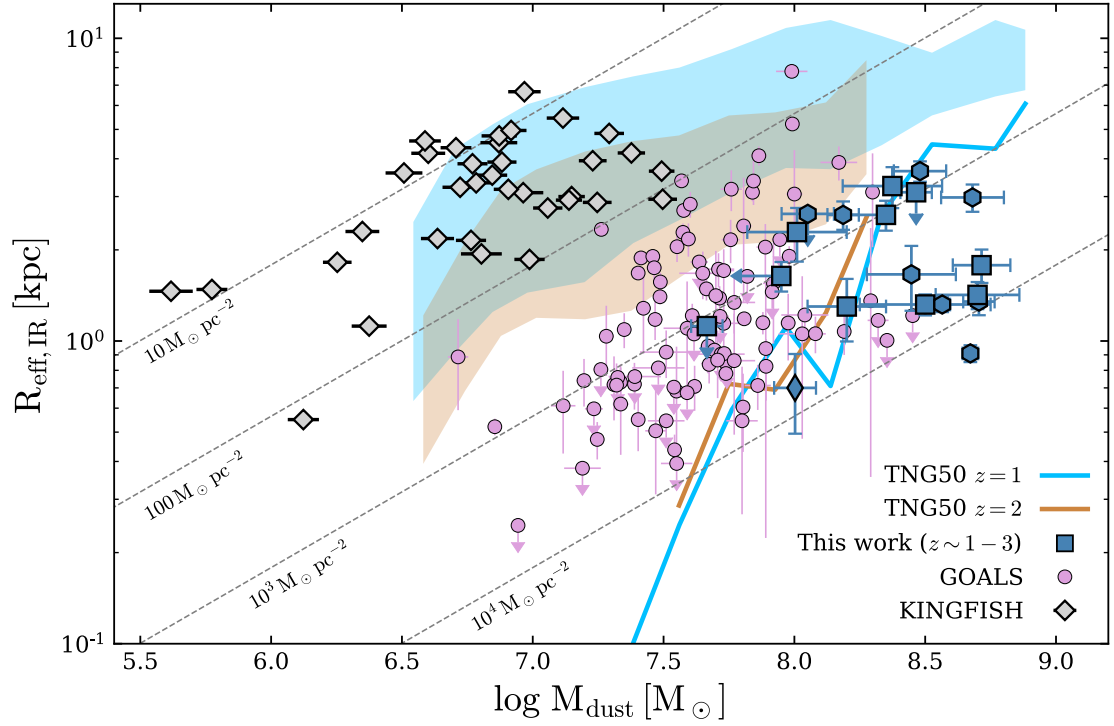


Figure 4.5 A comparison between the effective IR size and the total dust mass for this work (blue symbols, following $f_{\text{AGN,MIR}}$ classifications in Fig. 4.4), GOALS (purple circles), and KINGFISH (grey diamonds). Black dashed lines correspond to constant levels of gas mass surface densities assuming a dust-to-gas ratio of 0.01. The shaded regions represent the 16th-84th percentile distribution in dust-continuum size vs. dust mass from galaxies in the TNG50 cosmological simulation at $z \sim 1-2$ (Popping et al., 2022). Solid lines of the corresponding color represent TNG50 galaxies 2σ below the median. Luminous IR galaxies at $z \sim 1-2$ tend to have higher dust masses and be more extended than GOALS. The sizes we measure at $z \sim 1-3$ are consistent with the more compact (lower $R_{\text{eff},160}$) galaxies in TNG50 for fixed dust mass.

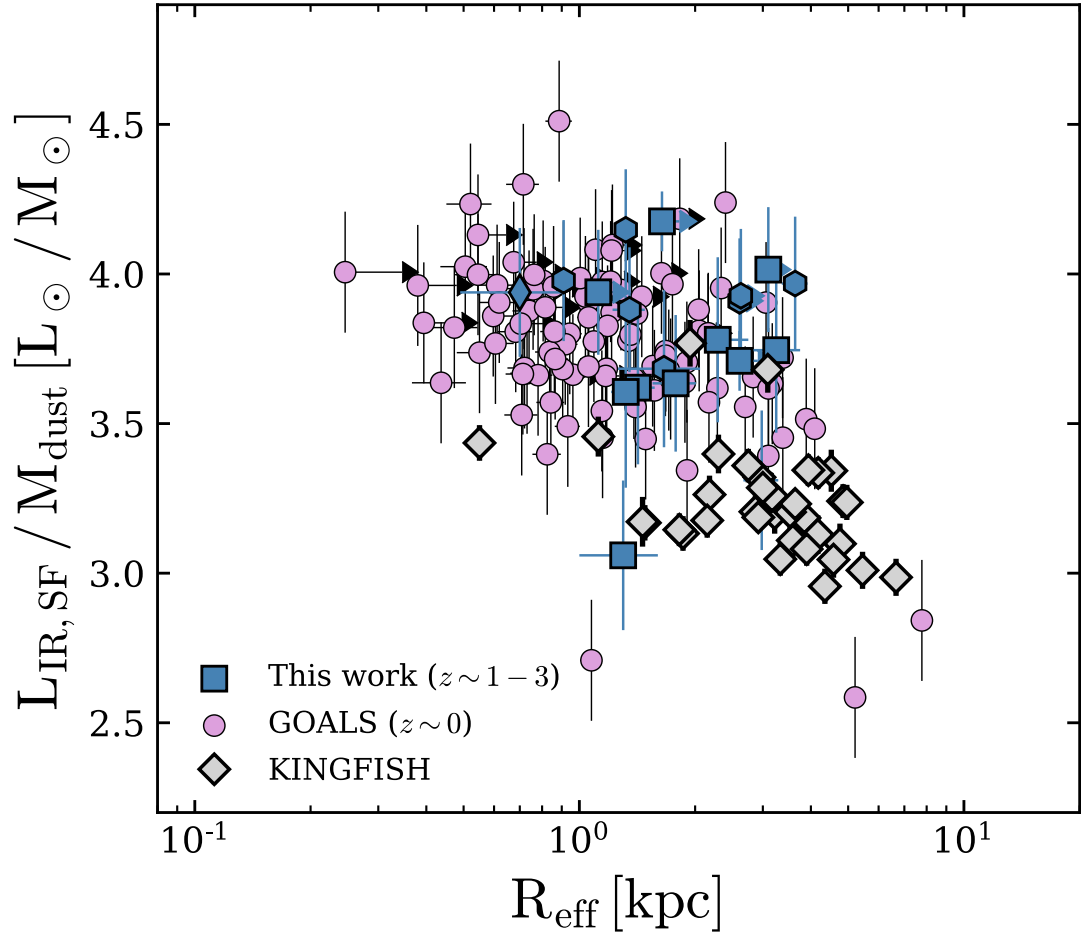


Figure 4.6 The ratio of total infrared luminosity to total dust mass as a function of IR size in $z \sim 0 - 2$ (U)LIRGs (GOALS, this work) and KINGFISH galaxies at lower star-formation rate surface densities. The legend follows Figures 4.4 and 4.5. Smaller galaxies in KINGFISH tend to have larger $L_{\text{IR}}/M_{\text{dust}}$ and eventually reach the average value for $z \sim 0 - 2$ (U)LIRGs by $R_{\text{eff},160} \sim 1 - 2$ kpc. The anti-correlation between $L_{\text{IR}}/M_{\text{dust}}$ and $R_{\text{eff},160}$ in (U)LIRGs is marginal and the full range in $L_{\text{IR}}/M_{\text{dust}}$ can be found at sizes between $\sim 0.4 - 4$ kpc.

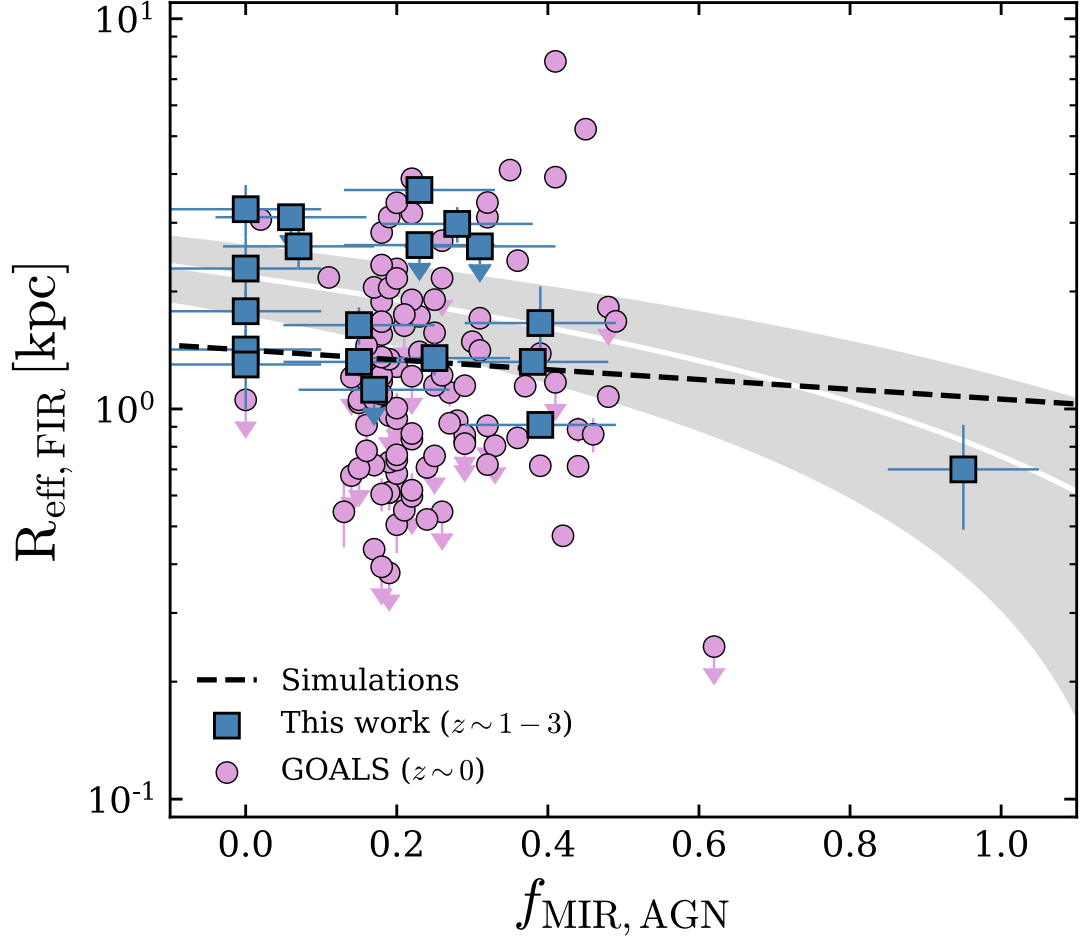


Figure 4.7 IR size vs. the fractional contribution of AGN to the integrated mid-IR emission ($f_{\text{AGN, MIR}}$). GOALS galaxies are shown with purple circles, and blue squares indicate the $z \sim 1-2$ ALMA-detected sample from this work. The shaded grey region encases the $\pm 1\sigma$ scatter about a best-fit linear trend to the $z \sim 1-2$ galaxies, and the black dashed line shows the trend measured from simulations at $\lambda_{\text{rest}} = 160 \mu\text{m}$ (McKinney et al., 2021b). At $z \sim 1-2$, dust-obscured galaxies tend to have smaller $R_{\text{eff, 160}}$ with increasing $f_{\text{AGN, MIR}}$, exhibiting a factor of ~ 2 decrease in the average sizes between $f_{\text{AGN, MIR}} = 0-0.4$. The one AGN-dominated ($f_{\text{AGN, MIR}} \sim 1$) galaxy at $z \sim 1-2$ also exhibits the smallest IR size by a factor of ~ 3 relative to the rest of the sample.

et al., 2017). Rather, variations in the dust temperature gradient may help explain some of the scatter in far-IR size for fixed L_{IR} in Figure 4.4.

The highest IR surface density sources are moderate to strong AGN consistent with Fujimoto et al. (2017) who find that X-ray AGN are preferentially found towards greater Σ_{SFR} . This suggests that AGN-host galaxies may also host vigorous star-formation and/or the contribution to L_{IR} from the AGN is underestimated. This latter scenario could arise from dust-reprocessing of AGN photons from the mid-IR out to far-IR/sub-mm wavelengths (McKinney et al., 2021b). We discuss the relation between far-IR sizes and mid-IR AGN strengths in Section 4.3.2.1.

GOALS galaxies span a range in $R_{\text{eff},160}$ on-average below that of the higher- z galaxies but within the range in $R_{\text{eff},160}$ of the Fujimoto et al. (2017) sample other than two very extended and nearby sources. This is in contrast to the continuous rise in the rest-frame optical sizes of non-dusty star-forming galaxies towards $z \sim 0$ (Shibuya et al., 2015), and likely reflects that dusty star-formation at $z \sim 0$ requires major mergers to compress gas in the centers, producing the nuclear and obscured starbursts found amongst GOALS galaxies (e.g., Sanders & Mirabel, 1996; Downes & Solomon, 1998; Bryant & Scoville, 1999; Soifer et al., 2000).

In Figure 4.5 we show the far-IR extent of the ALMA-detected sample, GOALS, and KINGFISH as a function of their total dust masses. Assuming a dust-to-gas mass ratio of 0.01 as is appropriate for massive $z \sim 0 - 2$ galaxies (e.g., Rémy-Ruyer et al., 2014; Popping et al., 2017; Shapley et al., 2020), we find that most (U)LIRGs would fall along an average $\Sigma_{\text{gas}} \sim 1000 M_{\odot} \text{pc}^{-2}$ at $z \sim 0$ and $z \sim 1 - 2$ as expected from their large star-formation rate surface densities (Kennicutt & Evans, 2012). This implies a Σ_{dust} one order of magnitude less than that required for an optical depth of unity at $\lambda_{\text{rest}} = 100 \mu\text{m}$, and the fact that $M_{\text{dust}} \propto R_{\text{eff,IR}}^2$ is consistent with optically thin dust (Draine & Li, 2007; Scoville et al., 2017b). We note that approximately 25% of GOALS galaxies at $\log M_{\text{dust}}/M_{\odot} < 8$ have upper limits on their IR size, which

could push the trend towards higher Σ_{gas} at low M_{dust} amongst the $z \sim 0$ LIRG population.

Popping et al. (2022) derived a simulated distribution in IR size by performing dust radiative transfer on galaxies from the Illustris TNG50 cosmological simulation (Nelson et al., 2019; Pillepich et al., 2019). We compare against this distribution in Figure 4.5 which represents galaxies on and above the star-forming main-sequence in TNG50. GOALS galaxies and our $z \sim 1 - 2$ ALMA-detected sample lie above the main-sequence, and fall within the parameter space in M_{dust} vs. $R_{\text{eff},160}$ spanned by simulated galaxies with sizes 2σ below the median trend. While the size analysis of Popping et al. (2022) does not extend to $z \sim 0$, the trend towards larger $R_{\text{eff},160}$ for fixed M_{dust} at lower redshift appears consistent with the sizes we measure in KINGFISH.

Figure 4.6 shows the ratio of L_{IR} to M_{dust} as a function of the effective IR radius, bringing together the quantities shown independently in Figures 4.4 and 4.5. The ratio of L_{IR} to total dust mass is an empirical tracer of the star-formation efficiency, which reflects the amount of star-formation sustained by a galaxy given its total gas content. (U)LIRGs at $z \sim 0 - 2$ are known to have similar $L_{\text{IR}}/M_{\text{dust}}$ ratios, although for fixed L_{IR} the star-formation efficiency is higher at $z \sim 0$ (Kirkpatrick et al., 2017). We find that the $L_{\text{IR}}/M_{\text{dust}}$ ratios for $z \sim 0$ and $z \sim 1 - 2$ (U)LIRGs are comparable at fixed $R_{\text{eff},160}$, with little to no anti-correlation with IR size. The more spatially extended KINGFISH galaxies have on-average lower $L_{\text{IR}}/M_{\text{dust}}$ than (U)LIRGs, but reach the average value of the dustier galaxies below $R_{\text{eff},160} \sim 2$ kpc.

4.3.2.1 Far-IR size as a function of mid-IR AGN fraction

Heavily dust-obscured AGN can produce high IR surface densities as the nuclear torus is heated to high temperatures. For example, the extraordinarily compact dust emission in the west nucleus of the local ULIRG Arp 220 has a radius of 74 pc (Scoville

et al., 2017a). Such heating of the dust by AGN can increase the central concentration of IR emission and drive the galaxy-scale effective radii down (e.g., McKinney et al., 2021b; Lamperti et al., 2021). We note that some star-forming galaxies at high- z do not necessarily exhibit systematically different IR sizes compared to sub-mm luminous quasars (e.g., Chen et al., 2021; Ansarinejad et al., 2022); however, prior works do not explicitly control for the AGN strength using mid-IR spectroscopy.

Using the *Spitzer*/IRS spectral decomposition between SF and AGN for our sample (Pope et al., 2008; Kirkpatrick et al., 2012) and GOALS (Stierwalt et al., 2013, 2014; Díaz-Santos et al., 2017), we show in Figure 4.7 the relationship between $R_{\text{eff},160}$ and $f_{\text{AGN,MIR}}$ from $z \sim 0 - 2$. GOALS galaxies exhibit no systematic correlation between the far-IR size and $f_{\text{AGN,MIR}}$ consistent with the comparison against PG QSOs in Lutz et al. (2016); however, the smallest systems in GOALS do exhibit the greatest mid-IR AGN fractions. This is consistent with Díaz-Santos et al. (2010) who find smaller mid-IR core sizes at higher $f_{\text{AGN,MIR}}$ using the spatial extent of emission measured through the *Spitzer*/IRS slit. The trend is stronger for the $z \sim 1 - 2$ ALMA-detected sample in this work, where $R_{\text{eff},160}$ decreases by a factor of ~ 2 between $f_{\text{AGN,MIR}} = 0 - 0.4$ (Table 4.3). Moreover, the one AGN-dominated galaxy in our sample also exhibits the smallest IR size. For comparison against simulations, we measure the effective radii from the IR emission modelled using *Gadget-2* coupled to the dust radiative transfer code *SUNRISE* presented in Hayward et al. (2011) and Snyder et al. (2013) as analyzed in McKinney et al. (2021b). This particular simulation was designed to emulate the properties of sub-mm galaxies around $z \sim 2$ (Hayward et al., 2011), and exhibits a $\sim 25\%$ decrease in the effective IR size as $f_{\text{AGN,MIR}}$ changes from 0 to 1 because the AGN adds more emission in the central region. This trend from the one simulation is shallower than the fit to our $z \sim 1 - 2$ galaxies but consistent within the uncertainties.

Table 4.3. Best-fit Parameters and their Uncertainties for Linear Fits to Data

x	y	m	b	σ^a	sample ^b
$f_{\text{AGN,MIR}}$	$R_{\text{eff,FIR}}$ [kpc]	-1.43 ± 0.8	2.2 ± 0.3	0.65	3
$\log \Sigma_{\text{IR}}/[\text{L}_\odot \text{ kpc}^{-2}]$	$\log L_{6.2}/M_{\text{dust}} [\text{L}_\odot/M_\odot]$	0.39 ± 0.08	-1.95 ± 0.7	0.12	1
$\log \Sigma_{\text{IR}}/[\text{L}_\odot \text{ kpc}^{-2}]$	$\log L_{6.2}/M_{\text{dust}} [\text{L}_\odot/M_\odot]$...	1.30	0.37	2,3
$\log \Sigma_{\text{IR}}/[\text{L}_\odot \text{ kpc}^{-2}]$	$\log L_{\text{IR,SF}}/M_{\text{dust}} [\text{L}_\odot/M_\odot]$	0.31 ± 0.11	0.3 ± 1.2	0.12	3
$\log \Sigma_{\text{IR}}/[\text{L}_\odot \text{ kpc}^{-2}]$	$\log L_{\text{IR,SF}}/M_{\text{dust}} [\text{L}_\odot/M_\odot]$	0.25 ± 0.02	1.15 ± 0.17	0.08	1,2,3
$\log \Sigma_{\text{IR}}/[\text{L}_\odot \text{ kpc}^{-2}]$	$\log \text{sSFR}/\text{sSFR}_{\text{MS}}$	0.34 ± 0.07	-2.05 ± 0.76	0.13	2
$\log \Sigma_{\text{IR}}/[\text{L}_\odot \text{ kpc}^{-2}]$	$\log \text{sSFR}/\text{sSFR}_{\text{MS}}$	0.19 ± 0.12	-1.46 ± 1.3	0.13	3
$\log \Sigma_{\text{IR}}/[\text{L}_\odot \text{ kpc}^{-2}]$	$\log \text{sSFR}/\text{sSFR}_{\text{MS}}$...	0.61	0.25	3

Note. — Fits take the functional form $y = mx + b$. For fits showing no slope the best-fit b and σ correspond to the y -column average and dispersion about the mean.

^a 1σ dispersion about the best-fit trend.

^b Samples included in fit: (1) KINGFISH, (2) GOALS, (3) ALMA-detected (U)LIRGs at $z \sim 1 - 2$ from this work.

4.4 Discussion

The dust properties of purely star-forming *Spitzer*/IRS-selected galaxies were studied extensively in Kirkpatrick et al. (2017). To briefly summarize their main findings, Kirkpatrick et al. (2017) demonstrated: (1) $z \sim 1 - 2$ galaxies exhibit lower $L_{\text{IR,SF}}/M_{\text{dust}}$ ratios and higher gas mass fractions than what are found at $z \sim 0$ for fixed L_{IR} , and (2) Galaxies at all redshifts fall along a common $L_{\text{IR,SF}}/M_{\text{dust}}$ relation when accounting for distance above the star-forming main-sequence. We now build upon this prior analysis to understand the role played by the IR sizes of galaxies in governing their star-formation and AGN-related properties.

4.4.1 ISM conditions and dust composition scale with IR surface densities

For fixed L_{IR} , galaxies at $z \sim 2$ exhibit more PAH emission per unit L_{IR} than local galaxies (Pope et al., 2013). In a small sample of ALMA-selected *Spitzer* targets, McKinney et al. (2020) demonstrated that this offset disappears for fixed Σ_{IR} . We expand upon this prior result using a sample three times larger and sizes pre-

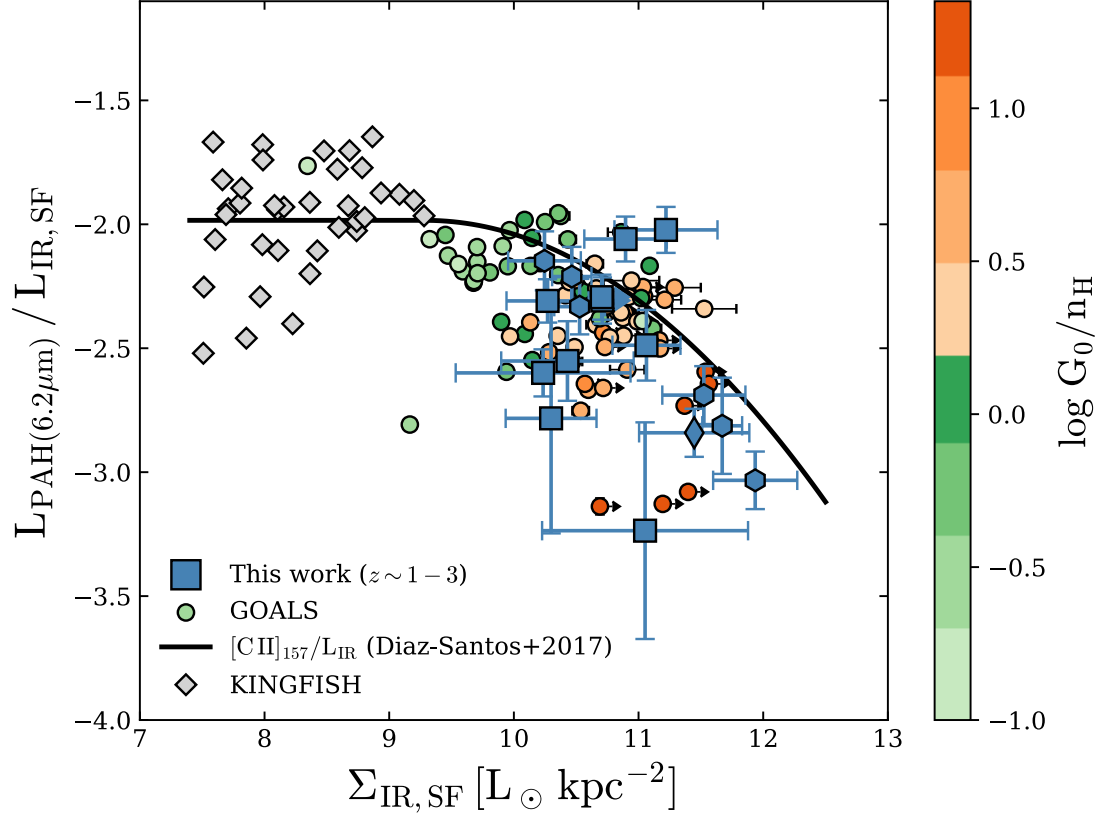


Figure 4.8 PAH/ L_{IR} vs. IR surface density. GOALS galaxies (circles) are colored by the ratio of the radiation field strength (G) to neutral gas density (n_{H}) in PDRs, derived from FIR find-structure line modelling (Díaz-Santos et al., 2017). For comparison, we also show the trend in $[\text{C II}]/L_{\text{IR}}$ from Díaz-Santos et al. (2017) as a black line derived after correcting the $[\text{C II}]$ emission for the fraction arising from neutral vs. ionized gas. KINGFISH (grey diamonds) cluster at lower Σ_{IR} about this trend. Galaxies at $z \sim 1 - 2$ (red squares) follow the local trend in PAH/ L_{IR} vs. Σ_{IR} , which exhibits a comparable turnover as found for the deficit observed in $[\text{C II}]$ emission at $\log \Sigma_{\text{IR}}/[L_{\odot} \text{ kpc}^{-2}] > 10$ accompanied by high G/n_{H} . This suggests a change in the ISM conditions for $z \sim 1 - 2$ dusty, star-forming galaxies comparable to those found amongst high IR surface density GOALS galaxies (McKinney et al., 2021a).

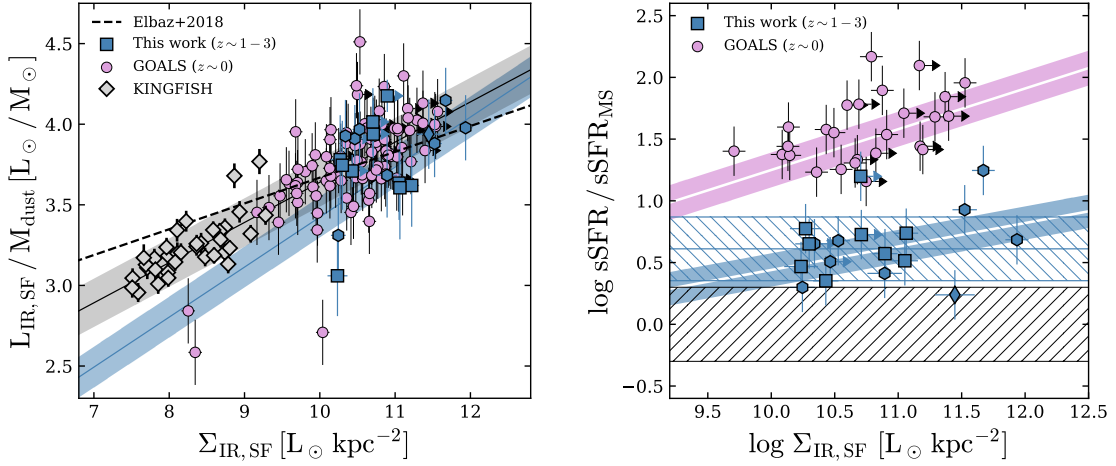


Figure 4.9 (*Left*) The ratio of AGN-corrected IR luminosity to total dust mass, a tracer of the star-formation efficiency, as a function of IR surface density. Labeling follows Fig. 4.4. A best-fit linear trend for the high- z galaxies is shown in blue, and a fit to all galaxies on the Figure is shown in black. The dot-dashed line shows the SFE and IR size relation from Elbaz et al. (2018) derived from $870 \mu\text{m}$ imaging of *Herschel*-selected (U)LIRGs normalized to the locus of our data as differences in SFR- and gas-mass derivations can change the absolute normalisation of the trend. We find a redshift-independent relation between the IR size and $L_{\text{IR}}/M_{\text{dust}}$ ratio where higher IR surface density galaxies exhibit evidence for higher star-formation efficiencies. (*Right*) Distance from the specific star-forming main-sequence as a function of Σ_{IR} for each galaxy’s redshift and stellar mass. The black hatched region encases the ± 0.3 dex canonical main-sequence scatter (Whitaker et al., 2014). (U)LIRGs at high IR surface density tend to be further above the main-sequence, a trend that is more pronounced at $z \sim 0$ (shaded grey line) than at $z \sim 1-2$ (shaded red line) where the data is equally well-fit with no Σ_{IR} -dependence (hatched red region).

dominantly measured along the RJ tail of cold dust emission. Figure 4.8 shows the $L_{\text{PAH}}/L_{\text{IR}}$ ratio as a function of Σ_{IR} at $z \sim 1 - 2$, and for GOALS and KINGFISH. We find the same $L_{\text{PAH}}/L_{\text{IR}}$ ratios at high and low redshift for fixed Σ_{IR} . Moreover, we recover an anti-correlation between $L_{\text{PAH}}/L_{\text{IR}}$ and Σ_{IR} reminiscent of the FIR fine-structure line deficit observed in low- and high- z dusty galaxies (Díaz-Santos et al., 2017; Zanella et al., 2018; McKinney et al., 2020). PAHs and FIR lines predominantly arise from photodissociation regions (PDRs) around sites of recent star-formation for actively star-forming galaxies (Tielens & Hollenbach, 1985b; Malhotra et al., 1997, 2001; Tielens, 2008; Beirão et al., 2012; Croxall et al., 2017; Díaz-Santos et al., 2017; Sutter et al., 2019), and thus the coincidence in their trends with respect to Σ_{IR} favors physical interpretations local to the young, dusty star-forming regions which the IR surface density is dominated by.

The low $L_{\text{PAH}}/L_{\text{IR}}$ ratios at high Σ_{IR} might indicate a change in the ISM conditions regulating the excitation of both FIR lines and PAH emission within dusty and young star-forming regions (e.g., Díaz-Santos et al., 2017). The high G/n_{H} ratios found amongst GOALS at $\log \Sigma_{\text{IR}}/[L_{\odot} \text{ kpc}^{-2}] > 10.7$ indicate that the average star-forming region sees a stronger radiation field, which can modify the PAH photoelectric heating efficiency (Bakes & Tielens, 1994; Galliano et al., 2008; Tielens, 2008) and lower the radiative coupling between stars and gas (McKinney et al., 2020, 2021a). Changes in the relative heating and cooling could lead to systematically high star-formation efficiency if PAHs photoelectrically convert a lower fraction of energy from the stellar radiation field into gas temperatures (Hollenbach & Tielens, 1999; McKinney et al., 2021a). Indeed, simulations that include variable photo-heating laws find the converse to be true: high photoelectric heating rates suppress star-formation due to excess heating (Forbes et al., 2016; Inoguchi et al., 2020; Osman et al., 2020). Systematic changes in the photoelectric heating efficiency might leave imprints on the mid-IR spectra as the ionization and/or grain size distribution of PAHs is modified (Draine

& Li, 2001; Maragkoudakis et al., 2020). The overlap between GOALS and $z \sim 1 - 2$ (U)LIRGs along canonical diagnostic plots of PAH grain properties suggests that the physical mechanisms observed at $z \sim 0$ are likely in place and playing an important role at higher- z (Figure 4.3, see also McKinney et al. 2020). We explore the efficiency of star-formation in the next section.

4.4.2 Dust-obscured galaxies form stars more efficiently at high IR surface densities

In Figure 4.9 (*Left*) we show the $L_{\text{IR,SF}}/M_{\text{dust}}$ ratio vs. Σ_{IR} . The $L_{\text{IR,SF}}/M_{\text{dust}}$ ratio is an empirical tracer of the global star-formation efficiency, which may systematically evolve with redshift (Scoville et al., 2017b). As stated, Kirkpatrick et al. (2017) demonstrated that, for fixed distance above the main-sequence, the star-formation efficiency of (U)LIRGs fall along the same relation between $z \sim 0 - 2$. We find a similarly redshift-independent result, where high IR surface density galaxies exhibit more efficient star-formation. Combined with KINGFISH which probes galaxies at lower star-formation rates and more extended sizes, the correlation persists linearly over ~ 5 orders of magnitude in IR surface density with comparatively shallow increase in star-formation efficiency by one order of magnitude. Kirkpatrick et al. (2017) find no correlation between $L_{\text{IR,SF}}/M_{\text{dust}}$ and the ISM extent measured from CO, radio, or Pa α for a handful of high- z galaxies and local LIRGs in GOALS (Rujopakarn et al., 2011). This could be due to their lower number statistics and/or inhomogeneous collection of size tracers, but as shown in Figure 4.6 we also do not find a correlation between $L_{\text{IR,SF}}/M_{\text{dust}}$ and the uniformly measured effective radii from far-IR wavelengths. These results are consistent with multiple studies in the literature demonstrating that luminosity surface densities more accurately reflect the gas and star-formation conditions in galaxies rather than the total luminosity or size alone

(e.g., Rujopakarn et al., 2011; Díaz-Santos et al., 2017; Elbaz et al., 2018; McKinney et al., 2020; Díaz-Santos et al., 2021).

The star-formation efficiencies are comparable between GOALS and the $z \sim 1 - 2$ (U)LIRGs in this study; however, the samples are different in terms of their position relative to main-sequence star-formation for their corresponding epochs (Kirkpatrick et al., 2017). Using the main-sequence parameterization from Speagle et al. (2014), we show in Figure 4.9 (*Right*) Σ_{IR} against the ratio of each galaxy’s specific star-formation rate (sSFR \equiv SFR/ M_*) to the main-sequence sSFR for the corresponding stellar mass and redshift. GOALS galaxies are typically a factor of ~ 10 above the main-sequence compared to a factor of ~ 4 in ALMA-detected $z \sim 1 - 2$ (U)LIRGs. As demonstrated first in Lutz et al. (2016), the IR surface density correlates with distance from the main-sequence in GOALS such that high IR surface density galaxies are undergoing stronger starbursts. We find no such correlation at $z \sim 1 - 2$ over a similar range in Σ_{IR} . At $z \sim 0$, galaxies likely need to undergo a major merger to induce the high gas mass surface densities to reach the high SFR surface densities found in GOALS (Sanders & Mirabel, 1996; Soifer et al., 2000). Indeed, 80% of the major mergers in GOALS have $\log \Sigma_{\text{IR}}/[L_{\odot} \text{ kpc}^{-2}] > 10.7$ (Díaz-Santos et al., 2017). This also pushes the GOALS galaxies into the strongly starbursting regime. At $z \sim 1 - 2$, (U)LIRGs span a range of nearly two orders of magnitude in Σ_{IR} with a similar spread in distance from the main-sequence ~ 0.5 dex as found locally, albeit shifted down. High- z (U)LIRGs can exhibit high and low dust-obscured star-formation rate surface densities for fixed position along the main-sequence. Indeed, Gómez-Guijarro et al. (2022b) even find high star-formation surface density galaxies with high star-formation efficiencies within the main-sequence using 1.1 mm ALMA observations (Gómez-Guijarro et al., 2022a). The comparable star-formation efficiencies (Fig. 4.9 *Left*) and dust properties (Fig. 4.8) show that the star-forming cores of GOALS galaxies are good local analogs to high- z (U)LIRGs in terms of their general star-

formation properties and ISM content despite occupying a fundamentally different region with respect to the main-sequence.

4.5 Conclusion

Using the ALMA archive, we measure IR sizes ($R_{\text{eff},160}$) and dust masses for a sample of 19 galaxies at $z \sim 1 - 2$ with existing *Spitzer*/IRS spectroscopy. We compare these high-redshift galaxies to local luminous IR galaxies in the GOALS survey (Armus et al., 2009) and KINGFISH galaxies at lower star-formation rates (Kennicutt et al., 2011). We combine the size and dust mass measurements with mid-IR spectral features to assess the degree by which changes in IR surface density drive changes in the total ISM content and conditions. Our main conclusions are as follows:

1. The total dust mass scales with $R_{\text{eff},160}$ amongst $z \sim 0 - 2$ (U)LIRGs, consistent with an average gas mass surface density of $\Sigma_{\text{gas}} \sim 1000 M_{\odot} \text{pc}^{-2}$ assuming GDR=100. We find IR sizes that are smaller for fixed dust mass relative to typical star-forming galaxies selected from the simulated galaxies in TNG50, but the simulations do reproduce this parameter space of high IR surface density dusty galaxies.
2. (U)LIRGs at $z \sim 1 - 2$ with higher mid-IR AGN fractions, evidence for stronger dust-obscured AGN, exhibit preferentially smaller far-IR sizes. This is not seen amongst $z \sim 0$ LIRGs when looking at far-IR sizes at wavelengths where the AGN contribution to dust emission is minimal.
3. The PAH/ M_{dust} ratio amongst (U)LIRGs does not evolve with redshift suggesting similar PAH mass fractions today and at cosmic noon. PAHs should not be used as total dust mass tracers for (U)LIRGs given the considerable scatter of ± 0.4 dex about the mean in PAH/ M_{dust} ; however, this scatter is significantly

lower for KINGFISH galaxies at $\log \Sigma_{\text{IR}}/[L_{\odot} \text{ kpc}^{-2}] < 9.5$. PAHs could be used to trace the total dust with higher accuracy in this regime if Σ_{IR} is known.

4. We find an anti-correlation between the PAH/ L_{IR} ratio and Σ_{IR} at $z \sim 1 - 2$ reminiscent of FIR cooling line deficits and down to lower IR surface densities than previously probed. This suggests that changes in ISM conditions regulating the PAH and FIR line emission for $z \sim 0$ galaxies are also likely present in the $z \sim 1 - 2$ LIRG population.
5. (U)LIRGs with higher IR surface densities show larger $L_{\text{IR}}/M_{\text{dust}}$ ratios, emblematic of more efficient star-formation. We find a common trend between Σ_{IR} and the star-formation efficiency spanning five orders of magnitude in Σ_{IR} up to $z \sim 2$ steeper than some previous works. This trend extends linearly from KINGFISH galaxies which have lower L_{IR} and more extended IR sizes.
6. Whereas $z \sim 0$ galaxies at high IR surface density tend to be further above the main-sequence, we find no correlation between Σ_{IR} and the distance above the star-forming main-sequence at $z \sim 1 - 2$. In other words, the extent of star-formation for fixed distance above the main-sequence is more varied at $z \sim 1 - 2$ than what is found locally. This is consistent with previous works finding high star-formation surface densities for $z \sim 2$ dusty galaxies on the star-forming main-sequence.

Despite occupying fundamentally different regimes with respect to the star-forming main-sequence, as well as having different L_{IR} , total dust mass, and IR sizes, the ratios between these quantities in high- and low-redshift (U)LIRGs are similar. Taken together, the results of this analysis paint a picture of dust-obscured galaxy formation in which the star-formation surface density sets the gas and dust conditions. Dusty galaxies with high star-formation rate surface densities exhibit efficient star-formation at all epochs. Dust-obscured star-formation at earlier cosmic times is likely to be a

scaled up version of what is found locally in the star-forming cores of IR-luminous galaxies, albeit sustained over larger areas supported by both increased gas fractions and potentially higher merger rates.

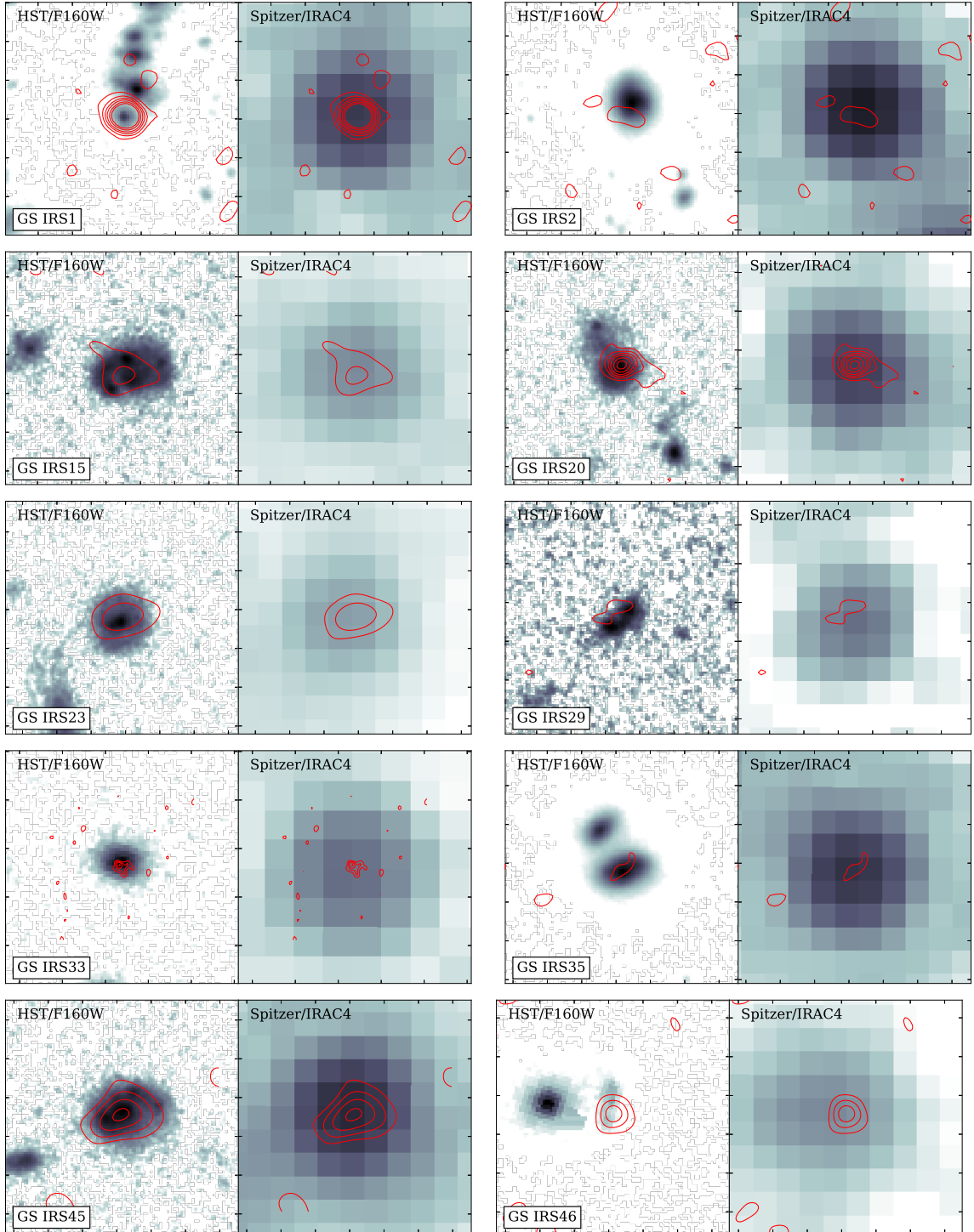


Figure 4.10 ALMA contours (red levels) on *HST*/F160W and *Spitzer*/IRAC4 images for each of the targets in our ALMA-detected catalog. The contours begin at 3σ and increase in steps of 2σ . Tick marks are spaced on each cutout by $1.''0$.

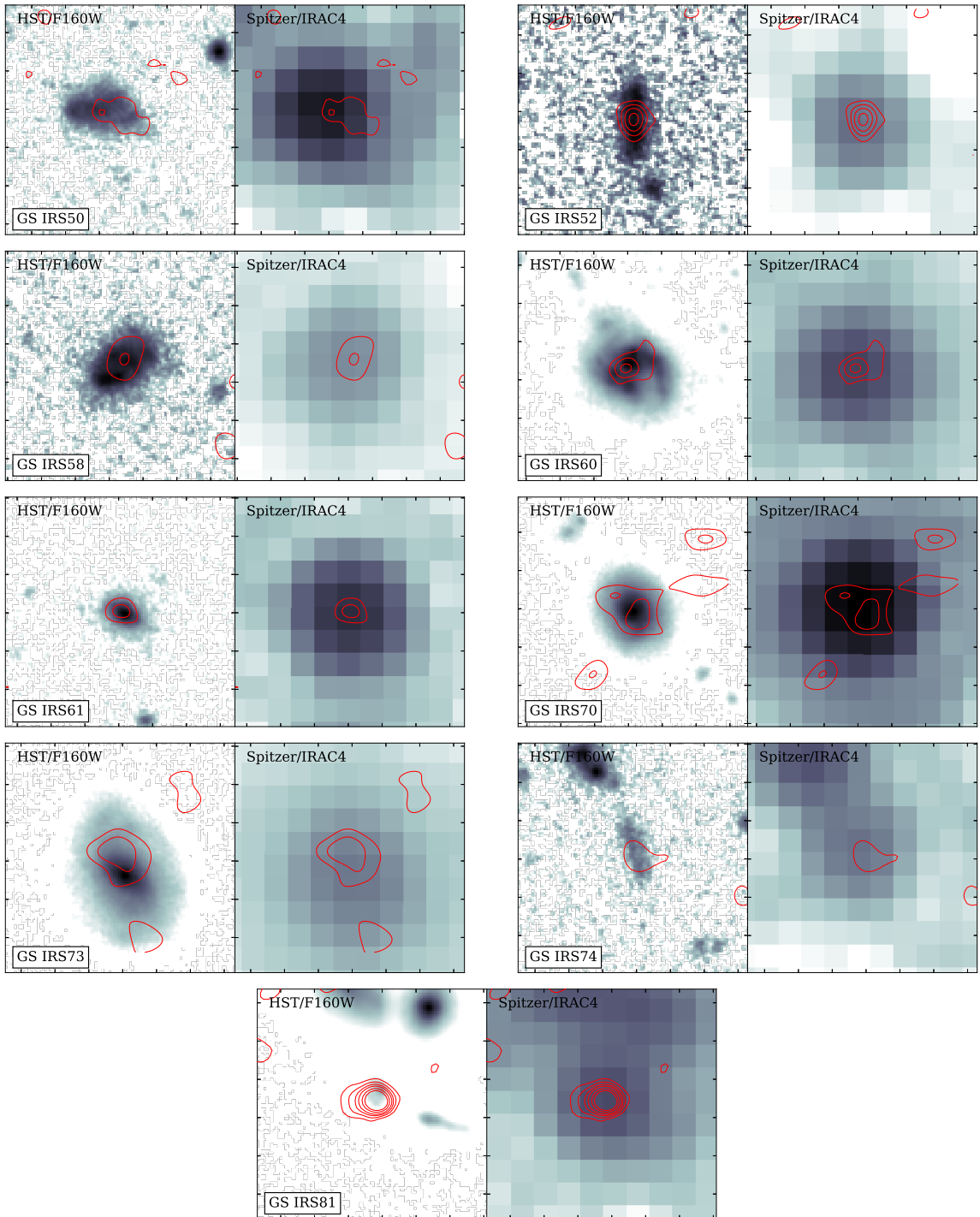


Figure 4.11 Continuation of Fig. 4.10.

CHAPTER 5

PHYSICAL GAS CONDITIONS FROM COMBINED FAR-INFRARED AND RADIO LINES AT $Z=2$

In this chapter, I present the results of a pilot program using the Very Large Array (VLA) to survey the ground state CO(1-0) transition in $z \sim 2$ star-forming galaxies with existing mid-infrared spectra of PAH emission detected by the *Spitzer* Infrared Spectrograph (IRS). Measuring CO(1-0) in galaxies at $z \sim 2$ is difficult given the high phase noise when observing at ~ 40 GHz, which is exacerbated for low-inclination targets like those in the GOODS-S field as the telescopes see more atmosphere. The primary goal of this pilot program was to establish the feasibility of detecting CO(1-0) at $z \sim 2$, and combine the data with PAH and [C II] emission to test the gas and dust conditions. The CO(1-0) transition is an important tracer of the coldest molecular gas, but most observations of CO at high- z measure $J_{upper} > 1$ transitions and correct down to the ground state (Carilli & Walter, 2013). Thus, assessing scaling laws against CO(1-0) rather than higher- J CO lines to measure quantities like molecular gas at high- z is an important test for a commonly used diagnostic. A subset of the galaxies in this program have existing (McKinney et al., 2020) and upcoming observations of far-IR [C II] emission (Cycle 9 PID:2022.1.00101.S, PI: McKinney). Combined detections of CO(1-0), [C II] and the total IR luminosity within the same galaxies collectively constrain the physical gas conditions around sites of recent star-formation. First, I check that all targets detected in CO(1-0) follow canonical scaling relations in the literature between CO and other tracers of gas and star-formation. Then using derived physical properties from photo-dissociation region modeling for

the one $z \sim 2$ galaxy detected in CO and [CII], I infer the gas conditions that give rise to the emergent IR and radio line emission and discuss their implications.

5.1 VLA Data

5.1.1 Description of Observations

We observed seven galaxies between GOODS-N and GOODS-S using the VLA/Q-band over two programs split between 2019 (PI McKinney, Project ID: VLA/19B-254) and 2021 (PI McKinney, Project ID: VLA/21A-036). The baseband configurations for each target across both programs are nearly identical, differing only in their central frequencies chosen to place the redshifted CO(1-0) line in the center of the A/C baseband. The native spectral resolution is $\sim 7 \text{ km s}^{-1}$ using the 8-bit WIDAR correlator with 128 channels, and we later re-bin to coarser sampling to achieve higher signal-to-noise at the cost of spectral resolution for this detection experiment.

For five of the seven targets observed, we obtained the complete number of cycles requested. One galaxy was observed for only half of the requested time, and has been removed from this analysis after inspecting the reduced data, which did not reach a sufficiently constraining sensitivity. The other incomplete observation target, GS IRS61, received five of six 1.5 hour cycles and has been included in this analysis because the final rms is within $\sim 33\%$ of the requested sensitivity. The positions of each target and the quantities derived from IRS spectra are listed in Table 5.1.

5.1.2 Decoherence

Q-band observations with the VLA can suffer from decoherence in the case of poor atmospheric conditions, particularly when high wind speeds introduce significant phase noise. Large phase variations can erase signal even if the final SNR would be sufficient to supposedly detect the source. This is an important effect to rule out when placing upper limits on our sources. As a check against decoherence, we

look at two calibration products in each measurement set: (1) continuum images of our Q-band phase calibrator J0348-2749, and (2) amplitude vs. baseline plots for each scan of the phase calibrator. In all observations, we clearly detect point-source continuum emission in the Q-band from J0348-2749 averaging over all scans. However, if significant phase noise is leading to decoherence on shorter timescales, we expect large amplitude variations over a single scan and particularly on long baselines. We visually inspect the visibilities per scan of the phase calibrator, and report minimal amplitude variations across all measurement sets. We re-imaged a subset of the observations (corresponding to sources with no obvious CO emission) excluding scans with relatively poorer phase noise, and did not find significant improvement in the final sensitivity. Therefore, decoherence is unlikely to wash away signal and upper limits are sufficiently constraining in the case of non-detections.

5.1.3 Reduction, Imaging and Spectral Extraction

We reduced the data using CASA with a modified pipeline calibration optimized for spectral line detection. We disabled Hanning smoothing and masked visibilities containing potential line emission from down-weighting. We next inspected pipeline products for quality, and made iterative adjustments to avoid over flagging data. We imaged the reduced cubes using `tclean` and a robust parameter of 2.0 to minimize the RMS at the cost of spatial resolution, a satisfactory trade-off for this detection experiment in which we did not aim to spatially resolve the CO(1-0) emission. During imaging, we re-bin the data from its native resolution to a resolution of $150 - 300 \text{ km s}^{-1}$ per spectral channel.

Figure 5.1 shows integrated intensity (moment 0) maps for GN IRS18, GN IRS25, and GS IRS20 collapsed around channels exhibiting CO(1-0) line emission in the data cubes. For sources with strong CO(1-0) signal, we find co-incident HST/WFC3 H_{160} detections of the galaxy. In the case of GN IRS18 and GN IRS25, the CO(1-0)

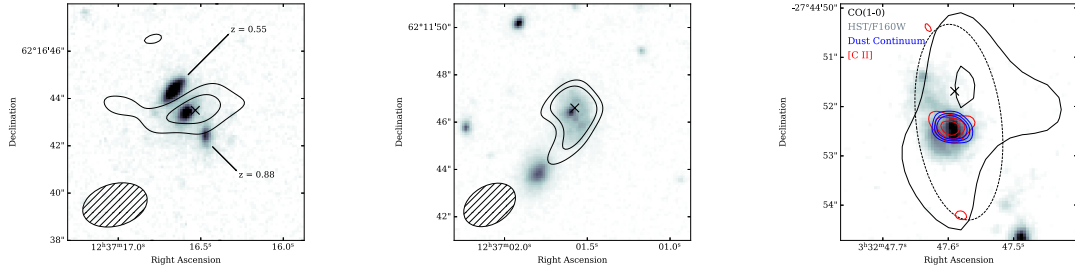


Figure 5.1 Collapsed CO(1-0) channel maps in GN IRS18 (*left*), GN IRS25 (*center*), and GS IRS20 (*right*) represented as black contours overlaid over *HST*/WFC3 H_{160} images from 3D-HST (Skelton et al., 2014; Grogin et al., 2011; Koekemoer et al., 2011). For the GOODS-N targets (*left*, *center*), we show $[3\sigma, 4\sigma]$ contours. For GS IRS20 whose CO(1-0) emission is detected at lower SNR, we show $[2\sigma, 3\sigma]$ contours as well as $[3\sigma, 5\sigma, 7\sigma]$ contours for the [C II] and dust continuum emission reported in McKinney et al. (2020). Black \times symbols on all images indicate the location of peak CO(1-0) emission. For GN IRS18 we label the low-redshift targets in the map by their redshifts derived from *HST*/grism (Brammer et al., 2012; Momcheva et al., 2016).

emission is marginally more extended than the beam, and we extract spectra to fully encase the extended components seen in the collapsed channel maps of Fig. 5.1. GN IRS18 is adjacent to two possible counterparts; however, these have been spectroscopically confirmed to lie at $z = 0.55$ and $z = 0.88$ using *HST*/grism (Brammer et al., 2012; Momcheva et al., 2016).

GS IRS20 is detected in the moment 0 map at lower signal-to-noise, and the $\sim 3\sigma$ signal is smaller than the beam; therefore, we extract GS IRS20’s spectrum through an aperture the size of the primary beam and centered on the CO(1-0) peak. As shown in the right-most panel of Fig. 5.1, GS IRS20’s integrated CO(1-0) emission is qualitatively consistent with the [C II] and dust continuum detected by ALMA at $\sim 0.''5$ resolution (McKinney et al., 2020); however, higher spatial resolution follow-up is necessary to localize the CO more accurately. Nevertheless, while the low SNR of GS IRS20’s CO(1-0) map ($\sim 3\sigma$) coupled with the large VLA/Q-band beam ($\sim 4'' \times 2''$) limit our ability to compare centroids, the CO(1-0) peak is aligned with the [C II] and dust continuum centroids along the beam’s major axis.

Table 5.1. IRS Sample and derived quantities from Spitzer spectra

Target	RA [J2000]	DEC [J2000]	$z_{\text{IRS}}^{\text{a}}$	$f_{\text{AGN,MIR}}^{\text{b}}$	$\log L_{6.2\mu\text{m}}$ [L_{\odot}]	$\log L_{11.3\mu\text{m}}$ [L_{\odot}]
GN IRS18	12:37:16.59	62:16:43.0	1.82	0.3	10.23 ± 0.07	9.93 ± 0.11
GN IRS25	12:37:01.59	62:11:46.0	1.72	0.0	10.28 ± 0.10	10.02 ± 0.12
GS IRS20	03:32:47.58	-27:44:52.0	1.93	0.2	9.99 ± 0.12	10.11 ± 0.10
GS IRS45	03:32:17.48	-27:50:01.4	1.63	0.0	10.27 ± 0.05	9.98 ± 0.06
GS IRS54	03:32:13.85	-27:43:12.0	1.89	0.4	9.91 ± 0.14	10.11 ± 0.08
GS IRS61	03:32:43.45	-27:49:01.0	1.76	0.1	10.18 ± 0.05	9.84 ± 0.05

^a Redshifts derived from Spitzer-detected PAHs have intrinsic uncertainties on the order of ± 0.02 owing to the spectral resolution.

^b $f_{\text{AGN,MIR}}$ is the integral of power-law continuum attributed to warm AGN-heated dust in the mid-IR divided by the total mid-IR flux in the IRS spectrum (Pope et al., 2008; Kirkpatrick et al., 2012). From the Spitzer spectra, $f_{\text{AGN,MIR}}$ can be measured to an accuracy of ± 0.1 .

4pt 4pt

5.1.4 Spectral Line Detections

We detect the CO(1-0) $\nu_{\text{rest}} = 115.2712$ GHz line at a peak (integrated) $\text{SNR} > 5$ ($\text{SNR} > 10$) in GN IRS18, GN IRS25, and GS IRS20. These spectra are shown in Figure 5.2 (both GN targets) and Figure 5.3 (GS IRS20). Notably, each line is found within 1σ of the expected redshifted frequency given all redshift priors. We fit each line with a Gaussian profile which we use to measure the FWHM and CO-derived redshifts. In the case of GS IRS20, the CO and [CII] redshift agree within $\Delta z/z = 4 \times 10^{-4}$ and the widths of each line are consistent around 300 km s^{-1} . For the GOODS-N targets, CO and PAH derived redshifts agree within $\Delta z/z \sim 10^{-3}$. We integrate below the spectrum over $1.5\times$ the FWHM (shaded regions in Fig. 5.2) to derive fluxes which we convert to the CO luminosities listed in Table 5.2.

For the galaxies without clear detections in their extracted spectra, we first jitter the aperture around the expected source coordinates by up to $1.''0$ searching for line

Table 5.2. Observations and CO measurements

Target	ν_{eff} [GHz]	Beam FWHM [arcsec]	$\text{rms}_{300 \text{ km/s}}$ [μJy]	$S_{\text{CO}(1-0)}\Delta v$ [mJy km s $^{-1}$]	FWHM [km s $^{-1}$]	$\log L_{\text{CO}(1-0)}$ [L_{\odot}]	$\log L'_{\text{CO}(1-0)}$ [K km s $^{-1}$ pc 2]
GN IRS18	41.45	2.8×1.8	82	176.9	1228	6.52	10.83
GN IRS25	42.83	2.3×1.6	113	173.8	681	6.53	10.84
GS IRS20	39.43	4.0×1.7	71	120.0	301	6.03	10.34
GS IRS45	43.47	1.2×0.57	142	< 362	...	< 6.3	< 10.7
GS IRS54	40.46	1.2×0.56	120	< 306	...	< 6.4	< 10.7
GS IRS61	41.26	1.47×0.62	83	< 211	...	< 6.2	< 10.5

emission above the noise. We also re-bin to coarser spectral resolution. No significant emission is detected in these observations. Thus, we set 3σ upper limits on the line flux from the rms properties of the cube which we use to place upper limits on the CO luminosity. Spectra extracted for the non-detections are shown in Figure 5.4 and all 3σ upper limits are included in Table 5.2.

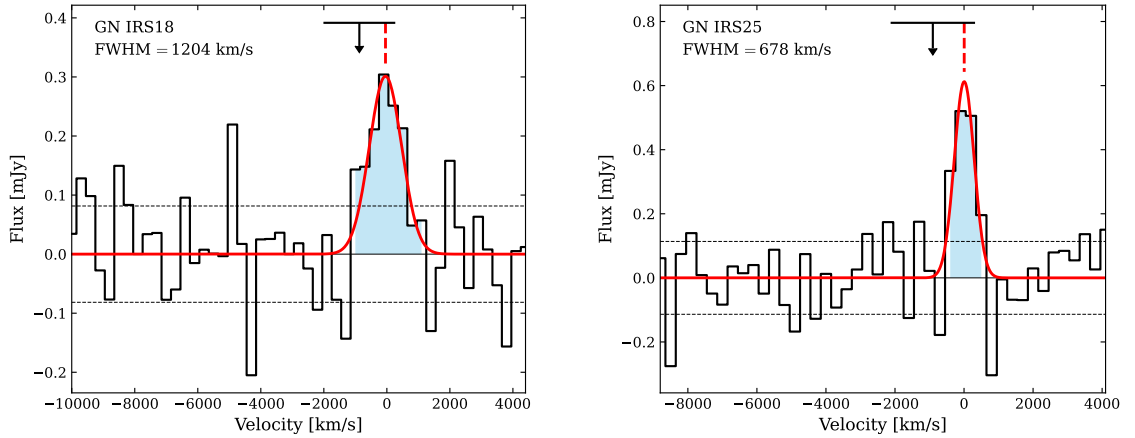


Figure 5.2 VLA/Q-band detections of CO(1-0) in GN IRS18 (*Left*) and GN IRS25 (*Right*). The data has been binned to a velocity resolution of 300 km s^{-1} . Gaussian fits to the data are shown in red. The black arrows along the top indicate where the CO line was expected given the PAH-derived redshift and its $\pm 1\sigma$ uncertainty. Vertical dashed red lines are the CO(1-0) line centers from the Gaussian fits. Horizontal dashed black lines show $\pm 1\sigma$ spectral noise. The gap in the GN IRS18 spectrum is due to noisy edge channels masked during the data reduction phase.

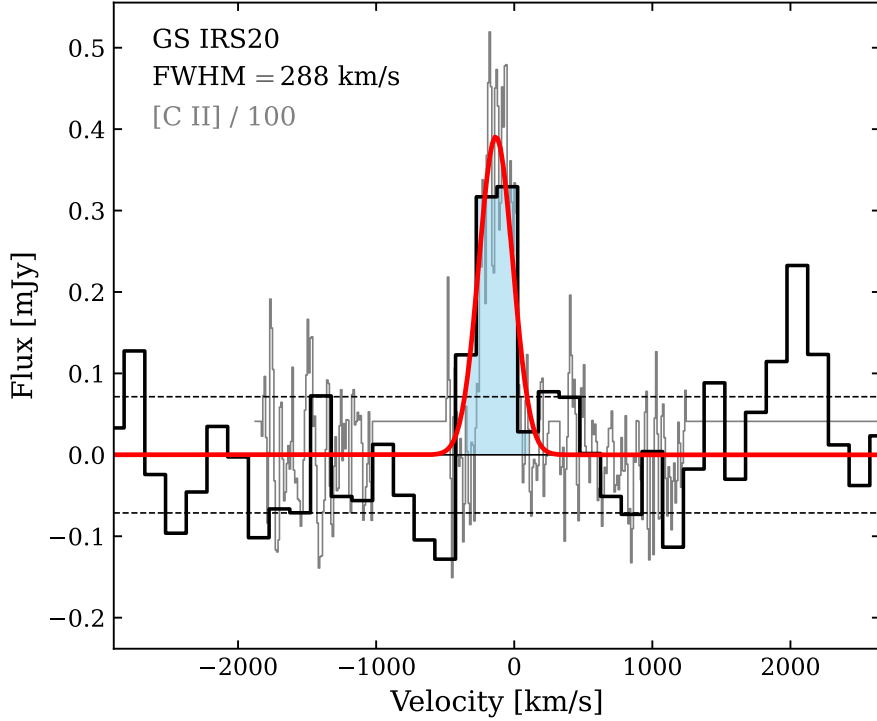


Figure 5.3 CO(1-0) in GS IRS20 (black), with a gaussian fit shown in red. The redshifted [C II] detection from ALMA is over-plotted in grey, scaled down by a factor of 100 (McKinney et al., 2020).

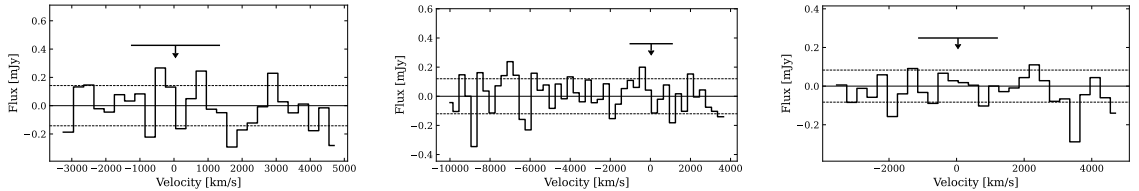


Figure 5.4 CO(1-0) upper limits for GS IRS45 (*Left*), GS IRS 54 (*Middle*), and GS IRS 61 (*Right*). The reference frequency used to set each velocity axis comes from the peak of the redshift posterior distribution when fitting the PAH features. Black arrows show the 3σ flux level adopted as upper limits, and have x -axis errors covering the redshift $\pm 1\sigma$ uncertainties.

5.2 Results

5.2.1 Scaling between CO, PAH, and IR luminosity

We detect CO(1-0) at $z \sim 2$ in three dusty galaxies, and place upper limits on a further three systems. The galaxies in our sample are IR-luminous and star-forming, and exhibit minimal contributions from active galactic nuclei to their mid-IR *Spitzer*/IRS

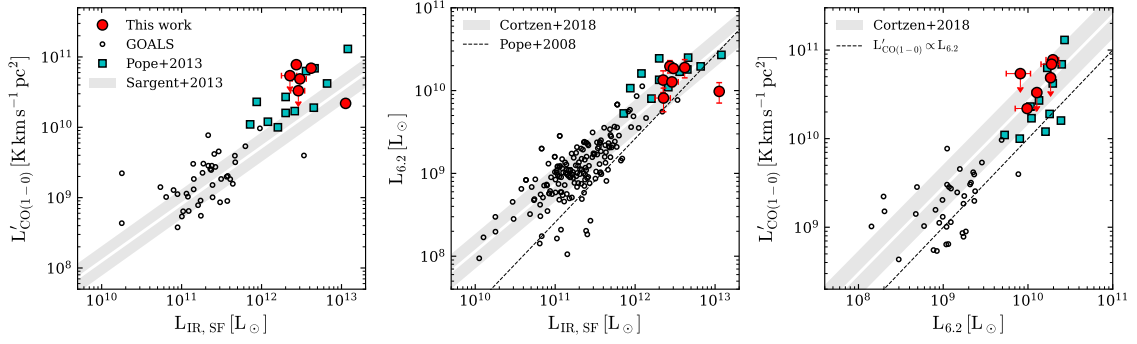


Figure 5.5 Scaling relations between tracers of dust-obscured star-formation and molecular gas. (*Left*) CO(1-0) luminosity vs. L_{IR} (corrected for AGN contribution) in $z \sim 0 - 3$ (U)LIRGs. We compare against prior works at $z > 0.5$ (Pope et al., 2008), and local calibrations from GOALS (Yamashita et al., 2017) and Sargent et al. (2013). (*Middle*) $L_{6.2\mu\text{m}}$ vs. L_{IR} in GOALS and $z \sim 1 - 3$ (U)LIRGs. Our data is shown for reference in red against prior studies. (*Right*): Scaling between $L_{6.2\mu\text{m}}$ and CO. We show for comparison previous calibrations of PAH emission as a molecular gas tracer in grey from Cortzen et al. (2019). The dashed black line shows the 1-1 relation.

spectra (Kirkpatrick et al., 2015). We compare these observations to CO observations of local star-forming LIRGs in GOALS (Yamashita et al., 2017), $z \sim 0.03 - 0.3$ galaxies in 5MUSES (Cortzen et al., 2019), and high- z IRS galaxies from Pope et al. (2008, 2013). To avoid uncertainties from higher $J/1-0$ line intensity corrections, and leveraging the VLA’s lower frequency coverage, we focus on comparison samples with CO(1-0) detections where possible.

Figure 5.5 shows scaling relations between CO(1-0) emission, IR luminosities¹, and PAH emission. In general, the CO(1-0) luminosities we derive from detections and upper limits are consistent with prior calibrations against L_{IR} and PAHs. This is an important result to highlight and speaks to the future success of high-frequency VLA observations targeting CO(1-0) in further $z = 2$ galaxies.

¹We multiply IR luminosities by $(1-f_{\text{AGN,IR}})$ to correct for the contribution of AGN to the integrated dust emission. We use Eq. 5 in Kirkpatrick et al. (2015) to derive $f_{\text{AGN,IR}}$ from $f_{\text{AGN,MIR}}$ as measured from the mid-IR *Spitzer*/IRS spectra (Pope et al., 2008).

5.2.2 Photo-dissociation Region Modeling

Since early far-IR observations of cold clouds, a number of numerical codes have been developed to predict atomic and molecular line emission emerging from a 1-dimensional slab as a function of its gas density, temperature, and radiation field strength (e.g., Glassgold & Langer, 1975; Tielens & Hollenbach, 1985b; Kaufman et al., 1999, 2006; Pound & Wolfire, 2008). These have been used to interpret the far-IR line emission of galaxies near and far (Díaz-Santos et al., 2017; Rybak et al., 2019), and provide key insight into gas conditions. For instance, Díaz-Santos et al. (2017) demonstrate using GOALS galaxies that above a critical IR surface density the ratio of the radiation field strength impinging upon gas (G) to the density (n) scales linearly with Σ_{IR} . Thus, at high star-formation rate surface densities the ISM is exposed to on-average stronger radiation fields that change the fractional strength of key cooling lines (Díaz-Santos et al., 2017) as well as the photoelectric heating of gas (McKinney et al., 2021a). To test if such conditions also manifest in $z \sim 2$ Galaxies, I use the Photo-Dissociation Region Toolbox (PDRT) code from Pound & Wolfire (2008) to measure G and n in GS IRS20, the one galaxy in this pilot sample detected in [C II] and CO(1-0).

Figure 5.6 shows the radiation fields and gas densities allowed by GS IRS20's [C II]/ L_{IR} and [C II]/CO(1-0) ratios under the PDRT models. PDRT irradiates a 1-dimensional slab of gas using a scaled radiation field normalized initially to the local Galactic value ($G_0 \equiv 1.6 \times 10^{-3} \text{ erg s}^{-1} \text{ cm}^2$, Habing 1968). To best compare against local LIRGs, we adopt the same assumptions and model sets used to derive G and n in GOALS galaxies (Díaz-Santos et al., 2017). We assume that 80% of the [C II] emission in GS IRS20 arises from the neutral phase based on the relation between the [C II] neutral fraction and star-formation rate surface density from Croxall et al. (2017). This is a conservative lower limit, and the final derived parameters do not change if we vary the [C II] fraction between 50%-100%.

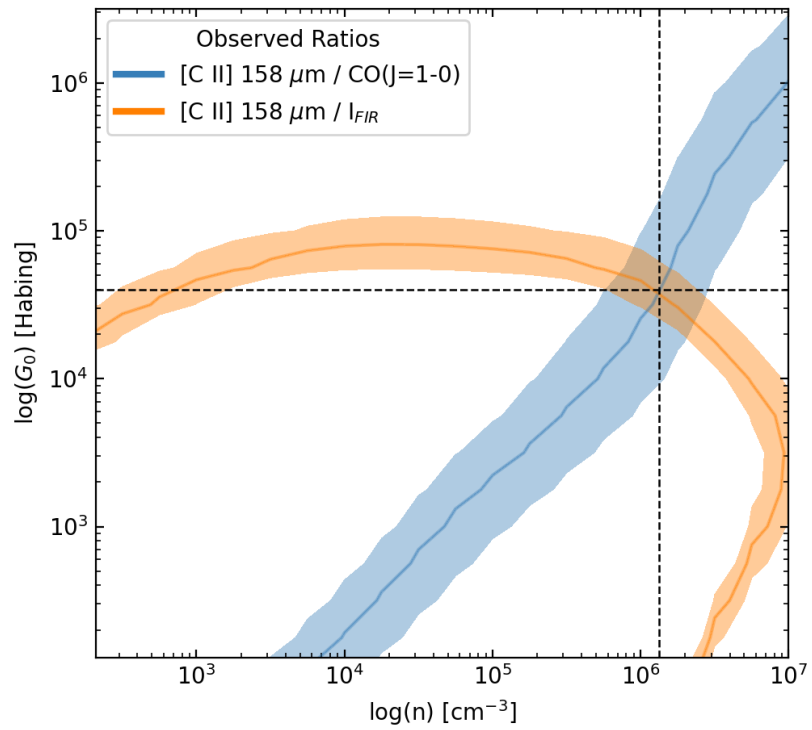


Figure 5.6 Radiation field strength (G_0) and hydrogen density (n_H) determined from PDR modeling using PDR ToolKit for GS IRS20. The best-fit solution favors extremely dense PDRs exposed to a strong radiation field.

GS IRS20 has a strong radiation field of $G/G_0 = 3.97 \times 10^4 \pm 1.9 \times 10^4$ and a very high density of $n/[\text{cm}^{-3}] = 1.34 \times 10^6 \pm 1 \times 10^6$. As shown in Figure 5.7, the radiation field strength we find is close to the maximum value found for GOALS, while GS IRS20’s density is nearly two orders of magnitude greater than any GOALS galaxy or local star-forming galaxy (Díaz-Santos et al., 2017; Malhotra et al., 2001). Only some sub-millimeter galaxies reach the density found for GS IRS20 (Cox et al., 2011; Danielson et al., 2011; Valtchanov et al., 2011; Alaghband-Zadeh et al., 2013; Huynh et al., 2014; Rawle et al., 2014; Bothwell et al., 2017; Cañameras et al., 2018). Such unusual conditions can be found in the nuclei of nearby star-forming galaxies as well as galactic PDRs around O and B stars (Stacey et al., 1991)². Since the [CII] and CO(1-0) luminosity is galaxy-integrated, these results suggests that the average gas conditions resemble either extreme OB PDRs or galactic nuclei.

5.3 Unusual ISM conditions in GS IRS20

There are three possible interpretations for where GS IRS20 falls relative to local and high- z star-forming galaxies and galactic star-forming regions on Figure 5.7. (1) The model results are not applicable because some amount of flux from either or both of [CII] and CO(1-0) has been missed, or the lines do not trace the same structures in the galaxy. (2) The model results are not applicable because the gas in GS IRS20 is on-average X-ray dominated, which changes its chemistry and excitation (Meijerink et al., 2007). This could arise if GS IRS20 hosts a stronger buried AGN than previously thought. (3) The PDRT best-fit conditions accurately reflect the galaxy-averaged conditions in GS IRS20, which are extreme relative to previous results in the literature. In this section, I consider these three possible scenarios.

²The analysis in Stacey et al. (1991) to derive G and n was made using [CII] and CO(1-0) line emission as was done for GS IRS20

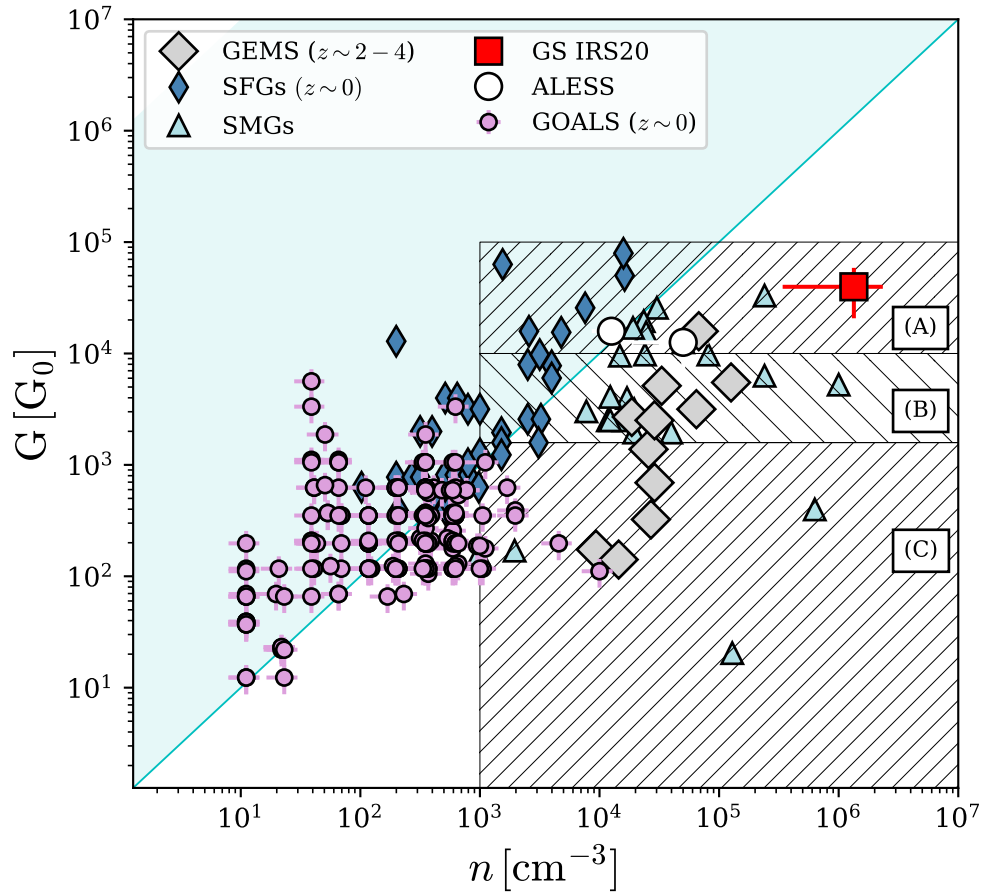


Figure 5.7 A collection of radiation field strengths (G/G_0) and densities in PDRs ($n/[\text{cm}^{-3}]$) for galaxies in the literature compared against GS IRS20 (red square). We compare against GOALS (Díaz-Santos et al., 2017), local star-forming galaxies (SFGs, Malhotra et al. 2001), and high- z sub-millimeter galaxies (SMGs, Cox et al. 2011; Danielson et al. 2011; Valtchanov et al. 2011; Alaghband-Zadeh et al. 2013; Huynh et al. 2014; Rawle et al. 2014; Bothwell et al. 2017; Cañameras et al. 2018; Rybak et al. 2019). The hatched regions depict the parameter space occupied by (A) local galactic nuclei and OB PDRs, (B) local starbursts, and (C) spiral galaxies and galactic molecular clouds, as determined by Stacey et al. (1991) and following Cañameras et al. (2018). The shaded blue region indicates $G/n_0 > 1 \text{ G}_0 \text{ cm}^3$, where this ratio scales linearly with the IR surface density (Díaz-Santos et al., 2017). The inferred radiation field and density in GS IRS20 are both particularly extreme relative to nearby and $z \sim 2 - 4$ star-forming galaxies.

5.3.1 Empirical challenges to PDR modeling

The [C II]/CO(1-0) ratio scales approximately linearly with the G/n ratio, but provides good constraint on the density over the narrow range in radiation intensities that the [C II]/IR ratio is confined to (Figure 5.6). Therefore, the best-fit modeled densities could be wrong if a significant amount of flux from either line were resolved out by ALMA or the VLA. This is not a concern for the VLA data of CO(1-0), as Fig. 5.1 clearly shows that the emission is unresolved on scales smaller than the synthesized beam. While the [C II] emission is marginally more extended than the $\sim 0.5''$ beam (McKinney et al., 2020), the data were taken in ALMA configuration C43-1 with a maximum recoverable scale of $4.4''$ at 650 GHz. We expect to detect all [C II] emission in GS IRS20 on scales below ~ 36.5 kpc which is more than 20 times the effective radius derived from the dust continuum. Therefore, we are likely not resolving out either [C II] or CO(1-0) flux in our interferometer measurements.

A major limitation to this study is the fact that the line diagnostics average over the $\sim 13 \text{ kpc}^2$ spatial extent of the galaxy. If the CO(1-0) emission is confined to a smaller area than the [C II], then the combined line ratios may not accurately describe co-spatial regions in the galaxy. This would lead to an over-predicted [C II]/CO ratio, which would consequently over predict the density yielding artificially high values. If the [C II] and CO emitting areas differ by a factor of 5, GS IRS20's density from the PDRT modeling would fall to $\sim 10^3 \text{ cm}^{-3}$, within the regime expected if GS IRS20's low [C II]/PAH arises from inefficient photoelectric heating as discussed in Chapter 3. While further observations of galaxy-integrated line intensities will help establish if the properties of GS IRS20 are more common place amongst $z = 2$ (U)LIRGs, spatially resolved analyses will be key for measuring accurate physical quantities. This will have to be done on scales $\sim 0.75 - 1$ kpc where the added time to resolve the source is not prohibitive. For example, ALMA's Band 9 receiver can achieve a maximum spatial resolution of 75 pc in the C-9 configuration; however, this would require > 100

hours of time on-source to reach the required surface brightness for a $> 5\sigma$ detection of [C II] in a $z = 2$ ULIRG. Another possibility is to use gravitationally lensed galaxies to achieve higher SNR detections of lines like [C II] at $z \sim 2$ (e.g., Cañameras et al., 2018). With the launch of *JWST*, it will also be possible to measure mid-IR spectra of PAHs in such sources - the capabilities for which have been absent since the end of *Spitzer*'s cryogenic mission.

5.3.2 Alternate heating sources in GS IRS20: X-ray dominated regions

PDRs are characterized by strong far-ultraviolet heating of gas and dust; however, the gas heating and chemistry structure can also be strongly influenced by X-ray radiation (Maloney et al., 1996). So called X-ray dominated regions (XDRs) can appear around supermassive black holes (Krolik & Lepp, 1989; Meijerink et al., 2007), or other astrophysical phenomenon such as X-ray binaries (e.g., Lebouteiller et al., 2017). Given GS IRS20's moderate mid-IR AGN fraction of $\sim 20\%$, evidence for at least some nuclear activity, I now discuss both the likelihood of this galaxy hosting a strong AGN, and what that would imply for its gas conditions.

X-ray photons arising from the accretion disk around a supermassive black hole represent one of the most reliable method for identifying strong AGN, but are not well suited for identifying weak to intermediate AGN obscured by dust (Hickox & Alexander, 2018). GS IRS20 does not have an X-ray counterpart in the deep X-ray coverage of GOODS-S (Brightman et al., 2014; Kirkpatrick et al., 2015); however, the dust continuum emission is exceptionally compact which supports the presence of a deeply obscured nuclear object. Indeed, the high radiation field strength inferred by the PDRT models could reflect to some degree a powerful ionizing source like an AGN instead of pure stellar heating.

There are a number of qualitative differences between PDRs and XDRs that could lead to different emergent line intensities from the gas in GS IRS20. XDRs have

higher line-to-total dust emission ratios as X-ray photons deposit energy directly into the gas. They also have lower $[\text{C II}]/[\text{O I}]$ ratios as more power gets channeled through higher critical density lines, as well as greater high- J CO line fluxes powered by X-rays maintaining hot temperatures deeper within clouds compared to PDRs (Meijerink et al., 2007; Wolfire et al., 2022). One way to test for XDRs securely would be to measure $[\text{O I}]$ $63 \mu\text{m}$ emission in GS IRS20, as XDRs are characterized by high $[\text{O I}]/[\text{C II}]$ ratios > 10 (Maloney et al., 1996). Unfortunately, $[\text{O I}]$ is currently inaccessible for $z < 5$ galaxies given the current capabilities of IR telescopes. In the meantime, *JWST* observations of GS IRS20 could quantify the AGN contribution in more detail by using spectral decomposition methods on higher SNR mid-IR spectra (Sajina et al., 2007; Pope et al., 2008), or by measuring high-ionization emission lines like $[\text{O IV}]$ and $[\text{Ne V}]$ that trace the AGN (Petric et al., 2011; Inami et al., 2013). Evidence for significant reservoirs of XDR gas in GS IRS20 would have implications for the co-evolution of AGN and stars within galaxies. This would support radiative feedback as a significant quenching mechanism regulating star-formation if X-ray photons of AGN-origin are capable of changing the conditions of star-forming gas across the host-galaxy. I explore the influence of AGN on their host-galaxies star-forming gas in the next Chapter using numerical simulations.

5.3.3 Extreme densities in GS IRS20

GS IRS20 has a low $[\text{C II}]/\text{PAH}$ ratio which for GOALS galaxies is exclusively found when $G/n > 1 G_0 \text{ cm}^3$ (Díaz-Santos et al., 2017; McKinney et al., 2021a). If the low photoelectric heating efficiency scenario outlined in Chapter 3 were the cause of GS IRS20's low $[\text{C II}]/\text{PAH}$ ratio reported in Chapter 2, then the expectation for this galaxy would be a high G/n ratio. Instead, the PDR models favor $\log G/n [G_0 \text{ cm}^3] < -1$ driven predominantly by the large inferred PDR gas density $> 10^6 \text{ cm}^{-3}$. In this high density regime, the $[\text{C II}]$ line is saturated (Goldsmith et al., 2012). This would

be a simple explanation for its low [C II] relative to both L_{IR} and PHAs, consistent with the argument put forth by Muñoz & Oh (2016) and favored by Rybak et al. (2019) in support of thermal saturation as the origin of the [C II] deficit at high L_{IR} and Σ_{IR} . Further observations of [C II], PAHs, and CO(1-0) at $z \sim 2$ are required to statistically test this scenario.

5.4 Conclusions

In this Chapter I report on the CO(1-0) line detections and upper limits derived from a pilot VLA program to measure cold gas diagnostics in *Spitzer*/IRS galaxies. The main results are as follows:

1. I detect CO(1-0) emission in three galaxies, and derive constraining upper limits for a further three. The inferred CO(1-0) luminosities are consistent with scaling relations between CO, PAH emission, and L_{IR} reported in the literature.
2. Using PDR models we measure the average radiation field strength and density in GS IRS20, which are both unusually high relative to values reported for low- and high-redshift dusty galaxies in the literature.
3. The high gas density in GS IRS20 favors scenarios in which its low [C II] emission is the product of line saturation. This mechanism does not require changes in the photoelectric heating efficiency to yield low [C II]/PAH ratios, but requires higher spatial resolution observations of the CO emission to confirm in this one galaxy.

This study demonstrates the feasibility of targeted VLA/Q-band observations of CO(1-0) in $z \sim 2$ galaxies, at the peak epoch for galaxy formation where the molecular gas is more commonly measured using $J_{\text{upper}} > 1$ CO transitions. Future observations following up ALMA and *JWST* sources can be used to gain insight into the physical gas conditions in high-redshift star-forming galaxies.

CHAPTER 6

DUST-ENSHROUDED AGN CAN DOMINATE HOST-GALAXY-SCALE COLD-DUST EMISSION

*This chapter is adapted from McKinney et al. (2021b) originally published in the *Astrophysical Journal*.*

It is widely assumed that long-wavelength infrared (IR) emission from cold dust ($T \sim 20 - 40$ K) is a reliable tracer of star formation even in the presence of a bright active galactic nucleus (AGN). Based on radiative transfer (RT) models of clumpy AGN tori, hot dust emission from the torus contributes negligibly to the galaxy spectral energy distribution (SED) at $\lambda > 60 \mu\text{m}$. However, these models do not include AGN heating of host-galaxy-scale diffuse dust, which may have far-IR (FIR) colors comparable to cold diffuse dust heated by stars. To quantify the contribution of AGN heating to host-galaxy-scale cold dust emission, we perform dust RT calculations on a simulated galaxy merger both including and excluding the bright AGN that it hosts. By differencing the SEDs yielded by RT calculations with and without AGN that are otherwise identical, we quantify the FIR cold dust emission arising solely from re-processed AGN photons. In extreme cases, AGN-heated host-galaxy-scale dust can increase galaxy-integrated FIR flux densities by factors of 2-4; star formation rates calculated from the FIR luminosity assuming no AGN contribution can overestimate the true value by comparable factors. Because the FIR colors of such systems are similar to those of purely star-forming galaxies and redder than torus models, broadband SED decomposition may be insufficient for disentangling the contributions of stars and heavily dust-enshrouded AGN in the most

IR-luminous galaxies. We demonstrate how kpc-scale resolved observations can be used to identify deeply dust-enshrouded AGN with cool FIR colors when spectroscopic and/or X-ray detection methods are unavailable.

6.1 Introduction

Most of the stellar mass in galaxies was assembled between a redshift of $z = 3$ to 1 (e.g., Carilli & Walter 2013; Madau & Dickinson 2014); at $z = 2$, the star-formation rate density (SFRD) of the Universe peaked, fueled by enhanced gas accretion from the intergalactic medium (Kereš et al., 2005, 2009; Genzel et al., 2008; Tacconi et al., 2010). Statistical X-ray and infrared (IR) observations of galaxies hosting active galactic nuclei (AGN) support the coincident mass growth of central supermassive black holes (SMBHs; Shankar et al. 2009; Aird et al. 2010; Delvecchio et al. 2014) and possibly SMBH-galaxy co-evolution (e.g., Ferrarese & Merritt 2000; Gebhardt et al. 2000; Kormendy & Ho 2013; Madau & Dickinson 2014). In particular, AGN feedback may be responsible for quenching star formation (e.g., Springel, 2005; Cicone et al., 2014) or/and maintaining quenched galaxies by suppressing cooling flows (e.g., Kereš et al., 2005; Croton et al., 2006; Bower et al., 2006). AGN feedback helps cosmological theories of galaxy evolution match observations – in particular, the number counts of massive and quenched galaxies at $z = 0$ (e.g., Bower et al. 2006; Nelson et al. 2018).

Testing this framework against observations, particularly at high redshift, is limited by the ability to separate the AGN and star-forming components of the spectral energy distributions (SEDs) of galaxies, as to test the ‘quasar mode’ of AGN feedback, it is necessary to simultaneously constrain the AGN luminosity and star formation rate (SFR) at a time when the AGN should be heavily dust-enshrouded (e.g., Di Matteo et al., 2005; Hopkins et al., 2008). The far-IR (FIR)/sub-millimeter regime is thus a powerful probe of dust-obscured mass assembly. It has long been known that dust-enshrouded AGN can dominate the total IR luminosity (e.g., Sanders et al.,

1988a), but it is typically assumed that AGN contribute negligibly to FIR emission at wavelengths longer than rest-frame $100\ \mu\text{m}$, as predicted by torus models (e.g., Fritz et al., 2006; Nenkova et al., 2008a,b). Consequently, cold dust emission is sometimes treated as a ‘safe’ SFR tracer even when an AGN dominates the bolometric luminosity of the galaxy by explicitly converting the FIR luminosity into an SFR value (e.g., Hatziminaoglou et al., 2010; Kalfountzou et al., 2014; Azadi et al., 2015; Gürkan et al., 2015; Stacey et al., 2018; Banerji et al., 2018; Wethers et al., 2020).

Alternatively, the full SED may be fit using an SED modeling code that includes an AGN component (e.g., Ciesla et al., 2015; Chang et al., 2017; Lanzuisi et al., 2017; Dietrich et al., 2018; Leja et al., 2018; Pouliaxis et al., 2020; Ramos Padilla et al., 2020; Yang et al., 2020). Such SED modeling codes generally assume that AGN contribute negligibly to cold-dust emission longward of $\sim 100\ \mu\text{m}$, and rely on SED model libraries generated by performing RT on AGN torus models. The resulting SEDs include hot dust emission from the torus *but not potential AGN-powered cold dust emission on host-galaxy scales by construction*, even though UV/optical photons emitted by the accretion disk or IR photons from the torus can in principle heat ISM dust directly and/or by progressive attenuation and re-radiation at longer wavelengths. That this possibility is realized in some systems is suggested by results indicating that the host galaxy can be responsible for a non-negligible fraction of the ionizing column density in some AGN (Hickox & Alexander 2018 and references therein). The origin of the far-IR emission in galaxies hosting luminous AGN has been debated over the past few decades (e.g., Downes & Solomon 1998; Page et al. 2001; Franceschini et al. 2003; Ruiz et al. 2007; Kirkpatrick et al. 2012, 2015). Over the years, a growing body of literature has been making the case for AGN-powered FIR emission in QSOs (e.g., Sanders et al., 1989; Yun & Scoville, 1998; Nandra & Iwasawa, 2007; Petric et al., 2015; Schneider et al., 2015; Symeonidis et al., 2016; Symeonidis, 2017;

Symeonidis & Page, 2018)); however, other works find conflicting results (e.g., Stanley et al. 2017; Shangguan et al. 2020; DiMascia et al. 2021).

A promising method for decomposing the far-IR SEDs into AGN and SF components directly relies on mid-IR spectroscopy (e.g., Pope et al. 2008). Kirkpatrick et al. (2012, 2015) use this technique to subtract AGN-heated dust from the SEDs of a sample of high- z dusty galaxies using mid-IR spectroscopic methods assuming all of the $\sim 80 - 90$ K dust emission is attributed to the AGN alone. These authors find that up to 75% of L_{IR} can be powered by AGN heating of the hot dust in galaxies with spectroscopic signatures of AGN in the mid-IR. Whether this conclusion extends to host-galaxy-scale cold dust emission at wavelengths past $100 \mu\text{m}$ is difficult to test empirically because of sparse wavelength coverage in the rest-frame far-IR/sub-mm and because dust re-processing erases information about the original energy source. Roebuck et al. (2016) applied Kirkpatrick et al.'s method to attempt to recover the AGN fraction of simulated galaxies, including the one employed in this work. Although the recovered and true AGN fractions were in qualitative agreement, Roebuck et al. (2016) found that SED decomposition underestimated the AGN contribution to the IR luminosity in some cases.

In this work, we build on previous work in which we used hydrodynamical simulations plus radiative transfer (RT) calculations to investigate the effects of galaxy-scale dust reprocessing of AGN torus emission (Younger et al., 2009; Snyder et al., 2013; Roebuck et al., 2016). Specifically, we use a hydrodynamical simulation of an equal-mass galaxy merger post-processed with RT to investigate the possibility that heating from a luminous AGN embedded within a dusty galaxy can power host-galaxy-scale cold dust emission at rest-frame wavelengths $\lambda > 100 \mu\text{m}$. We create initial conditions for two identical galaxies on a parabolic orbit. The hydrodynamical simulation evolves the system, including models for star formation, stellar feedback, black hole accretion and AGN feedback. Then, we perform dust RT calculations in post-processing for

various time snapshots to compute spatially resolved UV-mm SEDs of the simulated galaxy merger. By performing dust RT calculations both including and excluding the emission from the AGN, we can explicitly identify IR emission powered by the AGN on both torus and host-galaxy scales. This particular simulation is a massive, gas-rich, merger designed to be analogous to $z \sim 2 - 3$ submillimeter galaxies (SMGs), and it is indeed consistent with many properties of observed SMGs (Hayward et al., 2011, 2012, 2013). We chose this particular simulation because it exhibits a high SFR, a high AGN luminosity, and high dust ation; such systems are the most likely candidates for AGN powering host-galaxy scale cold-dust emission. We show that in this admittedly extreme system, dust-enshrouded AGN can be the dominant power source of cold-dust emission on host-galaxy scales, with cool FIR colors indistinguishable from those of purely star-forming galaxies. We estimate the potential bias in observations of galaxy SFRs and discuss implications for SED decomposition.

The remainder of this chapter is organized as follows: in Section 6.2, we discuss the details of our numerical simulation and RT calculations. Section 6.3 explains how we extract the AGN-powered dust emission and presents our main results. We discuss the implications of these calculations for inferred trends in galaxy evolution and some limitations of this work in Section 6.4. We summarize in Section 6.5. Throughout this work, we assume a Salpeter IMF and adopt a Λ CDM cosmology with $\Omega_m = 0.3$, $\Omega_\Lambda = 0.7$, and $H_0 = 70 \text{ km s}^{-1} \text{ Mpc}^{-1}$.

6.2 Simulation and Radiative Transfer Details

This work makes use of the results of RT calculations originally presented in Snyder et al. (2013). Our re-analysis focuses on the output from a `Gadget-2` simulation (Springel, 2005) of an idealized (non-cosmological) major merger of two identical disk galaxies. The initial conditions were generated following Springel et al. (2005). The initial halo and baryonic masses are $9 \times 10^{12} M_\odot$ and $4 \times 10^{11} M_\odot$, respectively. The

initial black hole mass is $1.4 \times 10^5 M_{\odot}$, and the initial gas fraction is 60%. Star formation and stellar feedback are modeled as described in Springel & Hernquist (2003) and Springel et al. (2005). Black holes grow via Eddington-limited Bondi-Hoyle accretion.

The RT code `SUNRISE` (Jonsson, 2006; Jonsson et al., 2010) was used to compute SEDs for seven viewing angles every 10 Myr throughout the simulation run. The outputs of the hydrodynamical simulation are used as input for the RT calculations, i.e., the former is used to specify the 3D distribution of sources of emission (stars and AGN) and dust. The ages and metallicities of the star particles are used to assign single-age stellar population SEDs to individual star particles. The metal distribution determines the dust density distribution; a dust-to-metals ratio of 0.4 was assumed. For more in-depth discussion of the simulation assumptions, sub-grid models, and numerical methods, see Snyder et al. (2013) and Hayward et al. (2011).

For each time snapshot of the merger simulation, different RT calculations were performed; they differ only in how the luminosity of the AGN is computed. The ‘fiducial’ RT runs use the accretion rate from the simulation to compute the AGN luminosity, assuming 10% radiative efficiency. We use luminosity-dependent AGN SED templates derived from observations of unreddened QSOs (Hopkins et al., 2007) as the input SEDs emitted by the AGN particle(s); see Snyder et al. (2013) for details. In the ‘AGN-off’ runs, the luminosity of the AGN is artificially set to zero (i.e., only stellar emission is considered in the radiative transfer calculations; note that AGN feedback is still included because the same hydrodynamical simulation is used as input, so these runs determine the impact of the AGN emission on the total SED *all else being equal*). Finally, in the ‘AGN-10x’ RT calculations, the luminosity of the AGN is artificially boosted by a factor of 10 (equivalent to assuming a radiative efficiency of 100% or an instantaneous accretion rate ten times the value computed in the simulation). As in the ‘AGN-off’ runs, the AGN feedback is not altered (the same hydrodynamical simulations are used) because we wish to isolate the effect of

the AGN on the SED. In other words, the input of a boosted AGN spectrum into the RT calculations is the only difference between the AGN-10x and AGN-off results. Snyder et al. (2013) performed these calculations simply to span a larger range in the AGN fractional contribution to the bolometric luminosity, but these should not be considered ‘unphysical’ by any means, as the relatively crude accretion model employed and the limited resolution of the hydrodynamical simulation may cause the BH accretion rate to be underestimated (e.g., Hayward et al., 2014; Angles-Alcazar et al., 2020). The Eddington ratio ($\lambda_{\text{edd}} \equiv L_{\text{AGN}}/L_{\text{edd}}$) varies from zero to one in the fiducial runs and thus spans a range of $\lambda_{\text{edd}} = 0 - 10$ in the AGN-10x runs. There is both theoretical (e.g., Begelman, 2002; Jiang et al., 2014) and observational (e.g., Kelly & Shen, 2013; Shirakata et al., 2019) evidence for super-Eddington accretion.

6.3 Results

For every snapshot and each of the seven viewing angles, we calculate the SED of the AGN-powered dust emission, i.e., the dust emission implicit in the input torus model SED plus the host-galaxy dust emission powered by the AGN (rather than stars). Our `SUNRISE` calculations with and without AGN emission are otherwise identical; therefore, taking the difference between the SEDs with and without AGN emission yields the SED of all photons of AGN origin, including those reprocessed by dust. Originally demonstrated in Roebuck et al. (2016) for our fiducial simulation (see their Fig. 2), this differencing technique is shown in Figure 6.1 for the AGN-10x run at t_{peak} , the simulation time when the ratio of bolometric AGN luminosity (L_{AGN}) to bolometric stellar luminosity (L_{SF}) reaches its maximal value of ~ 10 . At this time, the mass of the BH is $3.2 \times 10^8 M_{\odot}$, and it is accreting at a rate of $82 M_{\odot} \text{ yr}^{-1}$, while $\text{SFR} = 470 M_{\odot} \text{ yr}^{-1}$. The SEDs shown in Fig. 6.1 are the following:

- $L_{\lambda}^{\text{AGN}, 10\text{x}}$ – The attenuated+re-radiated SED corresponding to the AGN-10x run, where the luminosity of the AGN is artificially boosted by a factor of 10.

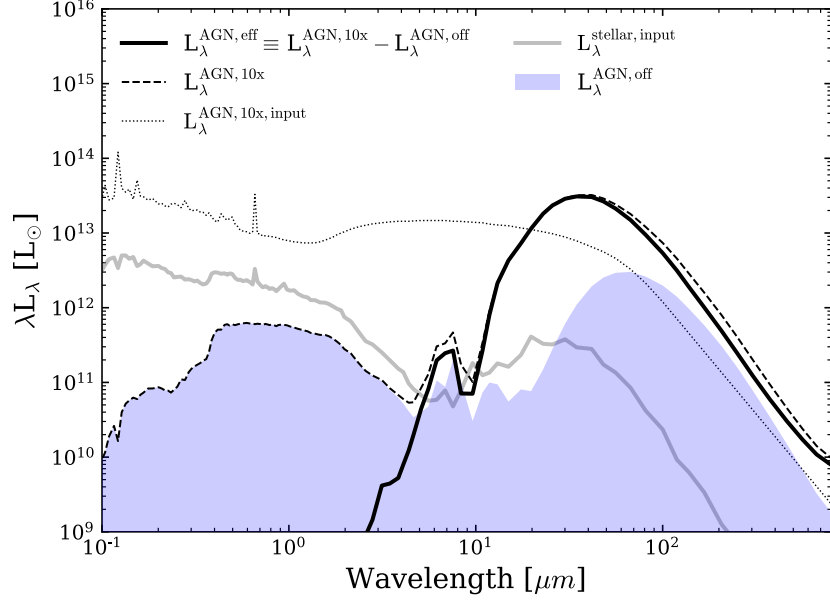


Figure 6.1 Rest-frame SED for the AGN-10x model (dashed line) at the time of peak $L_{\text{AGN}}/L_{\text{SF}}$, where the AGN dominates the bolometric luminosity and the time at which the AGN contributes maximally to the FIR luminosity during this simulation. The unattenuated AGN torus spectrum ($L_{\lambda}^{\text{AGN},10\text{x},\text{input}}$) is shown as a dotted line, and the unattenuated stellar spectrum is shown as a solid grey line ($L_{\lambda}^{\text{stellar},\text{input}}$). For the same simulation snapshot, we show the corresponding AGN-off SED shaded in blue. The effective AGN SED, calculated by taking the difference between the AGN-10x and AGN-off SEDs, is indicated by the solid line. This corresponds to the primary torus emission attenuated by dust *plus* host-galaxy-scale thermal dust emission powered by the AGN. Due to heavy dust obscuration experienced by the AGN, the AGN contributes negligibly to the UV-optical SED, but it dominates longward of a few microns, including the FIR cold dust emission traditionally associated with star formation.

- $L_{\lambda}^{\text{AGN},\text{off}}$ – The attenuated+re-radiated SED corresponding to the RT run where the luminosity of the AGN is set to zero.
- $L_{\lambda}^{\text{AGN},\text{eff}}$ – The “effective AGN SED” calculated from the difference between $L_{\lambda}^{\text{AGN},10\text{x}}$ and $L_{\lambda}^{\text{AGN},\text{off}}$, which removes stellar-heated dust emission, leaving behind only AGN photons, including IR photons from the torus that are absorbed by dust in the ISM re-radiated at progressively longer wavelengths.

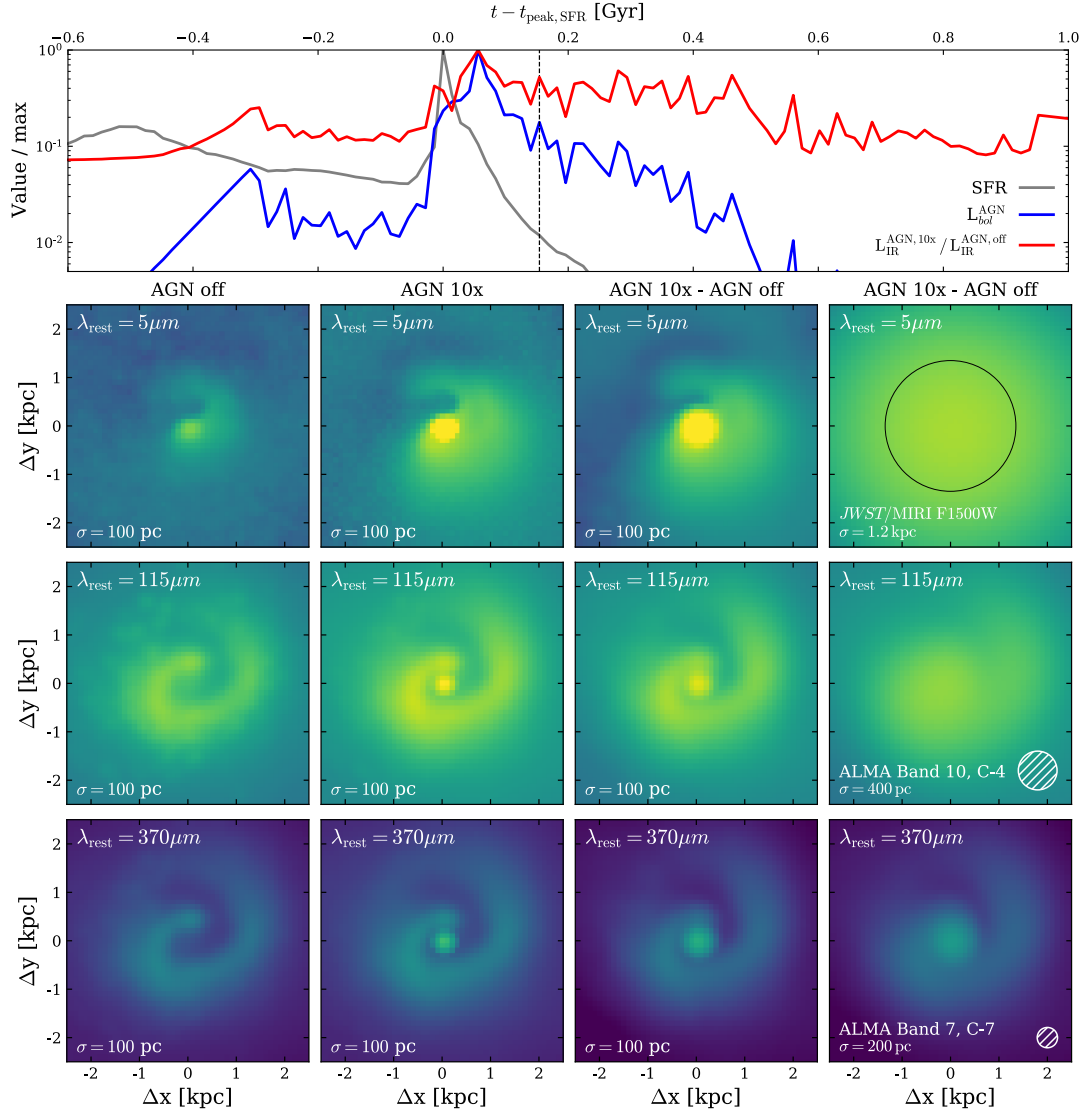


Figure 6.2 Emission maps of the simulated merger at a representative time following the peak SFR and peak bolometric AGN luminosity (marked by the dashed line in the top panel). The first (second) column shows maps of the emission at rest-frame wavelengths $15 \mu\text{m}$, $115 \mu\text{m}$, and $370 \mu\text{m}$ for the AGN-off (AGN-10x) RT run. The third column shows difference images between the AGN-10x and AGN-off maps, i.e., the dust emission powered directly by the AGN. The color scale and stretch is constant across all panels. For comparison with observations, we blur the images to 100 pc resolution, typical of spatially resolved studies of lensed systems at $z \sim 2$. In the far-right column, we further blur each map to the spatial resolution achievable with *JWST*/MIRI (*top*) and ALMA high-frequency observations in extended array configurations (*center, bottom*) for a galaxy at $z = 2$. The *JWST*/MIRI beam is shown as a solid black circle, and the ALMA beams as white hatched circles. The AGN-powered cold dust emission includes both a compact nuclear component and an extended component spanning a few kpc.

- $L_{\lambda}^{\text{AGN},10\text{x},\text{input}}$ – The input AGN SED (from Hopkins et al. 2007) in the AGN-10x run. This SED is integrated from $0.1 - 1000 \mu\text{m}$ to calculate L_{AGN} .
- $L_{\lambda}^{\text{stellar},\text{input}}$ – The unattenuated stellar spectrum, which is the same across all RT runs. This SED is integrated over $0.1 - 1000 \mu\text{m}$ to determine L_{SF} .

$L_{\lambda}^{\text{AGN},\text{eff}}$ peaks at $31 \mu\text{m}$, corresponding to an effective dust temperature (from Wien’s law) of 96 K, on the warm end of dust temperatures observed in AGN-host galaxies: Kirkpatrick et al. (2015) find that the warm dust component, attributed to AGN heating, is $\sim 80 - 90$ K for high- z ultra-luminous IR galaxies (ULIRGs; $L_{\text{IR}} > 10^{12} L_{\odot}$) with high AGN fractions. In the simulated SEDs, most of the IR emission between 10 and $50 \mu\text{m}$ comes from re-processed AGN photons, and $L_{\lambda}^{\text{AGN},\text{eff}}$ is greater than $L_{\lambda}^{\text{AGN},\text{off}}$ by a factor of $\gtrsim 2$ from $100 - 1000 \mu\text{m}$. In this particular (extreme) case, even the coldest dust is predominantly heated by the AGN.

The top panel of Fig. 6.2 shows the time evolution of the SFR, AGN luminosity, and fractional contribution of the AGN to the IR luminosity. Near coalescence of the two galaxies, there is a strong starburst. The SFR then rapidly decays due to gas consumption (there is no cosmological gas accretion in this idealized simulation) and AGN feedback. Approximately 50 Myr after the peak SFR, the AGN luminosity peaks. During this period, both the newly formed stars and AGN are deeply obscured by dust. The AGN contributes $> 30\%$ of the IR luminosity for ~ 0.5 Gyr, starting at the peak of the starburst. The AGN luminosity then declines, decreasing below 10% of its peak luminosity ~ 100 Myr later.

The lower part of Fig. 6.2 presents maps of the $5 \mu\text{m}$, $115 \mu\text{m}$ and $370 \mu\text{m}$ dust emission in the AGN-off (first column) and AGN-10x (second column) runs ~ 150 Myr after t_{peak} , a time at which there is significant dust-obscured star formation but the dust-enshrouded AGN dominates the luminosity ($L_{\text{AGN}}/L_{\text{SF}} > 1$); this time is marked by the dashed vertical line in the top panel. Given the short duration of the starburst and peak in AGN luminosity, most observations of heavily dust-obscured AGN should

probe this phase (subsequent to the peak SFR and AGN luminosity), so these maps should be considered ‘representative’. Fig. 6.2 also shows the difference between the AGN-10x and AGN-off simulations (third column), which captures the spatial extent of the dust emission *powered by the AGN*. These maps have been convolved with a Gaussian with FWHM of 100 pc, representative of spatially resolved studies of lensed systems at $z \sim 2-3$ (e.g., Swinbank et al., 2015; Sharda et al., 2018; Cañameras et al., 2017; Massardi et al., 2018). The third column shows that the cold dust emission at far-IR wavelengths $\gtrsim 100 \mu\text{m}$ powered by the AGN consists of a compact nuclear component and a lower-surface-brightness extended component on kpc scales, clearly demonstrating that photons from the AGN heat cold dust throughout the host galaxy.

In the fourth column of Figure 6.2, we show maps of the AGN-powered dust emission convolved to the spatial resolution that *JWST/MIRI* (*top*) and ALMA’s high-frequency, extended configurations (*center, bottom*) can achieve for an un-lensed galaxy at $z = 2$. With ALMA, the nuclear dust heated by the dust-enshrouded AGN can be resolved from the extended cold dust. At coarser spatial resolutions, imaging with *JWST/MIRI* can test for buried AGN heating host-galaxy dust by comparing central and extended emission on scales above and below ~ 1 kpc (solid circle), nearly equal to the half-mass radius of the system of 1.1 kpc. In Figure 6.3, we show the ratio of the flux within a simulated *JWST/MIRI* beam placed on the center of a mock observation to the total flux in the map, for MIRI filters with central wavelengths between 5 and 25 μm . Before the simulated aperture photometry, we first convolve the maps to the spatial resolution of JWST assuming the galaxy is at $z = 2$. As expected, the AGN-10x simulation exhibits more concentrated emission in all MIRI filters than the AGN-off run because of the strong, nuclear dust-heating source. The presence of this luminous dust-enshrouded AGN increases the fraction of the total flux within the central \sim kpc relative to the total flux by a factor of ~ 1.5 in most MIRI filters. IR imaging will be key for identifying such dust-enshrouded AGN because,

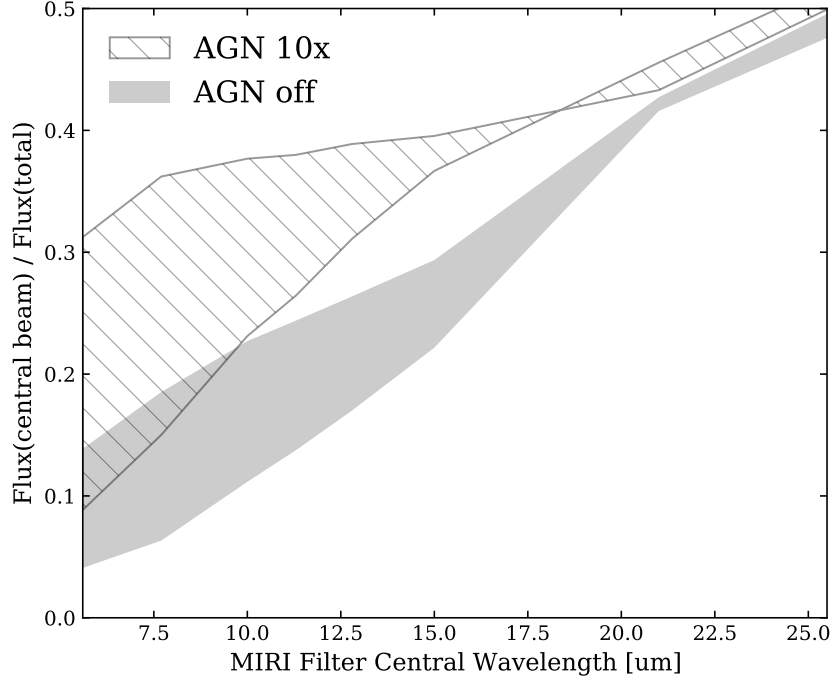


Figure 6.3 The ratio of flux within a simulated *JWST*/MIRI beam placed on the center of the galaxy relative to the total flux across the PSF-convolved map, for various MIRI filters. We show the results of such mock observations for the AGN-10x (hatched) and AGN-off (solid gray) runs at t_{peak} , the same snapshot used in Fig. 6.2. The maps have been redshifted to $z = 2$ and convolved with the wavelength-dependent PSF of *JWST*/MIRI. The shaded and hatched regions contain the range of simulated observations for all seven viewing angles. The presence of a powerful, dust-enshrouded AGN boosts the fraction of the total flux within the central beam by a factor of ~ 1.5 between observed wavelengths of $\sim 6 - 15 \mu\text{m}$. Mid-IR imaging at *JWST*'s resolution could be used to identify such dust-enshrouded AGN.

as we shall see below, the cold FIR colors would preclude distinguishing this source from a compact nuclear starburst based on the broadband FIR SED alone.

Having demonstrated that the AGN can power cold-dust emission on host-galaxy scales, we now quantify how the AGN affects the IR luminosity in different bands throughout the simulation. Taking the ratio of L_{IR} in the AGN-on and AGN-off simulations captures the fractional change in L_{IR} due to dust emission powered by photons of AGN origin. In Figure 6.4, we plot the ratio of integrated IR luminosities between the AGN-on and AGN-off simulations in four different wavelength bands

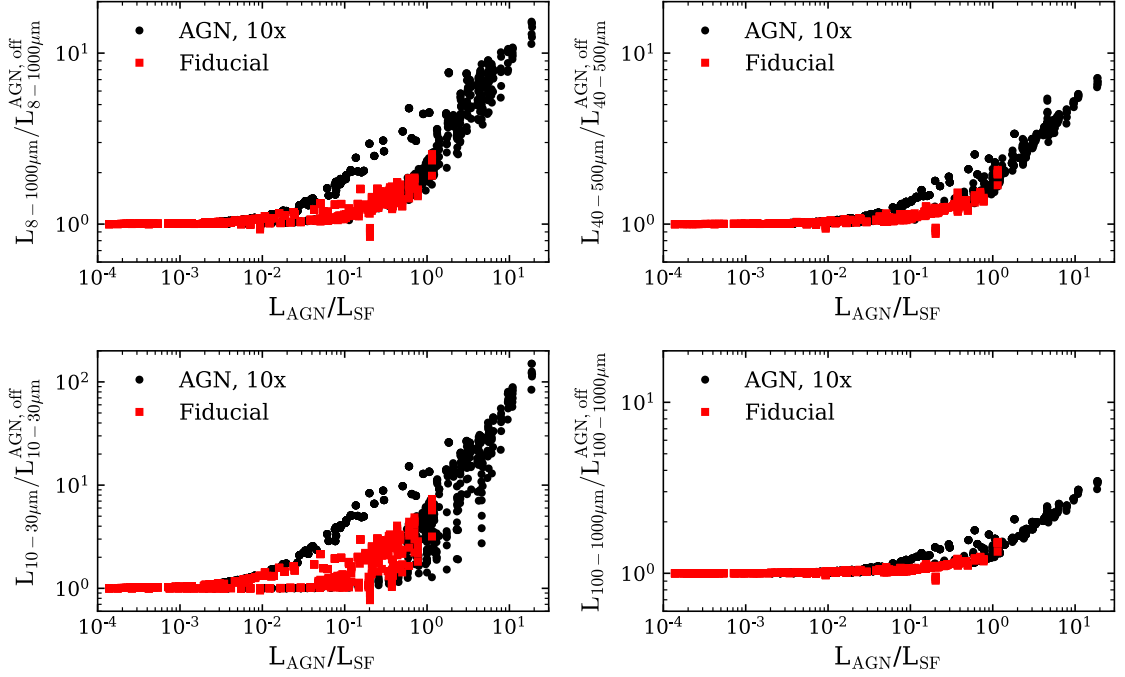


Figure 6.4 The ratio of the IR luminosity integrated in different bands for RT calculations with AGN+host galaxy-powered dust emission (‘fiducial’ or ‘AGN 10x’) relative to those with only host galaxy dust emission (‘AGN off’) vs. the ratio of bolometric AGN to star formation luminosity. Data from fiducial (AGN 10x) runs are shown as red squares (black circles). In each panel, we show data for all time snapshots and viewing angles. When the luminosity of the AGN is ten times that of star formation, it can boost the total IR (8-1000 μm) luminosity by an order of magnitude and the far-IR (40-500 μm) luminosity by a factor of ~ 7 . The cold-dust FIR luminosity (100-1000 μm), traditionally assumed to be powered exclusively by star formation, can be boosted by a factor of three. Therefore, depending on the precise wavelength range used, the SFR inferred from the IR or far-IR luminosity will overestimate the true SFR by a factor of 3 – 10.

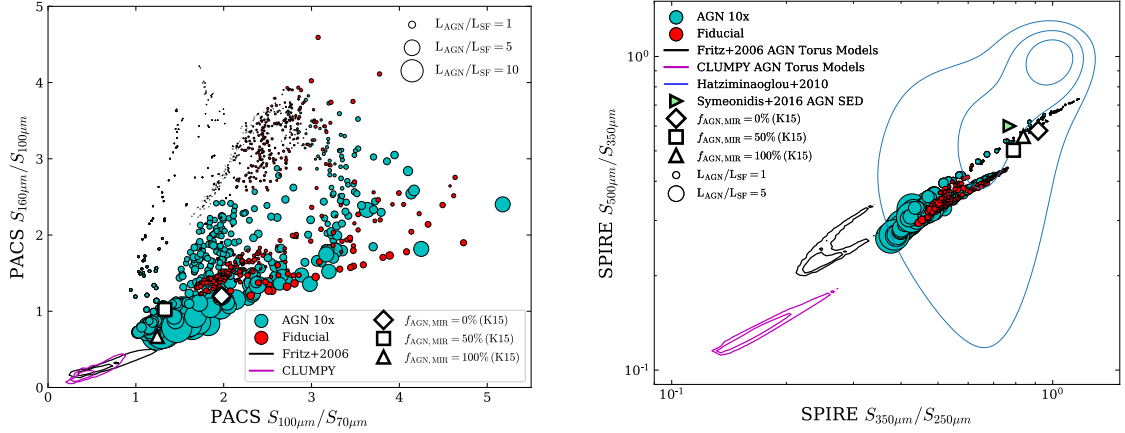


Figure 6.5 (*Left*) *Herschel* PACS $100\mu\text{m}/70\mu\text{m}$ vs. $160\mu\text{m}/100\mu\text{m}$ colors (assuming $z = 2$). Cyan and red points correspond to the AGN 10x and fiducial runs, respectively, and the size of each marker is proportional to $L_{\text{AGN}}/L_{\text{SF}}$. For comparison, we show the colors of empirical templates from Kirkpatrick et al. (2015) (K15) at $f_{\text{AGN,MIR}} = 0\%$ (diamond), $f_{\text{AGN,MIR}} = 50\%$ (square), and $f_{\text{AGN,MIR}} = 100\%$ (triangle). Magenta and black contours contain 95% and 68% of the distribution in *Herschel* colors spanned by the (Nenkova et al., 2008a,b) and Fritz et al. (2006) dusty AGN torus models, respectively. (*Right*) *Herschel* SPIRE $350\mu\text{m}/250\mu\text{m}$ vs. $500\mu\text{m}/350\mu\text{m}$ colors (assuming $z = 2$) following the same color scheme as the left panel. Blue contours contain the $z \sim 2$ AGN-hosting galaxy sample of Hatziminaoglou et al. (2010). Colors from the Kirkpatrick et al. (2015) SEDs are shown as described in the *left* panel, and we also include the SPIRE colors of the AGN SED from Symeonidis et al. (2016) (green triangle). The FIR colors of the simulated galaxies are redder (cooler) than those of *all* of the torus models and consistent with those of the observed galaxies, suggesting the ‘cold’ FIR colors of these AGN hosts are not necessarily indicative of ongoing star formation; instead, the FIR emission may be predominantly powered by dust-enshrouded AGN.

versus $L_{\text{AGN}}/L_{\text{SF}}$. The total (far-)IR luminosity from $8 - 1000 \mu\text{m}$ ($40 - 500 \mu\text{m}$) is boosted by a factor of ~ 10 (~ 7) as $L_{\text{AGN}}/L_{\text{SF}}$ increases from 1 to ~ 10 . The rise in L_{IR} with $L_{\text{AGN}}/L_{\text{SF}}$ is mostly driven by increased warm dust emission at shorter wavelengths, as shown in the $10 - 30 \mu\text{m}$ panel of Fig. 6.4. However, the integrated $100 - 1000 \mu\text{m}$ luminosity can be increased by the AGN by as much as a factor of ~ 3 , demonstrating that even the coldest dust emission can be powered by the AGN. This result is at odds with the notion that cold dust emission at these FIR wavelengths is predominantly heated by young stars even when an AGN dominates the bolometric luminosity of the galaxy (e.g., Stanley et al., 2017; Shangguan et al., 2020).

FIR colors are often used to distinguish AGN-powered and stellar-powered dust emission, as IR-selected galaxies that host AGN tend to have warmer IR colors than those that do not (e.g., de Grijp et al. 1987; Sanders et al. 1988b; but cf. Younger et al. 2009). For this reason, we present *Herschel* FIR color-color plots of the simulation runs in Figure 6.5, while also tracking the ratio of AGN luminosity relative to the star-formation luminosity ($L_{\text{AGN}}/L_{\text{SF}}$). High $L_{\text{AGN}}/L_{\text{SF}}$ tends to result in bluer colors; however, this is modulated by changes in extinction with time and viewing angle. Higher levels of extinction (A_V) for fixed $L_{\text{AGN}}/L_{\text{SF}}$ yield redder FIR colors. For comparison with observations, we also show the empirically derived galaxy SED templates of Kirkpatrick et al. (2015), which span a range in AGN contribution to the mid-IR emission, as well as the $z \sim 2$ Type 1 and Type 2 AGN sample of Hatziminaoglou et al. (2010). The simulated galaxies have FIR colors on the Wien side of the dust distribution (PACS photometry, Fig. 6.5, *left*) consistent with the observed galaxies. The SPIRE colors (Fig. 6.5, *bottom*), which trace the dust peak, of the simulated galaxies are somewhat bluer (warmer) than those of the majority of the observed galaxies by a factor of $\sim 2 - 3$ when $L_{\text{AGN}}/L_{\text{SF}} > 1$, but they are redder (colder) than those of *any* of the torus models in these two widely used torus SED libraries because the torus models do not include galaxy-scale cold dust emission.

Table 6.1. Maximal boosting of host-galaxy FIR dust emission by a dust-enshrouded AGN at selected wavelengths, and for integrated IR luminosities.

λ_{obs}	$z = 0$	$z = 1$	$z = 2$	$z = 3$
70 μm	3.8	10.8	30.9	47.4
100 μm	2.9	5.8	11.9	25.0
160 μm	2.4	3.4	5.2	8.5
250 μm	2.2	2.6	3.3	4.3
350 μm	2.3	2.3	2.7	3.2
500 μm	2.6	2.2	2.4	2.6

	Fiducial	AGN-10x
$L_{IR}(8 - 1000\mu m)$	2.5	14.4
$L_{FIR}(40 - 500\mu m)$	2.0	7.2
$L(10 - 30\mu m)$	6.7	142.7
$L(100 - 1000\mu m)$	1.5	3.2

Note. — Maximal boosting as a function of λ_{obs} is derived from the redshifted AGN-10x SED considering all timestamps and viewing angles. Generally, these maximum values occur around the most extreme snapshot in our simulations, where $L_{AGN}/L_{SF} > 10$, and should be interpreted as the maximum possible correction an IR SFR would require to accurately recover the true dust-enshrouded SFR under such admittedly extreme conditions.

These results suggest that the cool FIR colors of the observed AGN hosts are not necessarily evidence that their FIR cold-dust emission is powered by ongoing star formation; rather, the AGN itself may be the dominant power source for the cold-dust emission.

6.4 Discussion

6.4.1 Implications

Our simulations suggest that in extreme cases, AGN may dominate the FIR luminosity of a galaxy at all wavelengths. The central AGN in our simulations heats dust at radii greater than the half-mass radius of the system at times following merger

coalescence. Moreover, our simulations span a similar parameter space in FIR colors compared to observations but are redder than all dusty torus models from the CLUMPY (Nenkova et al., 2008a,b) and Fritz et al. (2006) AGN torus SED libraries, instead exhibiting colors that could be interpreted to indicate pure star formation. Consequently, without robust exclusion of a central deeply dust-enshrouded AGN, even cold-dust emission at $> 100 \mu\text{m}$ may be ‘contaminated’ by AGN-powered dust emission and thus not yield accurate SFRs.

Although the current consensus is that star formation dominates cold-dust emission at $\lambda > 100 \mu\text{m}$ (see Section 6.1), some empirical studies have suggested that AGN play an important role in powering dust emission even at these wavelengths (e.g., Sanders & Mirabel, 1996). For example, Symeonidis et al. (2016), Symeonidis (2017) and Symeonidis & Page (2018) show that optical through sub-mm emission in $z < 0.18$ QSOs and $z \sim 1 - 2$ extremely luminous IR galaxies can be dominated by AGN-heated dust out to kpc scales in the host galaxy. To fit a library of empirically-derived IR AGN SEDs, Kirkpatrick et al. (2012) and Kirkpatrick et al. (2015) require an $\sim 80 - 90$ K dust component, which they attribute to AGN heating of the dust. Given that the amount of obscuration in luminous quasars correlates with cold dust emission (e.g., Page et al., 2004, 2011; Chen et al., 2015), far-IR fluxes contaminated by buried AGN may be a systematic source of uncertainty when measuring star formation rates in galaxies lacking an AGN classification. As we show in Table 6.1, L_{IR} and L_{FIR} can be boosted by factors of ~ 10 and ~ 7 respectively by AGN-powered cold dust emission. This could lead to overestimates of IR SFRs by a factor of $\sim 2 - 3$ on average for the most extreme cases of AGN-heated dust at $z \lesssim 3$ in galaxies with high λ_{edd} and $L_{\text{AGN}}/L_{\text{SF}} > 1$.

For the reasons mentioned above, indicators of dust-obscured AGN activity are especially important when attempting to measure co-eval stellar and SMBH mass assembly. X-ray observations can identify Compton-thick QSOs in dusty galaxies

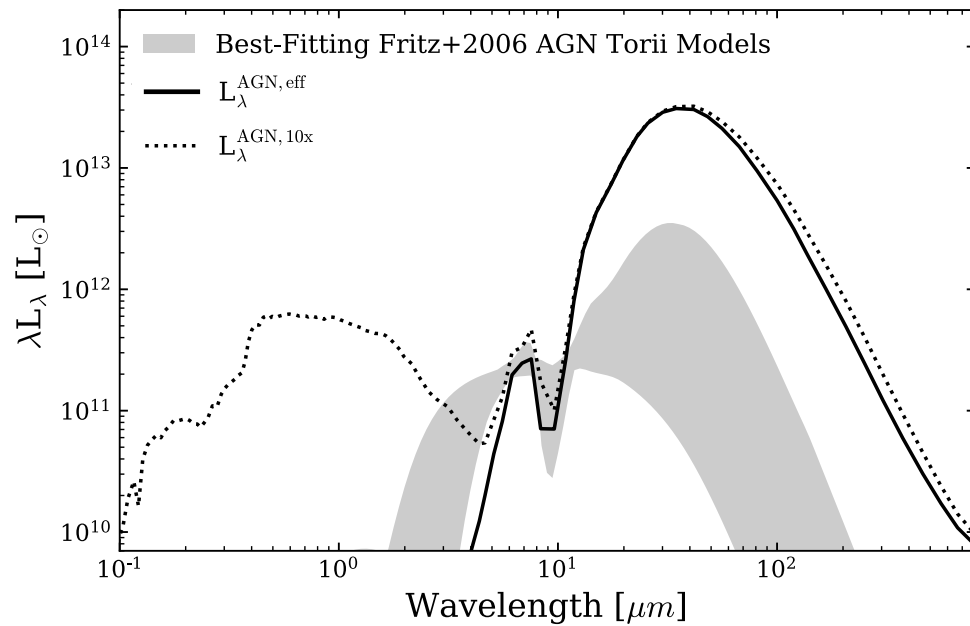


Figure 6.6 The total (*dotted black line*) and effective AGN (*solid black line*) SEDs already shown in Figure 6.1, but now compared against the dusty AGN torus models from Fritz et al. (2006). We fit the entire model library to the AGN 10x spectrum between 5–13 μm and show the domain of the top 100 best-fitting models as a shaded grey region. The torus model can reproduce our effective AGN SED’s mid-IR dust emission from $\sim 2 - 10 \mu\text{m}$ but drastically underestimates the FIR emission powered by the AGN. Thus, inferring the AGN contribution to the FIR using standard torus models would result in overestimating the SFR.

out to high redshifts (e.g., Brandt & Alexander 2015 and references therein). For example, using *Chandra* observations, Vito et al. (2020) discovered highly obscured AGN residing within two dusty, star-forming galaxies resident in a $z \sim 4$ proto-cluster, one of which is a Compton-thick QSO that has a luminosity comparable to the most-luminous QSOs known. The results presented in the present work suggest that these obscured AGN may power an appreciable fraction of the cold-dust emission from these galaxies. This example demonstrates the need for X-ray follow-up of systems purportedly harboring high levels of obscured star-formation. Alternatively, spectroscopic methods in the mid-IR ($\sim 3 - 30 \mu\text{m}$) may be used to discriminate between dust-enshrouded AGN and star-formation using high excitation emission lines (Spinoglio & Malkan, 1992) or polycyclic aromatic hydrocarbon (PAH) features + mid-IR continuum decomposition (e.g., Pope et al. 2008; Kirkpatrick et al. 2015). Presently, mid-IR spectroscopic techniques are the most sensitive method for identifying dust-enshrouded AGN at all levels of AGN strength relative to the luminosity of the host galaxy (Hickox & Alexander, 2018). Using, amongst other simulations, the fiducial run discussed in this work, Roebuck et al. (2016) find the fraction of $8 - 1000 \mu\text{m}$ luminosity attributed to AGN (the IR AGN fraction) to be a good predictor of the bolometric AGN fraction at times up to coalescence and at $A_V > 1$. For such dust-obscured AGN phases, quantifying the AGN fraction using mid-IR data may enable subtracting host-galaxy AGN-heated dust emission to derive accurate SFRs for AGN hosts (e.g., Kirkpatrick et al. 2017).

Spectroscopic methods and spatially resolved data for more galaxies will improve our understanding of obscured mass assembly; however, a revision of SED-fitting techniques is necessary to fully leverage the power of future observatories. In particular, our results suggest that in highly dust-obscured galaxies, the host-galaxy-scale dust emission cannot be considered decoupled from emission from the AGN, as is done in community-standard SED fitting codes. As we show in Figure 6.6, simpler IR SED

decomposition methods also suffer from the lack of AGN-heated cold dust, as it is common to subtract an AGN torus model from the FIR SED of a galaxy and assume the residual power arises from star formation alone. If we make this assumption for our simulation and subtract the best-fitting Fritz et al. (2006) AGN torus model from the total SED, then the residual IR emission would overestimate the true SFR by a factor of ~ 7 in the extreme case where $L_{\text{AGN}}/L_{\text{SF}}$ is maximal. SED fits which include an AGN may also need to consider an associated FIR cold-dust component that does not contribute to the inferred SFR.

6.4.2 Limitations of this work

We have presented a ‘case study’ of a single galaxy merger simulation. As emphasized above, the simulation is representative of $z \sim 2-3$ massive, rapidly star-forming, highly dust-obscured galaxies (SMGs), and we thus expect our results to only apply to the bright end of the IR luminosity function. It would be valuable to repeat our analysis using simulations that span a much broader range of properties and redshifts. Moreover, our results may be sensitive to the structure of the simulated galaxy’s ISM, which can be affected by both the mass and spatial resolution of the simulation and the sub-grid models used. For this reason, it would be worthwhile to repeat this analysis on simulations with much higher resolution and more sophisticated treatments of star formation, BH accretion, and stellar and AGN feedback (e.g., Angles-Alcazar et al., 2020).

6.5 Summary and Conclusions

We have analyzed synthetic SEDs of a hydrodynamical galaxy merger simulation generated via dust RT calculations to investigate the influence of dust-enshrouded AGN on host-galaxy-scale cold dust emission. Our main conclusions are as follows:

1. Heavily dust-enshrouded AGN can power significant cold-dust FIR emission on host-galaxy (kpc) scales; in this particular simulation, the AGN can boost the total IR luminosity by an order of magnitude and the FIR (100-1000 μm) luminosity by a factor of 3 (i.e., the AGN can be the primary heating source of cold dust).
2. Our simulations have FIR colors probing the Wien side of the dust emission consistent with those of $z \sim 2$ dusty galaxies, including AGN hosts and ‘purely star-forming’ galaxies. The FIR colors of our simulations tracing the dust peak are somewhat warmer than observed galaxies when $L_{\text{AGN}}/L_{\text{SF}}$ is high. However, in both regimes, the FIR colors of the AGN-powered dust emission are redder than those of any of the widely used AGN torus SED models that we considered.
3. Our results have important consequences for IR- and (sub)mm-selected galaxies, which are more likely to feature significant host-galaxy obscuration of AGN they host than are less-dust-obscured galaxies. For such systems, if a deeply dust-enshrouded AGN is present, the FIR emission may be powered by both young stars and the AGN. Applying standard torus models, which do not include host-galaxy-scale AGN-powered cold-dust emission, to decompose the SED may thus result in overestimating the SFR and underestimating the AGN fraction.

This work should be considered a ‘case study’ that demonstrates the need for caution when interpreting the FIR SEDs of galaxies that may host dust-enshrouded AGN. Spatially resolved observations (from, e.g., ALMA and *JWST*) and additional AGN diagnostics should be sought to confirm whether a dust-enshrouded AGN is present when studying such systems. Moreover, there is a need to develop AGN SED models that account for dust obscuration and emission from both the clumpy torus *and* the host galaxy rather than treating the AGN and its host as decoupled.

CHAPTER 7

SUMMARY AND FUTURE OUTLOOK

7.1 Summary of Dissertation

For most of cosmic time stars predominantly formed within luminous, dust-obscured and IR-bright galaxies (LIRGs). This thesis focuses on characterizing star-formation and the gas and dust conditions in LIRGs to better understand why LIRGs in the past have high star-formation rates. Within my thesis research, I have shown that the properties of star-formation in LIRGs depend strongly on their IR size. Compact star-formation exhibits distinct gas conditions from those found in lower star-formation rate surface density galaxies. At high IR surface densities in $z \sim 0$ LIRGs, changes in the dust grain size distribution drive low gas heating efficiencies (Ch. 3, McKinney et al. 2021a). These extreme conditions manifest in some $z = 1 - 3$ LIRGs which exhibit the low FIR line-to-PAH ratios observed locally (Ch. 2, Ch. 5, McKinney et al. 2020). At all redshifts, compact LIRGs form their stars more efficiently (Ch. 4), lending credence to paradigms in which the star-formation efficiency evolves over cosmic time with the size evolution of galaxies as an important component in the star-formation rate density. As stars form, the growth of heavily dust-obscured supermassive black holes can regulate the ISM state of their host-galaxies (Ch. 6, McKinney et al. 2021b), which may also play a significant role in the regulation of star-formation rates in the past when accretion rates were high. IR spectroscopy and resolved continuum observations combined with state-of-the-art simulations constitute a promising path for the continued study of dust-obscured mass assembly at all redshifts, wherein there lies a rich future for astrophysical research.

7.2 Future Work

The work presented in this dissertation has motivated a number of follow-up telescope programs I intend to explore. Recently, my program to expand the sample of $z \sim 1 - 3$ LIRGs with [CII] detections was accepted for observations during ALMA's Cycle 9 call (PI: J. McKinney, PID:2022.1.00101.S). This will provide statistical constraint on the [CII]/PAH ratio at cosmic noon by measuring [CII] in 13 galaxies with existing *Spitzer* spectra, effectively tripling the number of galaxies detected in both tracers between $z \sim 1 - 3$. For the first time, the principle cold gas cooling and heating mechanisms can be measured together at the peak epoch for galaxy formation with enough statistical weight to test for redshift evolution. Moreover, the program is designed to spatially resolve both [CII] and cold dust continuum emission, which I will use to constrain IR surface densities and the [CII] extent following Ch. 4. This will provide a much-needed census of [CII] emission in dusty galaxies at $z \sim 2$, and bridge the gap between local (e.g., GOALS, KINGFISH) and $z > 4$ [CII] surveys (ALPINE, Le Fèvre et al. 2019).

I have been making steady progress following up $z \sim 1 - 3$ *Spitzer* targets with the VLA in CO(1-0) to anchor heating and cooling diagnostics to the cold molecular gas content (PI: J. McKinney, PIDs: VLA/19B-254, VLA/21A-036). This is an important step for future spatially resolved studies of CO(1-0) to test Schmidt-like star-formation laws against dust grain heating physics combining the resolution of *JWST*/MIRI's IFU with radio interferometry. As demonstrated in Chapter 5, the CO(1-0) observations enable detailed PDR modeling in addition to constraining the total molecular gas content. Spatially resolving these diagnostics can be used to study where in a galaxy ISM conditions may power efficient star-formation.

The mid-infrared instrument (MIRI) on *JWST* has already taken exquisite mid-IR spectra of nearby galaxies as shown in Figure 7.1, the likes of which will dramatically improve our understanding of dust and its life-cycle in the interstellar medium.

However, similar studies cannot be done for a statistical sample at $z > 0$ because overheads to measure PAHs with MIRI Medium Resolution Spectroscopy (MRS) are prohibitive. A promising path forwards is to measure the $3.3\ \mu\text{m}$ PAH with the Low Resolution Spectrometer (LRS) on MIRI, a slit spectrometer with superior sensitivity than the MRS/IFU for unresolved sources. I submitted a highly ranked Cycle 1 proposal to execute such a program for 60 $z \sim 0.5 - 3$ LIRGs which I will re-submit during the impending Cycle 2 call. This spectroscopic program would measure the $3.3\ \mu\text{m}$ PAH line and $3.05\ \mu\text{m}$ H_2O water ice absorption feature in *Spitzer*/IRS targets between $z \sim 1.5 - 3$. This unique combination of data constrains fundamental parameters of dust in the ISM including the PAH grain size distribution, charge, and water ice content (Caselli & Ceccarelli, 2012; Maragkoudakis et al., 2020). Indeed, the redshift-independence of dust properties is an underlying assumption made when deriving most galaxy properties; however, this remains essentially untested.

A number of Cycle 1 *JWST* GO and GTO programs are designed for deep, high-resolution near-IR (0.04–0."16) and mid-IR (0.25–0."6) imaging. Notably, PRIMER¹ (Dunlop et al., 2021) and COSMOS-Web² (Casey et al., 2022) will map extragalactic legacy fields with NIRCam and MIRI, expecting to detect $> 10^5$ new galaxies out to $z \gtrsim 12$ that can be followed up with ALMA and the VLA. By selecting subsets of galaxies from these larger surveys on the basis of sizes, I will test the link between star-formation, ISM conditions and overall compactness up to the earliest cosmic epochs to better understand the origins of high star-formation rates at the peak of the star-formation rate density and beyond. COSMOS-Web in particular will cover the largest contiguous area for an extragalactic field, and is well-suited to detecting the rare, massive and possibly dusty galaxies at $z > 6 - 8$. During my upcoming post-doc position at UT Austin, I will work directly with COSMOS-Web to mea-

¹<https://www.stsci.edu/jwst/phase2-public/1837.pdf>

²<https://www.stsci.edu/jwst/phase2-public/1727.pdf>

sure the number counts of such sources, and characterize their ISM conditions with spectroscopic/sub-mm follow-up to study the history and conditions of rapid mass assembly necessary to produce the quiescent population in place at $z \sim 5$ (e.g., Merlin et al., 2019), only ~ 1.2 Gyr after the Big Bang.

Advances in numerical simulations offer an excellent way to study the consequences of varied physical schemes of star-formation and dust heating physics. Figure 7.2 shows the current state of zoom-in simulations, which can resolve the ISM on scales of ~ 10 pc. This resolution is critical for accurately generating synthetic observations of far-IR fine-structure lines originating from PDRs, which can be applied following the methodology developed in Ch. 6 (McKinney et al., 2021b) to test how AGN power IR spectral line emission in detail. Stochastic feeding of the central AGN may produce radial gradients in the warm vs. cold dust emission that can be used to infer times since prior accretion events in observations, and/or the fraction of IR emission powered by an AGN. I will test such scenarios by combining simulations with IR radiative transfer codes (`RADMC-3D`, Dullemond et al. 2012) coupled to non-equilibrium chemistry solvers (`CHIMES`, Richings et al. 2021) to more accurately simulate the IR emission of dusty star-forming galaxies. This will be particularly relevant for extending the [C II] analysis in my upcoming ALMA survey to galaxies that also host AGN, as [C II] emission could also be powered by reprocessed AGN photons. Accounting for such effects is crucial as far-IR lines become workhorse diagnostics for measuring the cold gas conditions at $z > 7$ (e.g., Hashimoto et al., 2019; Uzgil et al., 2021; Wong et al., 2022; Valentino et al., 2022).

7.3 Outlook for the next decade and beyond

A critical limit on the study of gas and dust in the ISM are the extant telescope facilities with IR capabilities. Mid-IR spectroscopy only recently reopened for extragalactic observations with MIRI on JWST, which will build upon the legacy

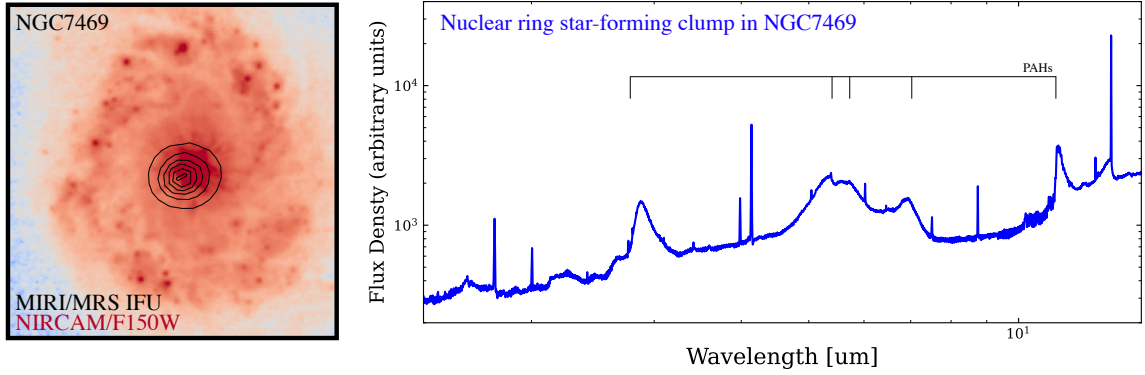


Figure 7.1 *JWST* observations of NGC7469, a star-forming galaxy in the GOALS sample that hosts a bright AGN. Data from the Cycle 1 ERS Program *A JWST Study of the Starburst-AGN Connection in Merging LIRGs* (PI: L. Armus, ID#1328). (Left) *JWST*/NIRCam F150W image with contour overlays extracted from the MIRI/MRS IFU. (Right) *JWST*/MRS spectrum of a star-forming clump within the nuclear star-forming ring of NGC7469 showing bright PAH emission lines (Lai et al., 2022). Data provided via private communication courtesy of T. Lai, V. U, and L. Armus.

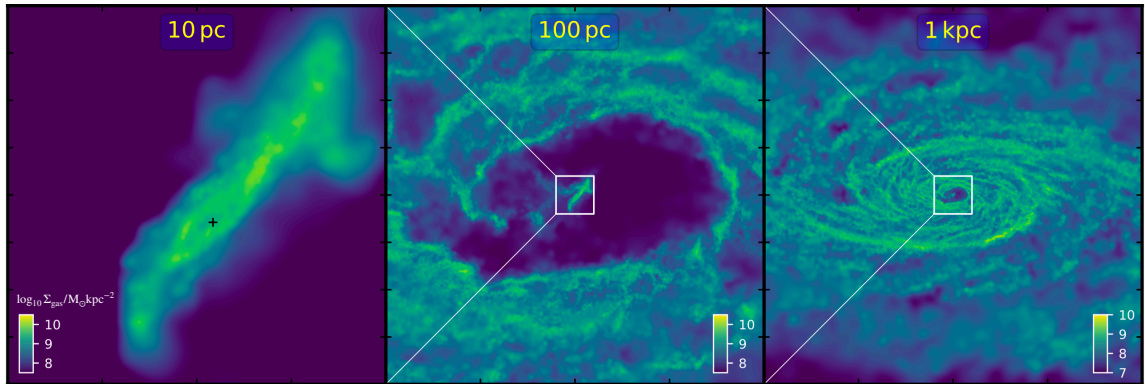


Figure 7.2 Snapshots from state-of-the-art simulations that resolve the ISM over six orders of magnitude in spatial scale and gas mass surface density. Synthetic continuum and spectral line maps from such high-resolution simulations can be used to constrain observations and make predictions for different heating and cooling scenarios. Figure from Anglés-Alcázar et al. (2021).

of *Spitzer*'s cryogenic mission. *JWST*/NIRCam+MIRI imaging can constrain the near through mid-IR sizes of galaxies up to high- z , which can be used in conjunction with interferometric follow-up to statistically link the IR sizes of galaxies and star-formation properties. ToLTEC recently saw first light on the Large Millimeter Telescope (LMT) and will measure extragalactic dust masses at unprecedented speeds

in large photometric surveys that will be made public to the community over the next few years of operations. The next-generation VLA (ngVLA) aims to begin science operations in 2035 and will increase both spatial resolution and sensitivities of the VLA by an order of magnitude. This profound increase in capabilities will enable the high- z study of radio lines like CO at higher statistics and in more detail. ALMA is in the process of upgrading the baseline width of receiver bands enabling efficient redshift searches and quicker integration times on continuum maps with similar implications for the study of far-IR fine-structure lines like [C II] and [O I] in the early Universe.

With SOFIA being defunded following the report of the National Academies (National Academies of Sciences, Engineering, and Medicine, 2021), ALMA is now the only facility with spectroscopic capabilities in the far-IR. Given ALMA’s relatively small field-of-view compounded with $< 50\% - 70\%$ atmospheric transmission at the frequencies needed to measure key FIR lines at $z \sim 1 - 3$, a space telescope with far-IR capabilities is required to statistically revolutionize our understanding of cold gas and dust for most of cosmic time. Figure 7.3 highlights the motivation for such a telescope mission, based in-part on the IR astronomy community response to NASA’s new probe-class \$1 Billion mission category. As demonstrated in Figure 7.3 *Left*, ALMA cannot access key far-IR lines below $z \sim 1$ and does not have the field-of-view or sensitivity to statistically match number counts of far-IR line-detected samples at $z \sim 0$ (e.g., Kennicutt et al., 2011; Díaz-Santos et al., 2013) or $z > 4$ (e.g., Le Fèvre et al., 2019). Figure 7.3 (*Right*) shows the potential survey capabilities of a cryogenically cooled far-IR space telescope with a realistic baseline sensitivity estimate based on the PRIMA concept mission (Bradford et al., 2022). If such far-IR capabilities were to be realized, spectral lines like [C II] and [O I] could be measured in L_{IR} -complete surveys of galaxies up to cosmic noon with unprecedented sample statistics, yielding the equivalent of four GOALS samples spread between $z \sim 0 - 1.5$.

These capabilities would be transformative for the extragalactic community, and I look forward to supporting their implementation.

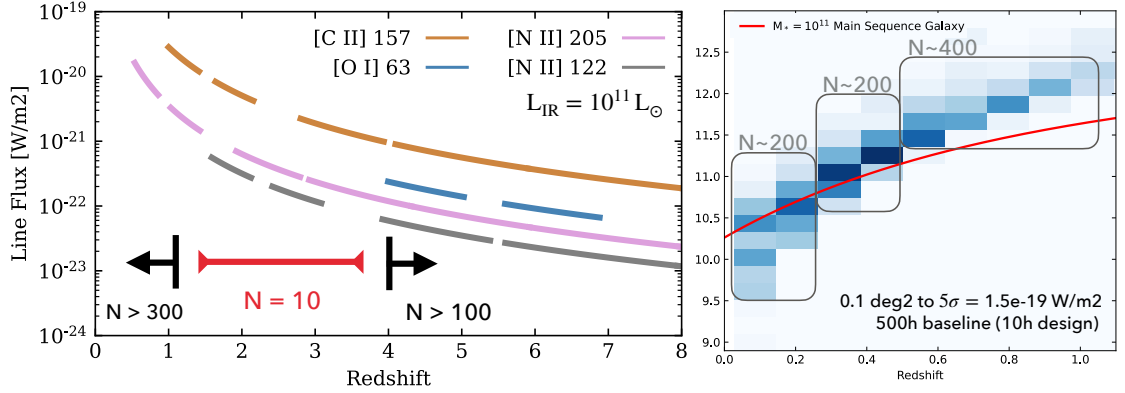


Figure 7.3 (*Left*) Predicted far-IR fine-structure line fluxes as a function of redshift for a galaxy with $\log L_{\text{IR}}/L_{\odot} = 11$. Discontinuities for each line indicate gaps in spectral coverage between the ALMA bands. At redshifts below $z \sim 0.5 - 1$, various IR facilities including *Herschel* and SOFIA have measured lines like [C II] in hundreds of galaxies (e.g., Kennicutt et al., 2011; Díaz-Santos et al., 2013). ALMA has now detected [C II] in over 100 hundred galaxies at $z > 4$ (e.g., Le Fèvre et al., 2019; Aravena et al., 2020; Fudamoto et al., 2022), but only 10 galaxies between $z \sim 1 - 3$ (Zanella et al., 2018; McKinney et al., 2020). (*Right*) Histogram of the number of galaxies in $L_{\text{IR}}-z$ space detected in a blind spectral line survey given the design specifications of a potential probe-class IR space telescope. Surveying an area of 0.1 deg^2 to a 5σ depth of $1.5 \times 10^{-19} \text{ W m}^{-2}$ would detect FIR lines in the equivalent of four GOALS samples out the $z \sim 1$.

7.4 Concluding Remarks

Now is an exciting time in extragalactic astrophysics. NASA recently released the first images from *JWST*, featuring incredible structures from massive clusters lensing background galaxies to complex dust emission in nearby mergers. The National Academies published a sweeping census of the field, highlighting major open questions to be answered in the next decade and outlining significant revisions to our community culture (National Academies of Sciences, Engineering, and Medicine, 2021). As both frontiers open for future study, I am thankful for having the opportunity to play one small role in unveiling the dusty Universe.

APPENDIX A

PAH-DERIVED REDSHIFTS AND LUMINOSITIES

In this section, we describe our method for measuring the PAH redshifts and luminosities that employs MCMC to fully capture the uncertainties. *Spitzer IRS* mid-IR spectra are shown in Figure 2.2, which we use to calculate the redshift probability distribution function $p(z)$ and PAH line luminosities for galaxies in our sample. Rest frame mid-IR wavelengths are host to a diverse range of spectral features from rotational lines of molecular hydrogen to bending and stretching modes of PAH molecules. In the low SNR regime characteristic of high-redshift observations, only the brightest PAH features remain distinctly observable. These features are intrinsically broad with intensities $I_\nu^{(r)}$ well-fit by Lorentzian (Drude) profiles:

$$I_\nu^{(r)} = \frac{b_r \gamma_r^2}{(\lambda/\lambda_r - \lambda_r/\lambda)^2 + \gamma_r^2} \quad (\text{A.1})$$

where following the convention of Smith et al. (2007), r specifies a given PAH complex with central wavelength λ_r , fractional full width at half maximum (FWHM) γ_r and central intensity b_r . Lorentzian profiles are the theoretical spectrum for a classical damped harmonic oscillator, and carry more power in their extended wings compared to a Gaussian. As a result, individual line emission is difficult to separate from adjacent PAH features, as well as any underlying stellar and dust continuum (see Smith et al. 2007 for examples at low-redshift).

Owing to the number of blended line profiles between $5 - 15\mu\text{m}$, PAH flux densities in this wavelength domain are sensitive to the measurement technique (see Smith

et al. 2007 for a thorough analysis). In particular, how the continuum around each PAH feature is estimated can lead to variations in measured line fluxes and equivalent widths by up to a factor of four (Sajina et al., 2007; Smith et al., 2007; Pope et al., 2008). For this reason, we focus our analysis on the $6.2\mu\text{m}$ and $11.3\mu\text{m}$ PAH luminosities, as these features are comparatively isolated from adjacent lines and trace the total PAH luminosity (L_{PAH}) with low scatter in local and high- z star-forming galaxies (Smith et al., 2007; Pope et al., 2008).

Inferring a redshift from PAH features at low SNR and low spectral resolution ($R \sim 100$) is complicated by the many broad and blended PAH lines. Prior to our ALMA observations, redshifts were determined via the spectral decomposition model of Kirkpatrick et al. (2015) which fits mid-IR spectra with an AGN power-law component, a fixed star-forming galaxy PAH template, and dust extinction. This model works well for separating AGN and star formation components (i.e., calculating $f_{\text{AGN,MIR}}$, Table 2.1), but does not always reproduce observed PAH intensities as demonstrated in Figure A.1 (*Left*). Peak emission at line center places the most constraint on a galaxy’s systemic redshift. Therefore, we adopt a simpler model of Lorentzian profiles plus a power-law continuum to fit only the $6.2\mu\text{m}$ and $11.3\mu\text{m}$ PAH complexes. Using this technique, we leverage the relatively isolated lines to measure the target’s redshift. In the rest-frame, our model is

$$I_\nu = N_{pl}\lambda^\alpha e^{-\tau_{\nu,pl}} + \sum_r I_\nu^{(r)}(b_r|\lambda_r, \gamma_r)e^{-\tau_{\nu,pl}} \quad (\text{A.2})$$

where N_{pl} is the power-law scale factor and α is the mid-IR spectral index. We assume a wavelength-dependent Milky Way dust attenuation law for the optical depth parameter $\tau_{\nu,pl}$ (Weingartner & Draine, 2001). This assumption has minimal to no impact on our results given that the primary purpose of the power-law component is to approximate continuum emission in the vicinity of each PAH feature. The second

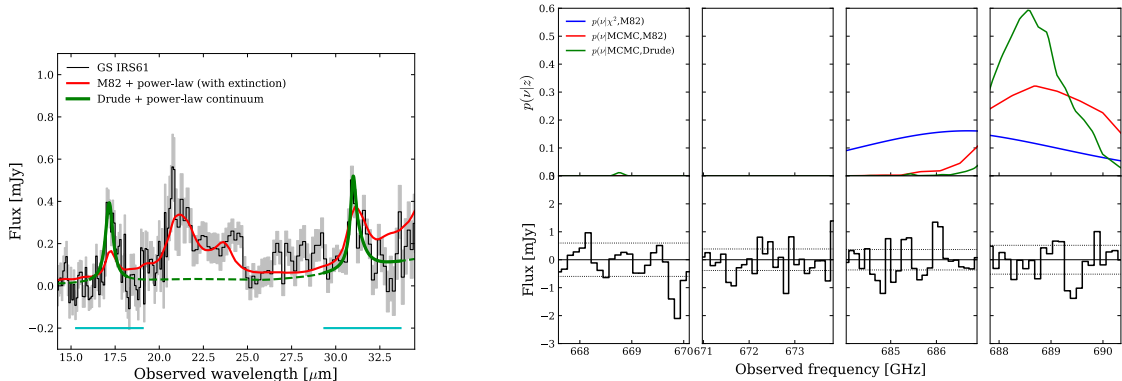


Figure A.1 The importance of model selection in estimating redshifts from PAH spectra. (*Left*): GS IRS61’s *Spitzer IRS* spectrum. Over-plotted in green is our best fit Lorentzian model to the $6.2\mu\text{m}$ and $11.3\mu\text{m}$ PAH complexes. Shown in red is the AGN-SFG decomposition model of Kirkpatrick et al. (2015), which we re-fit to GS IRS61’s spectrum using the same MCMC package as was used in fitting the other model. Regions included in the fit are shown with a solid line, whereas dashed lines indicate wavelengths masked from each model. (*Right*): Bottom panels show GS IRS61’s ALMA Band 9 spectrum, separated into regions of contiguous baseline coverage. Dotted black lines correspond to $\pm 1\sigma$. Upper panels show $p(\nu|z)$, the probability of [CII] being redshift to each observed frequency, for different fitting methods. Red and green lines correspond to the MCMC-derived redshift posteriors from fits in the *Left* panel. The blue line shows a Gaussian approximation of $p(\nu|z)$ from χ^2 minimization fits with the AGN-SFG decomposition model, originally used to plan the observations. From the green curve, we calculate the probability of having the [CII] line fall in the ALMA bandpass to be 0.93 in GS IRS61.

term in Equation A.2 sums over the various PAH complexes included in the fit, each described by a Lorentzian profile (Eq. A.1).

To fit for b_r and z , we fix the central wavelengths of the $6.2\mu\text{m}$ and $11.3\mu\text{m}$ PAH features (λ_r) and γ_r to their values derived in Smith et al. (2007). This implicitly assumes comparable dust grain properties between high- z (U)LIRGs and the inner kpc regions of galaxies from the *Spitzer* Infrared Nearby Galaxies Survey (SINGS; Kennicutt et al. 2003) used to calibrate the PAH free-parameters. Many such features observed in low- z star-forming galaxies are also seen in high- z dusty systems, suggesting that the grain properties responsible for the intrinsically brightest PAH complexes (e.g., $6.2\mu\text{m}$, $7.7\mu\text{m}$, $8.6\mu\text{m}$, $11.3\mu\text{m}$) do not change between $z \sim 2$ and to-

day (Pope et al., 2013; Kirkpatrick et al., 2015). Although the $6.2 \mu\text{m}$ peak can shift by $\Delta\lambda_r \sim 0.1 \mu\text{m}$ from target to target in the Milky Way, these variations are related to the illumination source and relatively stable for both individual and averaged H 2 regions and PDRs in the Milky Way which are expected to dominate mid-IR emission in star forming galaxies (Section 2.2.2 of Tielens 2008, van Diedenhoven et al. 2004).

We fit our model (Eq. A.2) to each *IRS* spectrum using the Markov Chain Monte Carlo (MCMC) code `emcee`, an open-sourced package designed to minimize the number of tunable parameters embedded in a Markov Chain algorithm (Foreman-Mackey et al., 2013). We assume uniform priors on N_{pl} , α , $\tau_{\nu,pl}$, z and b_r , and restrict the fit to spectral domains around the $6.2\mu\text{m}$ and $11.3\mu\text{m}$ PAH features (see cyan horizontal lines in Figure 2.2). The $6.2\mu\text{m}$ and $11.3\mu\text{m}$ features are unambiguous and readily identified by the code without confusion.

Once the fits have been run, we marginalize over all free parameters and extract from each MCMC chain a redshift posterior probability distribution function $p(z)$. We quote the redshift that maximizes the likelihood function as z_{IRS} , and adopt uncertainties from the minimum and maximum redshifts within the 68th percentile of $p(z)$. Next, we use the local continuum around the $6.2 \mu\text{m}$ and $11.3 \mu\text{m}$ line to estimate $L_{6.2\mu\text{m}}$ and $L_{11.3\mu\text{m}}$, following measurement methods used in the literature for direct comparison with published values (e.g., Uchida et al. 2000; Peeters et al. 2002; Pope et al. 2008, 2013). Error bars on $L_{6.2\mu\text{m}}$ and $L_{11.3\mu\text{m}}$ are derived using Monte Carlo analysis, whereby the observed spectrum is perturbed by pixel noise prior to re-calculating the line-flux and PAH feature luminosity. This process is repeated 1000 times, after which we quote the standard deviation of all iterations as the 1σ error. Final measurements and errors of z_{IRS} , $L_{6.2\mu\text{m}}$, and $L_{11.3\mu\text{m}}$ are provided in Table 2.1. We note that silicate absorption at $9.7 \mu\text{m}$ can potentially impact the $11.3 \mu\text{m}$ PAH feature shape and luminosity. There is little evidence for strong silicate absorption in the spectral decomposition shown in Fig. 2.2; however, the low SNR data is consistent

with optical depths of the $9.7\ \mu\text{m}$ feature $\tau_{9.7} \approx 0 - 2$. At this opacity, the $11.3\ \mu\text{m}$ PAH feature strength is decreased by a factor of 1.4 at most (Smith et al., 2007), which is within the uncertainty of our measurements of $L_{11.3\ \mu\text{m}}$.

APPENDIX B

CALCULATING THE PROBABILITY OF OBSERVING LINES FROM TOTAL BANDPASS COVERAGE

In this section, we consider the uncertainties on the redshifts coupled with limited bandpass windows to calculate probabilities of observing [CII] or any generalized line. This analysis is crucial before one can measure upper limits on [CII] from ALMA data containing frequency gaps in baseband coverage. In designing the ALMA Cycle 5 observations, redshifts were determined for each source by fitting a single star-forming PAH template to each galaxy. As demonstrated by Figure A.1 (*Left*), this method insufficiently matches the brightest PAH emission compared to a Lorentzian profile technique. While both fitting approaches estimate a redshift within $\pm 1\sigma$ of each other corresponding to $\Delta z = 0.014$ on average, differences on the order of $\Delta z \sim 0.01$ can shift the [CII] line in or out of the ALMA spectral windows at the highest frequencies. For this reason, our observations may have missed [CII] in some galaxies.

To quantify $p(l|\text{ALMA}, \Delta z)$, we take redshift posterior probability distributions from our MCMC fits to the IRS spectra (Section 3.1, Fig. 2.2) and from these, compute $p(\nu_{[\text{CII}]}|z)$: the probability [CII] would be redshifted to a given frequency. Next, we integrate $p(\nu_{[\text{CII}]}|z)$ first over all frequencies, and then over the frequency domain covered by our bandpass tunings which is typically ~ 10 GHz between 632 – 687 GHz not counting gaps between individual spectral windows. Thus, we quantitatively derive $p(l|\text{ALMA}, \Delta z)$ according to the following prescription:

$$p(l|\text{ALMA}, \Delta z) \equiv \frac{\sum_i \int_{\min(\nu_i)}^{\max(\nu_i)} p(\nu_{[\text{CII}]}|z) d\nu}{\int_{-\infty}^{+\infty} p(\nu_{[\text{CII}]}|z) d\nu} \quad (\text{B.1})$$

where the summation treats each ALMA spectral window independently and avoids gaps in wavelength coverage. Figure A.1 (*Right*) graphically demonstrates this technique for GS IRS61, the only galaxy in our observations where $p(l|\text{ALMA}, \Delta z) > 90\%$. Estimates of $p(l|\text{ALMA}, \Delta z)$ for all other targets are given in Table 2.2.

Additional redshift constraint from rest-frame optical spectroscopy can be used to improve the estimate of $p(l|\text{ALMA}, \Delta z)$. In principle, we would multiply optical redshift posteriors with our MCMC-derived $p(z)$ and integrate the product. We checked for optical spectroscopic redshifts by matching to catalogs from 3D-*HST* grism (Momcheva et al., 2016), VLT/FORS-2 (Vanzella et al., 2008), VANDELS (McLure et al., 2017), MUSE GTO surveys, and ALESS (Danielson et al., 2017). GS IRS50 and GS IRS58 have grism spectroscopic redshifts consistent with z_{PAH} but with higher uncertainty. GS IRS20 and GS IRS61 have C-grade VLT/FORS-2 spectra, and grism redshifts completely inconsistent with the PAH features in both galaxies by $\Delta z = 0.2 - 0.3$, greater than 10 times the uncertainty on their PAH-derived redshifts. GS IRS46 and GS IRS52 do not have optical spectra. In summary, no significantly accurate optical spectroscopic redshifts ($\Delta z < 0.01$) consistent with z_{PAH} were found that changed our results using only PAH fits.

BIBLIOGRAPHY

- Abdullah, A., Brandl, B. R., Groves, B., et al. 2017, *ApJ*, 842, 4
- Aird, J., Nandra, K., Laird, E. S., et al. 2010, *MNRAS*, 401, 2531
- Alaghband-Zadeh, S., Chapman, S. C., Swinbank, A. M., et al. 2013, *MNRAS*, 435, 1493
- Allamandola, L. J., Tielens, A. G. G. M., & Barker, J. R. 1989, *APJS*, 71, 733
- Alonso-Herrero, A., Pereira-Santaella, M., Rieke, G. H., et al. 2010, *Advances in Space Research*, 45, 99
- Andrews, B. H., & Thompson, T. A. 2011, *ApJ*, 727, 97
- Angles-Alcazar, D., Quataert, E., Hopkins, P., et al. 2020, arXiv e-prints, arXiv:2008.12303
- Anglés-Alcázar, D., Quataert, E., Hopkins, P. F., et al. 2021, *ApJ*, 917, 53
- Aniano, G., Draine, B. T., Hunt, L. K., et al. 2020, *ApJ*, 889, 150
- Ansarinejad, B., Shanks, T., Bielby, R. M., et al. 2022, *MNRAS*, 510, 4976
- Aravena, M., Boogaard, L., González-López, J., et al. 2020, *ApJ*, 901, 79
- Armus, L., Charmandaris, V., Bernard-Salas, J., et al. 2007, *ApJ*, 656, 148
- Armus, L., Mazzarella, J. M., Evans, A. S., et al. 2009, *PASP*, 121, 559
- Azadi, M., Aird, J., Coil, A. L., et al. 2015, *ApJ*, 806, 187
- Bakes, E. L. O., & Tielens, A. G. G. M. 1994, *ApJ*, 427, 822
- Banerji, M., Jones, G. C., Wagg, J., et al. 2018, *MNRAS*, 479, 1154
- Begelman, M. C. 2002, *ApJL*, 568, L97
- Beirão, P., Armus, L., Helou, G., et al. 2012, *ApJ*, 751, 144
- Bellocchi, E., Pereira-Santaella, M., Colina, L., et al. 2022, arXiv e-prints, arXiv:2204.02055
- Bendo, G. J., Draine, B. T., Engelbracht, C. W., et al. 2008, *MNRAS*, 389, 629

- Biggs, A. D., & Ivison, R. J. 2008, MNRAS, 385, 893
- Bigiel, F., de Looze, I., Krabbe, A., et al. 2020, ApJ, 903, 30
- Bothwell, M. S., Chapman, S. C., Tacconi, L., et al. 2010, MNRAS, 405, 219
- Bothwell, M. S., Aguirre, J. E., Aravena, M., et al. 2017, MNRAS, 466, 2825
- Bower, R. G., Benson, A. J., Malbon, R., et al. 2006, MNRAS, 370, 645
- Bradford, C., Glenn, J., Armus, L., et al. 2022, in American Astronomical Society Meeting Abstracts, Vol. 54, American Astronomical Society Meeting Abstracts, 304.07
- Brammer, G. B., van Dokkum, P. G., Franx, M., et al. 2012, APJS, 200, 13
- Brandl, B. R., Bernard-Salas, J., Spoon, H. W. W., et al. 2006, ApJ, 653, 1129
- Brandt, W. N., & Alexander, D. M. 2015, A&AR, 23, 1
- Brauher, J. R., Dale, D. A., & Helou, G. 2008, APJS, 178, 280
- Brightman, M., Nandra, K., Salvato, M., et al. 2014, MNRAS, 443, 1999
- Brisbin, D., Ferkinhoff, C., Nikola, T., et al. 2015, ApJ, 799, 13
- Bryant, P. M., & Scoville, N. Z. 1999, AJ, 117, 2632
- Buitrago, F., Trujillo, I., Conselice, C. J., et al. 2008, ApJL, 687, L61
- Bussmann, R. S., Pérez-Fournon, I., Amber, S., et al. 2013, ApJ, 779, 25
- Cañameras, R., Nesvadba, N., Kneissl, R., et al. 2017, A&A, 604, A117
- Cañameras, R., Yang, C., Nesvadba, N. P. H., et al. 2018, A&A, 620, A61
- Calapa, M. D., Calzetti, D., Draine, B. T., et al. 2014, ApJ, 784, 130
- Calistro Rivera, G., Hodge, J. A., Smail, I., et al. 2018, ApJ, 863, 56
- Capak, P. L., Carilli, C., Jones, G., et al. 2015, Nature, 522, 455
- Carilli, C. L., & Walter, F. 2013, ARA&A, 51, 105
- Carniani, S., Maiolino, R., Smit, R., & Amorín, R. 2018, ApJL, 854, L7
- Carniani, S., Maiolino, R., Pallottini, A., et al. 2017, A&A, 605, A42
- Caselli, P., & Ceccarelli, C. 2012, A&AR, 20, 56
- Casey, C., Kartaltepe, J., & Cosmos-Web. 2022, in American Astronomical Society Meeting Abstracts, Vol. 54, American Astronomical Society Meeting Abstracts, 203.02

Casey, C. M., Narayanan, D., & Cooray, A. 2014, PhR, 541, 45

Chang, Y.-Y., Le Floch, E., Juneau, S., et al. 2017, APJS, 233, 19

Chapin, E. L., Pope, A., Scott, D., et al. 2009, MNRAS, 398, 1793

Chapman, S. C., Smail, I., Windhorst, R., Muxlow, T., & Ivison, R. J. 2004, ApJ, 611, 732

Chary, R., & Elbaz, D. 2001, ApJ, 556, 562

Chen, C.-T. J., Hickox, R. C., Alberts, S., et al. 2015, ApJ, 802, 50

Chen, Z., Fang, G., Lin, Z., et al. 2021, ApJ, 906, 71

Chevance, M., Madden, S. C., Lebouteiller, V., et al. 2016, A&A, 590, A36

Chu, J. K., Sanders, D. B., Larson, K. L., et al. 2017, APJS, 229, 25

Cicone, C., Maiolino, R., Sturm, E., et al. 2014, A&A, 562, A21

Ciesla, L., Charmandaris, V., Georgakakis, A., et al. 2015, A&A, 576, A10

Cochrane, R. K., Hayward, C. C., Anglés-Alcázar, D., et al. 2019, MNRAS, 488, 1779

Conselice, C. J. 2014, ARA&A, 52, 291

Cormier, D., Madden, S. C., Lebouteiller, V., et al. 2015, A&A, 578, A53

Cormier, D., Abel, N. P., Hony, S., et al. 2019, A&A, 626, A23

Cortzen, I., Garrett, J., Magdis, G., et al. 2019, MNRAS, 482, 1618

Cox, P., Krips, M., Neri, R., et al. 2011, ApJ, 740, 63

Croiset, B. A., Candian, A., Berné, O., & Tielens, A. G. G. M. 2016, A&A, 590, A26

Croton, D. J., Springel, V., White, S. D. M., et al. 2006, MNRAS, 365, 11

Croxall, K. V., Smith, J. D., Wolfire, M. G., et al. 2012, ApJ, 747, 81

Croxall, K. V., Smith, J. D., Pellegrini, E., et al. 2017, ApJ, 845, 96

Curran, P. A. 2014, Monte Carlo error analyses of Spearman's rank test, [arXiv:1411.3816 \[astro-ph.IM\]](https://arxiv.org/abs/1411.3816)

Dale, D. A., Silbermann, N. A., Helou, G., et al. 2000, AJ, 120, 583

Dale, D. A., Smith, J. D. T., Schlawin, E. A., et al. 2009, ApJ, 693, 1821

Dale, D. A., Aniano, G., Engelbracht, C. W., et al. 2012, ApJ, 745, 95

Dale, D. A., Cook, D. O., Roussel, H., et al. 2017, ApJ, 837, 90

- Danielson, A. L. R., Swinbank, A. M., Smail, I., et al. 2011, *MNRAS*, 410, 1687
- Danielson, A. L. R., Swinbank, A. M., Smail, I., et al. 2017, *The Astrophysical Journal*, 840, 78
- De Breuck, C., Williams, R. J., Swinbank, M., et al. 2014, *The Messenger*, 156, 38
- de Grijp, M. H. K., Lub, J., & Miley, G. K. 1987, *AAPS*, 70, 95
- de Jong, T. 1977, *A&A*, 55, 137
- De Looze, I., Cormier, D., Lebouteiller, V., et al. 2014, *A&A*, 568, A62
- Decarli, R., Walter, F., Venemans, B. P., et al. 2018, *ApJ*, 854, 97
- Decarli, R., Walter, F., González-López, J., et al. 2019, *ApJ*, 882, 138
- Delvecchio, I., Gruppioni, C., Pozzi, F., et al. 2014, *MNRAS*, 439, 2736
- Di Matteo, T., Springel, V., & Hernquist, L. 2005, *Nature*, 433, 604
- Díaz-Santos, T., Alonso-Herrero, A., Colina, L., et al. 2010, *ApJ*, 711, 328
- Díaz-Santos, T., Charmandaris, V., Armus, L., et al. 2011, *ApJ*, 741, 32
- Díaz-Santos, T., Armus, L., Charmandaris, V., et al. 2013, *ApJ*, 774, 68
- . 2014, *ApJL*, 788, L17
- . 2017, *ApJ*, 846, 32
- Díaz-Santos, T., Assef, R. J., Eisenhardt, P. R. M., et al. 2021, *A&A*, 654, A37
- Dietrich, J., Weiner, A. S., Ashby, M. L. N., et al. 2018, *MNRAS*, 480, 3562
- DiMascia, F., Gallerani, S., Behrens, C., et al. 2021, *MNRAS*, arXiv:2102.08956 [astro-ph.GA]
- Downes, D., & Solomon, P. M. 1998, *ApJ*, 507, 615
- Draine, B. T., & Bertoldi, F. 1996, *ApJ*, 468, 269
- Draine, B. T., & Li, A. 2001, *ApJ*, 551, 807
- . 2007, *ApJ*, 657, 810
- Drew, P. M., & Casey, C. M. 2022, *ApJ*, 930, 142
- Dullemond, C. P., Juhasz, A., Pohl, A., et al. 2012, RADMC-3D: A multi-purpose radiative transfer tool, *Astrophysics Source Code Library*, record ascl:1202.015
- Dunlop, J. S., Abraham, R. G., Ashby, M. L. N., et al. 2021, PRIMER: Public Release IMaging for Extragalactic Research, JWST Proposal. Cycle 1, ID. #1837

Elbaz, D., Leiton, R., Nagar, N., et al. 2018, *A&A*, 616, A110

Engel, H., Tacconi, L. J., Davies, R. I., et al. 2010, *ApJ*, 724, 233

Fadda, D., Yan, L., Lagache, G., et al. 2010, *ApJ*, 719, 425

Ferrarese, L., & Merritt, D. 2000, *ApJL*, 539, L9

Finkelstein, S. L., Ryan, Russell E., J., Papovich, C., et al. 2015, *ApJ*, 810, 71

Forbes, J. C., Krumholz, M. R., Goldbaum, N. J., & Dekel, A. 2016, *Nature*, 535, 523

Foreman-Mackey, D., Hogg, D. W., Lang, D., & Goodman, J. 2013, *PASP*, 125, 306

Franceschini, A., Rodighiero, G., & Vaccari, M. 2008, *A&A*, 487, 837

Franceschini, A., Braito, V., Persic, M., et al. 2003, *MNRAS*, 343, 1181

Fritz, J., Franceschini, A., & Hatziminaoglou, E. 2006, *Monthly Notices of the Royal Astronomical Society*, 366, 767

Fudamoto, Y., Smit, R., Bowler, R. A. A., et al. 2022, arXiv e-prints, arXiv:2206.01886

Fujimoto, S., Ouchi, M., Shibuya, T., & Nagai, H. 2017, *ApJ*, 850, 83

Fujimoto, S., Ouchi, M., Kohno, K., et al. 2018, *ApJ*, 861, 7

Gallerani, S., Neri, R., Maiolino, R., et al. 2012, *A&A*, 543, A114

Galliano, F., Madden, S. C., Tielens, A. G. G. M., Peeters, E., & Jones, A. P. 2008, *ApJ*, 679, 310

Gebhardt, K., Bender, R., Bower, G., et al. 2000, *ApJL*, 539, L13

Genzel, R., Lutz, D., Sturm, E., et al. 1998, *ApJ*, 498, 579

Genzel, R., Burkert, A., Bouché, N., et al. 2008, *ApJ*, 687, 59

Genzel, R., Tacconi, L. J., Lutz, D., et al. 2015, *ApJ*, 800, 20

Gerin, M., Ruaud, M., Goicoechea, J. R., et al. 2015, *A&A*, 573, A30

Gerola, H., & Schwartz, R. A. 1976, *ApJ*, 206, 452

Giavalisco, M., Ferguson, H. C., Koekemoer, A. M., et al. 2004, *ApJL*, 600, L93

Glassgold, A. E., & Langer, W. D. 1975, *ApJ*, 197, 347

Goldsmith, P. F., Langer, W. D., Pineda, J. L., & Velusamy, T. 2012, *APJS*, 203, 13

Gómez-Guijarro, C., Elbaz, D., Xiao, M., et al. 2022a, *A&A*, 658, A43

- . 2022b, *A&A*, 659, A196
- Graciá-Carpio, J., Sturm, E., Hailey-Dunsheath, S., et al. 2011, *ApJL*, 728, L7
- Gregg, B., Calzetti, D., & Heyer, M. 2022, *ApJ*, 928, 120
- Grogin, N. A., Kocevski, D. D., Faber, S. M., et al. 2011, *The Astrophysical Journal Supplement Series*, 197, 35
- Gullberg, B., De Breuck, C., Vieira, J. D., et al. 2015, *MNRAS*, 449, 2883
- Gullberg, B., Swinbank, A. M., Smail, I., et al. 2018, *ApJ*, 859, 12
- Gullberg, B., Smail, I., Swinbank, A. M., et al. 2019, *MNRAS*, 490, 4956
- Gürkan, G., Hardcastle, M. J., Jarvis, M. J., et al. 2015, *MNRAS*, 452, 3776
- Habing, H. J. 1968, *BAIN*, 19, 421
- Hashimoto, T., Inoue, A. K., Tamura, Y., et al. 2018, arXiv e-prints, arXiv:1811.00030
- Hashimoto, T., Inoue, A. K., Mawatari, K., et al. 2019, *PASJ*, 71, 71
- Hatziminaoglou, E., Omont, A., Stevens, J. A., et al. 2010, *A&A*, 518, L33
- Hayward, C. C., Jonsson, P., Kereš, D., et al. 2012, *MNRAS*, 424, 951
- Hayward, C. C., Kereš, D., Jonsson, P., et al. 2011, *ApJ*, 743, 159
- Hayward, C. C., Narayanan, D., Kereš, D., et al. 2013, *MNRAS*, 428, 2529
- Hayward, C. C., Torrey, P., Springel, V., Hernquist, L., & Vogelsberger, M. 2014, *MNRAS*, 442, 1992
- Helou, G., Malhotra, S., Hollenbach, D. J., Dale, D. A., & Contursi, A. 2001, *ApJL*, 548, L73
- Helou, G., Roussel, H., Appleton, P., et al. 2004, *APJS*, 154, 253
- Herrera-Camus, R., Bolatto, A. D., Wolfire, M. G., et al. 2015, in *American Astronomical Society Meeting Abstracts*, Vol. 225, American Astronomical Society Meeting Abstracts #225, 109.02
- Hickox, R. C., & Alexander, D. M. 2018, *ARA&A*, 56, 625
- Hodge, J. A., Swinbank, A. M., Simpson, J. M., et al. 2016, *ApJ*, 833, 103
- Hogg, D. W., & Turner, E. L. 1998, *PASP*, 110, 727
- Hollenbach, D. J., & Tielens, A. G. G. M. 1999, *Reviews of Modern Physics*, 71, 173
- Hopkins, P. F., Hernquist, L., Cox, T. J., & Kereš, D. 2008, *APJS*, 175, 356

Hopkins, P. F., Richards, G. T., & Hernquist, L. 2007, *ApJ*, 654, 731

Houck, J. R., Soifer, B. T., Weedman, D., et al. 2005, *ApJL*, 622, L105

Hubble, E. P. 1926, *ApJ*, 64, 321

Hughes, D. H., Serjeant, S., Dunlop, J., et al. 1998, *Nature*, 394, 241

Hughes, T. M., Baes, M., Schirm, M. R. P., et al. 2016, *A&A*, 587, A45

Huynh, M. T., Kimball, A. E., Norris, R. P., et al. 2014, *MNRAS*, 443, L54

Ibar, E., Lara-López, M. A., Herrera-Camus, R., et al. 2015, *MNRAS*, 449, 2498

Ikarashi, S., Ivison, R. J., Caputi, K. I., et al. 2015, *ApJ*, 810, 133

Inami, H., Armus, L., Charmandaris, V., et al. 2013, *ApJ*, 777, 156

Inami, H., Armus, L., Matsuhara, H., et al. 2018, *A&A*, 617, A130

Inoguchi, M., Hosokawa, T., Mineshige, S., & Kim, J.-G. 2020, *MNRAS*, 497, 5061

Isobe, T., Feigelson, E. D., & Nelson, P. I. 1986, *ApJ*, 306, 490

Ivison, R. J., Swinbank, A. M., Swinyard, B., et al. 2010, *A&A*, 518, L35

Jiang, Y.-F., Stone, J. M., & Davis, S. W. 2014, *ApJ*, 796, 106

Jiménez-Andrade, E. F., Magnelli, B., Karim, A., et al. 2019, *A&A*, 625, A114

Jochims, H. W., Ruhl, E., Baumgartel, H., Tobita, S., & Leach, S. 1994, *ApJ*, 420, 307

Jones, A. P., Tielens, A. G. G. M., & Hollenbach, D. J. 1996, *ApJ*, 469, 740

Jones, G. C., Willott, C. J., Carilli, C. L., et al. 2017, *ApJ*, 845, 175

Jonsson, P. 2006, *MNRAS*, 372, 2

Jonsson, P., Groves, B. A., & Cox, T. J. 2010, *MNRAS*, 403, 17

Jourdain de Muizon, M., D’Hendecourt, L. B., & Geballe, T. R. 1990, *A&A*, 235, 367

Kaasinen, M., Walter, F., Novak, M., et al. 2020, *ApJ*, 899, 37

Kalfountzou, E., Stevens, J. A., Jarvis, M. J., et al. 2014, *MNRAS*, 442, 1181

Kartalpepe, J. S., Mozena, M., Kocevski, D., et al. 2015, *APJS*, 221, 11

Kaufman, M. J., Wolfire, M. G., & Hollenbach, D. J. 2006, *ApJ*, 644, 283

Kaufman, M. J., Wolfire, M. G., Hollenbach, D. J., & Luhman, M. L. 1999, *ApJ*, 527, 795

- Kelly, B. C., & Shen, Y. 2013, *The Astrophysical Journal*, 764, 45
- Kennicutt, Robert C., J. 1998a, *ARA&A*, 36, 189
- . 1998b, *ApJ*, 498, 541
- Kennicutt, Robert C., J., Armus, L., Bendo, G., et al. 2003, *PASP*, 115, 928
- Kennicutt, R. C., & Evans, N. J. 2012, *ARA&A*, 50, 531
- Kennicutt, R. C., Calzetti, D., Aniano, G., et al. 2011, *PASP*, 123, 1347
- Kereš, D., Katz, N., Fardal, M., Davé, R., & Weinberg, D. H. 2009, *MNRAS*, 395, 160
- Kereš, D., Katz, N., Weinberg, D. H., & Davé, R. 2005, *MNRAS*, 363, 2
- Kirkpatrick, A., Pope, A., Sajina, A., et al. 2015, *ApJ*, 814, 9
- Kirkpatrick, A., Pope, A., Alexander, D. M., et al. 2012, *ApJ*, 759, 139
- Kirkpatrick, A., Pope, A., Sajina, A., et al. 2017, *ApJ*, 843, 71
- Koekemoer, A. M., Faber, S. M., Ferguson, H. C., et al. 2011, *The Astrophysical Journal Supplement Series*, 197, 36
- Kormendy, J., & Ho, L. C. 2013, *ARA&A*, 51, 511
- Krolik, J. H., & Lepp, S. 1989, *ApJ*, 347, 179
- Lai, S., Armus, L., U, V., et al. 2022
- Lai, T. S. Y., Smith, J. D. T., Baba, S., Spoon, H. W. W., & Imanishi, M. 2020, arXiv e-prints, arXiv:2010.05034
- Lamperti, I., Harrison, C. M., Mainieri, V., et al. 2021, *A&A*, 654, A90
- Lang, P., Schinnerer, E., Smail, I., et al. 2019, arXiv e-prints, arXiv:1905.06960
- Langer, W. D., & Pineda, J. L. 2015, *A&A*, 580, A5
- Langer, W. D., Velusamy, T., Morris, M. R., Goldsmith, P. F., & Pineda, J. L. 2017, *A&A*, 599, A136
- Lanzuisi, G., Delvecchio, I., Berta, S., et al. 2017, *A&A*, 602, A123
- Laurent, O., Mirabel, I. F., Charmandaris, V., et al. 2000, *A&A*, 359, 887
- Le Fèvre, O., Béthermin, M., Faisst, A., et al. 2019, arXiv e-prints, arXiv:1910.09517
- Leavitt, H. S., & Pickering, E. C. 1912, *Harvard College Observatory Circular*, 173, 1

Lebouteiller, V., Cormier, D., Madden, S. C., et al. 2012, *A&A*, 548, A91

Lebouteiller, V., Péquignot, D., Cormier, D., et al. 2017, *A&A*, 602, A45

Leja, J., Johnson, B. D., Conroy, C., & van Dokkum, P. 2018, *ApJ*, 854, 62

Li, A., & Draine, B. T. 2001, *ApJ*, 554, 778

Lilly, S. J., Le Fevre, O., Hammer, F., & Crampton, D. 1996, *ApJL*, 460, L1

Liu, D., Schinnerer, E., Groves, B., et al. 2019, arXiv e-prints, arXiv:1910.12883

Luhman, M. L., Satyapal, S., Fischer, J., et al. 2003, *ApJ*, 594, 758

—. 1998, *ApJL*, 504, L11

Lutz, D., Sturm, E., Tacconi, L. J., et al. 2007, *ApJL*, 661, L25

Lutz, D., Berta, S., Contursi, A., et al. 2016, *A&A*, 591, A136

Madau, P., & Dickinson, M. 2014, *ARA&A*, 52, 415

Madau, P., Ferguson, H. C., Dickinson, M. E., et al. 1996, *MNRAS*, 283, 1388

Magdis, G. E., Rigopoulou, D., Hopwood, R., et al. 2014, *ApJ*, 796, 63

Maiolino, R., Carniani, S., Fontana, A., et al. 2015, *MNRAS*, 452, 54

Malhotra, S., Helou, G., Stacey, G., et al. 1997, *ApJL*, 491, L27

Malhotra, S., Kaufman, M. J., Hollenbach, D., et al. 2001, *ApJ*, 561, 766

Maloney, P. R., Hollenbach, D. J., & Tielens, A. G. G. M. 1996, *ApJ*, 466, 561

Maragkoudakis, A., Peeters, E., & Ricca, A. 2020, *MNRAS*, 494, 642

Marshall, J. A., Herter, T. L., Armus, L., et al. 2007, *ApJ*, 670, 129

Massardi, M., Enia, A. F. M., Negrello, M., et al. 2018, *A&A*, 610, A53

Matthee, J., Sobral, D., Boone, F., et al. 2017, *ApJ*, 851, 145

McKinney, J., Armus, L., Pope, A., et al. 2021a, *ApJ*, 908, 238

McKinney, J., Hayward, C. C., Rosenthal, L. J., et al. 2021b, *ApJ*, 921, 55

McKinney, J., Pope, A., Armus, L., et al. 2020, *ApJ*, 892, 119

McLure, R., Pentericci, L., & VANDELS Team. 2017, *The Messenger*, 167, 31

McMullin, J. P., Waters, B., Schiebel, D., Young, W., & Golap, K. 2007, in *Astronomical Society of the Pacific Conference Series*, Vol. 376, *Astronomical Data Analysis Software and Systems XVI*, ed. R. A. Shaw, F. Hill, & D. J. Bell, 127

- Meijerink, R., Spaans, M., & Israel, F. P. 2007, *A&A*, 461, 793
- Merlin, E., Fortuni, F., Torelli, M., et al. 2019, *MNRAS*, 490, 3309
- Momcheva, I. G., Brammer, G. B., van Dokkum, P. G., et al. 2016, *APJS*, 225, 27
- Mori, T. I., Sakon, I., Onaka, T., et al. 2012, *ApJ*, 744, 68
- Mowla, L. A., van Dokkum, P., Brammer, G. B., et al. 2019, *ApJ*, 880, 57
- Muñoz, J. A., & Oh, S. P. 2016, *MNRAS*, 463, 2085
- Murphy, E. J., Chary, R. R., Dickinson, M., et al. 2011, *ApJ*, 732, 126
- Murphy, E. J., Momjian, E., Condon, J. J., et al. 2017, *ApJ*, 839, 35
- Nandra, K., & Iwasawa, K. 2007, *MNRAS*, 382, L1
- National Academies of Sciences, Engineering, and Medicine. 2021, *Pathways to Discovery in Astronomy and Astrophysics for the 2020s*
- Nelson, D., Pillepich, A., Springel, V., et al. 2018, *MNRAS*, 475, 624
- . 2019, *MNRAS*, 490, 3234
- Nenkova, M., Sirocky, M. M., Ivezić, Ž., & Elitzur, M. 2008a, *The Astrophysical Journal*, 685, 147
- Nenkova, M., Sirocky, M. M., Nikutta, R., Ivezić, Ž., & Elitzur, M. 2008b, *The Astrophysical Journal*, 685, 160
- Nguyen, H. T., Schulz, B., Levenson, L., et al. 2010, *A&A*, 518, L5
- O’Dowd, M. J., Schiminovich, D., Johnson, B. D., et al. 2009, *ApJ*, 705, 885
- Okada, Y., Pilleri, P., Berné, O., et al. 2013, *A&A*, 553, A2
- Oomens, J., Tielens, A. G. G. M., Sartakov, B. G., von Helden, G., & Meijer, G. 2003, *ApJ*, 591, 968
- Osman, O., Bekki, K., & Cortese, L. 2020, *MNRAS*, 498, 2075
- Oteo, I., Ivison, R. J., Dunne, L., et al. 2016, *ApJ*, 827, 34
- Page, M. J., Carrera, F. J., Stevens, J. A., Ebrero, J., & Blustin, A. J. 2011, *MNRAS*, 416, 2792
- Page, M. J., Stevens, J. A., Ivison, R. J., & Carrera, F. J. 2004, *ApJL*, 611, L85
- Page, M. J., Stevens, J. A., Mittaz, J. P. D., & Carrera, F. J. 2001, *Science*, 294, 2516
- Pantoni, L., Massardi, M., Lapi, A., et al. 2021, *MNRAS*, 507, 3998

Peeters, E., Hony, S., Van Kerckhoven, C., et al. 2002, *A&A*, 390, 1089

Peeters, E., Spoon, H. W. W., & Tielens, A. G. G. M. 2004, *ApJ*, 613, 986

Pentericci, L., Carniani, S., Castellano, M., et al. 2016, *ApJL*, 829, L11

Pereira-Santaella, M., Alonso-Herrero, A., Rieke, G. H., et al. 2010, *APJS*, 188, 447

Petric, A. O., Ho, L. C., Flagey, N. J. M., & Scoville, N. Z. 2015, *APJS*, 219, 22

Petric, A. O., Armus, L., Howell, J., et al. 2011, *ApJ*, 730, 28

Pillepich, A., Nelson, D., Springel, V., et al. 2019, *MNRAS*, 490, 3196

Pope, A., Chary, R.-R., Alexander, D. M., et al. 2008, *ApJ*, 675, 1171

Pope, A., Wagg, J., Frayer, D., et al. 2013, *ApJ*, 772, 92

Popping, G., Somerville, R. S., & Galametz, M. 2017, *MNRAS*, 471, 3152

Popping, G., Pillepich, A., Calistro Rivera, G., et al. 2022, *MNRAS*, 510, 3321

Pouliasis, E., Mountrichas, G., Georgantopoulos, I., et al. 2020, *MNRAS*, 495, 1853

Pound, M. W., & Wolfire, M. G. 2008, in *Astronomical Society of the Pacific Conference Series*, Vol. 394, *Astronomical Data Analysis Software and Systems XVII*, ed. R. W. Argyle, P. S. Bunclark, & J. R. Lewis, 654

Privon, G. C., Ricci, C., Aalto, S., et al. 2020, *ApJ*, 893, 149

Puglisi, A., Daddi, E., Valentino, F., et al. 2021, *MNRAS*, 508, 5217

Ramos Padilla, A. F., Ashby, M. L. N., Smith, H. A., et al. 2020, *MNRAS*, 499, 4325

Rawle, T. D., Egami, E., Bussmann, R. S., et al. 2014, *ApJ*, 783, 59

Rémy-Ruyer, A., Madden, S. C., Galliano, F., et al. 2014, *A&A*, 563, A31

Ricca, A., Bauschlicher, Charles W., J., Boersma, C., Tielens, A. G. G. M., & Allamandola, L. J. 2012, *ApJ*, 754, 75

Richings, A. J., Faucher-Giguère, C.-A., & Stern, J. 2021, *MNRAS*, 503, 1568

Riechers, D. A., Hodge, J., Walter, F., Carilli, C. L., & Bertoldi, F. 2011, *ApJL*, 739, L31

Riechers, D. A., Bradford, C. M., Clements, D. L., et al. 2013, *Nature*, 496, 329

Rigopoulou, D., Hopwood, R., Magdis, G. E., et al. 2014, *ApJL*, 781, L15

Roebuck, E., Sajina, A., Hayward, C. C., et al. 2016, *The Astrophysical Journal*, 833, 60

- Rosen, H., & Novakov, T. 1978, *Atmospheric Environment*, 12, 923
- Rosenberg, M. J. F., van der Werf, P. P., Aalto, S., et al. 2015, *ApJ*, 801, 72
- Ruiz, A., Carrera, F. J., & Panessa, F. 2007, *A&A*, 471, 775
- Rujopakarn, W., Rieke, G. H., Eisenstein, D. J., & Juneau, S. 2011, *ApJ*, 726, 93
- Rybak, M., Calistro Rivera, G., Hodge, J. A., et al. 2019, arXiv e-prints, arXiv:1901.10027
- Rybak, M., Hodge, J. A., Greve, T. R., et al. 2022, arXiv e-prints, arXiv:2207.06967
- Saintonge, A., Lutz, D., Genzel, R., et al. 2013, *ApJ*, 778, 2
- Sajina, A., Yan, L., Armus, L., et al. 2007, *ApJ*, 664, 713
- Sajina, A., Yan, L., Fadda, D., Dasyra, K., & Huynh, M. 2012, *ApJ*, 757, 13
- Sajina, A., Yan, L., Lutz, D., et al. 2008, *ApJ*, 683, 659
- Salgado, F., Berné, O., Adams, J. D., et al. 2016, *ApJ*, 830, 118
- Sanders, D. B., & Mirabel, I. F. 1996, *ARA&A*, 34, 749
- Sanders, D. B., Phinney, E. S., Neugebauer, G., Soifer, B. T., & Matthews, K. 1989, *ApJ*, 347, 29
- Sanders, D. B., Soifer, B. T., Elias, J. H., et al. 1988a, *ApJ*, 325, 74
- Sanders, D. B., Soifer, B. T., Elias, J. H., Neugebauer, G., & Matthews, K. 1988b, *ApJL*, 328, L35
- Sanders, R. L., Shapley, A. E., Kriek, M., et al. 2015, *ApJ*, 799, 138
- Sandstrom, K. M., Bolatto, A. D., Bot, C., et al. 2012, *ApJ*, 744, 20
- Sargent, M. T., Daddi, E., Béthermin, M., & Elbaz, D. 2013, *Asociacion Argentina de Astronomia La Plata Argentina Book Series*, 4, 116
- Sargsyan, L., Samsonyan, A., Lebouteiller, V., et al. 2014, *ApJ*, 790, 15
- Sarmiento, R., & Scannapieco, E. 2022, *The Effects of Radiative Feedback and Supernova Induced Turbulence on Early Galaxies*
- Schaerer, D., Boone, F., Jones, T., et al. 2015, *A&A*, 576, L2
- Schmidt, M. 1959, *ApJ*, 129, 243
- Schneider, R., Bianchi, S., Valiante, R., Risaliti, G., & Salvadori, S. 2015, *Astronomy and Astrophysics*, 579, A60

Schutte, W. A., Tielens, A. G. G. M., & Allamandola, L. J. 1993, *ApJ*, 415, 397

Scott, S. E., Fox, M. J., Dunlop, J. S., et al. 2002, *MNRAS*, 331, 817

Scoville, N., Murchikova, L., Walter, F., et al. 2017a, *ApJ*, 836, 66

Scoville, N., Lee, N., Vanden Bout, P., et al. 2017b, *ApJ*, 837, 150

Shangguan, J., Ho, L. C., Bauer, F. E., Wang, R., & Treister, E. 2020, *ApJ*, 899, 112

Shankar, F., Weinberg, D. H., & Miralda-Escudé, J. 2009, *ApJ*, 690, 20

Shapley, A. E., Cullen, F., Dunlop, J. S., et al. 2020, *ApJL*, 903, L16

Sharda, P., Federrath, C., da Cunha, E., Swinbank, A. M., & Dye, S. 2018, *MNRAS*, 477, 4380

Shibuya, T., Ouchi, M., & Harikane, Y. 2015, *APJS*, 219, 15

Shibley, H. V., Papovich, C., Rieke, G. H., Brown, M. J. I., & Moustakas, J. 2016, *ApJ*, 818, 60

Shibley, H. V., Papovich, C., Rieke, G. H., et al. 2013, *ApJ*, 769, 75

Shirakata, H., Kawaguchi, T., Oogi, T., Okamoto, T., & Nagashima, M. 2019, *MNRAS*, 487, 409

Shivaei, I., Reddy, N. A., Shapley, A. E., et al. 2017, *ApJ*, 837, 157

Simpson, J. M., Smail, I., Swinbank, A. M., et al. 2015, *ApJ*, 807, 128

Skelton, R. E., Whitaker, K. E., Momcheva, I. G., et al. 2014, *APJS*, 214, 24

Smit, R., Bouwens, R. J., Carniani, S., et al. 2018, *Nature*, 553, 178

Smith, J. D. T., Draine, B. T., Dale, D. A., et al. 2007, *ApJ*, 656, 770

Smith, J. D. T., Croxall, K., Draine, B., et al. 2017, *ApJ*, 834, 5

Smolčić, V., Aravena, M., Navarrete, F., et al. 2012, *A&A*, 548, A4

Snyder, G. F., Hayward, C. C., Sajina, A., et al. 2013, *ApJ*, 768, 168

Soifer, B. T., Neugebauer, G., Matthews, K., et al. 2000, *AJ*, 119, 509

Speagle, J. S., Steinhardt, C. L., Capak, P. L., & Silverman, J. D. 2014, *APJS*, 214, 15

Spilker, J. S., Marrone, D. P., Aravena, M., et al. 2016, *ApJ*, 826, 112

Spinoglio, L., & Malkan, M. A. 1992, *ApJ*, 399, 504

Springel, V. 2005, *MNRAS*, 364, 1105

Springel, V., Di Matteo, T., & Hernquist, L. 2005, MNRAS, 361, 776

Springel, V., & Hernquist, L. 2003, MNRAS, 339, 289

Stacey, G. J., Geis, N., Genzel, R., et al. 1991, ApJ, 373, 423

Stacey, G. J., Hailey-Dunsheath, S., Ferkinhoff, C., et al. 2010, ApJ, 724, 957

Stacey, H. R., McKean, J. P., Robertson, N. C., et al. 2018, MNRAS, 476, 5075

Stanley, F., Alexander, D. M., Harrison, C. M., et al. 2017, MNRAS, 472, 2221

Stierwalt, S., Armus, L., Surace, J. A., et al. 2013, APJS, 206, 1

Stierwalt, S., Armus, L., Charmandaris, V., et al. 2014, ApJ, 790, 124

Sturm, E., Lutz, D., Tran, D., et al. 2000, A&A, 358, 481

Sutter, J., Dale, D. A., Croxall, K. V., et al. 2019, ApJ, 886, 60

Swinbank, A. M., Dye, S., Nightingale, J. W., et al. 2015, The Astrophysical Journal, 806, L17

Symeonidis, M. 2017, Monthly Notices of the Royal Astronomical Society, 465, 1401

Symeonidis, M., Giblin, B. M., Page, M. J., et al. 2016, Monthly Notices of the Royal Astronomical Society, 459, 257

Symeonidis, M., & Page, M. J. 2018, Monthly Notices of the Royal Astronomical Society, 479, L91

Tacconi, L. J., Genzel, R., Smail, I., et al. 2008, ApJ, 680, 246

Tacconi, L. J., Genzel, R., Neri, R., et al. 2010, Nature, 463, 781

Tacconi, L. J., Neri, R., Genzel, R., et al. 2013, ApJ, 768, 74

Tacconi, L. J., Genzel, R., Saintonge, A., et al. 2018, The Astrophysical Journal, 853, 179

Tadaki, K.-i., Iono, D., Hatsukade, B., et al. 2019, ApJ, 876, 1

Tielens, A. G. G. M. 2008, ARA&A, 46, 289

Tielens, A. G. G. M., & Hollenbach, D. 1985a, ApJ, 291, 722

—. 1985b, ApJ, 291, 747

Tran, Q. D., Lutz, D., Genzel, R., et al. 2001, ApJ, 552, 527

U, V., Sanders, D. B., Mazzarella, J. M., et al. 2012, APJS, 203, 9

Uchida, K. I., Sellgren, K., Werner, M. W., & Houdashelt, M. L. 2000, ApJ, 530, 817

Ueda, Y., Hatsukade, B., Kohno, K., et al. 2018, *ApJ*, 853, 24

Uzgil, B. D., Oesch, P. A., Walter, F., et al. 2021, *ApJ*, 912, 67

Valentino, F., Brammer, G., Fujimoto, S., et al. 2022, *ApJL*, 929, L9

Valtchanov, I., Virdee, J., Ivison, R. J., et al. 2011, *MNRAS*, 415, 3473

van der Wel, A., Franx, M., van Dokkum, P. G., et al. 2014, *ApJ*, 788, 28

van Dienenhoven, B., Peeters, E., Van Kerckhoven, C., et al. 2004, *ApJ*, 611, 928

Vanzella, E., Cristiani, S., Dickinson, M., et al. 2008, *A&A*, 478, 83

Veilleux, S., Rupke, D. S. N., Kim, D. C., et al. 2009, *APJS*, 182, 628

Vito, F., Brandt, W. N., Lehmer, B. D., et al. 2020, *A&A*, 642, A149

Voit, G. M. 1992, *MNRAS*, 258, 841

Walter, F., Decarli, R., Carilli, C., et al. 2012, *Nature*, 486, 233

Walter, F., Carilli, C., Neeleman, M., et al. 2020, *ApJ*, 902, 111

Watson, W. D., & Salpeter, E. E. 1972, *ApJ*, 174, 321

Weingartner, J. C., & Draine, B. T. 2001, *ApJ*, 548, 296

Wethers, C. F., Banerji, M., Hewett, P. C., & Jones, G. C. 2020, *MNRAS*, 492, 5280

Whitaker, K. E., Franx, M., Leja, J., et al. 2014, *ApJ*, 795, 104

Wingen, L. M., Low, J. C., & Finlayson-Pitts, B. J. 1998, *Journal of Chemical Education*, 75, 1599

Wolfire, M. G., McKee, C. F., Hollenbach, D., & Tielens, A. G. G. M. 2003, *ApJ*, 587, 278

Wolfire, M. G., Tielens, A. G. G. M., & Hollenbach, D. 1990, *ApJ*, 358, 116

Wolfire, M. G., Vallini, L., & Chevance, M. 2022, arXiv e-prints, arXiv:2202.05867

Wong, Y. H. V., Wang, P., Hashimoto, T., et al. 2022, *ApJ*, 929, 161

Wu, H., Cao, C., Hao, C.-N., et al. 2005, *ApJL*, 632, L79

Wu, Y., Helou, G., Armus, L., et al. 2010, *ApJ*, 723, 895

Yamashita, T., Komugi, S., Matsuhara, H., et al. 2017, *ApJ*, 844, 96

Yan, L., Chary, R., Armus, L., et al. 2005, *ApJ*, 628, 604

Yang, G., Boquien, M., Buat, V., et al. 2020, *MNRAS*, 491, 740

Younger, J. D., Hayward, C. C., Narayanan, D., et al. 2009, MNRAS, 396, L66
Yun, M. S., & Scoville, N. Z. 1998, ApJ, 507, 774
Yun, M. S., Scott, K. S., Guo, Y., et al. 2012, MNRAS, 420, 957
Zanella, A., Daddi, E., Magdis, G., et al. 2018, MNRAS, 481, 1976
Zavala, J. A., Casey, C. M., Manning, S. M., et al. 2021, ApJ, 909, 165
Zhao, Y., Lu, N., Xu, C. K., et al. 2013, ApJL, 765, L13